Fluid flow through connected sub-seismic features in mudstone

A thesis presented in fulfilment of the requirements for the degree of Doctor of Philosophy

Alistair McCay

University of Strathclyde
Department of Civil and Environmental Engineering
Faults and Fluid Flow Research Group

June 16, 2014

This thesis is the result of the author's original research. It has been composed by the author and has not been previously submitted for examination which has led to the award of a degree.

Signed:

Date:

Acknowledgements

So many people have contributed and helped in so many ways during my research eduction that I cannot, here, thank all who should be thanked, or even express my gratitude thouroughly enough to those who I am able to.

Becky and Zoe, without whose support and guidence my research would now be a memory of frustration and failure, instead of a positive experience about which I have tried to describe but gave up after deleting too many corny platitudes. So perhaps "pure, dead, brill!!!11!" would be best.

Yannick, Rachael and Euan. For patiently explaining to me the basics about rocks and stats, over and over.

Jenni, for being so understanding when I would dissapear for a time, yet again, to poke rocks. And for all the acid, ppfffzzzz.

Contents

List of Figures

List of Tables

Abstract

In the past decade, tight sandstones and shales are increasingly being considered for hydrocarbon production however there are still several scientific and technological obstacles to overcome to ensure unconventional reservoirs are economically viable. Compared with conventional reservoirs, such as permeable sandstone, there is a paucity of basic field research involving mudstone formations, partly due to their susceptibility to erosion making field studies difficult. Other direct applications are radioactive waste disposal and also CO_2 storage.

A 15 metre thick faulted shale unit, deposited in the distal zone of a submarine fan, was studied to investigate the controls on fluid flow through low permeability clastic rock. Turbidite flows are present within the shale as very thin (1-5mm) fine grained sandstone beds, channels and lenses which would not be picked up by wireline logging. The shale is cut by a series of conjugate faults and an associated fracture network; the faults have a maximum recorded throw of 10m i.e. at the limit of typical industry seismic surveys.

Field data show evidence for two distinct flow episodes; carbonate-filled veins and green alteration halos. Flow utilised a subgroup of both the fractures and the more permeable sandstone bands but this flow network varied between flow episodes. Flow modelling shows that the interplay between the structural and depositional features, often averaged out during upscaling processes, acts to significantly increase the connectivity of the flow network emphasising the importance of field statistical characterisation for predicting distributions of such small scale features.

Predictions based upon statistical analysis of data from sparsely distributed boreholes are likely to be needed to accurately characterise these sub-seismic flow networks. Key features that controlled permeability enhancement were closely spaced faults creating an interaction zone of high fracture density and networks with fluid flow conduits that connect to multiple other conduits.

Chapter 1

Introduction

> "The *ignorant* miner digs out the ore without any careful discrimination, while the *learned* first assays and proves it. What wonder then if we find the incompetent miner suffers loss, while the competent one is rewarded by an abundant return from his mining?" – Georgius Agricola

1.1 Research Justification

Mudstone accounts for roughly two thirds of the sedimentary rock covering the Earth's surface (Nichols 2009). Due to its prevalence, mudstone has provided valuable information about the geological history of the Earth; such as the correlation of rocks from the West coast of Scotland and the East Coast of North America indicating a shared geological history (Williams 1962). Beyond purely scientific values mudstone also has great economic importance. Organic rich mudstones provide the source for the hydrocarbons that power the modern world. The organic matter within the mudstones provide the starting material for the formation of hydrocarbons. While the low permeability properties mean that mudstones often trap the hydrocarbons in reservoirs after they have migrated away from the source rock (i.e. in conventional hydrocarbon resources). Without this trapping mechanism these

valuable resources would have leaked out to the surface over geological time and been degraded.

In the last decade unconventional hydrocarbon resources are increasingly being exploited. These unconventional resources include coal bed methane, shale oil and tight gas but (particularly in the U.S.A.) shale gas production has vastly increased in the last decade (Chew 2013). Shale gas resources occur when the natural gas produced in the mudstone (or shale) is then trapped within the low permeability source rock. The mudstone in this case is both the source rock and the reservoir. Such a low permeability reservoir requires stimulation to extract gas, this stimulation is known as "hydraulic fracturing" where high pressure injection of fluids into the shale reduces the effective stress in the rock bringing it to a critical stress state (Fossen 2010), under which the rock is liable to undergo fracturing (Cox 2010). Additionally at a critical stress state fractures are more likely to be hydraulically conductive (Barton et al. 1995). The fractures significantly raise bulk permeability allowing gas to be extracted. Despite these stimulation methods economic extraction relies on the identification of areas where gas has accumulated in large quantities within the target formation, often know as "sweet spots" within industry. These sweet spots exist either because of original organic matter distribution (Aplin and Macquaker 2011) or because of variations in fracture networks. Shale gas has transformed the natural gas market in North America (Pearson et al. 2012) and there are hopes it could have the same impact upon European markets (Energy and Climate Change Committee 2013). However the geology of European shale gas reservoirs can be quite different to the North American reservoirs and economic extraction of shale gas in Europe has not yet been proven.

With the effects of anthropogenic climate change possibly already being felt (Sahid 2012), more attention is being focussed upon carbon capture and storage as a bridging technology towards a low carbon economy. Mudstones are likely to form an integral component of the geological storage system, slowing the migration of injected CO_2 to the surface. Further understanding of how mudstone deforms with changing effective stress (caused by the pore pressure increase of a migrating gas

plume) will be essential to ensure the required CO_2 storage volumes are met (Gaus 2010) in order to make the technique viable. Another application is geological disposal of radioactive waste. Twenty five of the thirty nine countries with a radioactive waste legacy from nuclear activities have opted for deep geological disposal as the preferred waste management solution. Depending upon the regional geology, mudstones may form the target rock where the geological disposal facility (GDF) is buried e.g. mudstone is being considered as the host rock in France (Delay et al. 2007). Where a GDF is not located directly within mudstone, they may also provide part of the natural subsurface barriers between the GDF and the Earth's surface.

For each of these applications, further work understanding the heterogeneity of mudstones and how this affects fluid flow will help inform how best to manage related subsurface investigations. It may also lead to better interpretations of the results of these investigations and improve predictions and extrapolations about the rock surrounding boreholes and seismic cross-sections. The work conducted for this thesis aims to contribute to this area of knowledge. By completing a detailed field investigation in a mudstone with complicated sedimentary and structural features new information has been gained regarding the key controls over fluid flow in such geological settings.

1.2 Outline of this study

1.2.1 Aims and objectives

If present, faults and fractures could form conduits for fluid flow through otherwise low permeability mudstone. Previous studies of faults and of mudstone (discussed in chapter 2) have provided key information about fluid flow in the subsurface. However there remains a comparable lack of basic field evidence from faults and fractures within mudstone dominated units. This study will add to the knowledge by completing a detailed field investigation of a mudstone with complicated sedimentary and structural features; addressing the following questions:

- What were the controls over palaeo-fluid flow episodes in the studied mudstone outcrop?
- How are the fluid flow conduits spatially distributed? Both in 2D and with consideration to 3D systems.
- How have these fluid flow conduit distributions changed over time?
- What has been the effect of these spatial and temporal variations of fluid flow conduits on the permeability properties of the mudstone?

This study has addressed the research questions by:

- Acquiring new data from a mudstone natural analogue.
  - A suitable field area was located.
  - The site was surveyed, producing a detailed map recording evidence for past fluid flow through the rock.
  - The features which have controlled and influenced fluid flow through the geological history of the site were identified.
- A range of field data was analysed.
  - The features in the rock were qualitatively described including the influence they had on fluid flow.
  - The interplay between stress, fluid flow and rock properties were constrained.
  - The quantitative relationships between rock properties and evidence for fluid flow were identified.
- Scenario modelling to further explore the influence of key features on fluid flow through mudstone was performed.
  - Detailed field maps were used to model the locations and connectivity of fluid flow conduit features.

  - This enabled the determination of representative permeabilities for different features.

- Results from the field data was combined with the modelling to characterise the palaeo-fluid flow episodes through the mudstone outcrop and what the permeability properties were during these times.
- This information was used to explore how fluid flow behaviour predictions could be made in similar geological settings.

The outcrop selected is well suited for this investigation for several reasons:

- It has well exposed sedimentary and structural features
  - The exposure needed to be good enough to be able to collect fine scale (<1cm sized) connectivity data from features which potentially acted as fluid flow conduits and to allow this information to be extrapolated into a 3D understanding of the geological system.
- The outcrop has been tilted by 90^0
  - This has resulted in a cross section of a sedimentary sequence being exposed but without the difficulties that a cliff outcrop presents for collecting data
- The mudstone has been affected by low grade metamorphism
  - This has had the effect of strengthening the erosional resistance of the rock, while preserving the sedimentary and structural features
- There is evidence of multiple fluid flow episodes
  - This allows precise information to be collected about which features acted as conduits during palaeo-fluid flow episodes, and how these conduits evolved over time.

1.2.2 Structure of thesis

Chapter 2 provides the background information, which details what has previously been observed to be key influences over fluid flow in the subsurface. Chapter 2 begins discussing influences that are almost universal for all rock types before focussing on influences specifically for mudstone.

Chapter 3 begins by focussing on the background geology of the area. Exploring the wider geological setting will enable the findings from this field site to be put into a wider context; e.g. regional events may have caused fluid flow conduits in the mudstone to be created or changed over time.

The results from the detailed field study of the outcrop are presented in chapter 4 (sedimentary features) and chapter 5 (structural features). The distributions of the possible sedimentary and structural fluid flow conduits are quantified, and the probable sedimentary and structural controls on these distributions are discussed.

The evidence for which features behaved as conduits through different palaeo-fluid flow episodes is presented in chapter 6. The distribution of flowing features and the changing controls on these distributions are discussed. This information is used in chapter 7 to construct fluid flow models of different scenarios for the field site. These models are used to explore the degree of influence that different fluid flow conduits may have had on the overall permeability properties of the mudstone.

Chapter 8 brings the previous chapters' information together. This is to inform a discussion about how a similar formation would best be analysed during a future subsurface fluid flow characterisation study. Different survey techniques are compared for their effectiveness at detecting the fluid flow conduits identified in this study. This leads to discussions about how subsurface data sets are intrinsically incomplete but could still be used to accurately predict distributions of fluid flow conduits in the subsurface. Chapter 9 highlights the key conclusions and discusses potential future work which could lead to further improved identification of fluid flow conduits and thus characterisation of the fluid flow properties of faulted mudstones.

1.3 References

Aplin, A. C., Macquaker, J. H. S. 2011. Mudstone diversity: Origin and implications for source, seal, and reservoir properties in petroleum systems. *AAPG Bulletin*. v.**95** i.**12**. pp. 2031-2059.

Barton, C. A., Zoback, M. D. and Moos, D. 1995. Fluid flow along potentially active faults in crystalline rock. *Geology*. **v.**23 no.8. pp. 683-686.

Chew, K. J. 2013. The future of oil: unconventional fossil fuels. *Philosophical Transactions of The Royal Society*. **372**. pp. 1-34.

Cox, S. 2010. The application of failure mode diagrams for exploring the roles of fluid pressure and stress states in controlling styles of fracture-controlled permeability enhancement in faults and shear zones. *Geofluids*. v.**10**. pp. 217-233.

Delay, J., Rebours, H., Vinsot, A. and Robin, P. 2007. Scientific investigation in deep wells for nuclear waste disposal studies at the Meuse/Haute Marne underground research laboratory, Northeastern France. *Physics and chemistry of the Earth*. v.**32** i.**1-7**. pp. 42-57.

ENERGY AND CLIMATE CHANGE. (2013) *The Impact of Shale Gas on Energy Markets*. HC 785, 2012-2013. London: HMSO.

Fossen, H. 2012. Structural Geology. Cambridge University Press, New York.

Gaus, I. 2010. Role and impact of CO_2-rock interactions during CO_2 storage in sedimentary rocks. International Journal of Greenhouse Gas Control. v.**4** i.**1**. pp. 73-89.

Nichols, G. 2009. Sedimentology and Stratigraphy, Maldon: Blackwell Scientific Publications.

Pearson, I., Zeiewski, P., Gracceva, F., Zastera, P., McGlade, C., Sorrel, S., Speirs, J. and Thonhauser, G. 2012. Unconventional Gas: Potential Market Impacts in the

European Union. *EUR - Scientific and Technical Research series - ISSN 1831-9424*. doi : 10.2790/52499.

Sahid, S. 2012. Vulnerability of the power sector of Bangladesh to climate change and extreme weather events. *Regional Environmental Change*. v.**12** i.**3**. pp. 595-606.

Williams, A. 1962. The Barr and Lower Ardmillan Series (Caradoc) of the Girvan district, S.W. Ayrshire. *Transactions of the Royal Society Edinburgh*. **63**. pp. 629-667.

Chapter 2

Key concepts of subsurface fluid flow

> "If knowledge can create problems, it is not through ignorance that we can solve them." – Isaac Asimov

2.1 Subsurface fluid flow and influence of structural discontinuities

Fluids move through rocks in the interconnected pore spaces between grains. The ease at which fluids can move through these pore spaces is known as permeability. Permeability is not a direct function of pore space (porosity), because a large porosity does not necessarily mean those pore spaces are connected allowing fluids to move through the rock. For example, in mudstones permeability can be strongly influenced by the clay fraction of the rock (Yang and Aplin 2010). This is due to the small particles or grains blocking otherwise connected open pore space. In porous rocks permeability is generally considered to follow Darcy's law (equation 2.1) under laminar flow conditions (Darcy 1856).

$$Q = \frac{-kA}{\mu}\frac{P_b - P_a}{L} \tag{2.1}$$

where Q is discharge (m^3/s), k is permeability (m^2), A is cross-sectional area of unit (m^2), μ is viscosity of the fluid (Pas), $P_a - P_b$ is pressure drop over length (m).

Permeability (k) is the only rock property to appear in equation 2.1. Other than permeability, subsurface fluid flow is governed by fluid properties (μ, $P_a - P_b$) and the scale of observation (A, L). Fluid pressure is affected by lithology and structural discontinuities in the rock (Berg and Habeck 1982) for example low permeability formations can trap buoyant fluids allowing pressure to build up (e.g. a hydrocarbon column Fisher et al. 2001). In addition fluid pressure can also affect permeability properties of the rock by stimulating fractures (Jin and Johnson 2008) or pressure building up leading to break through of fluids through impermeable rock seals (Hesthammer and Fossen 2000, Fisher et al. 2001). Area and length are aspects related to the scale of observation and are not intrinsic properties of the rock. Scale of observation is important as it determines the size of features over which permeability properties can be accurately averaged. That is, the controls on fluid flow through a $1cm^3$ cube of rock will likely be connected pore spaces, changes in which may have a large effect on the overall permeability of that cube of rock. However in a $20m^3$ cube of rock such small isolated changes in individual pore fluid pathways will not have a significant overall influence on the permeability of the rock over $20m^-3$; if there are larger features present. Whereas the formation of a series of faults could influence the permeability over this larger rock volume.

Darcy's law is generally applicable when the scale of observation means that the rock material can be considered as homogeneous. That is, features that could cause small scale zones of permeability heterogeneity are much smaller than the rock mass being considered, allowing a permeability that can accurately characterise a representative elementary volume of the rock. At scales of interest for the industrial applications, discussed in section 1.1, faults create flow conduits (Fairley and Hinds 2004, Walsh et al. 1999, Cartwright et al. 2007, Rowland et al. 2008) or seals (Yielding et al. 1997, Vrolijk and Pluijm 1999, Faerseth 2006) meaning that Darcy's

law may be insufficient to predict subsurface fluid flow. This is because it would be difficult to assign an accurate permeability that generally represents a volume of rock which incorporates such large, discrete heterogeneities. Fracture networks in the rock may also act as fluid flow conduits (Talbot and Sirat 2001) but since fractures are generally smaller than faults, fractures tend to need to be present in networks to influence reservoir-scale fluid flow (Odling et al. 1999). Furthermore faults may influence or be associated with surrounding fracture networks (Curewitz and Karson 1997, Faulker et al. 2006, Cox 2010).

2.2 How faults influence subsurface fluid flow

The influence of faults and fracture networks on fluid flow vary in space and time. A single fault can display a range of properties in different locations; even along a single fault zone. Such heterogeneity can cause the fault to have a combined barrier-conduit behaviour (Caine et al. 1996). Stress changes (Micklethwaite 2008), mineral precipitation (Claesson et al. 2007) and fluid pressure (Miller et al. 2004) can change the conduit-barrier behaviour of a fault. Understanding these issues has been the driver of much research attempting to predict how these complicated structural features influence subsurface fluid flow (Faulkner et al. 2010), and how to incorporate such predictive workflows into fluid flow simulations (Jolley et al. 2007, Manzocchi et al. 1999, Yielding et al. 1997). In order to be able to accurately predict the influence that faults will have over subsurface fluid flow it is necessary to identify the key components of faults which determine their permeability and then constrain the properties of these key components.

Faults are a localisation of strain within rock (Twiss and Moore 1992). Strain is deformation relative to a reference length, and thus is unit-less. Localisation occurs when a significant fraction of the total rock volume does not deform (Couples and Lewis 2007). Therefore any distortion of a rock volume that does occur is achieved by movement in very discrete and spatially compact zones. Failure is often described as brittle or ductile. Where brittle behaviour is “a discrete event in which the failure

of the rock occurs, without significant prior deformation and without warning, at a particular stress" (Paterson 1978). Figure 2.1 shows this variation in behaviour, at brittle failure there is a large drop in stress as brittle deformational localisation (e.g. cracking) occurs in the rock. Rocks show a wide range of physical properties which affect their deformation, however experimental work shows brittle and ductile deformation does not just depend on the rock properties but also on the confining pressure (Desrues et al. 2007). With rocks undergoing high pressure being more likely to deform in a ductile manner.

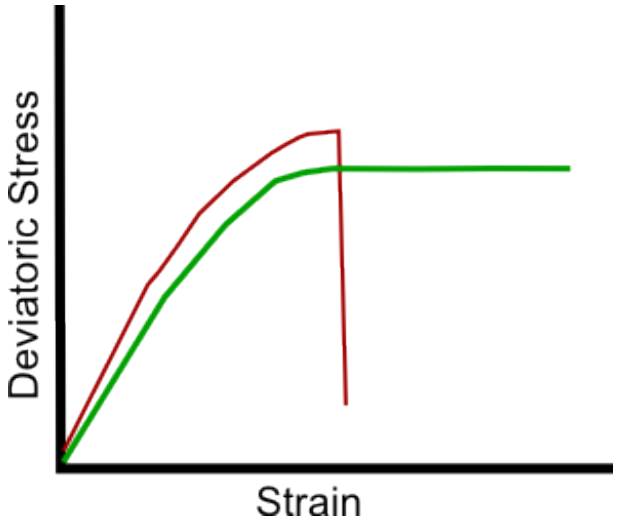

Figure 2.1: Generalised stress-strain curves for brittle (red) and ductile deformation (green).

Stress acts on materials which can resist shearing such as rock; fluids are an example of a material with no shear resistance. Stress is a measure of the force acting across a particular area on a surface and is usually measured in mega-pascals (MPa) in geology. Because stress is force per unit area, the same force will produce less stress if acting over a larger area. When a rock undergoes strain then usually parts of the rock have moved positions relative to each other. However a particular volume of rock may undergo strain homogeneously; i.e. parts of that volume of rock have not moved relative to each other but have moved relative to rock outwith that particular volume.

Faults are often are complicated zones of deformation. In a field outcrop faults can appear as a single planar localisation of strain (figure 2.2-a), however it is much more common to find that faults vary spatially (Caine et al. 1996, Aydin and Eyal 2002) with some areas presenting this single deformation structure but other areas of the same fault zone having a wide and complicated zone of damage (Childs et al. 1997, figure 2.2-b). Some host rocks will also behave in a ductile manner (van der Zee and Urai 2005, figure 2.2-c) or even combined ductile and brittle during deformation (Ishii 2012). Brittle-ductile behaviour is influenced by the depth of fault formation and the mechanical properties of the rocks. A fault zone may offset many different sedimentary layers and rock types which have varying mechanical properties (e.g. Young‘s modulus which is the ratio of strain produced by a different stress). So when layers of rock act to localise the strain then the layers deform differently (TerHeege et al. 2013) leading to a complicated architecture that is difficult to predict. Fault architecture has been found to control fault fluid flow behaviour (e.g. Caine et al. 1996, Shipton et al. 2005) so is a source of uncertainty in subsurface fluid flow understanding.

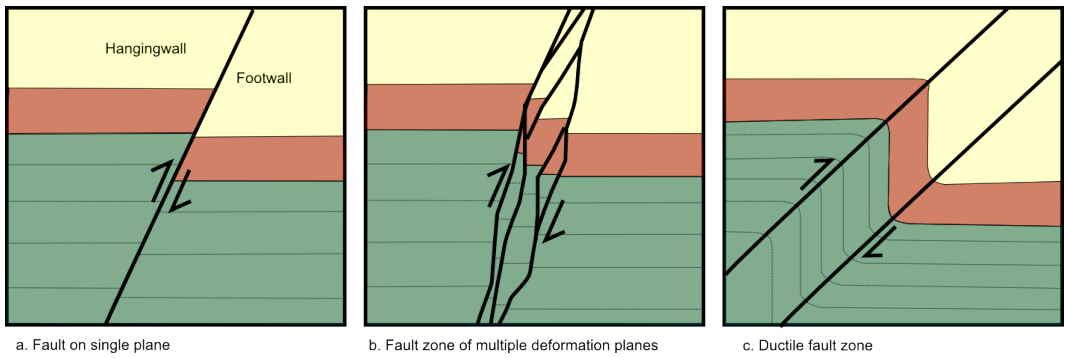

Figure 2.2: Examples of the structure of different fault zones. Faults studied in the field will often show different zones displaying characteristics of each one of these examples within the same fault. From Twiss and Moores 1992.

Complicated fault structures can also be formed by interaction between faults. Such as, relay (Nicol et al. 2002) and interaction zones (Micklethwaite and Cox 2004, Childs et al. 2002) which create regions of complicated structure. These regions often have enhanced permeability compared to the fault zone‘s host rock and also

compared to the portion of fault zone outwith this interaction area. This can be caused by: a higher density of fault related fractures in the interaction zone and tensile stress regime(Gartrell et al. 2004, Micklethwaite and Cox 2004), juxtaposition of two permeable units, or an immature relay ramp resulting in a continuous permeable unit between the two faults (Childs et al. 2002).

A wide range of observations have been made of fault zones acting as fluid flow conduits in outcrops (figure 2.3). There is evidence of diagenetic alteration surrounding fault related fractures (e.g. mineralisation induced colour changes Eichhubl et al. 2009) and mineralisation within fractures (Walker et al. 2012, Cox 2009) due to repeated circulation of fluids. Springs along fault zones can have significant variations in temperature (Fairley and Hinds 2004) and chemistry (Rowland et al. 2008), which demonstrates that discrete highly conductive flow paths exist along fault zones; transporting fluid from depth. Similarly, travertine mounds in Utah are evidence of CO_2 movement along fault planes (Burnside et al. 2013, Kampman et al. 2012). 3D techniques have occasionally permitted direct visualisation of fluid moving through faults in the subsurface (Cartwright et al. 2007, Ligtenberg 2005) corroborating surface observations with subsurface data.

However faults do not just act as flow conduits but can also behave as barriers or seals to fluid flow (Berg and Avery 1975, Fisher et al. 2001, Fisher and Knipe 2001, Steen et al. 2011). This barrier behaviour of faults can be caused by: cataclastic crushing of grains (Shipton et al. 2005, Davis et al. 2000), juxtaposition of sealing onto non-sealing reservoir units (Allan 1989), clay smear into the fault plane (Fisher and Knipe 2001), or cementation of the fault structure (Claesson et al. 2007).

Faults do not generally behave as just a conduit or just a barrier, but are often more accurately described as features with combined conduit-barrier permeability features (figure 2.4). Conduit-barrier fault behaviour occurs when some components of a fault may act as a barrier to flow across the fault e.g. shale smear, while other components act as a conduit to flow parallel with the fault e.g. connected fracture network due to fault related damage (Caine et al. 1996). Alternatively, a fault zone may behave generally sealing, except for a relay zone which acts as a leakage point

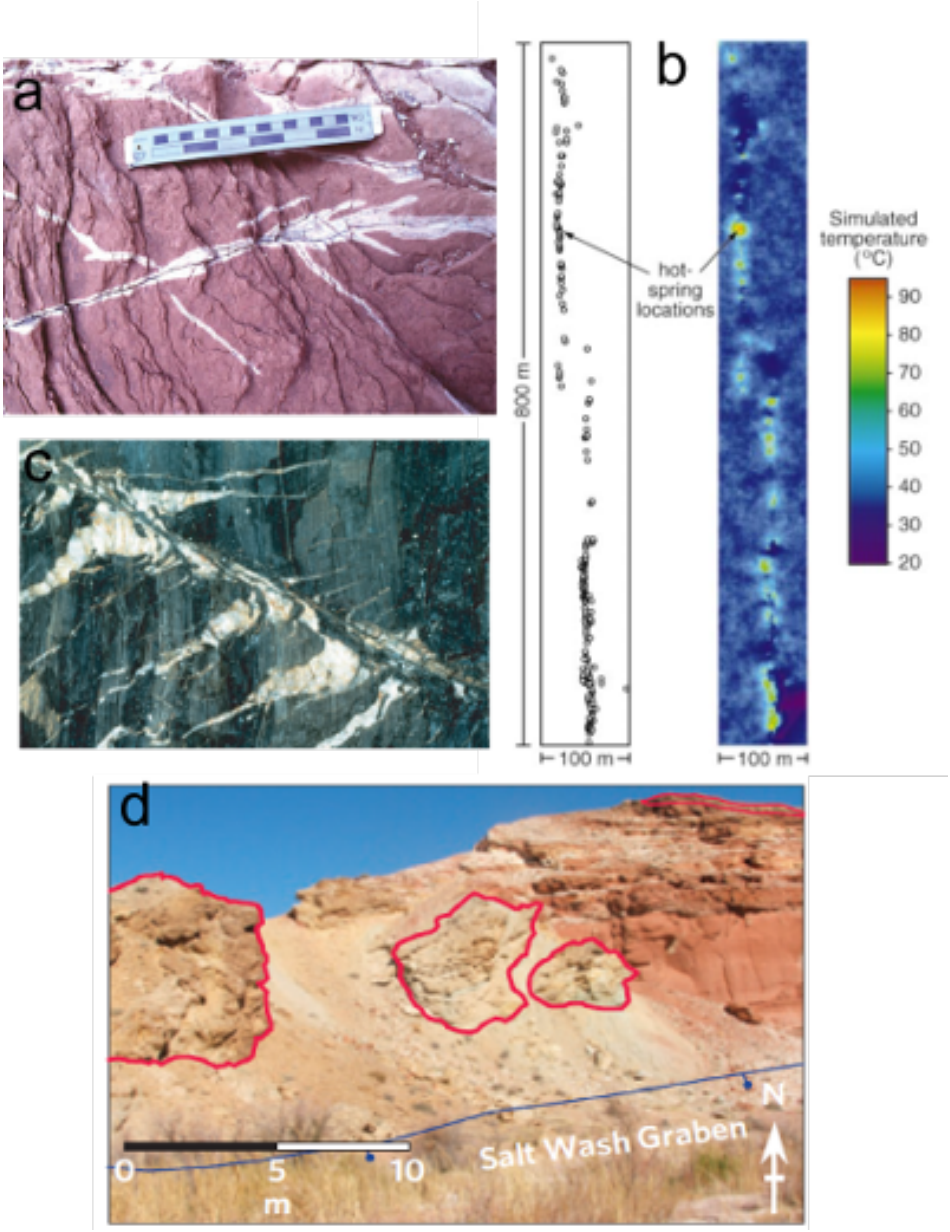

Figure 2.3: Examples of evidence of fault-related fluid flow. a, bleached halos around fractures that have contained hydrocarbons (Eichhubl et al. 2009). b, hot springs along two inferred fault planes. c, quartz veins from hydrothermal fluid system (Cox 2010). d, travertine mounds caused by CO_2 pulses released along a fault plane (Kampman et al. 2012).

(Childs et al. 2002).

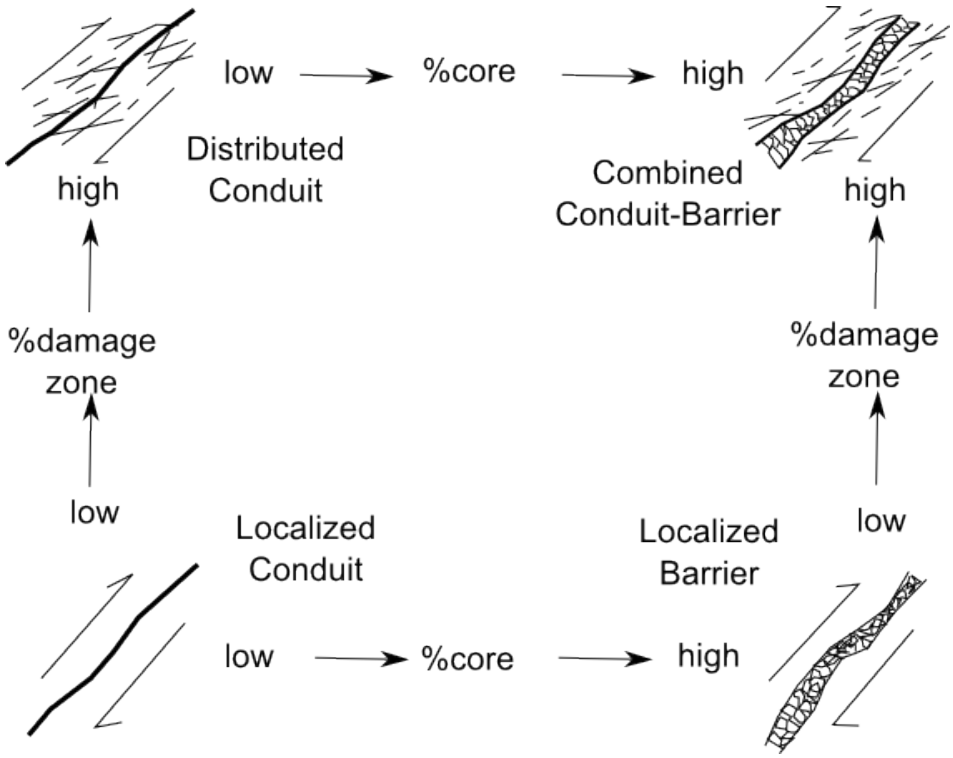

Figure 2.4: Cartoon of how variations of the localisation of damage within a fault zones leads to different fault permeability characteristics. From Caine et al. 1996.

The permeability properties of faults are not static, but can change as the geological system evolves. After earthquake events pulses of fluid can move through newly created or opened fractures (Micklethwaite 2008, Eichhubl and Boles 2000), pressure due to these fluids can also create aftershocks (Miller et al. 2004). Fault sealing processes (e.g. mineral vein precipitation) can then act to return the fault to barrier behaviour (Claesson et al. 2007). Such pulses of fluid are not only controlled by fault movement (i.e. earthquakes) but also by geo-chemical processes driving a fluid pulse (e.g, CO_2 Kampman et al. 2012).

The combination of the above effects make subsurface fault permeability properties very difficult to predict accurately. Additionally the size ranges of faults means it is not straight forward to average out their properties out into a representative

elementary volume that gives an accurate permeability characterisation of the rock; due to fluid flow often being focussed in relatively few conduit. Faults also create thin but long conduits or barriers within a protolith of contrasting fluid flow properties. Attempts to predict the sealing behaviour of faults (Yielding et al. 1997, Allan 1989) and incorporate these into reservoir models (Manzochhi et al. 1999) have been made based on the analysis of the rock properties which are offset or juxtaposed by the faults. However the above techniques were not designed to accommodate fault-parallel flow conduit behaviour of faults, and rely on simplifying the complicated fault properties; due to reservoir simulators being based on grids and fault properties needing to be incorporated within cells. Faults can also be explicitly represented in reservoir models when constructed as a finite element mesh (e.g. Matthai et al. 2007) which allows fault-parallel flow to be simulated. Even with the most sophisticated of models simplifications must be made to be able to represent the geology. This involves significant challenge in deciding what data requires simplification and how this should be done for different modelling purposes.

2.3 How fractures influence subsurface fluid flow

Fractures are planar or sub-planar discontinuities within the rock volume that can be from centimetres in scale to kilometres. A fracture is generally a very thin feature, normally consisting of two fracture surfaces separated by a void or mineral fill (figure 2.5). Fractures are generally split into two categories: shear fractures when shear displacement offsets the fracture surfaces, and joints are when there is no shear displacement between but there is opening normal to the fracture surfaces. The simplicity of the structure is generally (by many field engineers and hydrogeologists) what distinguishes a shear fracture from a fault, although some shear fractures with larger displacements of many metres are sometimes referred to as faults.

Fractures form when rock undergoes localisation of deformation in response to stress; in contrast unlithified porous material, such as sand, may deform by granular flow and not fracture if the stress on individual grains is not high enough. As a concept,

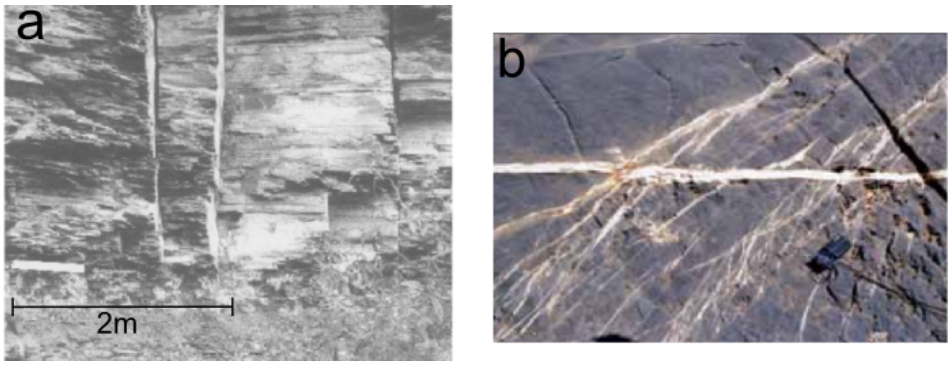

Figure 2.5: a. Vertical fractures (joints) in shale outcrop (From Lash et al. 2004). b. Intersecting vein arrays (From Virgo et al. 2013).

stress is often thought of as acting on the surfaces of an infinitesimal cube in the subsurface (figure 2.6). There are nine components of stress, three of which are normal stress and the other six are shear stresses.

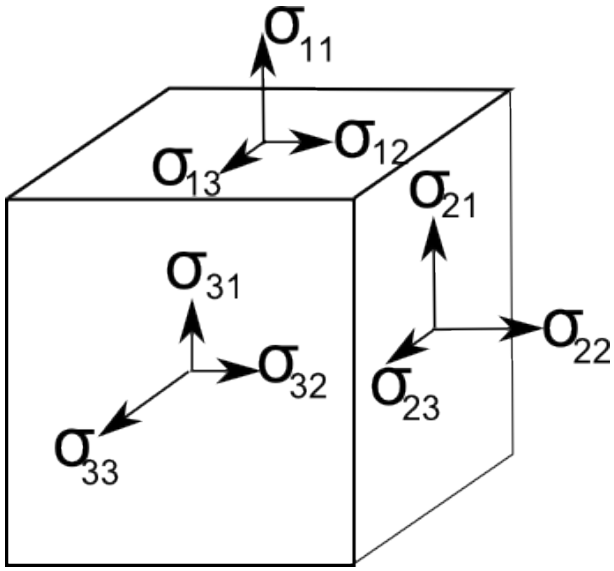

Figure 2.6: The components of stress which act on an infinitesimal cube in the subsurface. σ_{11}, σ_{22}, and σ_{33} are the normal stresses acting on the planes of the cubes. σ_{12}, σ_{13}, σ_{21}, σ_{23}, σ_{31}, and $\sigma 32$ are the shear stress components, two of which act on each plane.

These stress components can be represented on the following 3x3 matrix. Where the diagonal components are the normal stresses, and the off-diagonal components

the shear stresses shown in figure 2.6.

$$\begin{matrix} \sigma_{11} & \sigma_{12} & \sigma_{13} \\ \sigma_{21} & \sigma_{22} & \sigma_{23} \\ \sigma_{31} & \sigma_{23} & \sigma_{33} \end{matrix} \tag{2.2}$$

The infitesimal cube (shown in figure 2.6) can be orientated in such a way that the shear stress components cancel out. All that is left are the normal stress components, these are called the principal stresses.

$$\begin{matrix} \sigma_1 & 0 & 0 \\ 0 & \sigma_2 & 0 \\ 0 & 0 & \sigma_3 \end{matrix} \tag{2.3}$$

The principal stresses take up the diagonal normal stress components in the stress tensor matrix. The σ_1, σ_2, and σ_3 act perpendicular to each other and represent different values of normal stress acting on the rock as $\sigma_1 \geq \sigma_2 \geq \sigma_3$. Typically one of these principal stress vectors will act vertically while the other two act horizontally, however this is not always the case particularly to due deformation influencing the local stress field.

Joints and shear fractures form at different orientations to the principal stress vectors and thus represent the deformational response of the rock to different stress conditions (figure 2.7). Joints tend to form perpendicular to σ_3 and parallel to σ_1 and σ_2, whereas shear fractures usually form at +/- 30° to σ_1 dipping towards σ_3 (figure 2.7). The angle at which the shear fractures form is dependent on the internal friction of the rock (Byerlee 1978), but shear fractures are normally considered to form at +/- 30° for most rock types. This is due to the ratio between shear stress and normal stress being large at planes in this orientation (figure 2.8).

When a rock is on the verge of failure it is referred to as being critically stressed. The Coulomb failure criterion (Coulomb 1776) considers the shear stress (σ_s) and

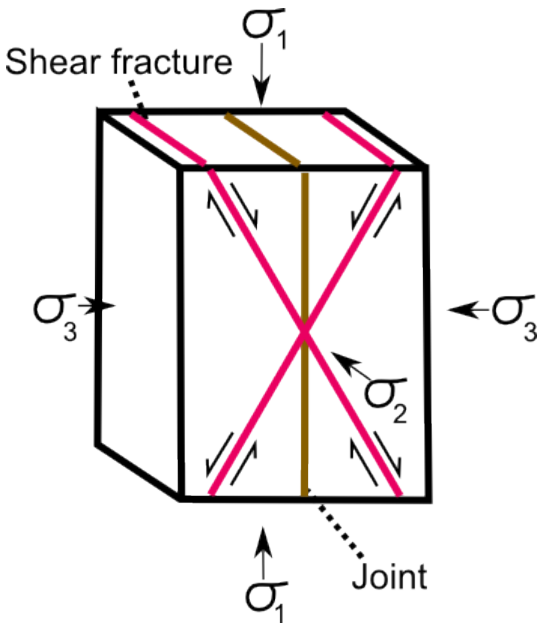

Figure 2.7: "Andersonian" orientations that joints and shear fractures will typically form at in response to applied stress, from Fossen 2009.

normal stress (σ_n) acting within the rock during critical stress as:

$$\sigma_s = C + \sigma_n tan\phi \tag{2.4}$$

where ϕ is the internal angle of friction, often 30°, and tanϕ is the coefficient of internal friction of rock which is typically 0.6 but can range between 0.47-0.7. C is the cohesion of the rock.

The Griffith failure criterion (Griffith 1921) is also commonly used when examining fracture propagation. The Griffith failure criterion is given by the following equation:

$${\sigma_s}^2 + 4T\sigma_n - 4T^2 = 0 \tag{2.5}$$

Where T is the tensile strength of the rock. When $\sigma_n = 0$ in the Griffith failure criterion then $\sigma_s = 2T$, which is equivalent of C in the Coloumb failure criterion. This allows the two criterion to be combined, as experimental data shows that the Griffith failure criterion is most accurate for tensile failure whereas the Coulomb criterion is more realistic in the higher stress values compressive failures.

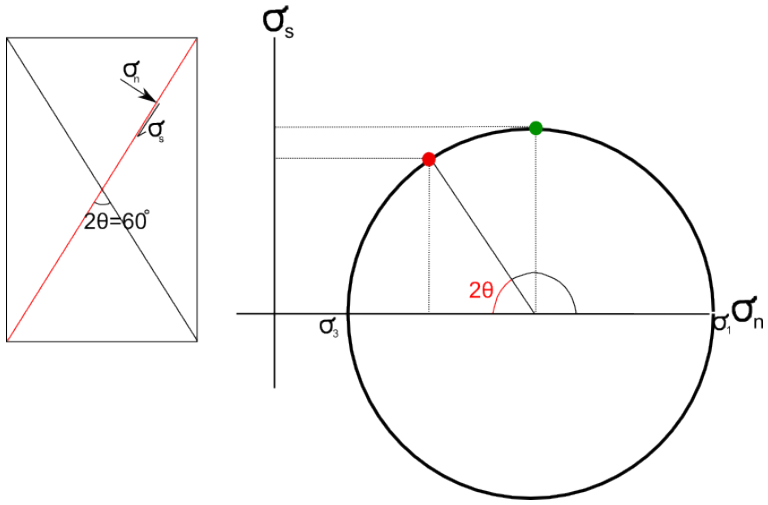

Figure 2.8: Idealised shear fracture (red) which is 60° to the other shear fracture. Mohr's circle shows that at maximum shear stress (green dot) normal stress is also high, where the normal stress acts to stop movement on the shear fracture. At the plane at the red dot (30° to σ_1) shear stress is slightly lower than at the green dot but normal stress is much lower. This means it is easier for a shear fracture to form along the plane represented by the red dot than the green dot. From Fossen 2012.

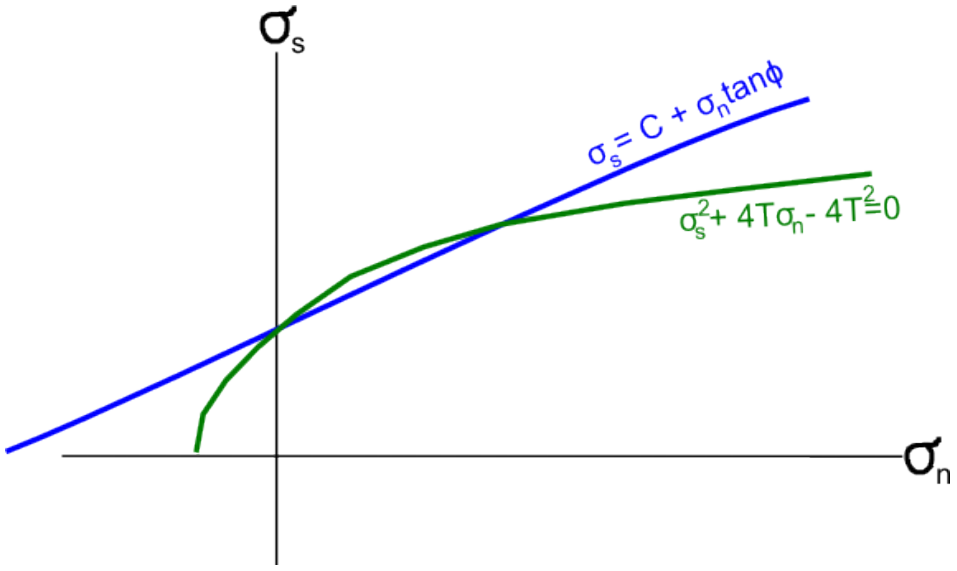

Figure 2.9: Coulomb and Griffith failure criterion plotted on graph of shear stress vs. normal stress.

The Griffith-Coulomb failure criterion can be effectively represented on a Mohr diagram (figure 2.9). A Mohr diagram is a two dimensional circular representation of the stress tensor. The Mohr circle is used to determine the different components of stress acting on planes in the rock. The stress conditions are graphically plotted on the Mohr diagram. The x-axis of these diagrams is normal stress (σ_n) and the y-axis is shear stress (σ_s).

The location and size of the Mohr circles depends both on the magnitude of stress and the differential stress ($\sigma_1 - \sigma_3$). Figure 2.10 shows an example of two Mohr circles plotted with a combined Griffith-Coulomb failure criterion. When the Mohr circles touch the failure criterion, plotted on the Mohr diagram as a line, the rock is critically stressed. In figure 2.10 one Mohr circle represents a critically stressed state (dashed circle-figure 2.10) as it touches the failure criterion. The other circle (solid circle-figure 2.10) represents a stable state of stress. The lower value of σ_1 for the critically stressed circle shows the importance of differential stress ($\sigma_1 - \sigma_3$) compared with maximum stress (σ_1) for understanding failure of rock. Figure 2.10 also shows how joints and shear fractures form in different stress regimes. Shear fractures form when the Mohr's circle touches the sloping part of the failure criterion (in blue on figure 2.10) whereas joints form in the "tensile" area of the Mohr diagram where the failure criterion curves to become vertical (in green on figure 2.10).

True tensile stresses are relatively rare in the subsurface, but yet joints are still observed in many outcrops. Tensile stresses may occur due to cooling related contraction of magmatic rocks, or uplift of rocks containing residual stress (Engelder 1985). However tensile conditions can also be caused by fluid pressures in the subsurface. Effective stress (σ'_n) is used to illustrate this concept:

$$\sigma'_n = \sigma_n - P_f \tag{2.6}$$

where P_f is fluid pressure.

Due to fluid pressure acting equally on σ_1 and σ_3, increasing fluid pressure has the effect of moving the Mohr circle to the left along the axis towards the failure envelope

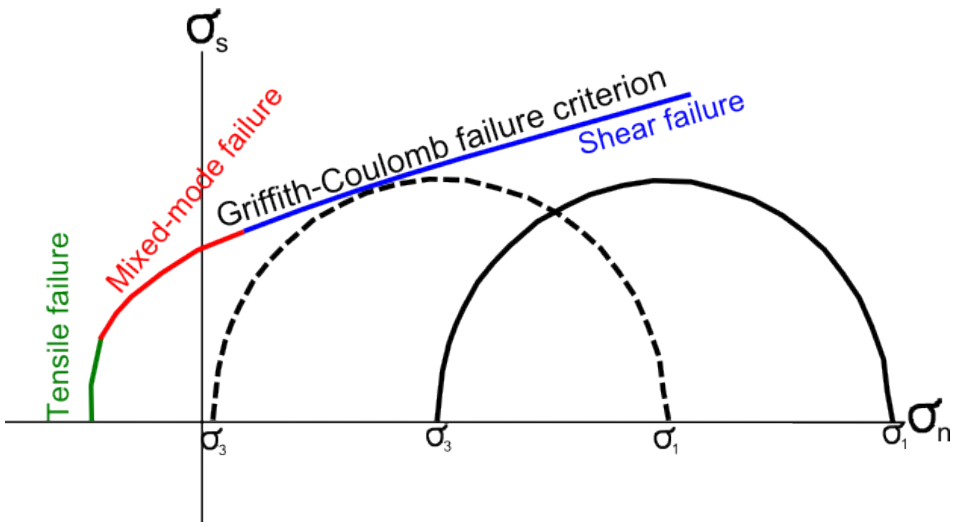

Figure 2.10: Example of Mohr circles used to understand rock failure, these represent a 2D approximation, using only σ_1 and σ_3 on the x-axis. The circle is drawn between σ_1 and σ_3, this area represents different raios of shear and normal stress found in the rock. If a circle touches the failure envelope this means the rock is critically stressed and close to failure (dotted circle). The solid-line circle is in a stable state of stress. The failure criterion used in this example is a combined Griffith-Coulomb, although other criteria are used depending on the analysis needed.

(figure 2.11); thus bringing the rock closer to failure. When the differential stress is relatively small ($\sigma_1 - \sigma_3 < 4T_0$), the Mohr circle will intersect the failure criterion in the tensile stress area. This can occur when $P_f > \sigma_3$ causing σ_3' to be negative and therefore effectively tensile.

The failure criteria discussed above are for intact rock. However fractures can form in networks, meaning that the initiation and propagation of an individual fracture will not occur in isolation, but is influenced by other fractures. A fractured rock mass may have reduced cohesion compared to intact rock if the fracture-blocks lose contact, so tensile stress can be accommodated by dilatancy of pre-existing fractures rather than the formation of new joints. However rock may regain cohesion if fractures become filled by mineral precipitation forming veins. Fractures also create a surrounding zone which can influence the initiation, propagation, and termination of

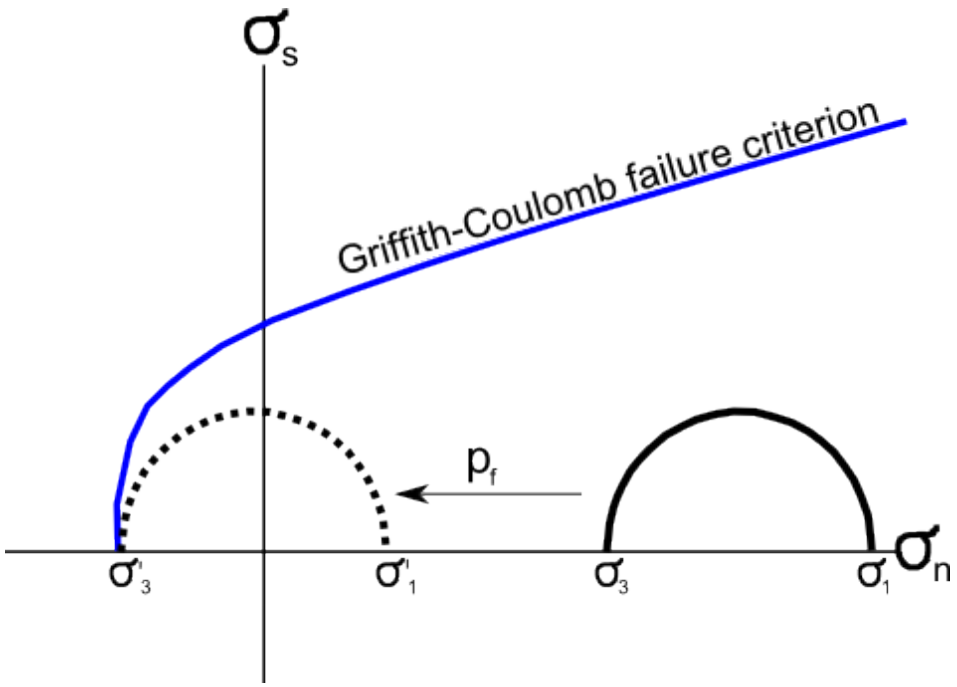

Figure 2.11: Mohr diagram showing the effect of fluid pressure on a Mohr circle. Fluid pressure moves the rock to a critical state of stress in the region of the diagram where joint formation occurs.

nearby fractures (Pollard and Segall 1987). Stress perturbations may cause joints to be retarded from propagating nearby other joints, or cause propagating fractures to curve towards those pre-existing fractures (Dyer 1988). Propagating fractures may also terminate when intersecting with a pre-existing fracture, due to the stresses not transferring across the free surface of the fracture. Layering of sedimentary rock also influences fracture propagation as mechanical properties (such as Young‘s modulus) varies between layers (Brenner and Gudmundsson 2004). Additionally the sedimentary layers may be poorly bonded together terminating fracture propagation (Cooke and Underwood 2004).

Individual fractures may not be large enough to have a significant impact on regional fluid flow patterns. However fracture networks have been observed to strongly influence subsurface fluid flow in a range of settings. In crystalline rocks fractures are the source of inflow in underground research laboratories (Talbot and Sirrat

2001) and fractures are also exploited to create flow within geothermal reservoirs (Genter and Traineau 1996). Evidence for palaeo-fluid flow circulation in fracture networks has also been observed in mineral veins (Eichhubl and Boles 2000) and in the presence of alterations surrounding fractures (Eichhubl et al. 2009). The connectivity of fractures is vital for networks to have a strong influence on fluid flow over large distances; particularly for low permeability rocks. The connectivity of a fractured network is influenced by fracture density, orientation distribution, and length distribution of the fractures (Odling et al. 1999).

Observations of natural fracture networks indicate that flow tends to be highly compartmentalised, with only a relatively few fractures responsible for the majority of the flow in fracture networks in granite (Black and Barker 2006, Talbot and Sirat 2001, Losh et al. 1999). This is due to flow being concentrated within the back bone of the fracture network, i.e. those fractures that do not form "dead ends" to fluid flow in the network. Alternatively this could be due to channelling of flow within individual fracture planes (Abelin et al. 1987) where 20% of the fracture plane is made up of channels. Such backbone networks were investigated using the mathematical ideas from percolation theory (Berkowitz 1995). Percolation theory investigates the density of randomly orientated lines it takes to fully connect four sides of a square and what the network of connected lines looks like compared with those which are not part of the connecting network. The results from percolation theory are comparable with those observations from natural fracture systems, as in percolation theory only a fraction of the total number of lines present are actually involved with the connected network (figure 2.12). However randomly orientated distributions of fractures do not generally occur in nature due to fracture orientations being dependent on stress orienations. So the ideas of percolation theory have been modified to represent more accurately distributed fracture networks (Manzocchi 2002).

These combined effects of fracture interaction and fluid flow compartmentalization in fracture networks mean that although the growth and propagation of individual fractures may be understood; fracture networks are complicated features which cre-

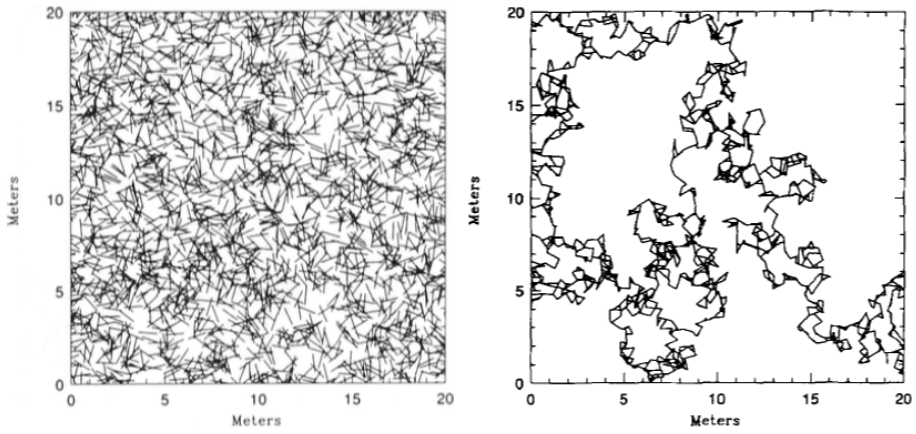

Figure 2.12: Example of a randomly orientated distribution with negative length distribution of lines (fractures) with the associated "backbone" or connected network on right image. From Berkowitz 1995

ate very difficult to predict flow behaviours (Makel 2007). The controls on fluid flow vary between fracture networks depending on fracture network connectivity, aperture distribution, and fracture length distribution. For flow in fracture networks to be fully understood quantitative data about fracture properties, such as orientation, density and controls on propagation in a system need to be collected.

2.4 Fluid flow properties of mudstone

Intact mudstone is a low permeability rock, with typical permeability values of between 10^{-6} and 10^{-2} mD (Todd and Mayes 2005, Dewhurst and Siggins 2006, Armitage et al. 2011) with the variation largely due to the clay fraction of the rock (Yang and Aplin 2010), i.e. more clay leading to lower permeability; although many mudstone formations have varying permeability heterogeneity. Permeability tends to be higher parallel to bedding planes due to fissility of grains (Armitage et al. 2011) although some are quite homogeneous e.g. Boom Clay in France and Belgium (Mazurek et al. 2008). Mudstone units are often interbedded with coarser material, such as siltstone or sandstone (Nichols 2009), due to depositional cycles.

For example, turbidite flows can cause such material heterogeneity in mudstone (Figure 2.13, Bouma 1962). Turbidite formations can present complicated reservoirs for hydrocarbon exploration (Weimer et al. 2000) as production is achieved through the interconnection of many sedimentary facies where permeability and porosity properties can be different over the boundaries of overlapping turbidite deposits.

This thesis investigates a mudstone unit which hosts the very distal remnants of turbidite flows. The distal regions of turbidite systems have been studied to understand depositional environments (e.g. Crimes 1973, Walker 1967). Walker 1967 also discusses the influence of sand-rich turbidite sheet system on hydrocarbon migration, but does not link this with structural influences. Distal turbidtes would be generally expected to form seals to hydrocarbon flow, even with coarser grained bands or permeability heterogeneity. Therefore faults and fracture networks could be expected to provide fluid flow conduits, if present in this type of rock (Dewhurst et al. 1999, Ingram and Urai 1999). Shale gas exploration relies on the concepts of how fractures in distal turbidite formations are responsible for the majority of fluid flow. As an example, the sedimentary setting of the Bowland shale (where significant quantities of UK shale gas reserves are located) is deep water with turbidite channel bodies (Pater and Baisch 2011)

Previous mudstone studies have investigated the permeability properties of mudstone formations using core samples (Bolton et al. 2000, Aplin and Macquaker 2011) rather than field outcrops. Outcrop studies provide a vital scale bridge between information from small scale samples and large-scale data (e.g. seismic). Previous studies in faulted mudstone or turbidite sequences have focussed at scales of seismically resolvable faults which cut thick sedimentary features (Roggero et al. 2012, Manzocchi et al. 2007, Cartwright et al. 2007). Seismically resolvable faults are those which have a large enough throw to be detected by seismic surveys. The offset beds are what are typically visible from the seismic surveys, so a fault with larger throw will create a visible offset of these markers on the resolved seismic image. Subseismic faults are those faults which do not offset the beds enough to be confidently resolved on a seismic image. A typical rule of thumb is that faults with

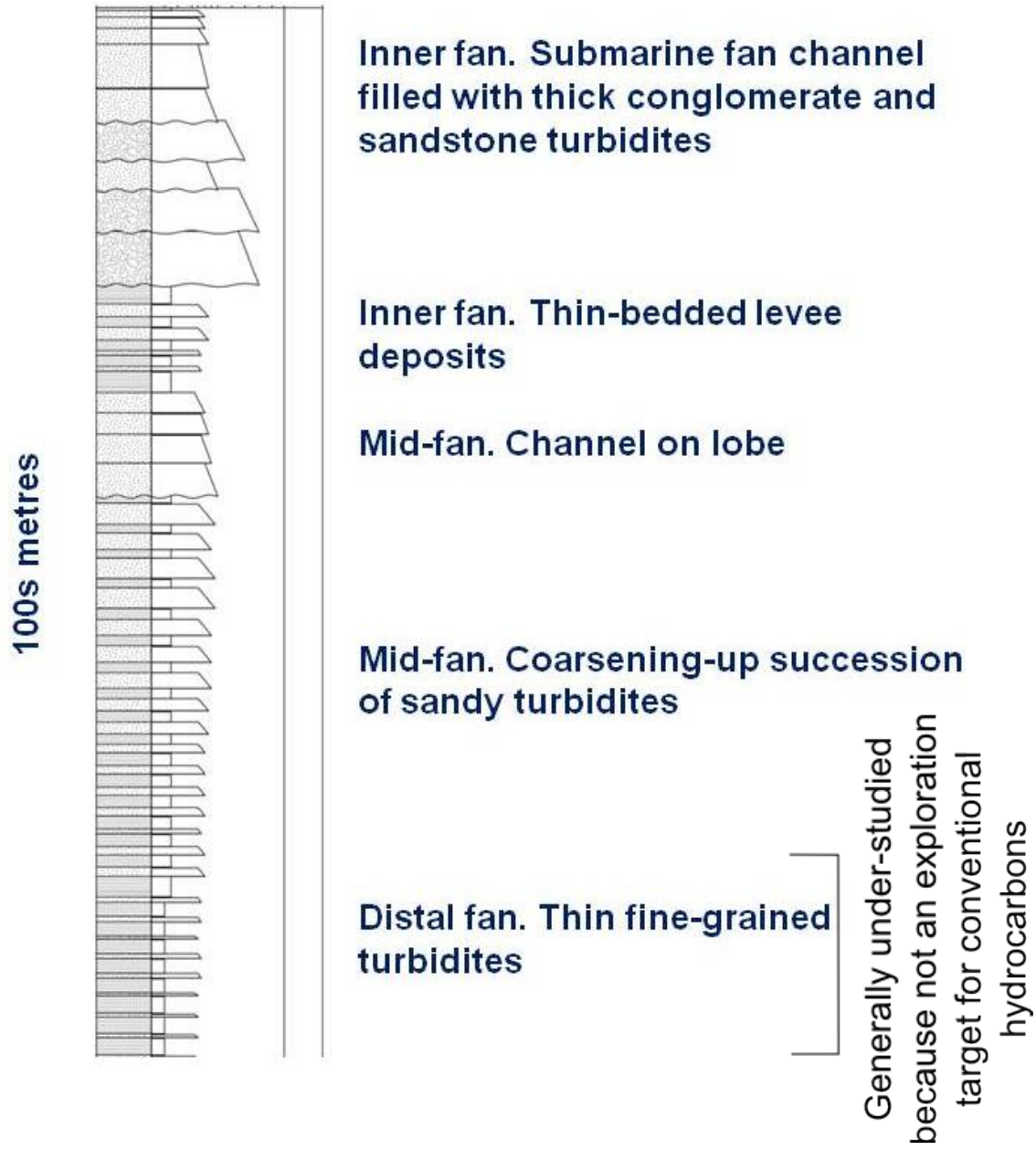

Figure 2.13: Example of sedimentary log expected in different areas of a submarine fan depositional environment. With coarser units due to turbidite mass flows transporting material from shallow to deeper areas. From Nichols 2009.

throws of less than 10m will be subseismic. The focus was on these larger features as this is where conventionally recoverable hydrocarbons would located. This focus has

resulted in much fewer field studies investigating the features that have controlled past fluid flow events in mudstone compared to other sedimentary rocks (Kampman et al. 2012, Eichhubl et al. 2009, Eichhubl and Boles 2000, Zecchin and Caffau 2012). One reason is that poorer resistance to erosion means that mudstone outcrops are less common than the tougher sandstone and carbonate outcrops. Outcrop studies have been conducted for shale gas research focussing on linking joint spatial distribution with deformational history (e.g. Engelder et al. 2009, Lash et al. 2004, Evans 1994). However chemical evidence for which features acted as palaeo-fluid flow conduits were not collected as this was not the focus of these studies.

There is a relative lack of information from outcrop studies investigating what are the controlling fluid flow features in a mudstone-dominated heterogeneous environment, and how these controls have evolved. A study of an outcrop of mudstone where palaeo-fluid flow conduits can be identified could provide new and useful information to support current conceptual understanding of these systems (e.g. Ingram and Urai 1999). This could help to constrain what the controls are over subsurface fluid flow in complicated structural and sedimentary settings.

2.5 References

Abelin, H., Birgesson, L., Gidlund, J. Moreno, L. Neretnieks, I., Widen, H. and Argen, J. 1987. 3D-migration experiment-Report 3: Performed experiments, results and evaluation. *Stripa Project Technical Report.* Swedish Nuclear Fuel and Waste Management (SKB). Stockholm.

Allan, U. S. 1989. Model for Hydrocarbon Migration and Entrapment Within Faulted Structures. *AAPG Bulletin.* v.**73** i.**7**. pp. 803-811.

Aplin, A. C., Macquaker, J. H. S. 2011. Mudstone diversity: Origin and implications for source, seal, and reservoir properties in petroleum systems. *AAPG Bulletin.* v.**95** i.**12**. pp. 2031-2059.

Aydin, A. and Eyal, Y. 2002. Anatomy of a Normal Fault with Shale Smear: Implications for Fault Seal. *AAPG Bulletin.* v.**86**. pp.1367-1381.

Armitage, P. J., Falkner, D. R., Worden, R. H., Aplin, A. C., Butcher, A. R. and Iliffe, J. 2011. Experimental measurement of, and controls on, permeability and permeability anisotropy of caprocks from the CO_2 storage project at the Krechba Field, Algeria. *Journal of Geophysical Research - Solid Earth.* v.**116**. 10.1029/2011JB008385

Berg, R. R. and Habeck, M. H. 1982. Abnormal pressures in the lower Vicksburg, McAllen Ranch field, South Texas. *Gulf Coast Association of Geological Societies Transactions.* v.**32**. pp. 247-253.

Berkowitz, B. 1995. Analysis of Fracture Network Connectivity Using Percolation Theory. *Mathematical Geology.* v.**27** i.*4*. pp. 467-483.

Bolton, A. J., Maltman, A. J. and Fisher, Q. 2000. Anisotropic permeability and bimodel pore-size distributions of fine-grained marine sediments. *Marine and Petroleum Geology.* v.**17** i.**6**. pp. 657-672.

Bouma, A. H. 1962, Sedimentology of some Flysch deposits: A graphic approach to

facies interpretation, Elsevier, pp. 168.

Brenner, S. L. and Gudmundsson, A. 2004. Arrest and aperture variation of hydrofractures in layered reservoirs. *From*: Cosgrove, J. W. and Engelder, T. (eds). *The Initiation, Propagation, and Arrest of Joints and Other Fractures*. Geological Society, London, Special Publications. **231**. pp. 117-128.

Burnside, N. M., Shipton, Z. K., Dockrill, B. and Ellam, R. M. 2013. Man-made versus natural CO_2 leakage: A 400 k.y. history of an analogue for engineered geological storage of CO_2. *Geology*. v.**41** no.**4**. pp. 471-474.

Byerlee, J. D. (1978). Friction of rocks. *Pure and Applied Geophysics*. v.**116**. pp. 615-626.

Caine, J.S., Evans, J.P. and Forster, C.B. 1996. Fault zone architecture and permeability structure. *Geology*. v. **24** No. **11**. pp. 1025-1028.

Cartwright, J., Huuse, M. and Aplin, A. 2007. Seal bypass systems. *AAPG Bulletin*. v.**91** no.**8**. pp. 1141-1166.

Childs, C., Watterson, J. and Walsh, J. J. 2002. Fault overlap zones within developing normal faults systems. In: *Extensional Tectonics: Faulting and Related Processes*. (edited by Holdsworth, R. E. and Turner, J. P.) The Geological Society of Londong, Key issues in Earth Sciences. **2(2)**, pp. 25-29.

Childs, C., Walsh, J. J. and Watterson, J. 1997. Complexity in fault zone structure and implications for fault seal prediction. *In*: Hydrocarbon seals - Importance for exploration and production. (Eds. Moller-Pedersen, P. and Koestler, A. G.), Norwegian Petroleum Society (NPF), Special Publication **7**, 61-72.

Claesson, L., Skelton, A., Graham, C. and Morth, C-M., 2007. The timescale and mechanisms of fault sealing and water-rock interaction after an earthquake. *Geofluids*. v.**7**. pp. 427-440.

Cooke, M.L. and Underwood, C. A. 2000. Fracture termination and step-over at bedding interfaces due to frictional slip and interface opening. *Journal of Structural*

Geology. v.**23**. pp. 223-238.

Coulomb, C. A. 1776. *Essai sur une application des regles des maximis et minimis a quelquels problemesde statique relatifs, a la architecture.* Mem. Acad. Roy. Div. Sav., v.**7**. pp. 343-387.

Couples, G. D. and Lewis, H. 2007. Introduction: the relationship between damage and localization. *From*: Lewis, H. and Couples, G. D. (eds) *The Relationship between Damage and Localization.* Geological Society, London, Special Publications, **289**, pp. 1-6.

Cox, S. 2010. The application of failure mode diagrams for exploring the roles of fluid pressure and stress states in controlling styles of fracture-controlled permeability enhancement in faults and shear zones. *Geofluids.* v.**10**. pp. 217-233.

Crimes, T. P. 1973. From limestones to distal turbidites: a facies and trace fossil analysis in the Zumaya flysch (Paleocene-Eocene), North Spain. *Sedimentology.* v.**20**. i**1**. pp. 105-131.

Curewitz, D. and Karson, J.A. 1997. Structural setting of hydrothermal outflow: Fracture permeability maintained by fault propagation and interaction. *Journal of Volcanology and Geothermal Research.* **79**. pp. 149-168.

Darcy, H. Les Fontaines Publiquesa de la Ville de Dijon, Dalmont, Paris (1856).

Department for Environment, Food and Rural Affairs (DEFRA) and Department for Business Enterprise and Regulatory Reform (2008) *Managing Radioactive Waste Safely: A Framework for Implementing Geological Disposal.* http://mrws.decc.gov.uk/ [accessed at 04 September 2012]

Desrues, J., Besuelle, P. and Lewis, H. 2007. Strain localization in geomaterials. *From*: Lewis, H. and Couples, G. D. (eds) *The Relationship between Damage and Localization.* Geological Society, London, Special Publications, **289**, pp. 47-73.

Dewhurst, D. N. and Siggins, A. F. 2006. Impact of fabric, microcracks, and stress field on shale anisotropy. *Geophys. J. Int.* v.**165**. pp. 135-148.

Dewhurst, D. N., Yang, Y. and Aplin, A. C. 1999. Permeability and fluid flow in natural mudstones. *From*: Elmore, R. D., Muxworthy, A. R., Aldana, M. M. and Mena, M. (eds). *Muds and Mudstones: Physical and Fluid-Flow Properties*. **158**. pp. 125-135.

Dyer, R. 1988. Using joint interactions to estimate paleostress ratios. *Journal of Structural Geology* v.**10**. pp. 685-699.

Eichhubl, P., and Boles, J. R. 2000. Rates of Fluid Flow in Fault Systems–Evidence for Episodic Fluid Flow in the Miocene Monterey Formation, Coastal California. *American Journal of Science*. v.**300** no.**7**, pp. 571-600

Eichhubl P., Davatzes, N. C. and Becker, S. P. 2009. Structural and diagenetic control of fluid migration and cementation along the Moab fault, Utah. *AAPG Bulletin*. v.**93** i.**5**. pp. 653-681.

Engelder, T., Lash, G. G. and Uzcategui, R. S. 2009. Joint sets that enhance production from Middle and Upper Devonian gas shales of the Appalachian Basin. *AAPG Bulletin*. v.**93** no.**7**. pp. 857-889.

Engelder, T. 1985. Loading paths to joint propagation during a tectonic cycle: an example from the Appalachian Plateau, U.S.A. *Journal of Structural Geology*. v.**7**. pp. 459-476.

Evans, J. P., Forster, C. B. and Goddard, J. V. 1997. Permeability of fault-related rocks, and implications for hydraulic structure of fault zones. *Journal of Structural Geology*. v.**19** i.**11**. pp. 1393-1404.

Evans, E. M. 1994. Joints and decollement zones in the Middle Devonian shale: evidence for multiple deformation events in the central Appalachian Plateau. *Geological Society of America Bulletin*. v.**106**. 447.460.

Faerseth, R. B. 2006. Shale smear along large faults: continuity of smear and the fault seal capacity. *Journal of the Geological Society*. v.**163**. pp. 741-751.

Fairley, J.P. and Hinds, J.J. 2004. Rapid transport pathways for geothermal fluids in an active Great Basin fault zone. *Geology*. v.**32**. pp. 825-828.

Faulkner, D. R., Jackson, C. A. L., Lunn, R. J., Schlische, R. W., Shipton, Z. K., Wibberly, C. A. J. and Withjack, M. O. 2010. A review of recent development concerning the structure, mechanics and fluid dlow properties of fault zones. *Journal of Structural Geology*. v.**32**. pp 1557-1575.

Fisher, Q.J., Harris, S. D., McAllister, E., Knipe, R. J. and Bolton, A. J. 2001. Hydrocarbon flow across faults by capillary leakage revisited. *Marine and Petroleum Geology*. v.**18**. pp. 251-257.

Fisher, Q.J. and Knipe, R.J. 2001. The permeability of faults within siliclasitc petroleum reservoirs of the North Sea and Norwegiann Continental Shelf. *Marine and Petroleum Geology*. v.**18**. pp. 1063-1081.

Gartrell, A., Zhang, Y., Lisk, M. and Dewhurst, D. 2004. Fault intersections as critical hydrocarbon leakage zones: integrated field study and numerical modelling of an example from the Timor Sea, Australia. *Marine and Petroleum Geology*. vol **21**. pp. 1165-1179.

Genter, A. and Traineau, H. 1996. Analysis of macroscopic fractures in granite in the HDR geothermal well EPS-1, Soutlz-sous-Forets, France. *Journal of Volcanology and Geothermal Research*. v.**72** i.**1-2**. pp. 121-141.

Griffith, A. A. 1921. The phenomena of rupture and flow in solids.

Hesthammer, J. and Fossen, H. 2000. Uncertainties associated with fault sealing analysis. *Petroluem Geoscience*. v.**6**. pp. 37-45.

Ingram, G. M and Urai, J. L. 1999. Top-seal leakage through faults and fractures: the role of mudrock properties. *From*: Aplin, A. C., Fleet, A. J. and Macquaker, J. H. S. (eds). *Muds and Mudstones: Physical and Fluid-Flow Properties*. Geological Society, London, Special Publication. **158**. pp. 125-135.

Ishii, E. 2012. Microstructure and origin of faults in siliceous mudstone at the

Horonobe Underground Research Laboratory site, Japan. *Journal of Structural Geology*. v.**34**. pp. 20-29.

Jin, Z. H. and Johnson, S. E. 2008. Primary oil migration through buoyancy-driven multiple fracture propagation: Oil velocity and flux. *Geophysical Research Letters*. v.**35**. DOI: 10.1029/2008GL033645

Jolley, S. J., Barr, D., Walsh, J. J. and Knipe, R. J. (eds) *Structurally Complex Reservoirs*. Geological Society, London, Special Publications, **292**, 309-336.

Kampman, N., Burnside, N. M., Shipton, Z. K., Chapman, H. J., Nicholl, J. A., Ellam, R. M. and Bickle, M. J. 2012. Pulses of carbon dioxide emissions from intracrustal faults following climatic warming. *Nature Geoscience*. v.**5**. pp. 352-358.

Lash, G., Loewy, S. and Engelder, T. 2004. Preferential jointing of Upper Devonian black shale, Appalachian Plateau, USA: evdience supporting hydrocarbon generation as a joint-driving mechanism. *From*: Cosgrove, J. W. and Engelder, T. (eds). *The Initiation, Propagation, and Arrest of Joints and Other Fractures*. Geological Society, London, Special Publications. **231**. pp. 129-151.

Ligtenberg, J.H. 2005. Detection of fluid migration pathways in seismic data: implications for fault seal analysis. *Basin Research*. v.**17** i.**1**. pp. 141-153.

Makel, G. H. 2007. The modelling of fractured reservoirs: constraints and potential for fracture network geometry and hydraulics analysis. *From*: Jolley, S. J., Barr, D., Walsh, J. J. and Knipe, R. J. (eds) *Structurally Compex Reservoirs*. Geological Society, London, Special Publications, **292**, 219-233.

Manzocchi, T. Walsh, J.J., Nell, P. and Yielding, G. 1999. Fault Transmissibility Multipliers for Flow Simulation Models. *Petroleum Geoscience*. v.**5**. pp. 53-63.

Manzocchi, T., 2002. The connectivity of two dimensional networks of spatially correlated fractures. *Water Resources Research*. v.**38**. DOI:10.1029/2000WR000180

Manzocchi, T., Walsh, J. J., Tomasso, M., Strand, J., Childs, C. and Haughton,

P. D. W. 2007. Static and dynamic connectivity in bed-scale models of faults and unfaulted turbidites. 2007 *From*: Jolley, S. J., Barr, D., Walsh, J. J. and Knipe, R. J. (eds) *Structurally Complex Reservoirs*. Geological Society, London, Special Publications, **292**, 309-336.

Matthai, S. K., Geiger, S., Roberts, S. G., Paluszny, A., Belayneh, M., Burri, A., Mezentsev, A., Lu, H., Coumou, D., Driesner, T. and Heinrich, C. A. 2007. Numerical simulation of multi-phase fluid flow in structurally complex reservoirs. *From*: Jolley, S. J., Barr, D., Walsh, J. J. and Knipe, R. J. (eds) *Structurally Complex Reservoirs*. Geological Society, London, Special Publications, **292**, 405-429.

Mazurek, M., Alt-Epping, P., Bath, A., Gimmil, T., amd Waber, H.N. Natural Tracer Profiles Across Argillaceus Formations: The CLAYTRAC Project. OECD 2008. Report NEA no. 6253. OECD/NEA Paris, France.

Micklethwaite, S. 2008. Optimally orientated "fault-valve" thrusts: Evidence for aftershock-related fluid pressure pulses? *Geochemistry, Geophysics, Geosystems*. v.**9**. 10.1029/2007GC001916

Micklethwaite, S. and Cox, S. F. 2004. Fault-segment rupture, aftershock-zone fluid flow, and mineralization. *Geology*. v.**32** no.**9**. pp. 813-816.

Miller, S. A., Collettini, C. Chiaraluce, L., Cocco, M., Barchi, M. and Kaus, B. J. P. 2004. Aftershocks driven by a high-pressure CO_2 souce at depth. *Nature*. v.**427**. pp. 724-727.

Nichols, G. 2009. Sedimentology and Stratigraphy, Maldon: Blackwell Scientific Publications.

Nicol, A., Gillespie, P., Walsh, J. J. and Childs, C. 2002. Relay zones between mesoscopic thrust faults in layered sedimentary sequences. *Journal of Structural Geology*. v.**24**. pp. 709-727.

Odling, N. E., Gillespie, P., Bourgine, B., Castaing, C. Chiles, J-P., Christensen, N. P., Fillion, E., Genter, A., Olsen, C., Thrane, L. Trice, R. Aarseth, E. Walsh, J. J.

and Watterson, J. 1999. Variations in fracture system geometry and their implications for fluid flow in fractured hydrocarbon reservoirs. *Petroleum Geoscience*. v.**5**. pp. 373-384.

Pater, C. J. and Baisch, S. 2011. Geomechanical Study of Bowland Shale Seismicity: Synthesis Report.

Paterson, M. S. 1978. *Experimental Rock Deformation - The Brittle Field*. Springer, Berlin.

Pollard, D. D. and Segall, P. 1987. Theoretical displacement and stresses near fractures in rock: with applications to faults, joints, veins, dikes and solution surfaces. *In*: Atkinson, B. K. (ed.) *Fracture Mechanics of Rock*. Academic Press, London. pp. 277-350.

Pöyry Energy Limted. 2011. The 2010 UK Radioactive Waste Inventory: Main Report. Cumbria: Nuclear Decommissioning Authority. Available at: http://www.nda.gov.uk/ukinv [accessed 04 September 2012]

Roggero, F., Lerat, O., Ding, D. Y., Berthhet, P., Bordenave, C., Lefeuvre, F. and Perfetti, P. 2012. History Matching of Production and 4D Seismic Data: Application to the Girassol Field, Offshore Angola. *Oil and Gas Science and Technology*. v.**67** i.**2**. pp. 237-262.

Rowland, J.C., Manga, M. and Rose, T.P. 2008. The influence of poorly interconnected fault zone flow paths on spring geochemistry. *Geofluids*. v.**8** i.**2**. pp. 93-101.

Shipton, Z. K., Evans, J. P. and Thompson, L. B. 2005. The Geometry and Thickness of Deformation-band Fault Core and its Influence on Sealing Characteristics of Deformation-band Fault Zones. In: *Faults, fluid flow, and petroleum traps: AAPG Memoir*. Sorkhabi, R. and Tsuji, Y. (eds). **85**. pp. 181-195.

Steen, A.K. Nunn, J.A. and Hanor, J.S. 2011. Indications of formation water flow and compartmentalization on the flank of a salt structure derived from salinity and

seismic data. *Geofluids*. v.**11** i.**2**. pp. 199-208.

Talbot, C. J. and Sirat, M. 2001. Stress control of hydraulic conductivity in fracture-saturated Swedish bedrock. *Engineering Geology*. v.**61**. pp. 145-153.

TerHeege, J. H., Wassing, B. B. T., Orlic, B., Giger, S. B. and Clennell, M. B. 2013. Constraints on the Sealing Capacity of Faults with Clay Smears from Discrete Elemenet Models Validated by Laboratory Experiments. *Rock Mechanics and Rock Engineering Journal*. v.**46**. pp. 465-478.

Todd, D. K. and Mays, L. W. 2005. *Groundwater Hydrology*. Hoboken. John Wiley and Sons Incorporated.

Twiss, R.J. and Moores, E.M. Structural Geology, WH Freeman and Company, Oxford (1992).

Virgo, S. Arndt, M. Sobisch, Z. and Urai, J. L. 2013. Development of fault and vein networks ina carbonate sequence near Hayl al-Shaz, Oman Mountains. *GeoArabia*. v.**18** no.**2**. pp. 99-136.

Vrolijk, P., and van der Pluijm, B. A. 1999. Clay gouge. *Journal of Structural Geology*. v.**21**. pp. 1039-1048.

Walker, R., Holdsworth, R., Imber, J. and Ellis, D. 2012. Fault-zone evolution in layered basalt sequences: a case study from the Faroe Islands, NE Atlantic Margin. *Geological Society of America Bulletin*. v.**124**. pp. 1382-1393.

Walker, R. G. 1967. Turbidite Sedimentary Structures and their Relationship to Proximal and Distal Depositional Environments. *Journal of Sedimentary Petrology*. v.**37** no.**1**. pp. 25-43.

Walsh, J.J., Waterson, J. Bailey, W.R. and Childs, C. 1999. Fault relays, bends and branch-lines. *Journal of Structural Geology*. v.**21**. pp. 1019-1026.

Weimer, P., Slatt, R. M., Dromgoole, P. Bowman, M. and Leonard, A. 2000. Developing and Managing Turbidite Reservoirs: Case Histories and Experiences: Results

of the 1998 EAGE/AAPG Research Conference. *AAPG Bulletin*. v.**84** no.**4**. pp. 453-465.

Yang, Y. and Aplin, A. C. 2010. A permeability-porosity relationship for mudstones. *Marine and Petroleum Geology*. v.**27** pp. 1692-1697.

Yielding, G., Freeman, B. and Needham, D.T. 1997. Quantitative fault seal prediction. *AAPG Bulletin*. v.**81** i.**6**. pp. 897-917.

Zecchin, M. Caffau, M. 2012. The vertical compartmentalization of reservoirs: An example from an outcrop analog, Crotone Basin, southern Italy. *AAPG Bulletin*. v.**96** i.**1**. pp. 155-175.

van der Zee, W. and Urai, J.L. 2005. Processes of normal faults evolution in a siliciclastic sequence: a case study from Miri, Sarawak, Malaysia. *Journal of Structural Geology*. v.**27**. i.**12**. pp. 2281-2300.

Chapter 3

Geological setting

> "Far be it from me to suggest that geologists should be reckless in their drafts upon the bank of Time; but nothing whatever is gained, and very much is lost, by persistent niggardliness in this direction." – Charles Lapworth

3.1 Introduction

A field area of mudstone outcrop was selected for detailed study of controls on palaeo-fluid flow episodes, for reasons outlined previously in chapter 1. This chapter outlines the geological history of the mudstone formation containing the field area. This will allow the features that may have acted as fluid flow conduits to be related to the larger geological events and processes which formed and deformed the mudstone formation investigated in this study.

3.2 Geological background

The field site is located within an Ordovician inlier in the Midland Valley Terrane of Scotland (figure 3.1). The Midland Valley has undergone several stages of deposition, burial and uplift but is not as deformed as other Scottish terranes.

During the Ordovician the area that is now known as the Midland Valley was in the Southern Hemisphere, lying on the Southern coast of the palaeo-continent Laurentia (figure 3.2). The Iapetus Ocean existed to the South East of the Midland Valley and had, by this time, started the long process of closing. The Iapetus Ocean separated Scotland from England and Wales which were part of the micro-continent Avalonia. The final closure of the Iapetus in mid-late Sulurian resulted in oblique collision of Avalonia with this sector of Laurentia (Strachan 2012).

The oceanic plate of the Iapetus ocean was being subducted under the Laurentian continental plate (Torsvik et al. 1996, figure 3.2). Subduction zones such as this will often create three distinct areas, that are found in three different arcs or areas of the subduction zone (Stűwe 2007, figure 3.3). The magmatic arc is formed by the heat and pressure caused by the interaction of the two plates, which is also uplifted by the plate collision. The fore-arc basin is the area where sediment is deposited, after being transported from the eroding volcanic mountains of the magmatic arc. The accretionary prism forms when sections of the Oceanic Plate are accreted against the continental plate, this creates ophiolitic rocks.

Different sections of the palaeo-subduction zone are represented in the exposed outcrop in the Girvan area (figure 3.4). The Ballantrae Complex consists of serpentinites and pillow basalts that are typical of an oceanic plate and are interpreted to be an ophiolite. The Benan conglomerates and the Ardmillan Group represent the fore-arc basin to the North West of the accretionary prism. The clasts in the Benan Conglomerates are of ophiolitic and igneous rock types which would be transported from the magmatic arc. The sediments in the Girvan area have palaeo-flow indicators showing transport from the North West to the South East (Williams 1962) and the size of the igneous conglomerate clasts (of over two metres diameter) suggests

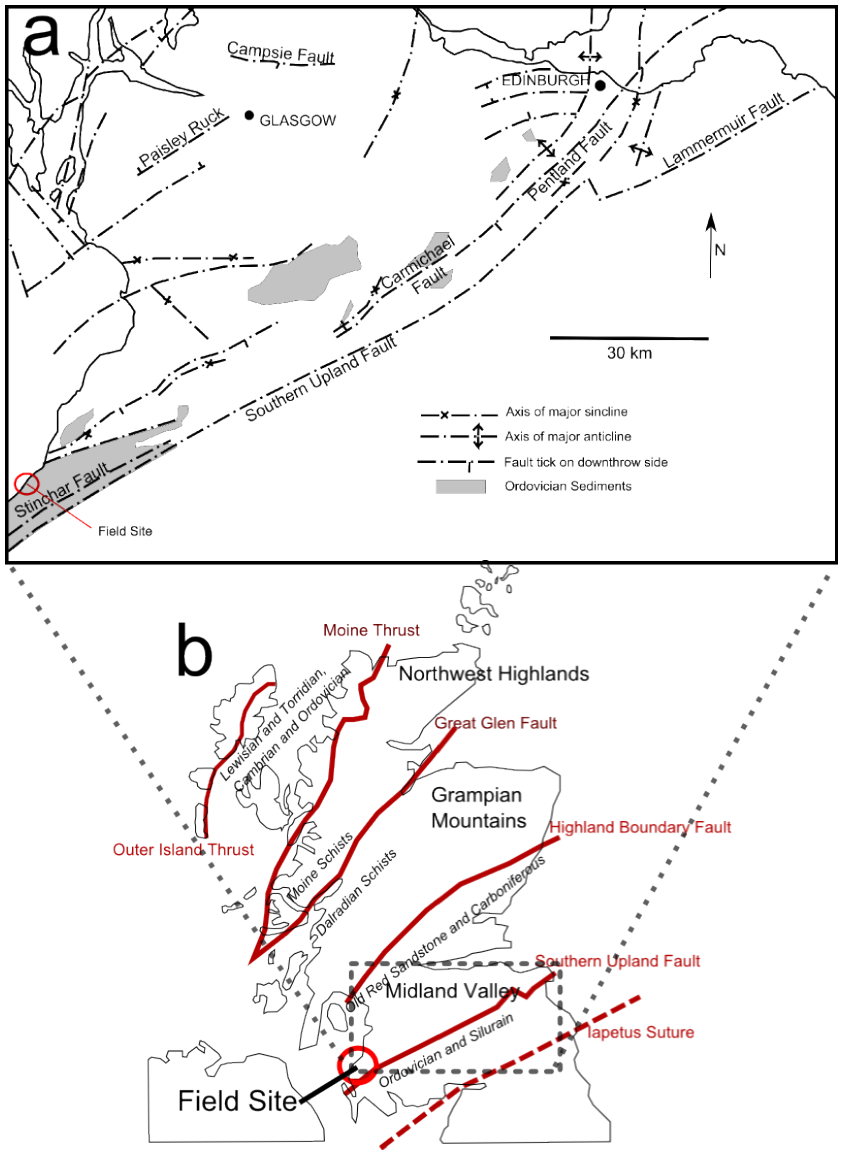

Figure 3.1: a. Map showing the location of the field site in the Midland Valley. The main structural discontinuities of The Midland Valley are shown as well as the Ordovician inliers, from *Cameron and Stephenson 1985*. b. Location of field site in relation to the main Geological divisions and structural features (red lines) of Scotland, from *Lawson and Weedon 1992*

a local source. However no rocks belonging to a magmatic arc are exposed to the North West of Girvan where the source rocks would be expected.

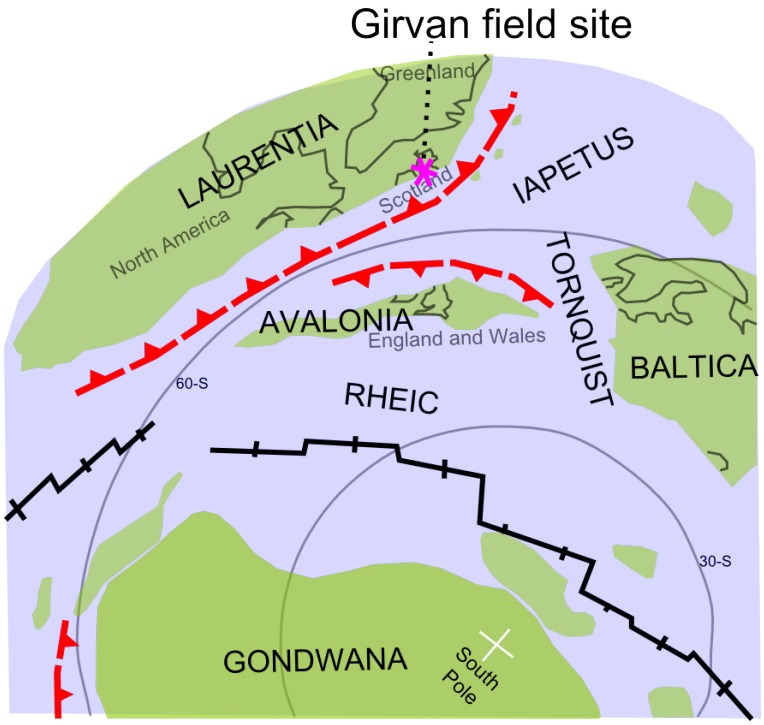

Figure 3.2: Mid-Ordovician geography. Midland Valley is located on the South East coast of Laurentia next to where the Iapetus Oceanic plate is being subducted under the Laurentian continental plate. Avalonia and Baltica are moving towards Laurentia, due to a shrinking Iapetus Ocean but growing Rheic Ocean. Spreading centres are shown as black lines and subduction zones as red lines with ticks. From *Cocks and Torsvik 2006*.

The field site is part of the Ardmillan Group (figure 3.5). The Ardmillan Group consists of layers of greywackes, sandstones, siltstones, mudstones and thin limestones, these were deposited in deeper waters (>400m deep) than the conglomerates they cover (figure 3.6, Lawson and Weedon 1992). These sediments were deposited in the Late Ordovician Caradoc and Ashgill series. Palaeo-current indicators of the Ardmillan Group show transport towards the South East, indicating similar transport and directions as the underlying conglomerates (figure 3.6).

The Ardmillan Group has been interpreted to have been deposited in a submarine fan environment (Ince 1984). Submarine fans consist of sediments that were mainly deposited by mass flow processes. The composition of a fan is strongly controlled

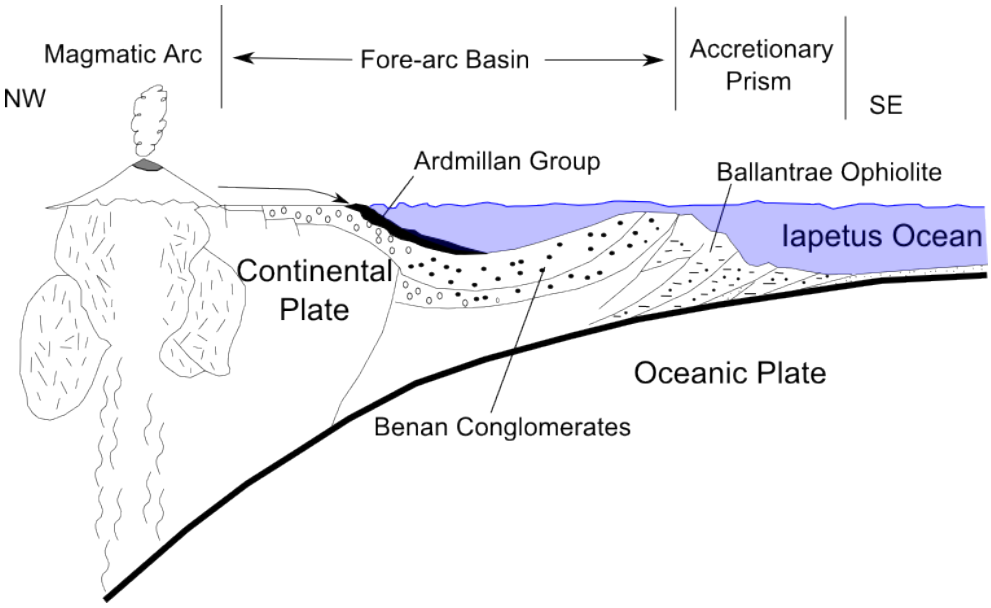

Figure 3.3: Overview of depositional setting of the Girvan area during mid to late Ordovician. Iapetus Oceanic plate is being subducted under Laurentian continental plate. A volcanic mountain range is formed at the magmatic arc, from the high temperatures and pressures of the colliding plates creating magma and causing uplift. In the fore-arc basin eroded sediment is deposited, sourced from the magmatic arc. Parts of the Oceanic Plate are emplaced in the accretionary prism as ophiolites. Adapted from *Lawson and Weedon 1992*.

by the type of sediment supplied (Nichols 1999). Submarine fans can be gravel-rich, sand-rich, mixed sand and mud, or mud-dominated systems, the type of material transported and deposited in the fan influences the complex architecture of the fan system. Fans can show a range of deposition architectures of channels, lobes and sheets.

Figure 3.7 shows a fence diagram of how the Benan Conglomerate and Ardmillan Group were deposited in relation to each other, compared with a cartoon diagram of a submarine fan system. The sandstone, siltstone and mudstone dominated parts of the Ardmillan group may represent different depositional positions on the fan. The basin bounding faults which control sedimentation on the fan have been interpreted due to significant variations in sediment thicknesses of the Benan Conglomerate.

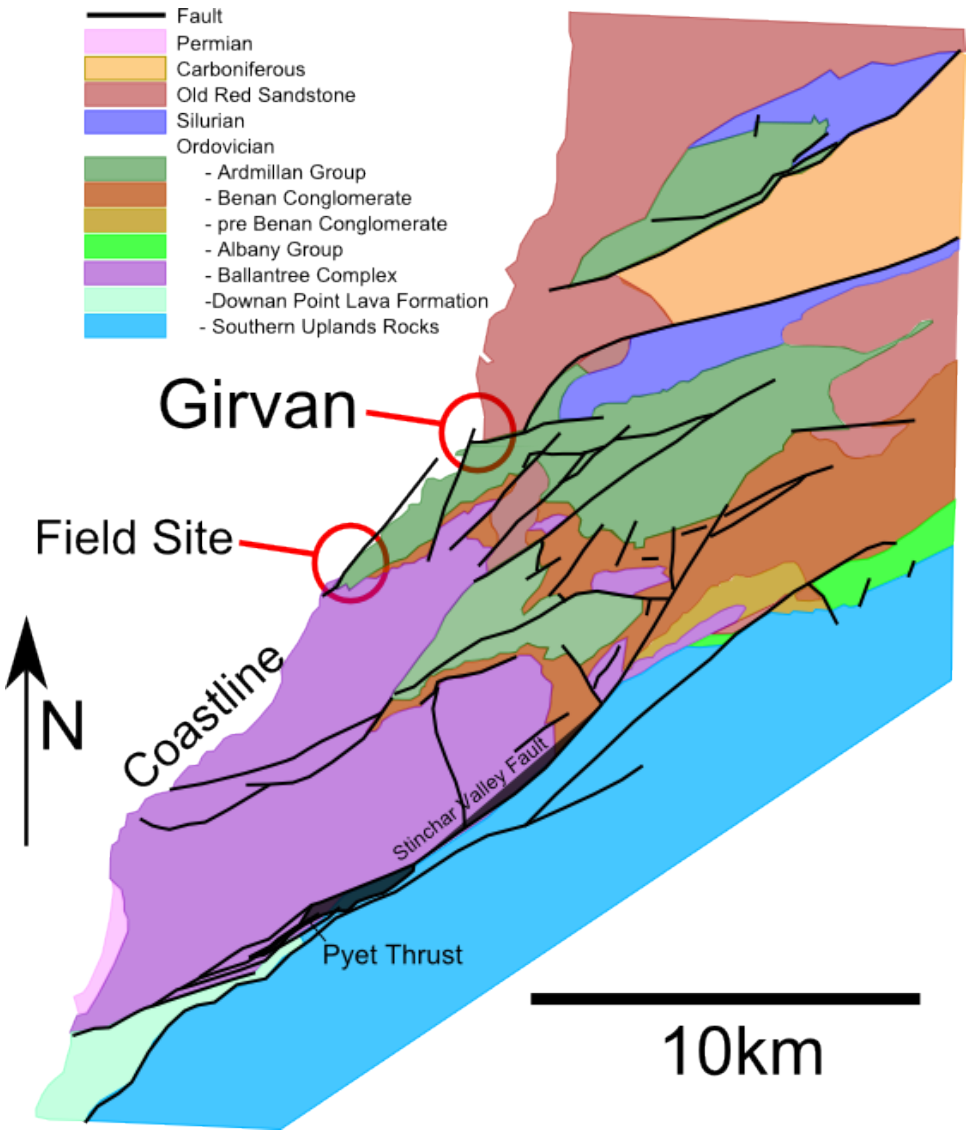

Figure 3.4: Geological map of the Girvan area. Accretionary prism is represented by Ballantrae Complex of serpentinites and pillow basalt. Benan Conglomerates are made of igneous clasts (probably sourced from local magmatic arc) and ophiolitic material. The Ardmillan Group represent Girvan cover sequences and host the field site. Changing terrestrial depositional conditions in the area are shown by the Devonian sandstone and Carboniferous deposits.*Lawson and Weedon 1992*

Some beds of the Ardmillan Group have evidence of being deposited via turbidity currents. These occur where part of the slope collapses transporting significant

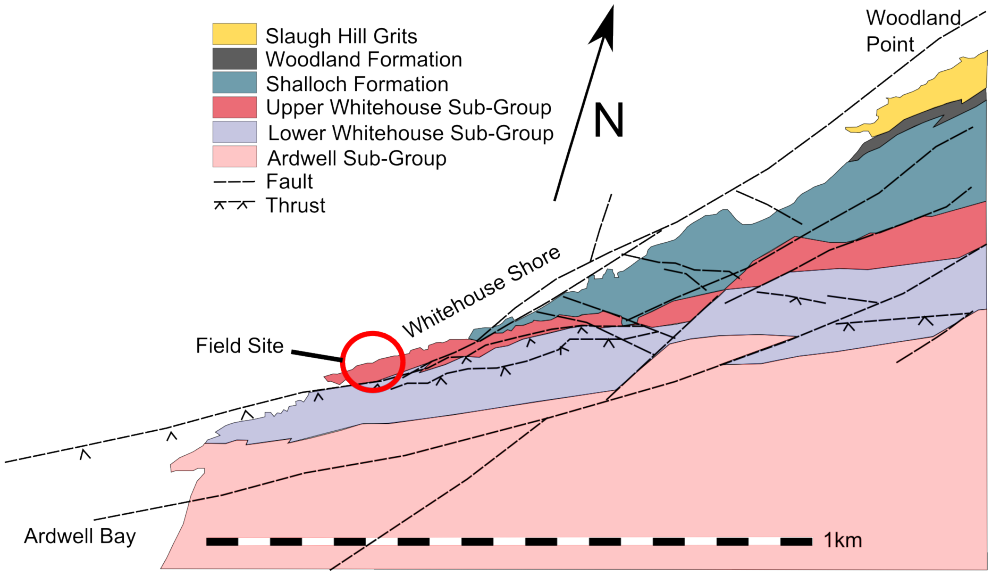

Figure 3.5: Geological map showing groups and formations that make up the "Post-Benan Conglomerate Sediments" in figure 3.4. Sediments were deposited in deep water (>400m) and consist of greywackes, sandstones, siltstones and mudstone along with thin limestone in places. The sediments were deposited in the Caradoc and Ashgill. Thrust faults have moved the Lower Whitehouse Sub-Group towards the sea over the Upper Whitehouse Sub-Group. Adapted from *Lawson and Weedon 1992.*

amounts of material out over the lower fan and outer fan mudstones (figure 3.7).

The Upper Whitehouse Sub-Group (figures 3.5 and 3.6) is exposed on the Whitehouse Shore (figure 3.8), along with the Lower Whitehouse Sub-Group. The Lower Whitehouse Sub-Group is represented by the series of distal turbidites of the Three Mile Formation (figure 3.8). The Penwhapple Formation is missing from the exposure, representing roughly 200m of sediment, as the Whitehouse Thrust Fault has moved the Three Mile Formation North West over the Penwhapple formation.

Immediately North West of the Whitehouse Thrust Fault are the oldest deposits of the Upper Whitehouse Sub Group with the Myoch Formation at its base (figure 3.8). The sediments of the lower Myoch Formation are predominantly green mudstones before changing to the predominantly red mudstone layer, which hosts the field site. The red mudstone contains thin (often $\leq$1cm thick) sandstone bands, discussed in

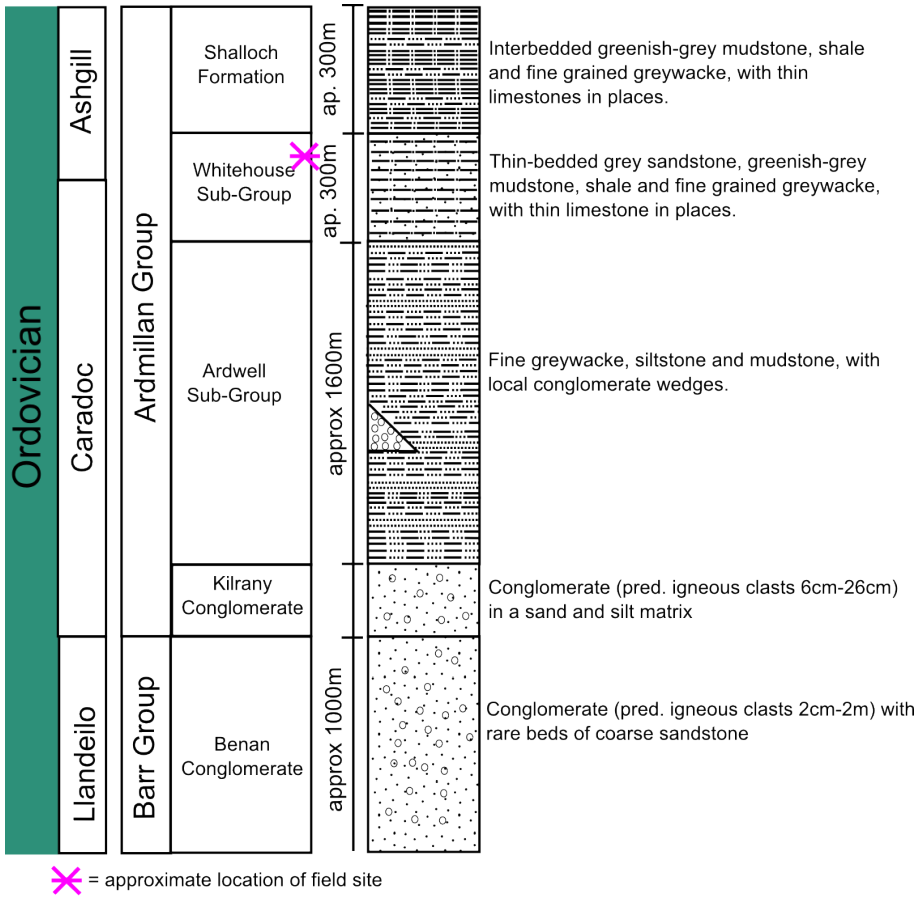

Figure 3.6: Stratigraphic column showing conglomerates and cover sequences found in the Girvan area and mapped in figures 3.4 and 3.5. Initial shallow marine conglomerate deposition gives way to the deeper marine Ardmillan Group. Column made using information from BGS geological map of Girvan

chapter 4. The Myoch Formation is overlain by the Mill Formation. The rocks of the Mill Formation are a green/grey mudstone which in the field looks to be a similar material to the Myoch formation of the field site. The Myoch and Mill Formation are separated by a small thrust which is related to the Whitehouse Thrust Fault. The Shalloch Formation is the youngest rock exposed in this area of the Whitehouse Shore, it consists of sandstone and mudstone layers approximately 10cm-1m thick, the sandstone layers protrude due to their higher erosional resistance.

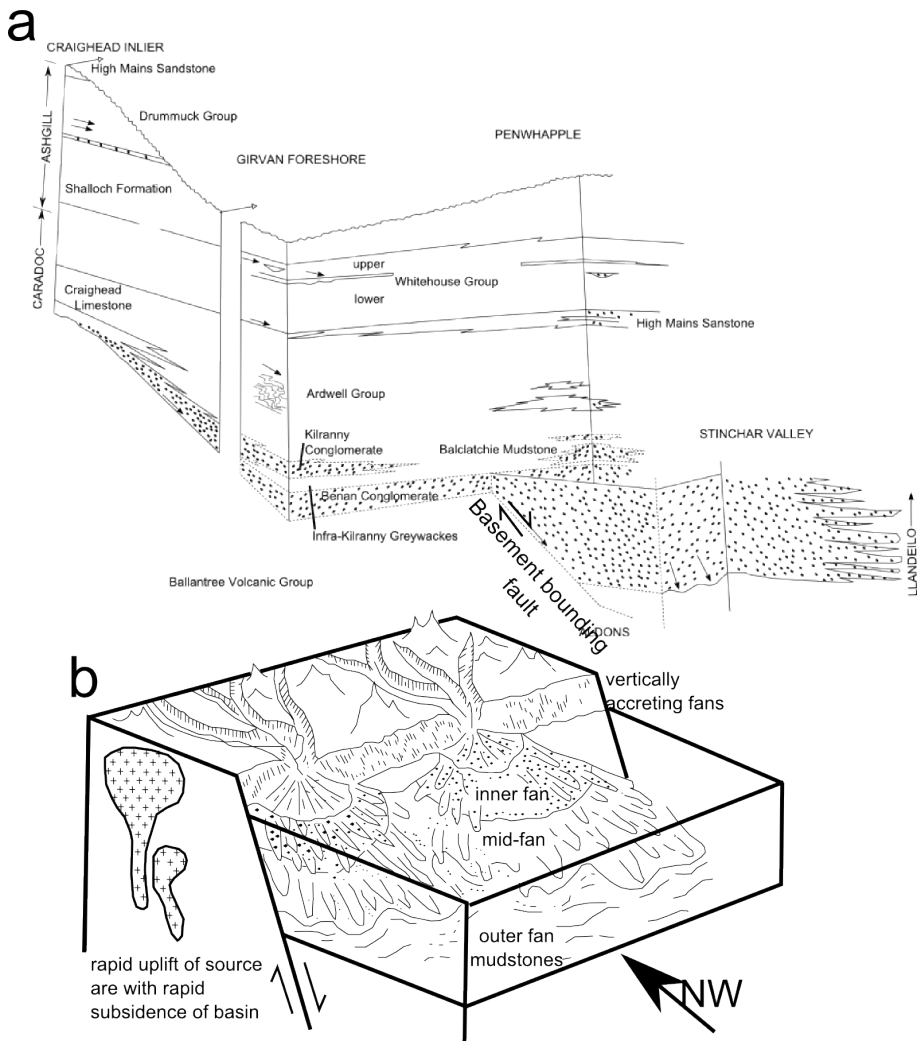

Figure 3.7: . Late Ordovician deposits from submarine fan system at Girvan. Significant variation in the Benan Conglomerate are evidence of rapid fault-related subsidence. Adapted from Ingham 1978. b. Example of a submarine fan overlying a basin bounding fault. Sediments will generally be coarser in the upper fan. Channels of coarser grains cut through the finer grained lobes creating complicated heterogeneity within the fan system. After Ince 1984 and Strachan 2012.

The Upper Whitehouse Sub-Group has been interpreted to have been deposited in deep shelf and ocean floor settings distal to the submarine fan (Ingham 1978). These settings would put the depositional area in the vicinity of the outer fan mudstones shown in figure 3.7.

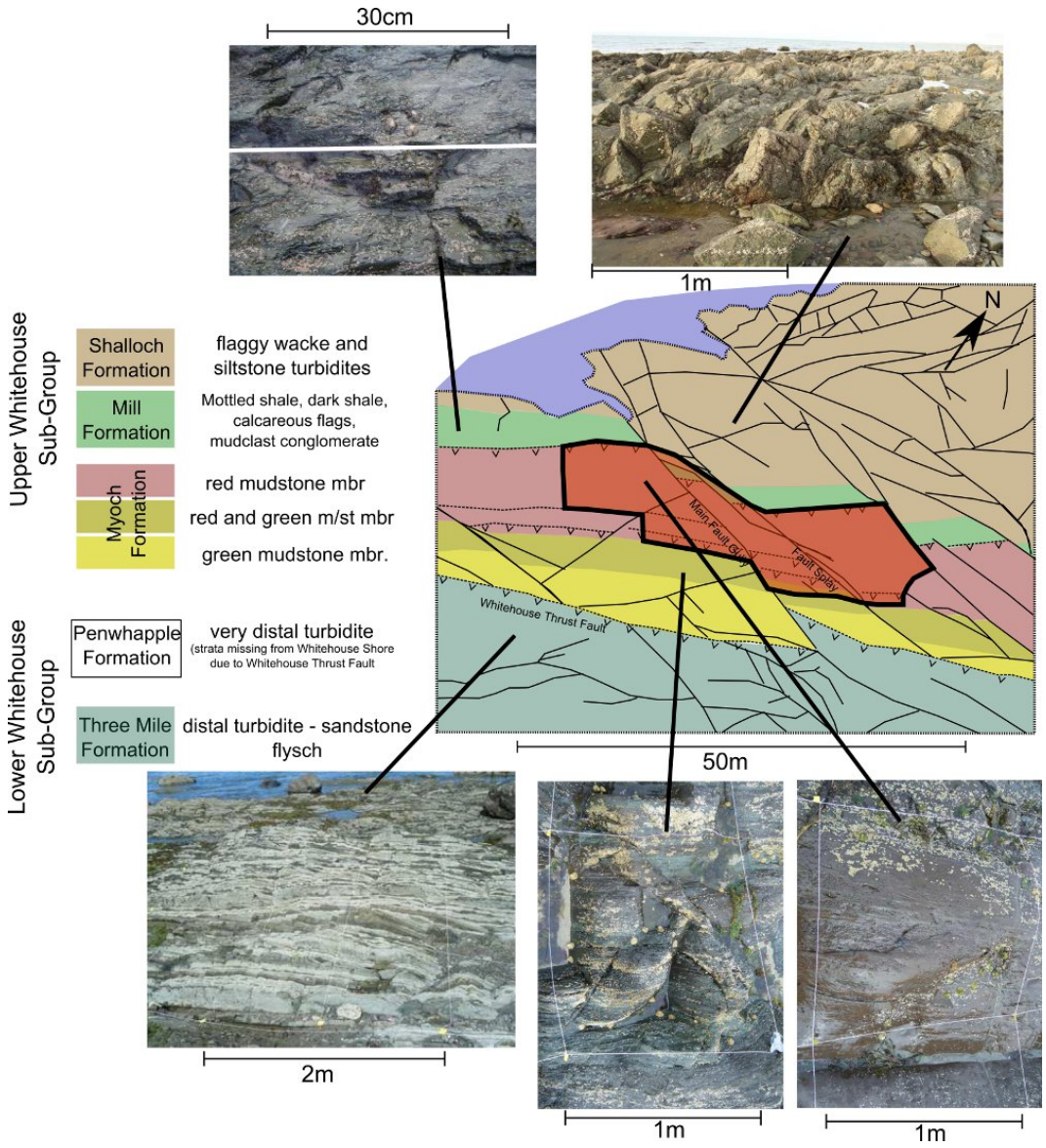

Figure 3.8: Formations of the Whitehouse Shore Sub-Group observable in the central area of the Whitehouse Shore. Photographs show outcrop examples of each formation. Whitehouse Thrust Fault moves Lower Whitehouse Sub-Group, towards the sea, over the Upper Whitehouse Sub-Group resulting in the Penwhapple Formation being missing from this area of exposure. The bedding for each of these formations is near vertical. Adapted from Dr. Ingham's map in Lawson and Weedon 1992.

The beds of the Whitehouse Group are near vertical in the exposures on the Whitehouse Shore, with the beds running approximately WSW-ENE. This large scale rotation of the beds indicates folding probably due to NW-SE compression. During the Silurian the micro-continent of Avalonia collided with this region of Laurentia (figure 3.9) resulting in reigonal NW-SE compression (Woodcock 2012). Hundreds of kilometres to the East the "harder" collision of Baltica with Laurentia created an orogenic belt. However the collision of West Avalonia seems to have created a "softer" collision in the Girvan area (Woodcock 2012) resulting in relatively mild deformation.

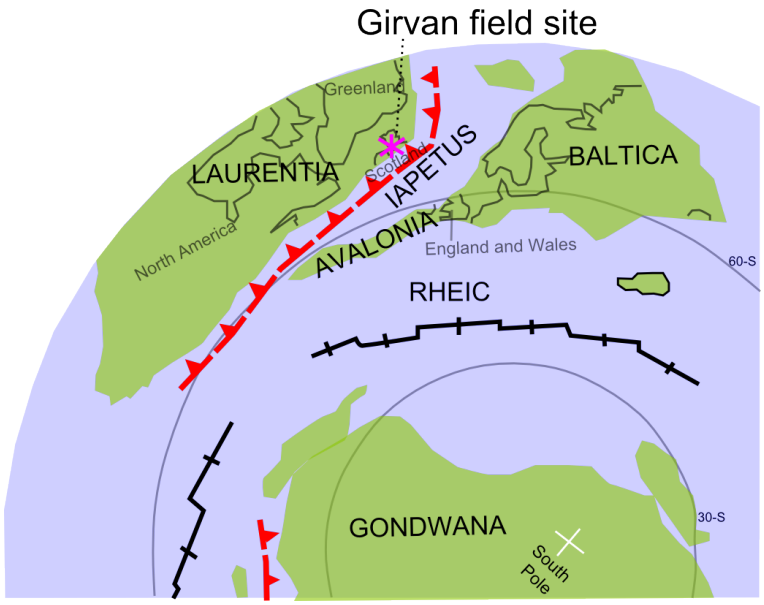

Figure 3.9: The closing of the Iapetus Ocean during the Late Ordovican/Early Silurian ≈440Ma. Avalonia and Baltica have collided prior to their impending collision with Laurentia due to the closing Iapetus. From *Cocks and Torsvik 2006.*

The Whitehouse Thrust Fault is orientated to accommodate the same direction of compression as the earlier folding (figure 3.10). Conjugate dextral and sinstral faults can be seen on the Whitehouse Shore that offset the beds and thrust faults (figure 3.8). These have previously been interpreted to represent the final brittle deformation around the Late Silurian (Ingham 1978). The horizontal displacements of these conjugate faults is defined by the offset of the sub-vertical beds, displacements are

usually relatively small being less than ten metres.

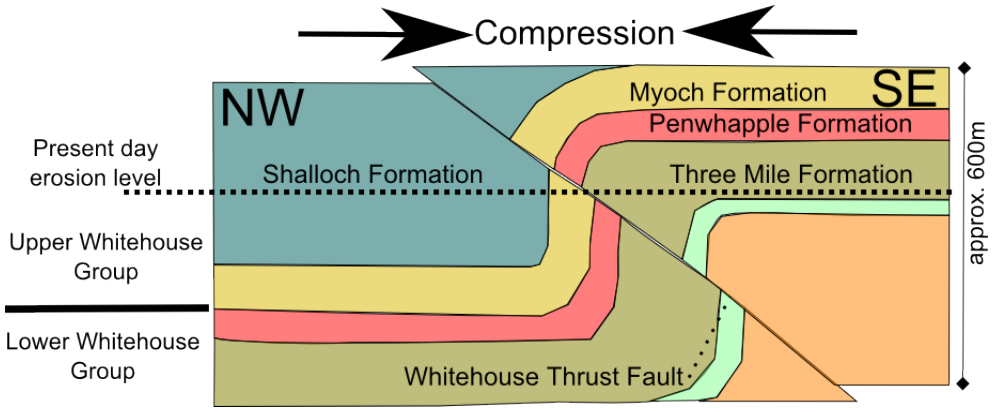

Figure 3.10: Cartoon of deformation of Whitehouse Sub-Group during closure of Iapetus Ocean. Initial folding was followed by thrusting, pushing Lower Whitehouse Sub-Group over Upper Whitehouse Sub-Group leading to missing formations in the present day exposure.

With the closure of the Iapetus the Devonian saw a change to non-marine deposition, represented by outcrops of Old Red Sandstone in the Girvan area (figure 3.4). However, beyond general burial and uplift processes it is not until the Tertiary that the rocks of the Whitehouse Shore show evidence of further geological activity. Tertiary dykes related to the Arran Dyke Swarm cut through the rocks of the Whitehouse Shore, these dykes are approximately orientated NW-SE and were emplaced around 58Ma (Dagley et al 1978). The field site (figure 3.8) is approximately 100 metres from the nearest dyke and appears unaffected by this event.

Large boulders are distributed throughout the Whitehouse Shore, which are glacial erratics often consisting of conglomerates made of granite clasts. Recent glacial activity finally exposed the modern site before retreating and emplacing the erratics.

The geological processes discussed in this chapter formed then deformed the rocks at the Whitehouse Shore. This has led to a heterogeneous sedimentary and structural setting. Observations of the fluid flow pathways of this complicated formation are presented in the following chapter. These pathways exist because of the geological history of the formation, and any patterns or relationships discovered are related

back to this geological history.

3.3 References

Cameron, I.B. and Stephenson, D. 1985. British Regional Geology: The Midland Valley of Scotland, *British Geological Survey*

Cocks, L. R. M. and Torsvik, T. H. 2006. European geography in a global context from the Vendian to the end of the Palaeozoic. *From*: Gee, D. G. and Stephenson, R. A. (eds). *European LIthosphere Dynamics*. Geological Society, London, Memoirs, **32**. pp. 83-95.

Ince, D. (1984). Sedimentation and tectonism in the middle Ordovician of the Girvan district, SW Scotland. *Transactions of the Royal Society of Edinburgh: Earth Sciences*. v.**75**. pp. 225-237.

Ingham, J. K. 1978. Geology of a continental margin 2: Middle and Late Ordovician transgression. Geol. J. Spec. Issue No. 10, 115-138.

Lawson, J.D. and Weedon, D.S. 1992. Geological Excursions around Glasgow and Girvan. *Geol. Soc. Glasgow.* 1992 pp.496

Nichols, G. 1999. Sedimentology and Stratigraphy, Maldon: Blackwell Scientific Publications

Strachan, R. A. 2012. Mid-Ordovician to Silurian Subduction and Collision: Closure of the Iapetus Ocean. In: Woodcock, N. H. and Strachan R. A. ed. 2012 *Geological History of Britain and Ireland*. Blackwell Publishing Ltd. pp. 110-111.

Stűwe, K. 2007. Geodynamics of the Lithosphere: An Introduction. Springer, New York.

Torsvik, T. H., Smethurst, M. A., Meert, J. G., Van der Voo, R., McKerrow, W. S., Brasier, M. D., Sturt, B. A. and Walderhaug, H. J. 1996. Continental break-up and collision in the Neoproterozoic and Palaeozoic – A tale of Baltica and Laurentia. *Earth-Science Reviews*. v.**40** i.**3-4**. pp. 229-258.

Williams, A. 1962. The Barr and Lower Ardmillan Series (Caradoc) of the Girvan district, South-Western Ayrshire. London: Geological Society of London.

Woodcock, N. H. 2012. Early Devonian Sedimentary and Magmatic Interlude and Iapetus Closure. In: Woodcock, N. H. and Strachan R. A. ed. 2012 *Geological History of Britain and Ireland*. Blackwell Publishing Ltd. pp. 110-111.

Chapter 4

Sedimentology: features and processes

> "*The distant past* consisted of epochs of paroxysmal and catastrophic action interposed between periods of comparative tranquillity" – William J. Whewell

4.1 Introduction

This chapter details the observations and data collected about the sedimentology of the Myoch Formation within the field site. The sedimentology of the field site has been studied because the material heterogeneity of mudstones has previously been shown to have significant influence over fluid flow through mudstone (Aplin and MacQuaker 2011). Therefore, relating the depositional processes to the distribution of sedimentary facies within the mudstone could help with predicting the fluid flow properties of similar rocks currently at depth. Grain-scale investigation allows details to be gained about the mudstone and sandstone which can contribute understanding about the depositional and deformational processes undergone by the rock;

although the size of sand grains are orders of magnitude larger than mud/clay particles are. These investigations will provide useful information about the properties of the rock which could influence subsurface fluid flow.

The chapter is split into three parts:

1. General observations (sections 6.5.2 and 4.3) about the red mudstone and sandstone laminations. Field and laboratory observations were used to describe the rock features, properties and composition.

2. Statistical data (section 4.4) collected from the field was used to verify observations about the sedimentology of the red mudstone and sandstone laminations, and to determine any relationships which may be important for understanding the fluid flow properties of the rock.

3. Discussion of depositional and deformation processes (section 4.5). The observations and statistics collected from the field site were brought together to understand how the various processes undergone by the rock may have influenced the sedimentary features of the site. This understanding is then used to discuss how the factors controlling fluid flow could be predicted and detected in future sub-surface investigations.

4.2 Sedimentary features at the "bed scale"

The red mudstone of the Myoch Formation is interbedded with sandstone bands. These sandstone bands are near vertical, with measured dips of 80-86°, due to post-depositional roation of the formation. From hand-lens observations in the field of specimen the red mudstone was found to contain very fine grains of quartz but with a significant fraction of clay sized grains. The clay fraction was estimated from hand specimen from the area where grains were too small to be individually identified, as clay particles are too small to be differentiated without microscopic observations.

The distribution of grain sizes in the sandstone band were also observed to be from medium sand to clay.

The mapped distribution of the sandstone bands within the red mudstone is shown in figure 4.1. Small scale structural features are not shown on this map to focus on the sedimentary features. These structural features offset the sandstone bands in places and are discussed in detail in chapter 5.

The sandstone bands are not evenly distributed across the red mudstone. There are some areas with high prevalence of sandstone bands (blue circle, figure 4.1) and other areas with sparsely populated with sandstone bands (red circle, figure 4.1).

The sandstone bands show significant variation in size and shape. The sandstone bands are often extensive and can be traced along the exposure for over ten metres (figure 4.2-a). Other bands are only visible for a few metres then pinch out back into the red mudstone. Some of the sandstone features are even shorter than this, being exposed for as little as 10cm along-strike (figure 4.2-b). The sandstone bands are all very thin features, the thickest is 7cm thick (figure 4.2-a) but most are one centimetre or less (red arrow figure4.2-a). The stereonet in figure 4.1 shows that the sandstone bands are steeply dipping but not quite vertical. This would mean that the thickness measurements are an overestimate of the true sandstone band thickness. The shallowest sandstone band dip was recorded as 84°, for a sandstone band of 1cm thickness this would give a measured thickness on the surface of $\frac{1}{sin\theta} = 1.005cm$. A thickness correction for bedding dip has therefore not been made as this difference is less than what can be accurately measured in the field.

Based on field observations; the sandstone laminations have been divided into three general categories: 1. Continuous sandstone bands. 2. Sandstone bands made of smaller individual lenses resembling pseudonodules described in previous studies (e.g. Haughton et al. 2003), hereafter called "pseudonodule bands" to differentiate from the continuous bands. 3. Isolated lenses of sandstone.

Continuous sandstone bands are defined as those bands which have fully connected sandstone material along their trace (figure 4.3). These continuous sandstone bands

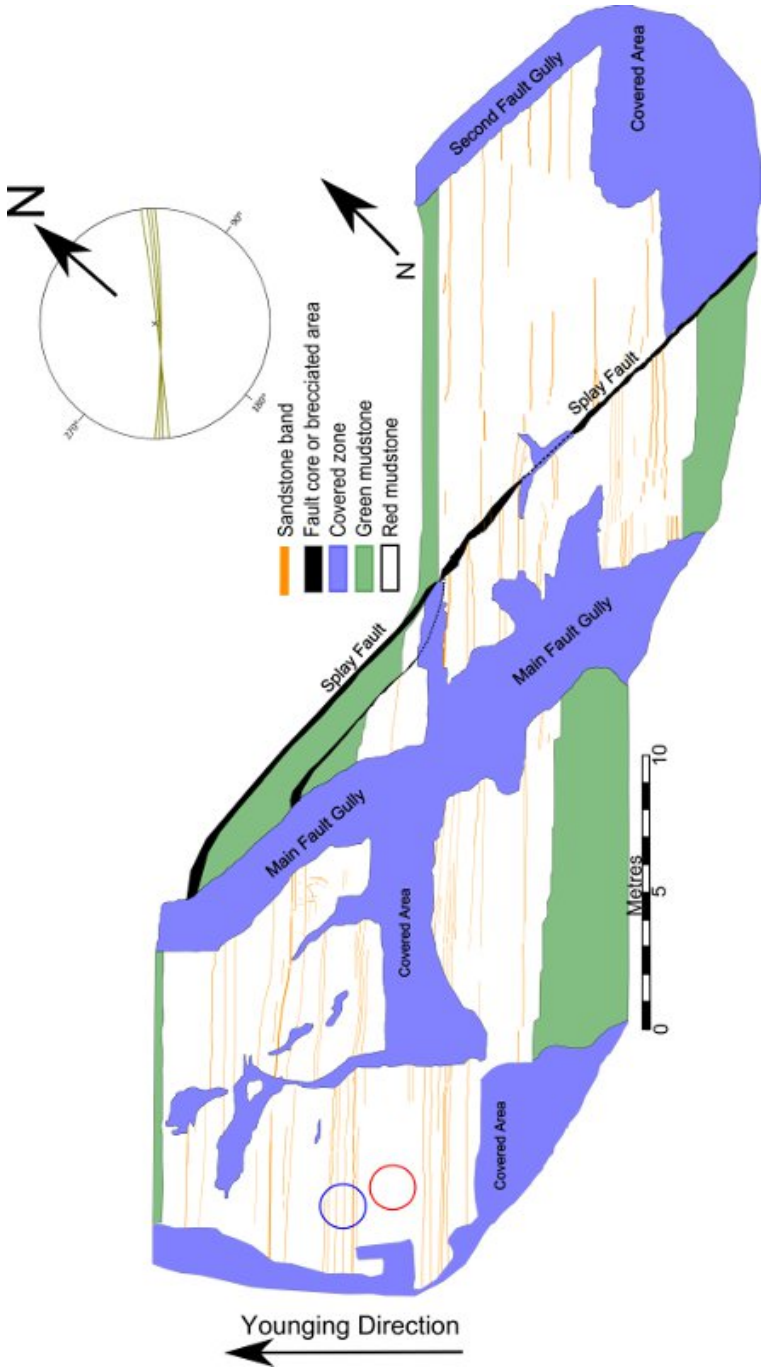

Figure 4.1: Detailed map of field area showing distribution of sedimentary features. Smaller scale structural features are not shown, however the main faults remain to provide context where sandstone bands are offset. Stereonet shows sandstone band orientations, n.b. stereonet is orientated in same direction as the map.

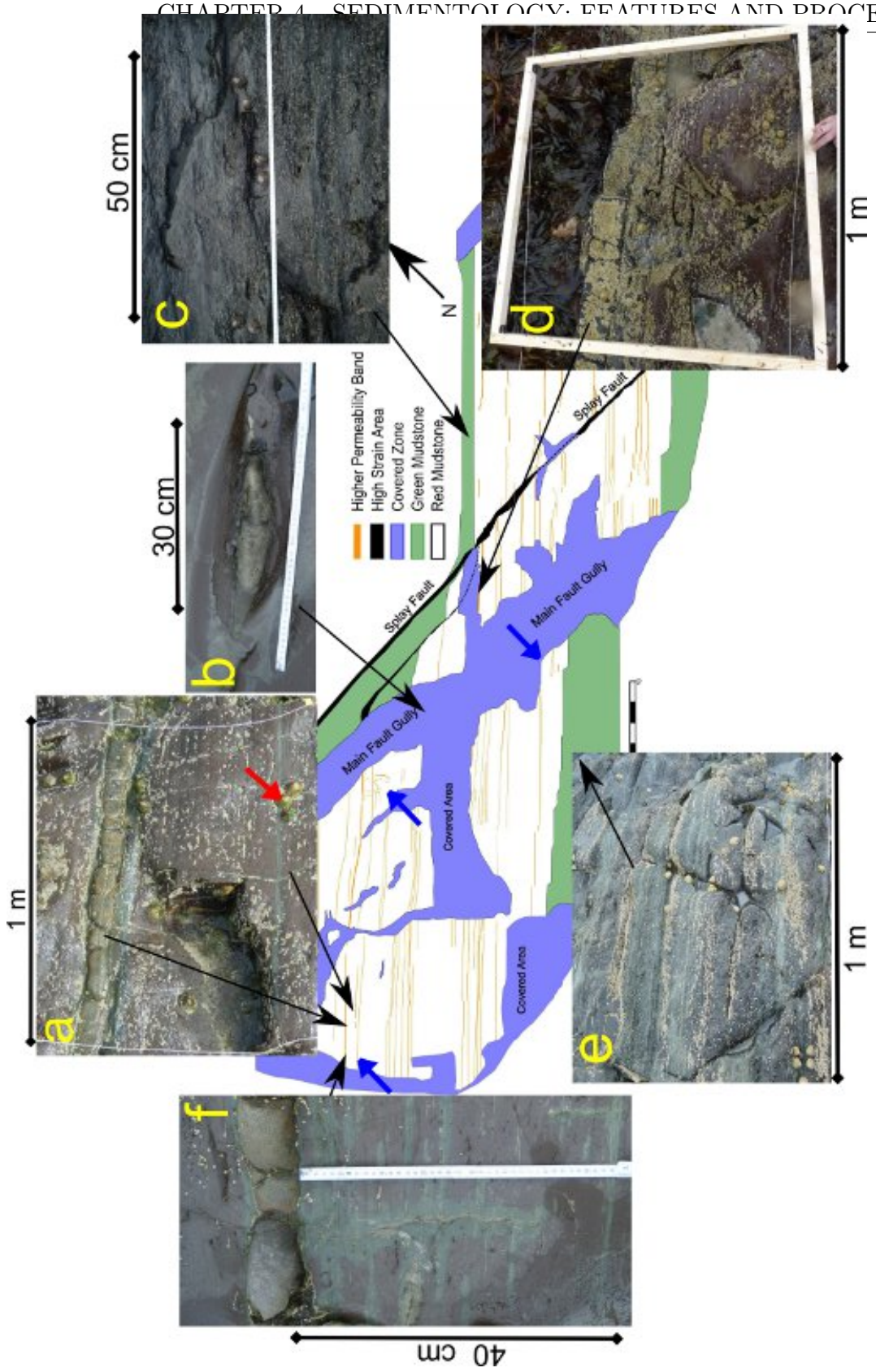

Figure 4.2: Sedimentary features located in the field site. a. (upper band) Extensive thick sandstone band and (lower band) extensive thin sandstone band within red mudstone. b. Sandstone channel surrounded by red mudstone. c. Grey/green mudstone d. extensive thick sandstone band contained in red mudstone. e. green mudstone f. Sandstone injectite perpendicular to sandstone bands. N.b. The thick sandstone band at the top of a.is the same as the band in d and f demonstrating how one band can be traced across the outcrop.

tend to be less than one centimetre thick such as the example shown in figure 4.3. The continuous sandstone bands can be traced through the red mudstone for many tens of metres; as long as exposure quality is sufficient for observation.

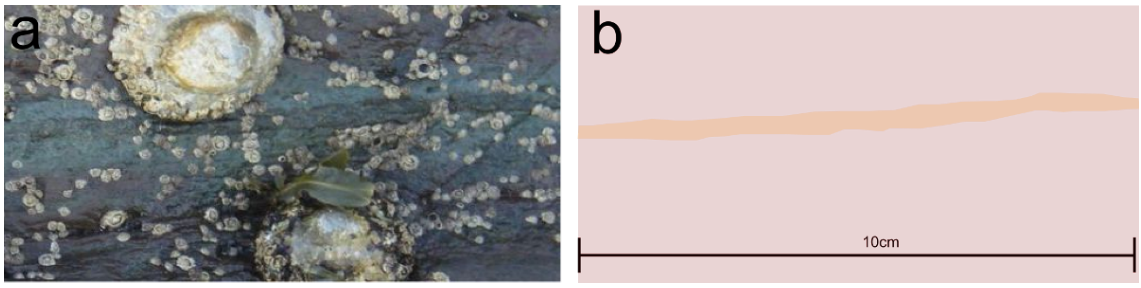

Figure 4.3: Thin sandstone band contained within red mudstone. The green alteration surrounding the band is discussed in detail in later chapters. Image "a" is a photograph taken in the field, image "b" is a tracing of image "a" to clarify the location of the sandstone band in the photograph.

Two examples of continuous sandstone bands are shown in the photographs in figure 4.2-a. The thicker of the two bands is in the upper part of the photograph. It is seven centimetres thick although there is slight variation in the thickness (+/- one centimetre) along its trace. This thick sandstone band is the thickest observed within the red mudstone, and is clearly exposed on either side of the fault making it a key feature which can be used to gauge horizontal fault separation. The lower band (red arrow, figure 4.2-a) is more representative of the rest of the continuous sandstone bands population. This thinner sandstone band is highlighted in figure 4.2-a by a green alteration halo, this alteration is discussed in chapter 6. This thinner sandstone band is only a few millimetres thick but presents a continuous trace of sandstone which can be followed for tens of metres across the exposure.

The pseudonodule sandstone bands consist of several individual sandstone lenses, each lens is usually less only a few centimetres long, which are closely spaced at milimetres to centimetres apart. Figure 4.4 is an example of one of these pseudonodule bands where lenses of various sizes are observed to occur though the mudstone in long lateral layers. Similar to the continuous sandstone bands the pseudonodule bands can be traced for tens of metres across the mudstone.

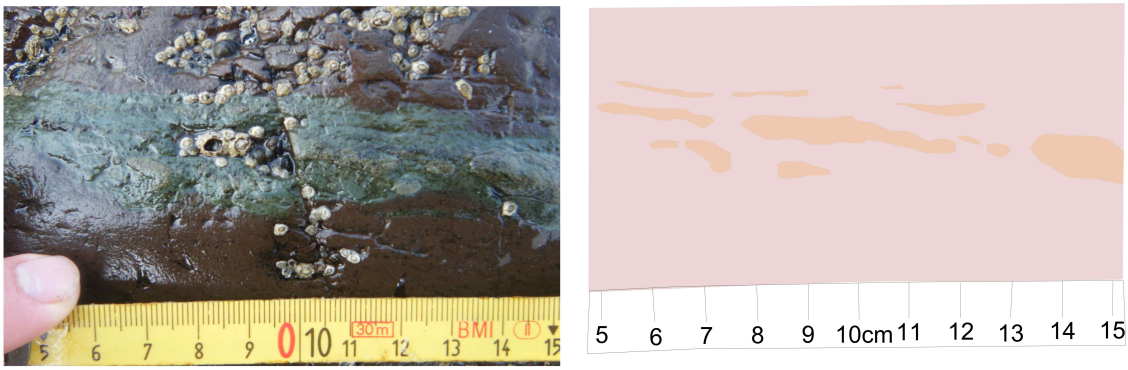

Figure 4.4: Pseudonodule band that is exposed as a series of individual sandstone lenses. Image on right is tracing to clarify details of left-hand photograph.

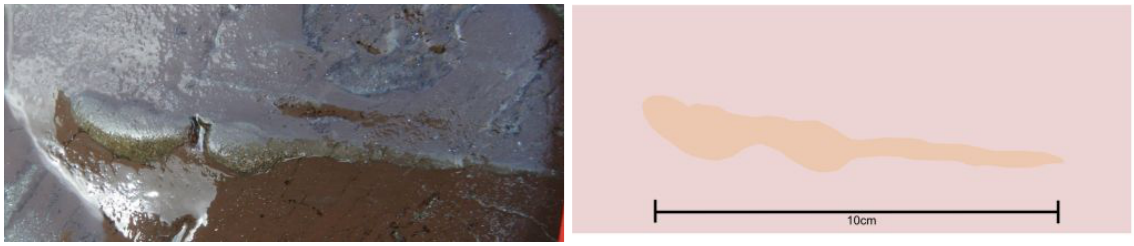

Figure 4.5: Isolated single lens of sandstone contained within the red mudstone.

Isolated single lenses of sandstone are observed in five locations within the red mudstone (figures 4.2-b and 4.5). These isolated lenses are between 10cm (figure 4.5) and 50cm long and are of similar thickness to the continuous sandstone bands. Thin sandstone sheets and isolated lenticular lobes such as these are typical of outer fan areas of muddy submarine deposition systems (Nichols 2009, Basilici 1997). The features shown in figures 4.3 and 4.5 fit with previous interpretations (Ince 1984) of the depositional environment of the Myoch formation as being deposited in deep sea distal to a submarine fan. Thin sandstone bands such as these have been documented previously as thin-bedded sand-mud couplets of Facie C2.3 in the classification of deep water facies by Pickering et al. (1986).

All of the above sedimentary features have sharp contacts with the mudstone, allowing clear determination of where the sandstone band ends and the mudstone begins. Additionally no grading of grain size was observed in any of the features.

Sandstone injectites are an additional sedimentary feature observed at the field site, these are related to post-depositional deformation. Sandstone injectites cut through the mudstone perpendicular to the sandstone bands (figure 4.2-f). The sandstone bands and laminations are the source of material for the injectites, as the injectites are always observed to begin at a junction with a sandstone band, and are of the same material. These injectites have been previously observed in rocks with similar depositional environments, e.g. Oligocene Taveyannez sandstone of Eastern Switzerland (Sinclair and Cowie 2003). Soft sediment mobilization structures, such as sandstone injectites are caused by a combination of processes. The beds may be temporarily weakened, as fluids in the sandstone create buoyancy effects on the grains. Alternatively pore fluid pressure may negate the inter-grain cohesion by sustaining additional loading of the sediment. If the rocks covering this buoyant sediment fractures then the overpressurised sediment-filled fluid can flow up into these fractures (Maltman and Bolton 2006).

4.3 Sedimentary features at the "grain scale"

Seven samples were collected for micro-structural investigation; one sample of the red mudstone, one sample of sandstone (figure 4.6-f) from the thickest sandstone band (figure 4.2-a), five samples from pseudonodule bands (figure 4.6-a–e).

Two techniques were used to gain grain scale information; optical microscope and scanning electron microscope (SEM). The optical microscope allowed grains down to very fine sand (63μm) to be identified, and the SEM down to clay grain sizes (5μm). These classifications are according to the Udden-Wentworth grain-size scale for clastic sediments. Optical microscope and SEM observations allowed grain identification, and collection of data about grain size, grain shape and sorting analysis.

The main grain types identified in both the mudstone and sandstone are quartz, biotite, feldspars and metal oxides (figure 4.7). Identification of minerals was conducted by shape and optical analysis of the grains on thin section using the optical

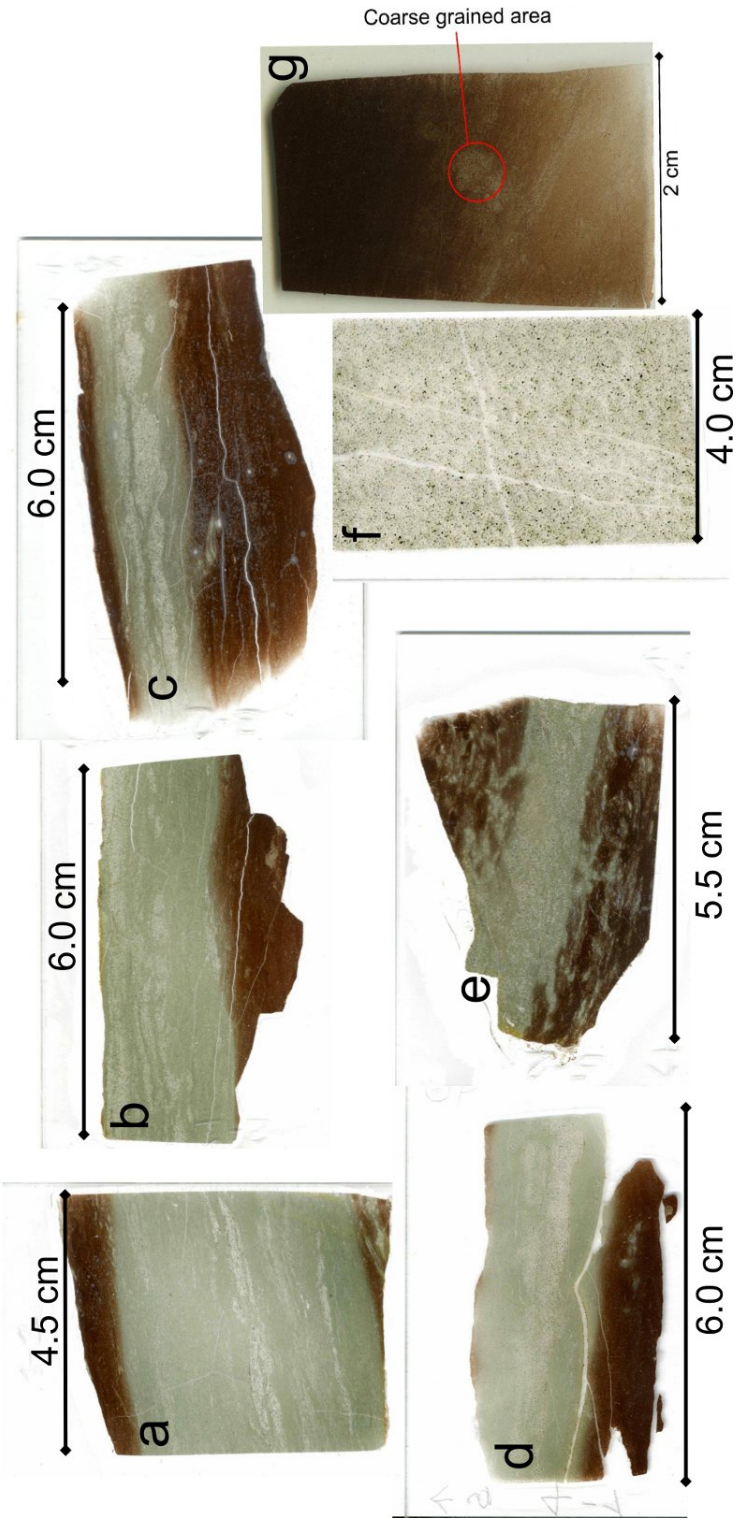

Figure 4.6: Examples of thin sections of sandstone bands. The sandstone bands in a-e are surrounded by a green reduction halo, beyond which the red mudstone can be seen. f is from a particularly thick sandstone band which is wider than the thin section plate so does not show any surrounding mudstone. g shows an area of red mudstone with no sandstone band however some material heterogeneity can be seen by the highlighted area of coarser grained material.

microscope. The grain types are consistent between the all the sampled sandstone bands (figure 4.8) as well as for the mudstone in each of the samples. Having the same grain type suggests that the material that comprises the mudstone and sandstone comes from the same source. The grains of the sandstone and the mudstone are sub-angular to sub-rounded (figures 4.8 and 4.9).

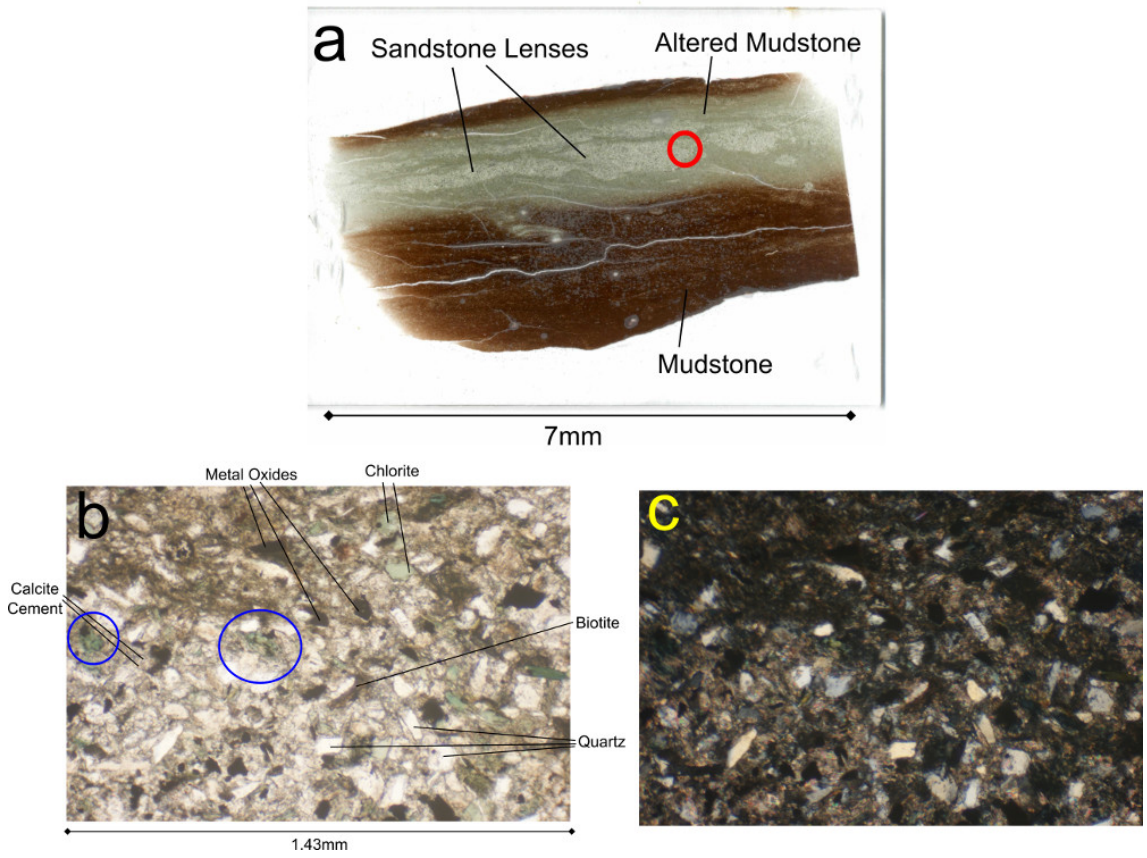

Figure 4.7: Image b of thin section of sandstone band with plane polarised light, where the microscop is focussed on the red circle of image a. Image b is the same area but with cross polarised light. The main mineral constituents of the rock are labelled. A significant area of the thin section is too fine grained to be analysed with the optical microscope.

The sandstone bands are defined as quartz-rich lithic wacke (Pettijohn 1995). Using point counting on the images taken from the thin sections (figure 4.8) the observable mineral composition of the sandstone bands was estimated to be quartz 56%, lithic

fragments (biotite, chlorite and metal oxides) 32% and feldspar 12%. The clay content of the sandstone bands is 20%. The mineral composition of the mudstone was estimated from the SEM images (figure 4.9) and is: quartz 10%, lithic fragments 27% and feldspar 63% with a clay content of 50%. On both the sandstone and the mudstone 50 points were used to gain the estimates of mineral composition.

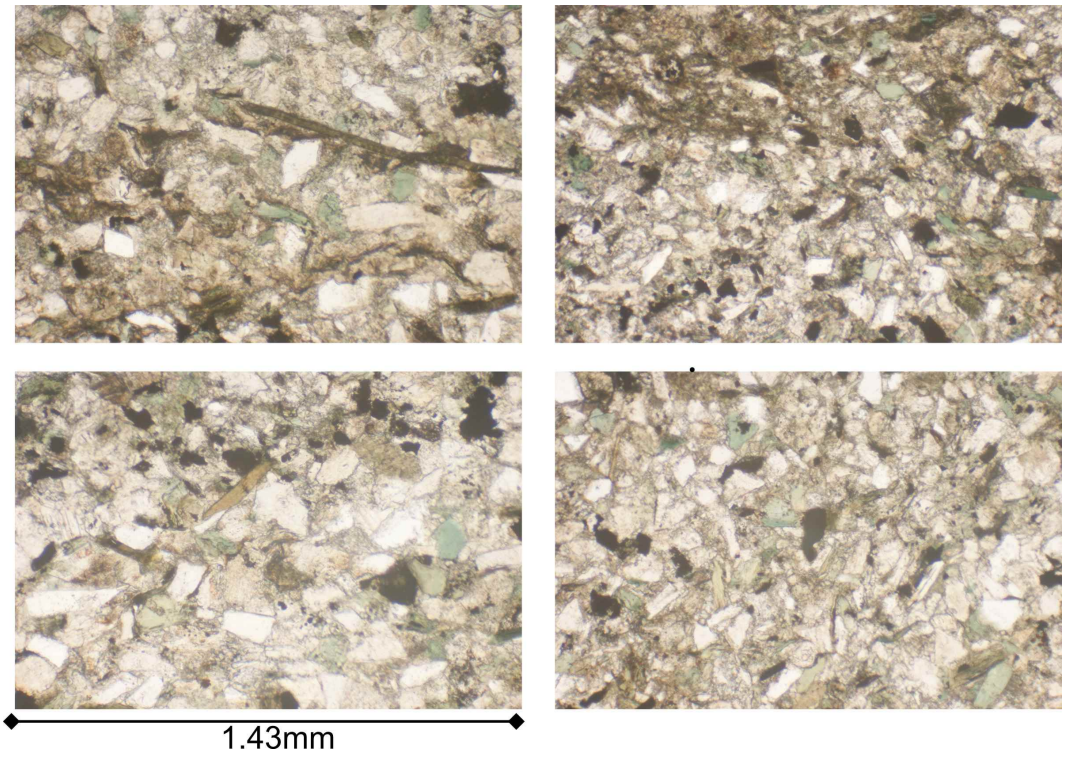

Figure 4.8: Four microscope images, each from a different sandstone band. The images show that the four sandstone bands consist of the same material. Local differences in grain size and clay content that can be seen between the images may be due to natural heterogeneity of the rock.

The metal oxides were identified as being iron or titanium oxides using the backscatter electron technique on the SEM (Hall and Lloyd 1981). The iron oxides could be responsible for the colour of the mudstones of the Myoch formation (Van Houten 1973), with the red and green mudstones showing differences in the oxidation states of the iron oxides (McBride 1974, Eichhubl et al. 2004). Some of the grains of chlorite contain parts that are still biotite (red circles - figure 4.7) which indicates

low-grade metamorphism as not all the biotite has altered to chlorite. Low-grade metamorphism fits with the bed scale observations of relatively undeformed sediment.

The grain size of mudstone ranges from clay to a very fine sand ($< 5\mu m$ to $80\mu m$), although grains of very fine sand are rare and most of the grains are silt ($< 63\mu m$) or smaller. The grain size of the sandstone generally ranges from $17\mu m$ (medium silt) to a maximum measured grain size of $148\mu m$ medium sand. The grain sizes are poorly sorted. Grain size measurements were made on image analysis software (imagej) using images taken from the optical microscope for the sandstone bands and SEM for the mudstone. The grain sizes were estimated by manually tracing out the grains.

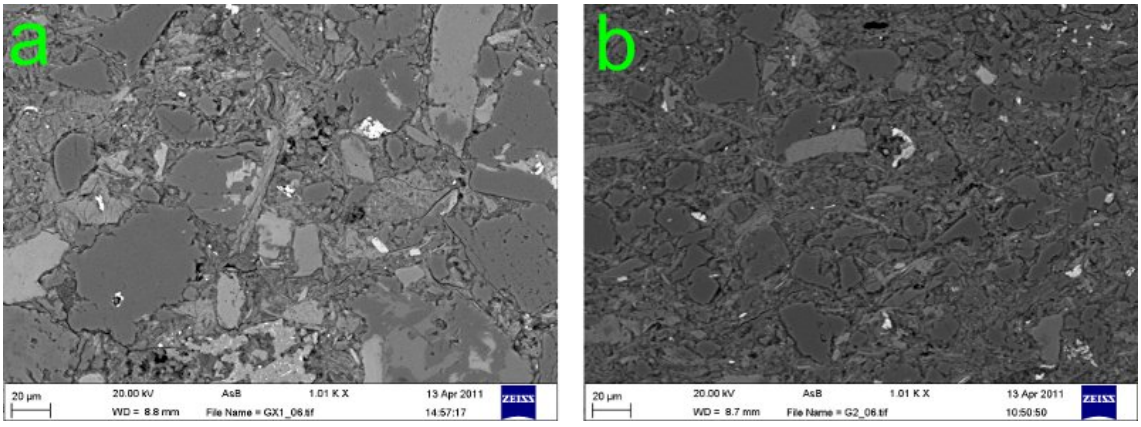

Figure 4.9: SEM image of a. A coarser grained area of the mudstone. b. A finer grained area of the mudstone. The poorly sorted mudstone has a grain size of between 5 and 80 microns; clay to coarse silt, with a few grains composed of very fine sand. The grains are predominantly quartz and feldspar with minor metal oxides (bright white minerals) including iron, titanium and magnesium.

The grain-scale observations are consistent with previous interpretations of deposition of the Myoch Formation. The general poorly sorted and fine grained nature of the mudstones would mean the rock is probably low permeability, such as a typical cap-rock of between 10^{-8}mD and 10^{-3}mD (Armitage et al. 2011, Yang and Aplin 2007, Brace 1980). Turbidites can have great ranges in permeabilities from 10 to

1000mD (Fugelli and Olsen 2007) however these ranges are for turbidites which are proximal and sand rich. The distal turbidites in this study are likely lower permeabilities than the range for these sand rich turbidtes; as these are poorly sorted and have finer grain sizes. However there is chemical evidence for the sandstone bands being conduits for fluid flow through the mudstone (presented in chapter 6) implying the sandstone bands could be orders of magnitude more permeable than the mudstone.

4.4 Statistics of the sandstone bands

Quantitative data regarding the distribution of the sandstone bands was collated. It is anticipated that this will help to inform predictions during future subsurface investigations within similar geological settings. The patterns found can be related to the depositional and deformational processes, the controls on sedimentary feature distribution and properties in order to improve understanding in this geological environment.

Three data sets have been collected about the sandstone bands within the red mudstone: 1) the distribution of the sandstone bands, 2) the thickness of the sandstone bands, 3) the connectivity and extent of individual sandstone bands. To collect this data a survey tape was laid out perpendicular to bedding in two locations(figure 4.10).

The position of each sandstone band along the transects were recorded, as well as the thickness of the band (section 4.4.2). Additionally, a qualitative assessment was made of the connectivity of the individual lenses making up the sandstone band and how far the sandstone band extends away from the scanline (section 4.4.3).

Scanline 2 was conducted on a particularly stormy day where data collection was difficult. In such windy and wet conditions it was not possible to collect the fine scale data required to analyse the sandstone bands. In addition to that the exposure of scanline 2 was poorer than scanline 1, which meant that it was not possible to

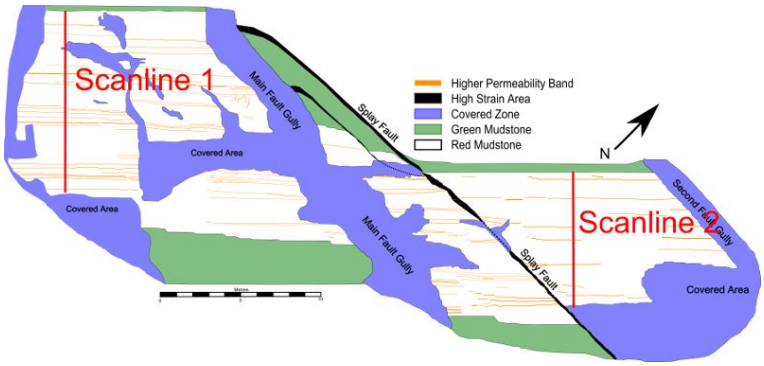

Figure 4.10: Location of survey tape for the scanline over the red mudstone.

colelct the fine scale detail even under good conditions. Therefore the data from scanline 2 has not been used in the analysis.

It would have been very useful to collect data from several scanlines at different locations along the outcrop. Both to ensure the scanlines were representative of the rock as a whole and to investigate sedimentary variations. However scanline 1 was chosen (as was the field site location in general) because of the quality and quantity of exposure. There was no other location found on the outcrop that would have been suitable for a comparative scanline.

4.4.1 Distribution of sandstone bands

A graphic log of sandstone bands within the red mudstone is shown in figure 4.11-a. Only two rock types were observed; red mudstone shown in pink and the sandstone bands shown in orange. Areas where the outcrop was not exposed due to cover by rock pools are shown in blue with a red cross (8.0m – 9.0m and 10.1m to 11.0m).

The sandstone bands are not distributed evenly through the mudstone. There are areas where many sandstone bands are present over a short distance of the transect and areas where no sandstone bands are recorded for more than half a metre (2.0m – 2.75m figure 4.11).

Figure 4.12 zooms in on the first two metres of figure 4.11 with accompanying photos

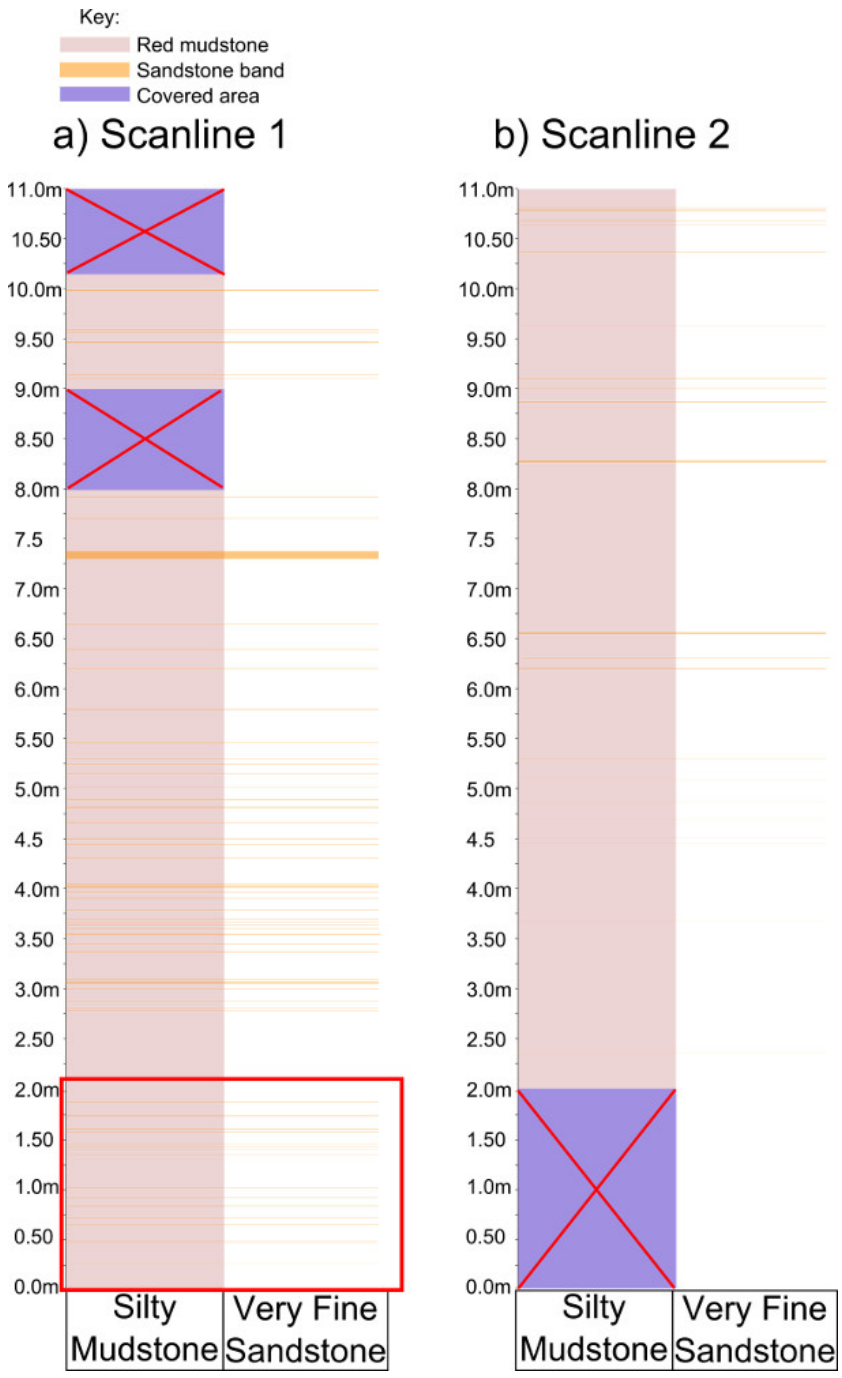

Figure 4.11: Graphical image representation of the material which is intersected by the two scanlines. Red box shows contains areas shown in figure 4.12.

to allow more detail to be seen. Some of the sandstone (1.3m – 1.5m, figure 4.12) are the continuous bands but other areas show a collection of pseudonodule bands (0.45m – 0.5m, figure 4.12).

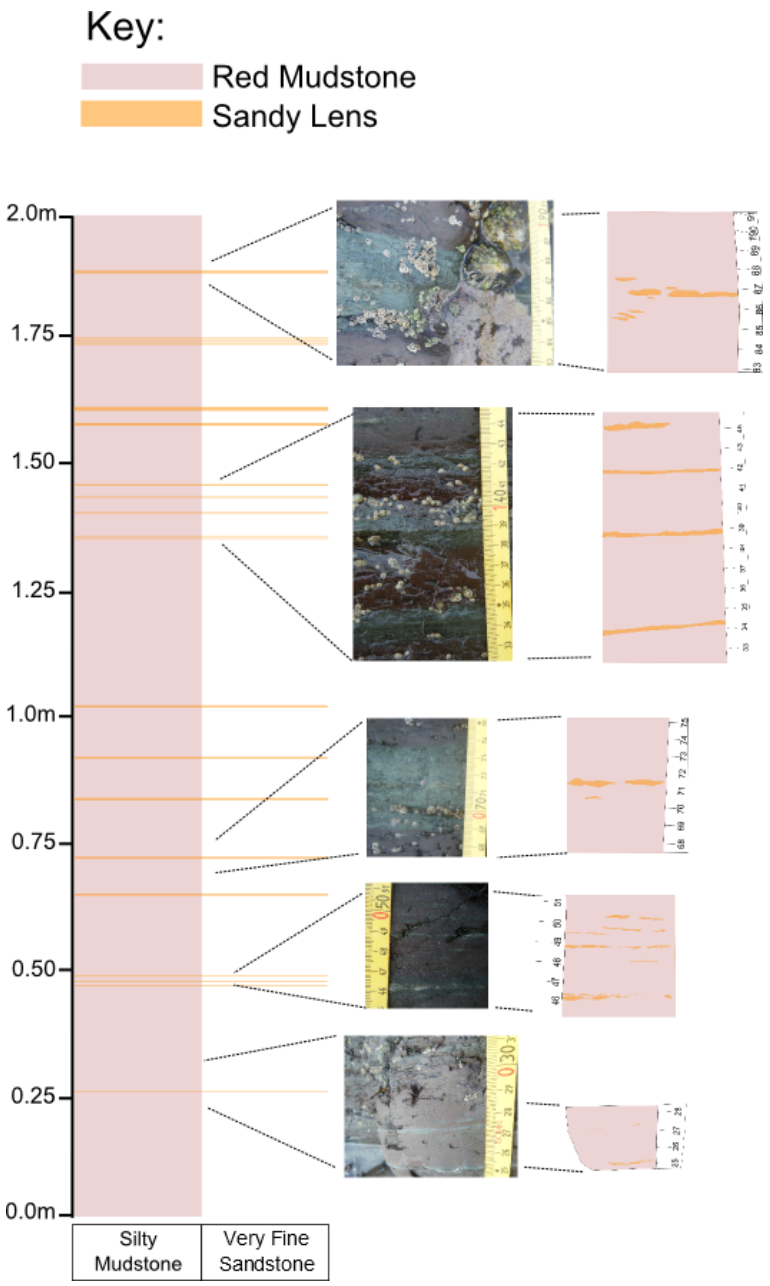

Figure 4.12: Section of the scanline south of the fault, zoomed in areas show extra detail of the sandstone bands and photographs of the area represented.

65 sandstone bands were recorded in the mudstone, representing 3.6% net-to-gross of the total thickness of the red mudstone; similar ratios (2% sandstone) are found in equivalent depositional environments (Basilici 1997). Although there are many sandstone bands within the 12 metres of the scanline the very thin nature of the sandstone bands means that overall they haven't greatly contributed to the amount of material present in the Myoch Formation. Chemical alteration of the surrounding rock shows that sandstone bands acted as fluid flow conduits which is discussed in chapter 6. In addition the thinness of the sandstone bands could make them difficult to reliably detect during subsurface investigations where even very detailed wireline logs can get only resolutions of 5mm with careful logging, these issues are explored further in chapter 8.

4.4.2 Sandstone band thickness

The thickness data taken from the scanline across the red mudstone are shown as a histogram in figure 4.13. Accurate thickness data were collected using a digital calliper which is accurate to $\pm$0.01mm; the sandstone bands protrude slightly from the mudstone which aided accurate collection of thickness measurements. However the data is likely unreliable below one millimetre due to the difficulty in identifying by eye features this small in the field.

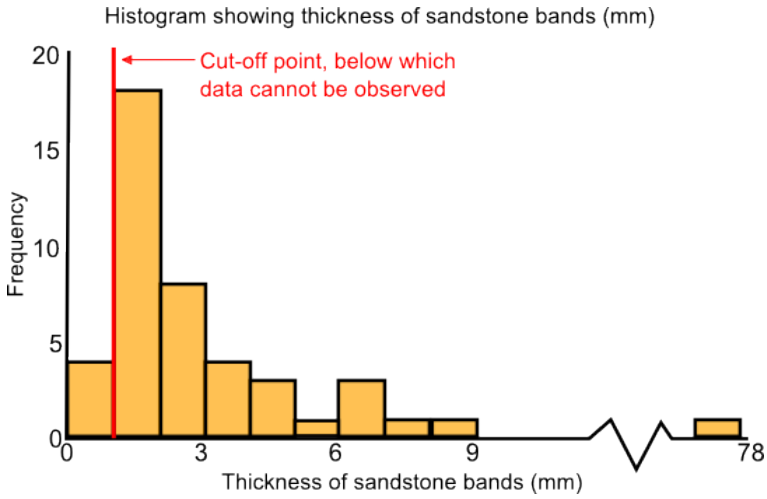

Figure 4.13: Histogram showing frequency of sandstone band thicknesses found within the red mudstone.

Thinner sandstone bands are more common than the thicker bands (figure 4.13). Almost half (18 out of 40) of the sandstone bands are thinner than two millimetres. While above seven millimetres thickness only one sandstone band exists in each thickness range. The one sandstone band much thicker than the others (77-78mm figure 4.13) is shown in photographs in figure 4.2-a,d and f and can be traced across the field site.

The band thicknesses in figure 4.14-b show a strong match to a negative exponential distribution when plotted as cumulative distribution (figure 4.14). An R^2 value of 0.97 shows that a negative exponential line of $1.7 - (0.18log(x))$ is a very good fit

to the data. How this distribution of sandstone band thickness fits in with data collected from other outcrops is discussed in chapter 8.

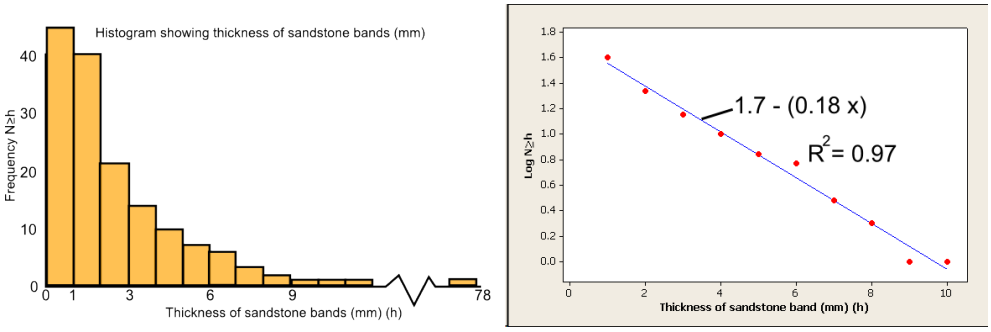

Figure 4.14: a Histogram showing frequency of sandstone bands of greater than "h" thickness ($N > h$). b. liner/log plot of the cumulative frequency of the sandstone band thicknesses.

4.4.3 Lateral connectivity and extent of sandstone bands

The one dimensional scanlines (section 4.4.1) have provided a representation of the distribution of the sandstone bands within the red mudstone. However from a one dimensional scanline it is impossible to quantitatively characterise the lateral behaviour of the sandstone bands (section 4.4.2). The sandstone bands are not all well connected features as there are the pseudonodule bands made of unconnected features (figures 4.3, 4.4) and five isolated lenses of sandstone 4.5). The aim of this section is to categorise the connectivity and lateral extent of the sandstone bands. This will be used to asses how the sandstone bands influence the fluid flow through the mudstone in chapter 6.

Two assessments of the sandstone bands were taken from scanline one; connectivity and extent. These assessments were taken by measuring along parallel to the sandstone bands when they were intersected by the scanline. This allowed measurements to be taken which were perpendicular to the scanline.

Connectivity and extent are both effectively 2D measurements of features that were created within a 3D depositionary system. The material was transported from the

NW (Ingham 1978), so today looking down into the outcrop means we are looking towards the origin of the sediment. Therefor these sandstone band represent a cross-section perpendicular to the direction of material transport. Which will need to be taken into account for the connectivity and extent of the sandstone bands.

Connectivity

Connectivity gives a measure to determine whether the sandstone is a single connected bed (figure 4.3) or a collection of individual lenses (figure 4.4) such as the pseudonodule bands. Low connectivity is defined as when there is a discernible break in the sandstone at intervals of less than ten centimetres, medium when the break in the sandstone is at intervals of between ten centimetres and one metre, high when the sandstone is unbroken for distances greater than one metre, as shown in figure 4.15.

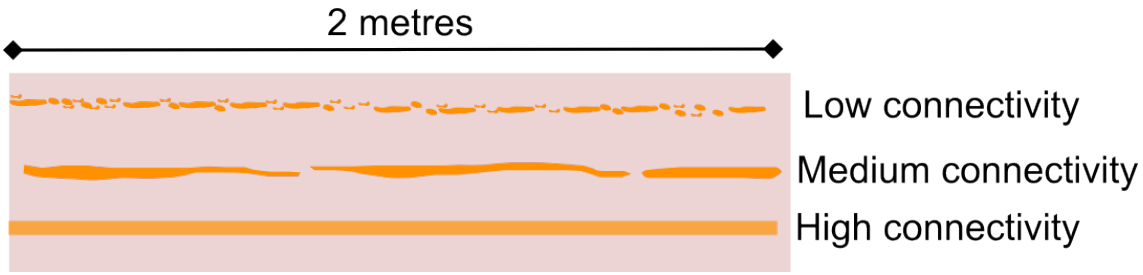

Figure 4.15: Cartoon with examples of the classifications used for connectivity.

Twenty six out of the forty bands (65%) assessed show low connectivity (figure 4.16), meaning the pseudonodule bands are the most common type of band, however this also includes the few isolated lenses. The connected beds (figure 4.3) are relatively rare in the mudstone outcrop with only six (15%) of the bands intersected by the scanline showing high connectivity.

Thick sandstone bands are more likely to be of higher connectivity than the thin sandstone bands (figure 4.17). The median thickness of low connectivity bands is 1.7mm and for medium/high connectivity bands (grouped together) is 3.1mm. A

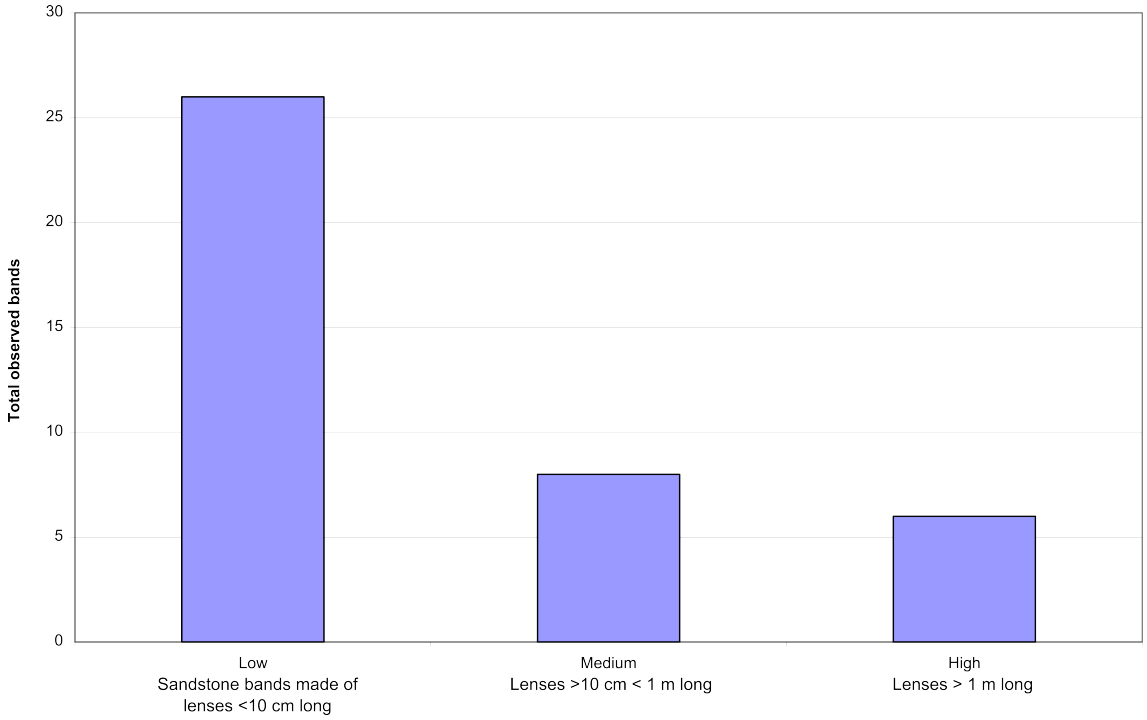

Figure 4.16: Graph showing the connectivity of sandstone bands along scanline one.

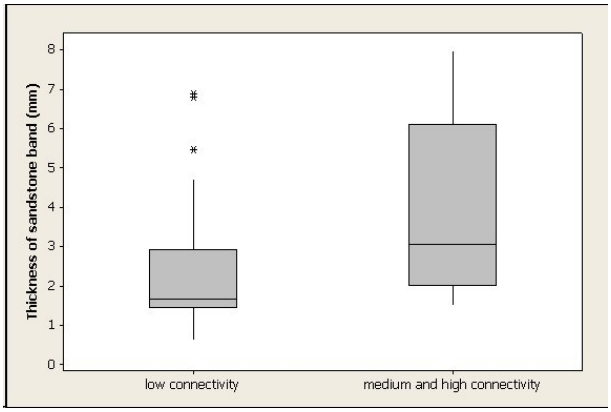

Figure 4.17: Box plot showing differences in thickness of sandstone bands between those classified as low connectivity and those of medium and high connectivity.

Mann-Whitney test was performed and the differences in medians was found to be significant at greater than 95% confidence.

This connectivity is for a cross section perpendicular to the direction of transport.

These pseudonodule sandstone bands could possess much better connectivity in 3D than in 2D. With the pseudonodules representing channels the could interconnect in the direction of transport.

Extent

Extent is an assessment of how far an entire sandstone band can be traced across the field site. When assessing the extent of a sandstone band the connectivity of the individual lenses making up a pseudonodule band is ignored as they have been interpreted as one depositional feature. This allows bands with poor connectivity to still be classed as having high extent (figure 4.18). Exposure cover and faults can cause difficulty in assessing when a sandstone band has been pinched out back into the mudstone; but the bands could be matched up over faults or cover with confidence. Since the measurement of extent is perpendicular to the direction of transport it effectively represents the width of the turbidite lobes.

The sandstone bands were classified for extent as follows. A sandstone band of low extent can not be traced for more than ten centimetres, medium extent bands can be only be traced for a length of between ten centimetres and one metre, high extent bands can be traced for over one metre.

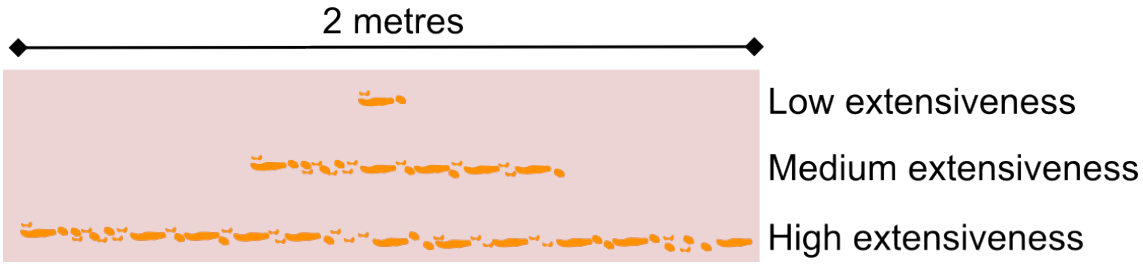

Figure 4.18: Cartoon with examples of the classifications used for extent. Each of the sandstone bands shown here would be classified at "low connectivity" (figure 4.15) due to the individual lenses that make up the sandstone bands.

The data in figure 4.19 show that most of the sandstone bands can be traced for metres across the site, even the pseudonodule bands (figures 4.4 and 4.18). This

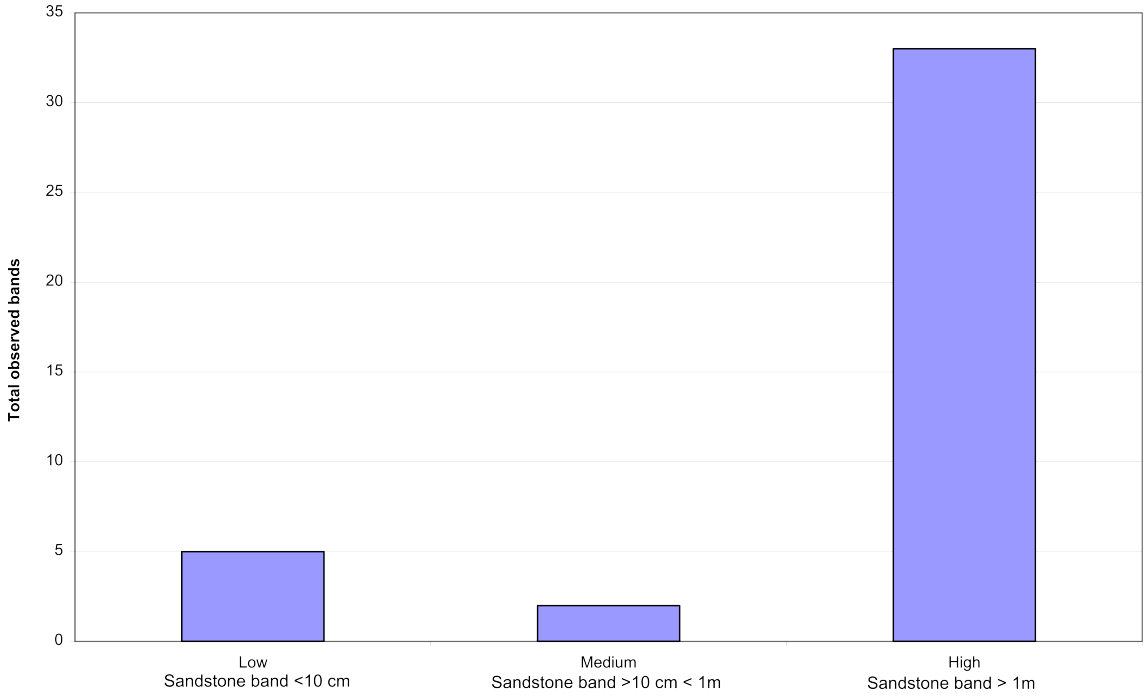

Figure 4.19: Graph showing the extensiveness of sandstone bands along scanline one.

indicates that even the psuedonodule bands could have been deposited over extensive areas. The sandstone bands with high extent have more chance than low extent bands of connecting two otherwise isolated fractures, because they are present over a larger area. These implications are discussed further in chapters 6 and 8.

4.5 Discussion: sedimentology

4.5.1 Key findings from sedimentary investigation

- Bands of coarser material are distributed throughout the mudstone.
- The thickness of the sandstone bands follows an exponential distribution.
  - This could mean that such thin features are predictable based on distribution of thicker features. This concept is explored in chapter 8.
- Many sandstone bands are made up of "low connectivity" pseudonodules.
  - How the permeability properties of the pseudonodule bands differ from the continuous bands is explored in chapter 6.

4.5.2 Depositional processes that formed the sandstone bands

Depositional processes have created complicated pseudonodule sandstone bands made of individual lenses of sandstone. Continuous sandstone bands also exist but the pseudonodule bands are much more prevalent. Both of these features are likely to be the distal remnants of turbidite flows on submarine fans. A number of processes may have contributed to many of the bands being a complicated series of individual lenses rather than a single thin sheet of sandstone. Some of these potential processes are discussed below.

Bioturbation can disturb sedimentary structures in laminated mudstones. Bioturbation caused by organisms burrowing into the sediment deposited on the ocean floor. High grades of bioturbation can results in beds becoming unrecognisable in sedimentary rocks. However no burrows or bores were identified in the mudstone visually or using the optical microscope or SEM, therefore bioturbation is likely not the caused of the individual lenses making up the sandstone laminations.

Density differences between the sandstone and mudstone may also be the cause behind the shapes of the sandstone laminations. Ball and pillow structures are created when adjacent sediments have different densities (Owen 2003), and are common at the bases of sandy turbidite beds deposited onto mudstone (Nichols 2009). Typically the sandstone will be the denser material and sink into the mudstone. This process leaves behind distinctive anticlinal shapes in the sandstone bed. These anticlinal shapes were not seen in the sandstone at this field site. The mud may also be forced into the overlying sediment creating a flame like structure if the sediments have differing densities. These were also not observed in the Myoch formation providing further evidence that this is unlikely to be the mechanism behind the individual sandstone lenses. N.b. flame structures are very well preserved in the underlying Threemile Formation.

Reworking at the field site may also explain the pseudonodule bands. The pseudonodule bands could well have been deposited as continuous sandstone bands. Pickering et al. (1986) note that bottom currents in deep water deposition environments can remove fines from sandy turbidite deposits, resulting in a coarser grained band. Pickering et al. (1986) also described that this effect leads to "thin, irregular, poorly sorted, structureless, mixed-composition, iron-manganese coated, coarse grained sand countourites" which is very similar to the sandstone bands found at the field site. The pseudonodules can occur due to remobilisation of units, where the thin sandstone layer is sheared and rotated forming these irregular facies. Reworking of the formation soon after initial deposition, is the most likely cause of the pseudonodule bands.

4.5.3 Possible porosity and permeability properties of the mudstone and sandstone bands

Porosity and permeability are important properties for predicting fluid flow through sedimentary rocks. These two properties are not fixed, but will vary in due to natural variability in the rocks. They will also vary in time, as various processes act

upon the rock between its initial deposition and then eventual outcropping at the surface. The deposited rock will initially undergo compaction, due to the weight of the sediment deposited above. Compaction can lead to vast losses in porosity and is the dominant process at lower temperatures below 70°C (Aplin and Macquaker 2011). Such compaction would cause the expulsion of water that was in the pores of the pre-compacted mud. However in low permeability material the water is trapped within the formation leading to overpressure. Many chemical processes such as redox reactions and mineral precipitation and dissolution lead to changes in the porosity and permeability of rocks, as the pore spaces are clogged, reduced, or even opened. Such changes in porosity and permeability of the rock will affect the fluid-flow behaviour over time.

The porosity of mud is upto 85% or 90% immediately after deposition which can be reduced to only 5% after 6km of compaction(Aplin and Macquaker 2011). This would lead to an associated permeability loss as porosity and permeability are correlated (Yang and Aplin 2010), however there can be upto 3 orders of magnitude range of permeability for a given porosity value of mudstone. Mudstones with similar clay content to the mudstone studied in the field site and were relatively deeply buried (around 3km) were found to have porosity of 0.205 - 0.210 and vertical permeability of 10^{-9}mD (Yang and Aplin 2007). These porosities are higher than those quoted for mudstones with lower clay content (pf between 0.1 and 0.2), this could be because the high clay content lowers the permeability stopping fluid expulsion from the pores. Then the pressurised fluid stops pore collapse.

Upon deposition the silty components of turbidites (similar in consistency to the sandstone bands here) have a porosity of around 0.7 (Giradclos et al. 2007). Such porosity values in turbidite settings have been found to reduce to 0.5 with 500m of burial (Hamilton 1976). The sandstone bands have also been cemented by carbonate. This carbonate cement would have the effect of filling the pore space (Budd 2002), reducing the porosity.

The properties of both the mudstone and sandstone bands was likely one of initial high porosity which was quickly diminished due to burial related compaction. For

the sandstone bands this would have likely led to a loss in permeability as pore networks closed or were diminished, which would have been further exasperated by the carbonate cementation. The relatively high clay content of the mudstone, however, probably meant that the mudstone had litle permeability to lose during compaction. As the small clay particles may have stopped an inter-connected pore system developing.

4.6 References

Aplin, A. C. and Macquaker, J. H. S. 2011. Mudstone diversity: Origin and implications for source, seal and reservoir properties in petroleum systems. *AAPG Bulletin*. v.**95**, No.**12**. pp. 2031-2059.

Armitage, P. J., Faulkner, D. R., Worden, R. H., Aplin, A. C., Butcher, A. R. and Iliffe, J. 2011. Experimental measurement of, and controls on, permeability and permeability anisotropy of caprocks from the CO_2 storage project at the Krechba Field, Algeria. *Journal of Geophysical Research: Solid Earth*. v.**116** i.**B12**. DOI: 10.1029/2011JB008385

Basilici, G. 1997. Sedimentary facies in an extensional and deep-lacustrine depositional system: the Pliocene Tiberino Basin, Central Italy. *Sedimentary Geology*. **109**. pp. 73-94.

Brace, W. 1980. Permeability of crystalline and argillaceous rocks. *International Journal of Rock Mechanics and Mining Science and Geomechanics*. v.**17** no.**5**. pp. 241-251.

Budd, D. A. 2002. The Relative Roles of Compaction and Early Cementation in the Destruction of Permeability in Carbonate Grainstones: A Case Study from the Paleogene of West-Central Florida, U.S.A. *Journal of Sedimentary Research*. v.**72** No.**1**. pp 116-128.

Eichhubl, P., Taylor, W. L., Pollard, D. D. and Aydin, A., 2004. Paleo-fluid flow

and deformation in the Aztec Sandstone in the Valley of Fire, Nevada-Evidence for the coupling of hydrogeologic, diagentic, and tectonic processes. *Geological Society of America Bulletin*. v.**116** no.**9**. pp. 1120-1136.

Fugelli, E. M. G. and Olsen, T. R. Delinating confined slope turbidite systems offshore mid-Norway: The creataceous deep-marine Lysing Formation. *AAPG Bulletin*. v.**91**. no.**11**. pp. 1577-1601.

Funk, J. E., Slatt, R. M. and Pyles, D. R. 2012. Quanitification of static connectivity between deep-water channels and stratigraphically adjacent architectural elemnts using outcrop analogues. *AAPG Bulletin*. v.**96** no.**2**. pp. 277-300.

Giradclos, S., Schmidt, O. T., Sturm, M., Ariztegui, D., Pugin, A. and Anselmetti, F. S. 2007. The 1996 delta collapse and large turbidite in Lake Brienz. *Marine Geology*. v.**241**. pp. 137-154.

Hall, H. G. and Lloyd, G. E. 1981. The SEM examination of geological samples with a semiconductor back-scattered electron detector. *American Mineralogist*. v.**66**. pp. 362-368.

Hamilton, E. L. 1976. Variations of density and porosity with depth in deep-sea sediments. *Journal of Sedimentary Petrology*. v.**46** No.**2**. pp. 280-300.

Haughton, P. D. W., Barker, S. P. and McCaffrey, W. D. 2003 'Linked' debrites in sand-rich turbidite systems - origin and significance. *Sedimentology*. v.**50** i.**3**. pp. 459-482.

Ince, D. (1984). Sedimentation and tectonism in the middle Ordovician of the Girvan district, SW Scotland. *Transactions of the Royal Society of Edinburgh: Earth Sciences*. v.**75**. pp. 225-237.

Ingham, J. K. 1978. Geology of a continental margin 2: Middle and Late Ordovician transgression. Geol. J. Spec. Issue No. 10,

Maltman, A. J., and Bolton, A. 2003. How sediments become mobilized. *From:* Van Rensbergen, P., Hillis, R. R., Maltman, A. J. and Morley, C. K. (eds) *Subsurface*

Sediment Mobilization. Geological Society, London, Special Publications, **216**, 9-20.

McBride, E. F. 1974. Significance of Color in Red, Green, Purple, Olive, Brown, and Gray Beds of Difunta Group, Northeastern Mexico. *Journal of Sedimentary Petrology*. v.**44** no.**3**. pp. 760-773/

Nichols, G. 2009. Sedimentology and Stratigraphy, Maldon: Blackwell Scientific Publications

Owen, G. 2003. Ball-and-Pillow (pillow) structures. In: *Encyclopedia of Sediments and Sedimentary Rocks* (Ed. Middleton, G. V.) Kluwer Academic Publishers, Dordrecht; 39-40.

Pickering, K., Stow, D., Watson, M. and Hiscott, R. 1986. Deep-Water Facies, Processes and Models: A review and Classification Scheme for Modern and Ancient Sediments. *Earth Science Reviews*. v.**23**/ pp. 75-174.

Sinclair, H. D. and Cowie, P. A. 2003. Basin-Floor Topography and the Scaling of Turbidites. *The Journal of Geology*. v.**111**. pp. 277-299.

Van Houten, F. B. 1973. Origin of red beds: A review – 1961-1972. *Annual Review of Earth and Planetary Sciences*. v.**1**. pp. 39-61.

Yang, Y. and Aplin, A. C. 2007. Permeability and petrophysical properties of 30 natural mudstones. *Journal of Geophysical Research: Solid Earth*. v.**112** i.**B3**. DOI: 10.1029/2005JB004243

Yang, Y. and Aplin, A. C. 2010. A permeability-porosity relationship for mudstones. *Marine and Petroleum Geology*. v.**27**. pp. 1692-1697.

Chapter 5

Structural framework

> "When considering the formation of faults, we have generally to deal with systems of forces which existed in past geological time" – Ernest M. Anderson

5.1 Introduction

This chapter focuses on the structural features observed at the field site: thrust faults, strike-slip faults, shear fractures and joints. Structural features such as these can provide conduits for fluid flow (Caine et al. 2010, Younger and Manning 2010, Micklethwaite and Cox 2006, Rowland and Sibson 2004, Hinds et al. 2003, Eichubl and Boles 2000) thereby influencing or controlling the fluid flow properties of the bulk rock mass.

It should be noted that the structural features discussed in this chapter occurred after folding caused the beds of the field area to be tilted near-vertical. This means that usual relationships between bed offsets and different types of faults do not apply to this field site.

This chapter is split into three sections:

- **Section 5.2** Detailed mapping of the structural features is presented, providing an overview of the distribution and locations of the structural features. Field observations of the thrust faults, strike-slip faults, shear fractures and joints are described along with illustrative photographs.
- **Section 5.3** Quantitative data is used to test various relationships of the distribution and properties of the structural features.
- **Section 5.4** The information and data collected from the field site is used to aid discussion about the deformational history and the implications for fluid flow through the mudstone.

5.2 Mapped structural features

The detailed map of the structural features is shown in figure 5.1. The mapped sedimentary features presented in chapter 4 are not shown in figure 5.1 in order to focus on the structural details. Both the sedimentary and structural details will be shown together in the following chapter.

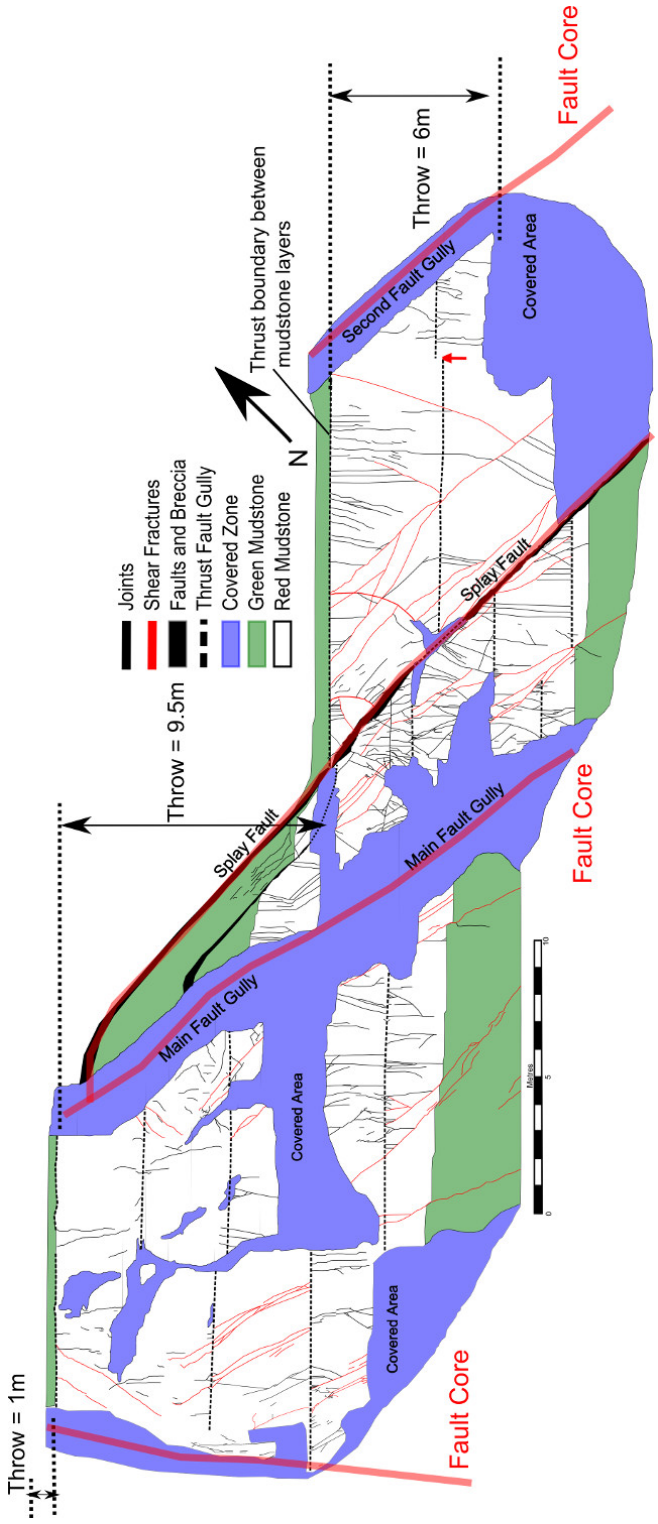

Figure 5.1: Detailed map created of field area showing distribution of structural features. Thrusts are dotted lines running across the map. Thick red lines show the locations and estimated locations of the strike-slip fault cores. Shear fractures are shown as thin red lines while the joints are black lines.

5.2.1 Thrust faults

Four thrust faults (shown as thick black dotted lines on figure 5.1) have been identified over the field site. These thrust faults are synthetic in orientation with the Whitehouse Shore Thrust Fault (Chapter 3 figure 3.8), which moved the Lower Whitehouse Formation over the Upper Whitehouse Formation. These features were identified as thrust faults due to their synthetic orientation with the Whitehouse Shore Thrust Fault, additionally previous work at the field site has identified these features as thrust faults (Ingham 1978). The thrust faults were measured to have a dip direction of SE, erosion of the surfaces meant an accurate dip was difficult to achieve but dip is estimated to be approximately 30°. The thrust faults are likely the oldest structural feature at the field site, although they formed after the folding event which brought the beds to their present day near vertical state. Strike-slip faults and shear fractures offset the thrust faults indicating that the thrust faults precede these features which are discussed in the following sections.

Thrust faults are exposed as gullies (figure 5.2) running E-W through the field site. In the middle of the gullies is a thin (less than two centimetres) brecciated zone that is the "fault core" of the thrust fault. The gullies are formed due to the lower erosional resistance of the thrust fault breccia compare with the surrounding mudstone. The thrust faults are extensive features and can be traced for tens of metres across the rock exposure, in places however they could not be traced due to cover or particularly poor exposure. The thrust faults are exposed parallel or sub-parallel with the bedding. The thrust fault in the NE of the field site has probably been offset by a shear fracture (red arrow - figure 5.1), however the exposure the exposure in this small area was not good enough to be certain of the cause; although an unexposed shear fracture (orientated antithetic to the main strike-slip fault) would produce this effect.

A thrust fault is a type of reverse fault which is formed when compressive strain is accommodated by one body of rock moving over another body of rock (figure 5.3. Thrusts are often described as low angled ($< 30°$) reverse faults and can have

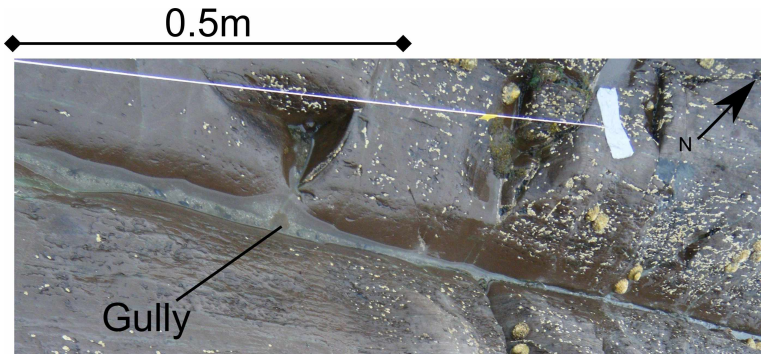

Figure 5.2: Example of a bedding parallel gully created by the brecciated material within the thrust fault fault being more prone to erosion from the tides.

large displacements of many tens of kilometers in some cases. Usually a thrust fault fault will result in the replication of strata in a borehole. However because tilting occurred prior to thrusting on this field site then thrusting has resulted in the some strata being lost to the exposure.

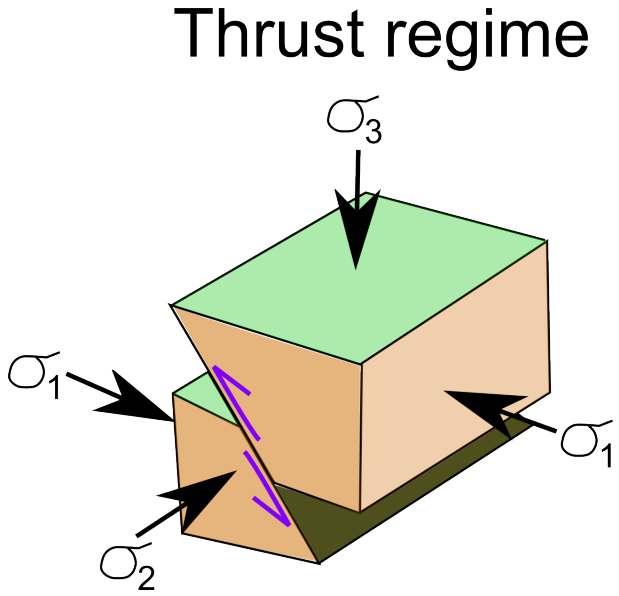

Figure 5.3: Cartoon showing idealised thrust fault with associated stress field.

5.2.2 Strike-slip faults

Three strike-slip faults are observed at the field site, two of which bound the field site along the NE and SW while the third runs through the middle of the field site. The middle or main strike-slip fault has the greatest offset of the strike-slip faults in the field site; also a splay runs off this main strike-slip fault, labelled as "splay fault" in figure 5.1. The locations of the cores of the three strike-slip faults and the splay fault are shown as thick red lines in figure 5.1, the core locations have been interpreted due to the cover over the gullies created by the strike-slip fault zones (figure 5.4). However the presence of the strike-slip faults is clearly evident due to the clear offset of bedding by several metres. Despite the significant debris cover over the strike-slip fault zones.

The stratigraphic boundary of the red mudstone has been horizontally offset by less than 10 metres. Tidal and wave erosion have removed any slickenlines from the strike-slip fault surfaces which would have provided information about the three dimensional strike-slip fault displacements. Therefore the offsets of the strike-slip faults are minimum values because there may be some unobservable vertical component to the offsets. The main strike-slip fault has a dextral horizontal offset of 8m and the splay fault a dextral horizontal offset of 1.5m. The strike-slip fault bounding the NE of the field site has a dextral horizontal offset of 6m and the strike-slip fault bounding the SW of the field site is the smallest with 1m of sinstral horizontal offset.

The strike-slip faults are part of a series of conjugate brittle faults which cut the sediments along the Whitehouse Shore, which were discussed in section 3 (figure 3.8). These strike-slip faults on the field site fit with the general trend of approximately E-W dextral and N-S sinstral faults of the Whitehouse Shore (Ingham 1978).

Strike-slip faults are a class of fault that are formed when both maximum (σ_1) and minimum (σ_3) are horizontal but perpendicular to each other (figure 5.5). These strike-slip faults are often steeply dipping. Usually they wouldn't displace beds (unless they had an additional component of vertical movement) but on the Girvan

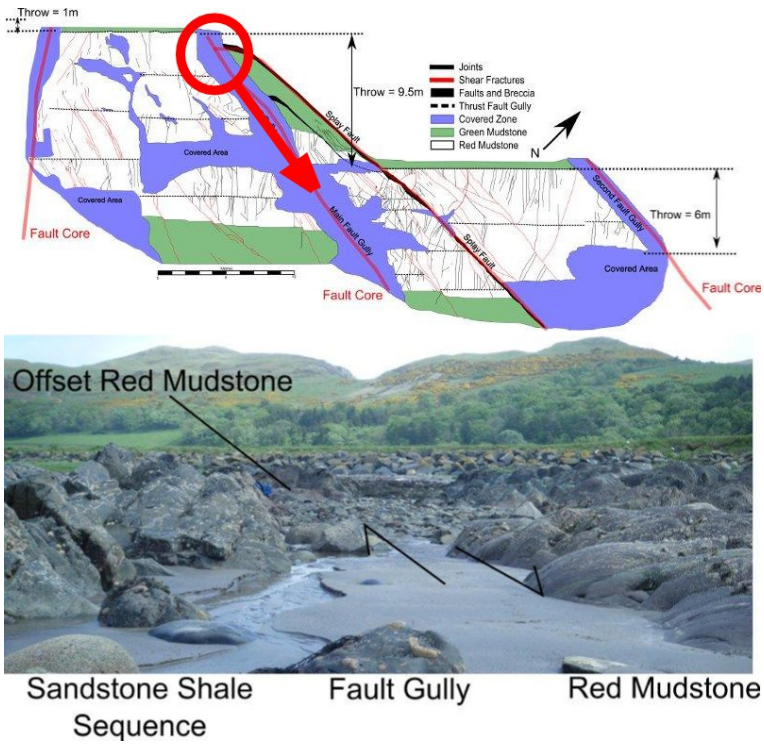

Figure 5.4: View looking along strike southern East down a gully formed by erosion of one of the larger strike-slip faults in the Upper Whitehouse Group. Fault has vertical offset of 9.5m. The gully is the central area covered by sand at low tide (blue are in above map). On the right of the gully is the red mudstone while directly to the left of the gully is the overlying red mudstone. These units are juxtaposed due to slip across the strike-slip fault.

foreshore the beds were previously rotated to be near-vertical. Therefore this strike-slip movement would offset the beds.

Fault zone architecture

The cover over the strike-slip faults made it nearly impossible to gain information about the fault structure however the fault core of the main strike-slip fault was partially exposed after excavating the covering sand with a spade. The splay fault was naturally exposed in places, while the NE and SW field site bounding faults were

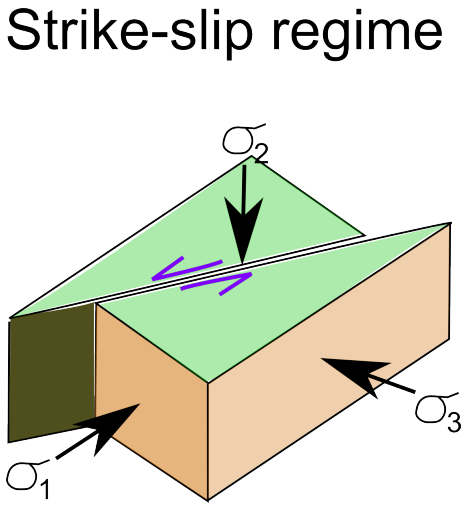

Figure 5.5: Cartoon showing idealised srike-slip fault with associated stress field.

unexposed and could not be excavated. A further fault core was naturally exposed (figure 5.6-d) approximately 10 metres to the NE beyond the NE boundary of the field site. This fault core was used to compare observations from the excavated main strike-slip fault.

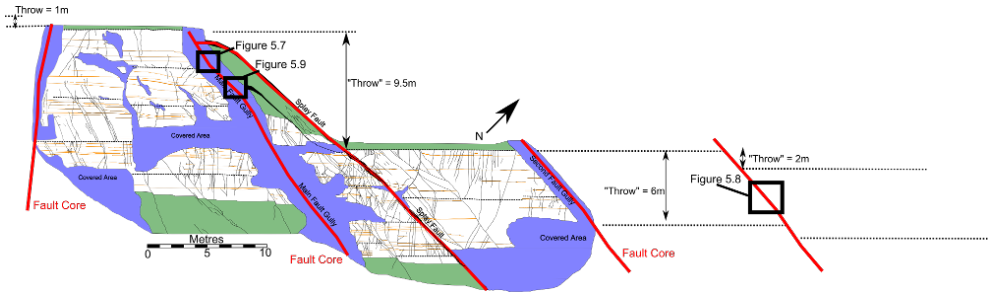

Figure 5.6: Section of map from figure 5.1 showing locations of fault zone architecture photos. The location around figure 5.8 is a fault zone not mapped due to generally poor exposure but the fault core is relatively well exposed so may be an analogue to the main fault zone studied. Black boxes show locations of figures 5.7, 5.8 and 5.9.

The main strike-slip fault was excavated at the location of figure 5.7 shown in figure 5.6, at this location the main strike-slip fault contains a brecciated zone. The brecciated zone varied in width from 25cm to 15cm (figure 5.7) along the exposed section. The breccia is uncemented and consisted of pebble sized clasts of red

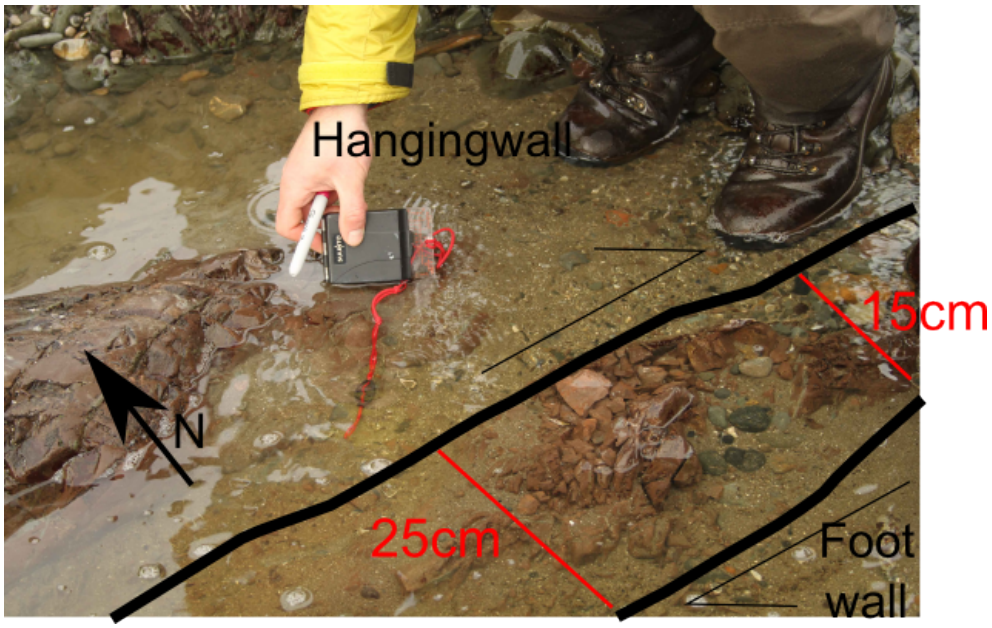

Figure 5.7: This photograph was taken after an "excavation" partially exposed the fault core. The thick black lines outline the brecciated fault core. The fault core varies in width from 25cm to 16cm in this limited exposure.

mudstone that could be removed by hand, this brecciated material is also present in the strike-slip fault exposed off the field site (located on figure 5.6 and shown in 5.8). The excavated brecciated fault core is bound on either side by slip surfaces, and the surrounding rock is relatively undeformed compared to the fault core. The slip surface on the southern side of the strike-slip fault core is less than one centimetre thick, while the northern slip surfaces is 2-3 centimetres thick and hosts a calcite vein (discussed in the following chapter). Both slip surfaces are observed to have a sharp boundary with the surrounding undeformed rock and the brecciated fault core. It is across the brecciated fault core, between the slip surfaces, where the majority of the strain of the strike-slip fault zone is accommodated (Brogi 2008, Berg and Skar 2005).

Deformational features exist in the rock immediately surrounding the fault core in area d on figure 5.1. Sandstone bands are dragged towards the fault (figures 5.8 and 5.9). Fault related drag of sedimentary layers is a phenomenon usually associated

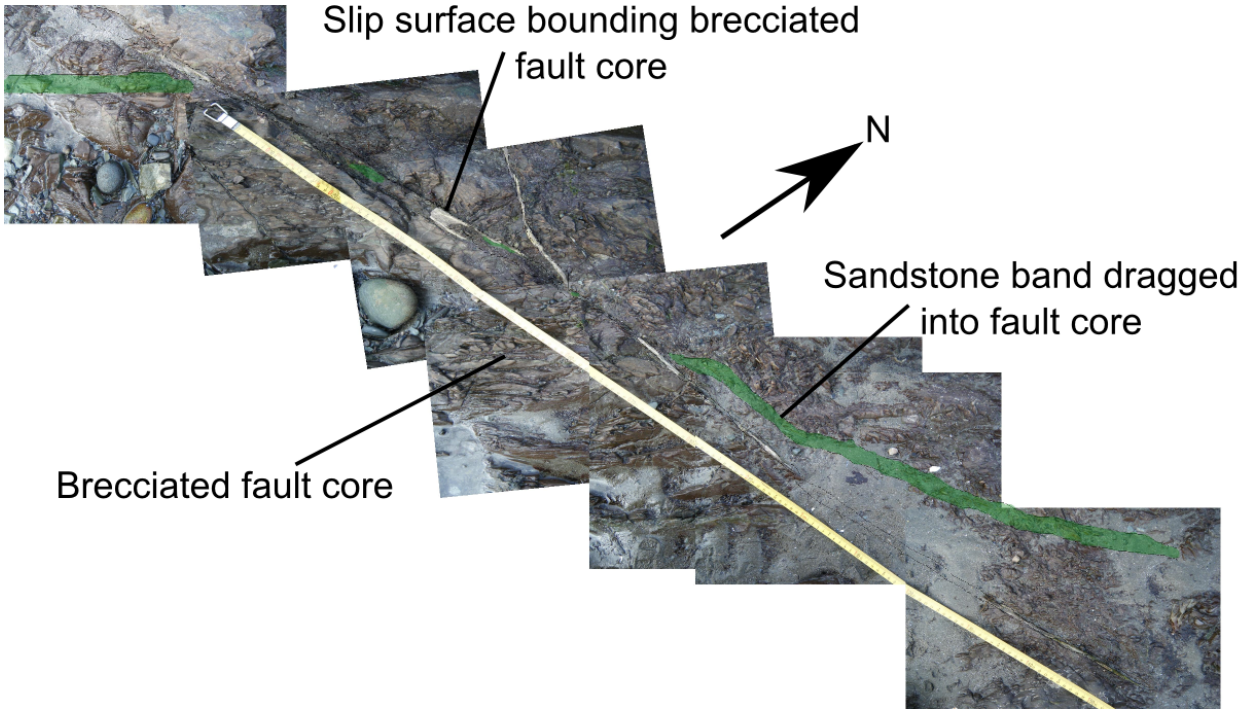

Figure 5.8: Photo-montage of exposed strike-slip fault location shown in figure 5.6. Sandstone band with green reduction halo is dragged into fault core before emerging on the other side. Carbonate veining is observed intermittently along the fault core. Breccia associated with the strike-slip fault occurs on the left of the fault core. Location of this photo-montage is shown on figure 5.6.

with more ductile materials, such as a shale layer within a sandstone-dominated formation (Burhannudinnur and Morley 1987). This deformation appears to have been partially accommodated with a series of shear fractures (shear fractures in figure 5.9). A series of joints are also present in the rock around the strike-slip fault. These joints are well-connected with each other and some of the shear fractures and were not observed to leave any isolated unconnected features in this zone.

5.2.3 Shear fractures and joints

Shear fractures are characterised across the field site by their centimetre scale offsets of the sandstone bands and thrust faults (figure 5.10). The shear fractures differ

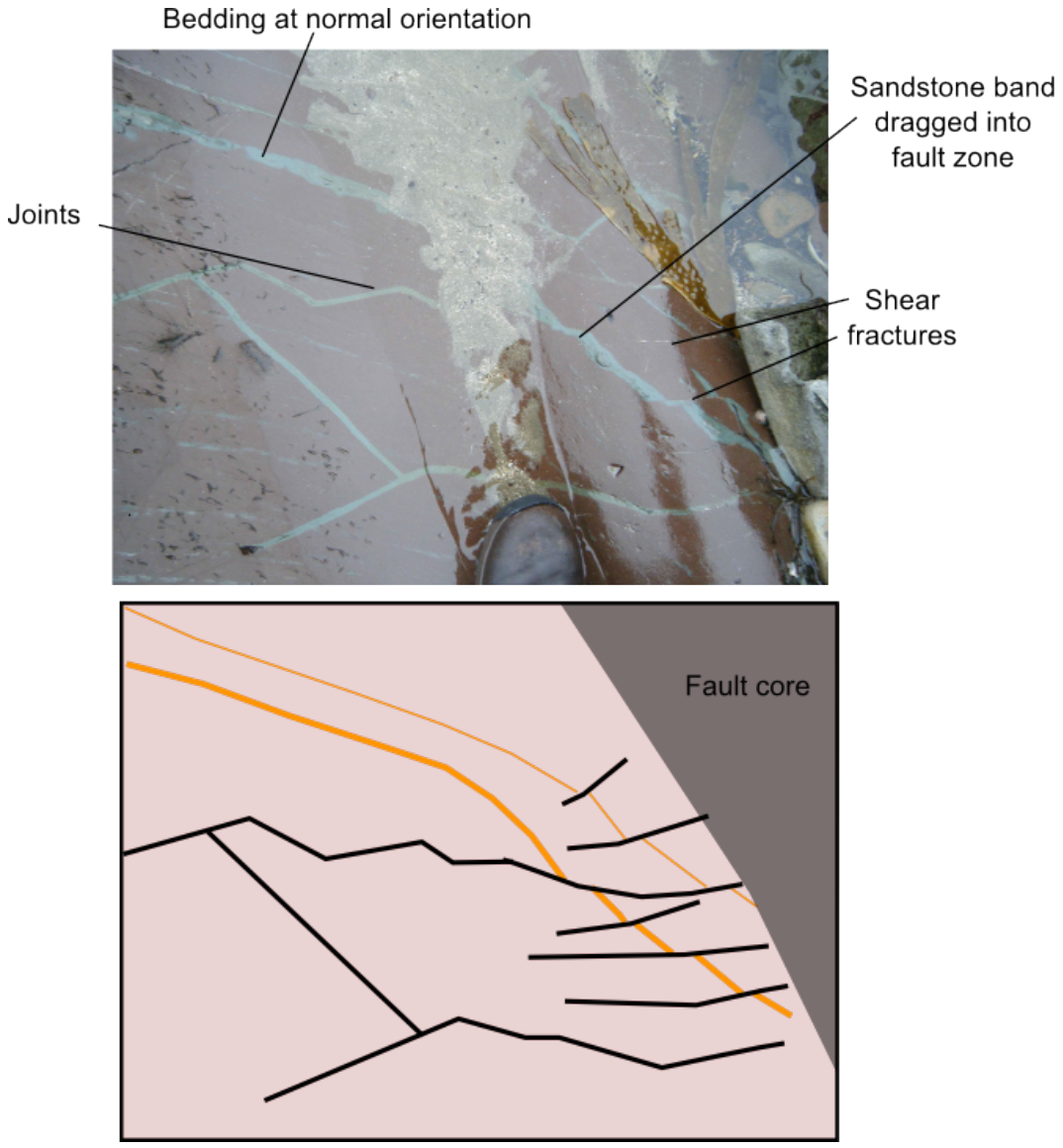

Figure 5.9: Photograph showing features that are present in the vicinity of the fault core. Features are under three centimetres of water when photograph was taken so some minor reflection and distortion is present. The location of this photo is shown on figure 5.6. Note: central region of photograph is partially covered by sand deposited by the tide.

from the strike-slip faults, not just by smaller offsets but by much simpler internal structure. The shear fractures consist of a single slip plane without any breccia or observable drag of bedding.

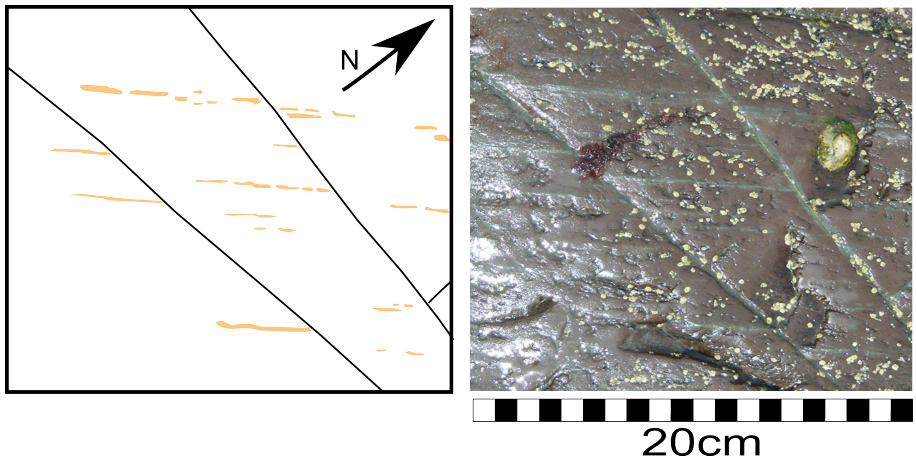

Figure 5.10: Right lateral shear fractures with single slip plane.

Some shear fractures terminate against the thrust faults (blue arrow - figure 5.1). When this happens a series of feather like pinnate joints (figure 5.11) exist in the vicinity of the termination. (Twiss and Moore 1992 - pg. 41, Wilkins 2001). Pinnate fractures are not observed where shear fractures propagate through and offset the thrust faults.

Joints are characterised as fractures with no observable offset (figure 5.12, section 2.3). Cross cutting relationships indicate that shear fractures precede joints. Joints terminate against shear fractures and shear fractures are not observed to offset joints. However some joints are filled by sandstone injectite material (figure 5.13). These sandstone injectites subset of joints are offset by shear fractures , indicating the injectites precede the shear fracturing.

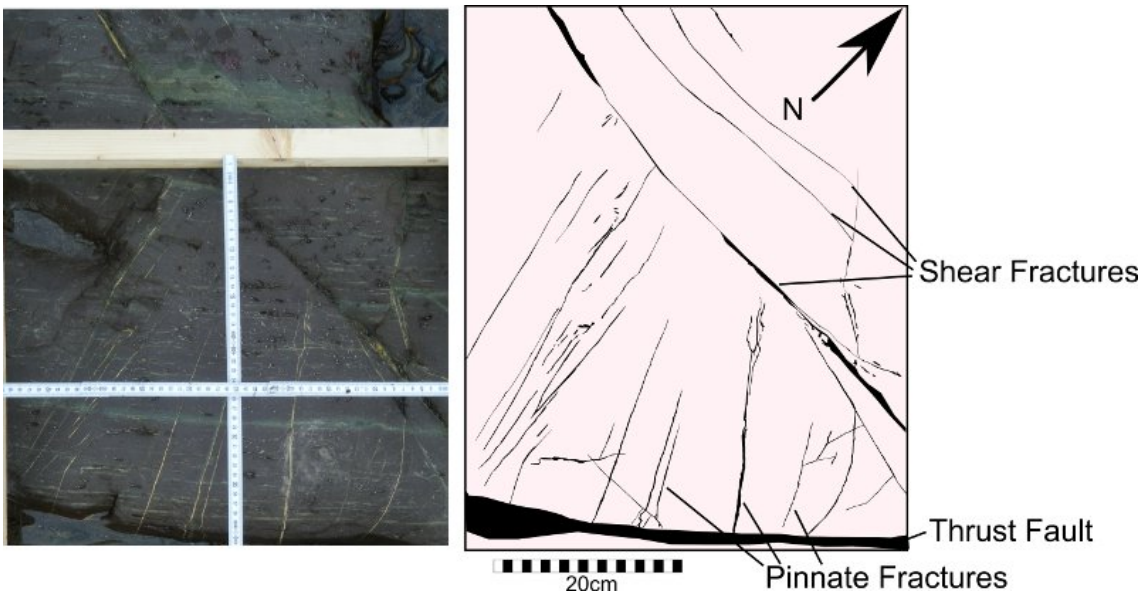

Figure 5.11: Pinnate joints where a shear fracture intersects and is terminated by a pre-existing thrust fault. The pinnate joints may form here as the movement on the shear fracture creates an area of tensile stress in the area within the acute angle formed between the shear fracture and thrust fault.

Figure 5.12: Examples of a joint cluster, some joints terminate against each other or the sandstone band. The joints do not cause any observable offset of the sandstone band running through the middle of the figure.

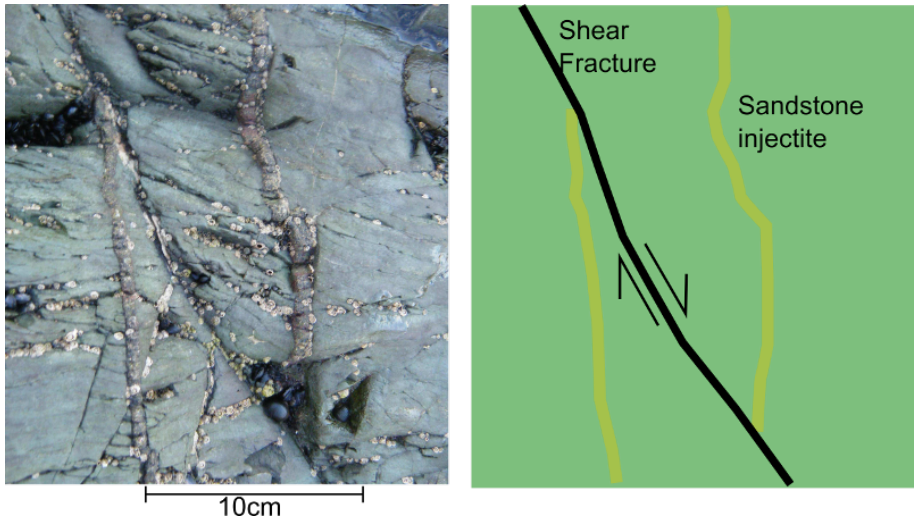

Figure 5.13: A sandstone injectite is offset by a shear fracture. Implying that the injectite predates the shear fracturing events.

5.3 Quantitative analysis of the fracture networks and the influence of faulting

The field site has been split into three structural areas as field observations indicated that there were different fracture properties in each of these areas. These areas are separated by the strike-slip faults and are termed as the southern, central, and northern areas (figure 5.14). In this section quantitative data and statistics are used to test the observed differences between these fault-separated areas. Differing fracture properties influencing fluid flow have previously been observed on opposite sides of normal faults (Nelson et al. 2008), data and statistical analysis is used to investigate the distribution of fracture properties on this field site.

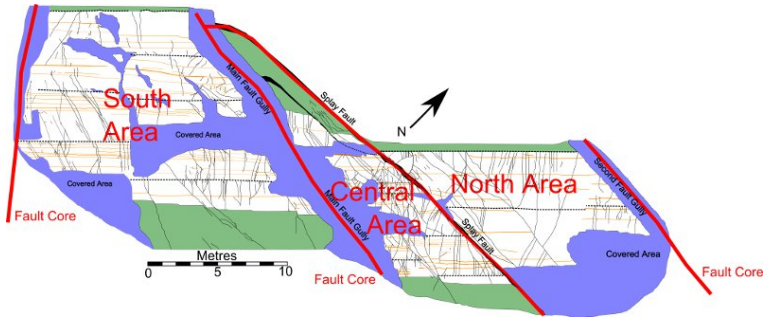

Figure 5.14: Structural areas bounded by the strike-slip faults. The "southern area" lies between the main fault gully and the antithetic fault to the southern West of the field site with a throw of one metre. The "central area" lies between the main fault gully and the splay fault. The "northern area" is between the splay fault and the second fault gully.

Fractures are approximately 2D planar features but are spatially distributed in 3D. However the field site is a 2D window into this 3D spatial distribution. This can lead to bias when collecting orientation data, as fractures which are orientated perpendicular to the outcrop are more likely to be exposed on the surface (Terzaghi 1965). This means that the orientation data (section 6.4.5) is a sample of the 3D fracture network, and that the connectivity (section 5.3.4 is likely an underestimate. However they still provide information to the properties of the 3D system.

5.3.1 Orientation differences between shear fractures and joints

Orientations of shear fractures and joints were collected from the Girvan field site using a compass clinometer. Shear fractures and joints were differentiated visually in the field, if there was observable slip across a fracture it was designated as a shear fracture, if no slip could be observed it was designated as a joint.

The shear fracture and joint orientation data are presented in stereonet and rose diagrams in figure 5.15. Note that all of the stereonets and rose diagrams have been rotated to align with the map orientation in figure 5.1. The yellow line in the stereonets gives a typical orientation of the sandstone bands, based from the data shown in figure 4.1 in chapter 4.

The shear fractures are preferentially orientated WNW-ESE (figure 5.15-b), with other collections of shear fractures striking NW-SE and NNW-SSW. Shear fractures tend to be approximately 45^0 to the sandstone bands, i.e. no shear fractures are parallel or sub-parallel to the sandstone bands. The large collection of shear fractures striking WNW-ESE are synthetic to the strike of the main strike-slip fault (figure 5.15).

The largest collection of joints strike NW-SE, with a spread in joint orientation from W-E through to N-S. The joints have a similar range of strike orientations as the shear fractures but the NW-SE preference of joints contrasts with that of WNW-ESE for shear fractures.

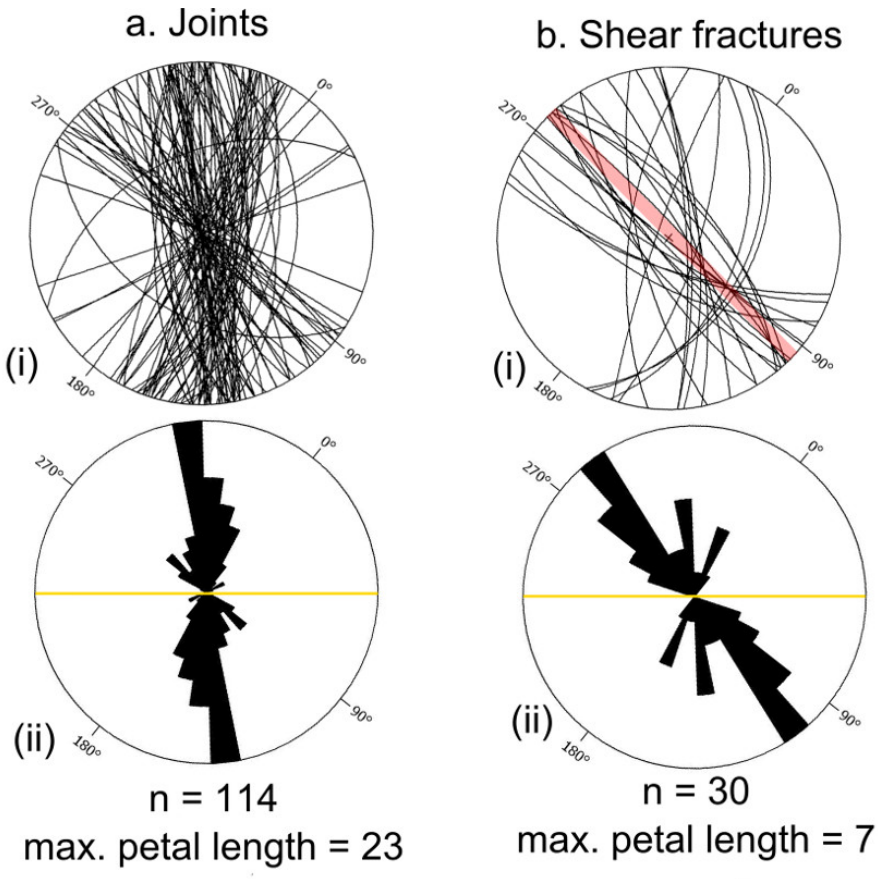

Figure 5.15: a. Rose diagram of 114 Joint strike data, maximum bin size is 23. b/ Rose diagram of 31 shear fracture strike maximum bin size is 7. Bins in a. and b. are 10° wide. Thicker red line on b. shows the strike of the main strike-slip fault.

5.3.2 The influence of strike-slip faults upon orientations of shear fractures and joints

Stereonets showing the orientation of shear fractures and joints in each of the three strike-slip fault bounded areas are shown in figure 5.16. Data were collected from 65 fractures in the southern area, 45 in the central area, and 20 in the northern area.

In the southern area a significant proportion (31 out of 65) of fractures strike NW-SE, with another smaller group of 13 fractures striking around W-E. Most of the W-E striking fractures (8 out of 13) are shear fractures, whereas the NW-SE striking

fractures are mostly joints with 27 of the 31 fractures being joints.

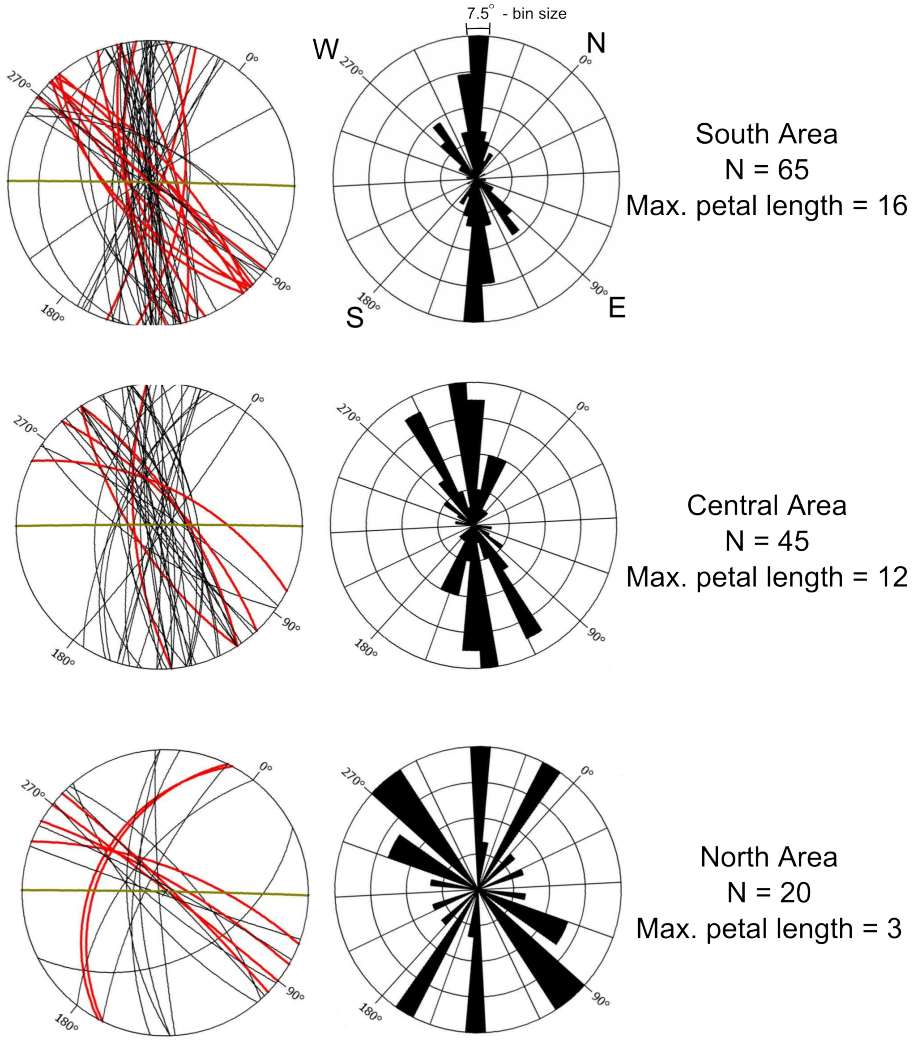

Figure 5.16: Stereonets showing strike and dip data of recordable fractures throughout the field site. Number of fractures in; southern area 65, central area 45, southern area 20. Red great circles are shear fractures, black great circles are joints. Note the bin size is different for each rose diagram.

The largest group of fractures in the central area strike NW-SE and another cluster at WNW-ESE, with another smaller group striking at NNW-SSE. The spread of orientations in the central area is wider than in the southern area, with a higher fraction of the fractures (44% compared with 23% in the southern area) striking

outside the NW-SE orientation. There are only five shear fractures in the central area data set, four of which strike WNW-ESE or approximately W-E while only one strikes NW-SE.

The northern area shows a large group of fractures striking WNW-ESE or W-E, with one smaller group between N-S and NW-SE. Shear fractures only appear in the W-E or N-S directions while the joints show a range of orientations.

The general trend of fracture orientation is similar for each of the three field areas. Shear fractures are more likely to strike approximately W-E or N-S and joints predominantly strike NW-SE but with spread out to W-E and N-S. The southern area fractures are more likely to strike NW-SE whereas the central area and northern area show greater spread of fracture orientations.

5.3.3 Influence of strike-slip faults on fracture density

Fracture density data were collected throughout the field site. The data were collected using circular scanlines, a method proposed by Mauldon (2000) to minimize sampling bias. This method determines the fracture trace density of the rock, defined as the number of fracture trace centres per unit area ($fracs/m^2$).

The method involves placing a circle on the outcrop and then counting fracture trace endpoints within each circle (figure 5.17). The fracture trace density for any given circular scanline is found with the equation:

$$\rho = \frac{m}{2\pi r^2} \tag{5.1}$$

where ρ is the fracture density, m is the number of fracture trace endpoints within the circle and r is the radius of the circle. If figure 5.17 is used as an example and assuming a radius of one metre then m would be 12 and ρ would be $1.9 fractures/m^2$.

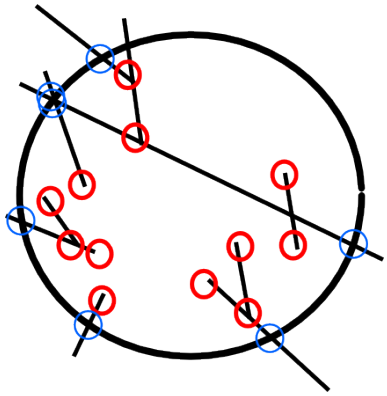

Figure 5.17: Example of the data collected from a circular scanline. Black lines are fractures. Red circles are fracture trace endpoints counted to calculated fracture density. Blue circles are intersections with the circle used to calculate fracture intensity, a different measure not used in this thesis.

Forty six circular scanlines were placed over the field site (figure 5.18), the locations of the scanlines are shown in figure 5.18. A mixture of circular scanlines with diameters of 0.6m (smaller circles on figure 5.18) and 1.2m (larger circles on figure 5.18) were used to collect fracture trace density data. Differences in circle diameter

do not influence the fracture trace density values obtained (Rohrbaugh et al. 2002), as long as the circles are larger than the size of intact rock between the fractures.

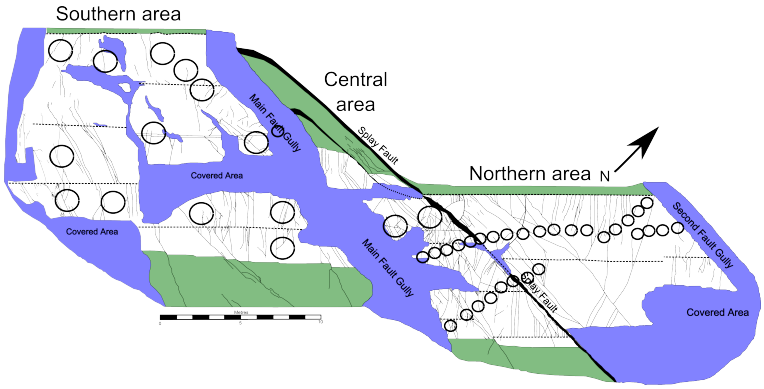

Figure 5.18: Map of field site with locations and sizes of circular scanlines used to survey the fractures. Positions of scanlines are constrained by quality of outcrop (lack of barnacles and seaweed needed for accurate data collection). There are 13 circles in the southern area, 13 in the central area, and 19 in the northern area.

The fracture trace density for each circle is plotted against perpendicular distance from the main strike-slip fault core in figure 5.19. Distance from the strike-slip fault (x-axis figure 5.19) is taken from the edge of the fault core to the centre of the circular scanline. The three strike-slip fault areas are shown in figure 5.19 as well as the locations of the fault cores and any surrounding covered zones shown in grey.

In the southern area the median fracture trace density is $3.1 fracs/m^2$, with a maximum of $8.1 fracs/m^2$. This agrees with the mapping which showed relatively sparse and sometimes isolated fractures within the southern area. One data point lies within the main fault gully (shown within the grey are on figure 5.19) between the footwall and central area, it has significantly higher fracture density than the other data in the southern area. This data point was collected from the main fault gully which is usually covered in debris but the tide had uncovered this small section temporarily. No other section of the main fault gully was uncovered so it is not clear if this data point is representative of the fracture trace density near to the strike-slip fault.

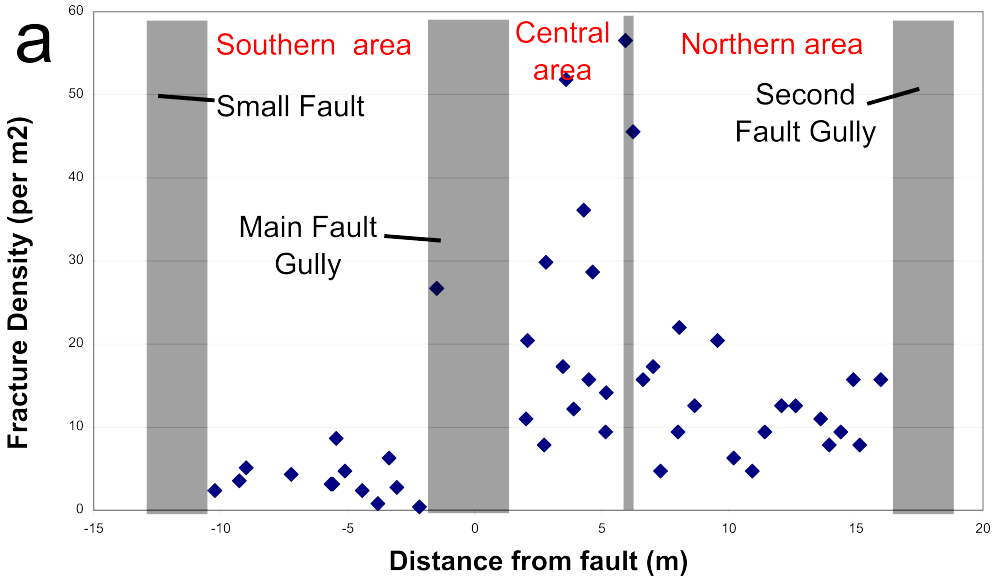

Figure 5.19: Values of fracture density obtained from the circular scanlines with distance to the main strike-slip fault. Positive x axis numbers show distance northern of the main strike-slip fault and negative x axis numbers show distance southern of the main strike-slip fault. Grey zones mark the locations of the strike-slip faults that bound the areas of the field site.

All but one of the fracture trace density values in the central area are higher than any of the values in the southern area. This is reflected in the median fracture trace density of $15.7 fracs/m^2$ being five times higher than the southern area median value. The density values from the central area are also very variable, ranging from $8 fracs/m^2$ to $56 fracs/m^2$. However half of the central area values are below $20 fracs/m^2$ showing a data skew towards lower values. Two of the highest values are from circular scanlines that intersect the splay fault, this high fracture trace density is due to smaller fractures between larger shear fractures (figure 5.20).

The fracture density in the northern area ranges from $5 fracs/m^2$ to $23 fracs/m^2$ and has a median of $12.6 fracs/m^2$. The northern area also shows variable fracture trace densities, but much less so than the central area.

The three strike-slip fault-bounded areas show significantly different fracture trace density values and ranges. The southern area has low fracture trace density except

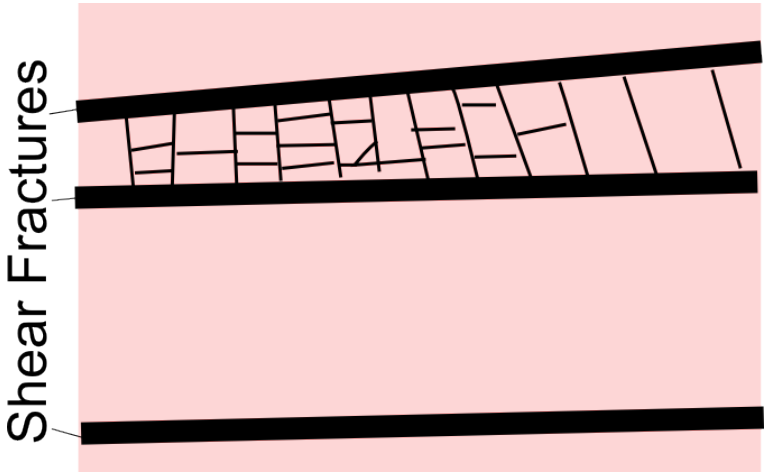

Figure 5.20: Cartoon of fracture laddering effect found between closely spaced shear fractures. Between the two closely space shear fractures many smaller fractures form between the two shear fractures creating a zone of high fracture density (Pollard and Aydin 1988). This effect is not observed when the shear fractures are further apart as in the lower portion of the cartoon.

for an anomalously high value in the main fault gully. The northern area has comparatively "medium" fracture trace density values with a constant spread of values between 5 and $23 fracs/m^2$. The central area has much higher fracture trace density in some scanlines than any other recorded on the field site, but half of the values in the central area are smaller, more similar to the data values found in the north area.

5.3.4 Influence of strike-slip faults on fracture connectivitiy

Data were collected on fracture connectivity in the southern, central, and northern areas of the field site. The data were collected from the structural map (figure 5.1) where for each fracture the number of connections with other fractures were counted. Connections with thrust faults and sandstone bands were not counted, as the aim was to focus on the differing fracture connectivities in the three different field areas in this chapter. In the following chapter connections between fractures, thrust

faults, and sandstone bands are considered together. No data could be collected where fractures were under significant cover on the field site.

The connectivity data in the southern area shows a large skew towards low fracture connectivity, with the majority of fractures having zero or only one connection. Almost half of the fractures (117 out of 258) are not connected to any other fractures in the southern area. At least 75% of the fracture have one or fewer connections. The three highest values (of 7, 6 and 5 connections) each only have one fracture.

The central area also shows a large skew towards low fracture connectivity, however a much lower proportion of fractures have zero connections with only 28 out of the 210 fractures having no connections. This low number of fractures with zero connections is reflected in the first quartile value of one, meaning that 75% of the fractures in the central area have at least one connection. The third quartile value of 2 means that at least 25% of the fractures have two or more connections. A fracture having two connections is important as this means the fracture can act as a fluid flow conduit between two other fractures, whereas a fracture with only one connection cannot.

The northern area has the same skew towards low fracture connectivity. The median number of connections per fractures is one, the same as for the southern and central areas. The first quartile value is 0 like the southern area, but the third quartile value is two like the central area.

The southern area therefore shows the lowest fracture connectivity and the central area the highest. The northern area has the most varied fracture connectivity values, with a large number of fracture with no connections but also the fracture with the most number of connections of the whole field site (13 connections).

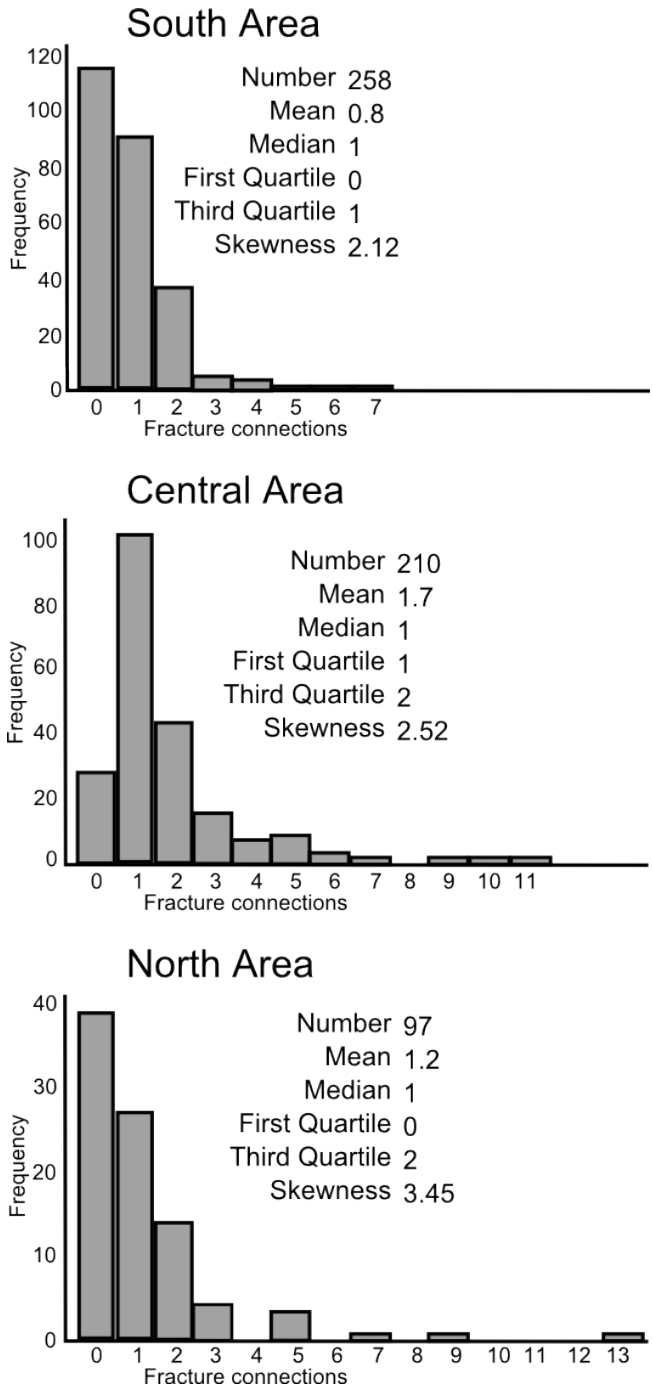

Figure 5.21: Fracture connectivity in different areas of field site.

5.3.5 Variation in controls on fracture termination between the strike-slip fault bounded areas.

The shear fractures and joints terminate against the sedimentary and structural features as well as each other (section 5.2). Data were collected about the features where shear fractures and joints were observed to terminate.

Four different modes of fracture termination have been identified across the field site. They are:

1.) **Fracture termination** against other fractures.

2.) **Tipline termination** when a joint or shear fracture terminates within the mudstone (figure 5.22-2) i.e. against no observable discontinuity.

3.) **Sandstone band termination** where a fracture has terminated upon contact with a sandstone band (figure 5.22-3).

4.) **Thrust termination** when thrust faults present a discontinuity which joints and shear fractures terminate against (figure 5.22-4) however some shear fractures offset the thrust faults.

Termination mode 1 would result in a fracture connection as counted in the previous section (section 5.3.4). However not all fracture connections would be a termination. If the fractures cross making an X shape then this is not counted as a termination, but if one fracture abuts against another (figure 5.22-1) then this is counted as a termination for the abutting fracture. Termination modes 2 (thrust fault terminations) and 4 (sandstone band terminations) also result in connections of features while mode 3 (tipline terminations) results in no connections at the end of the fracture. These terminations and connections could have influence over fluid flow paths which is discussed in detail in the following chapter.

The ratios of the four fracture termination modes in the different field areas and for the field site as a whole are shown in figure 5.23. 93 terminations were recorded in the southern area, 73 in the central area and 52 in the northern area. Some fracture

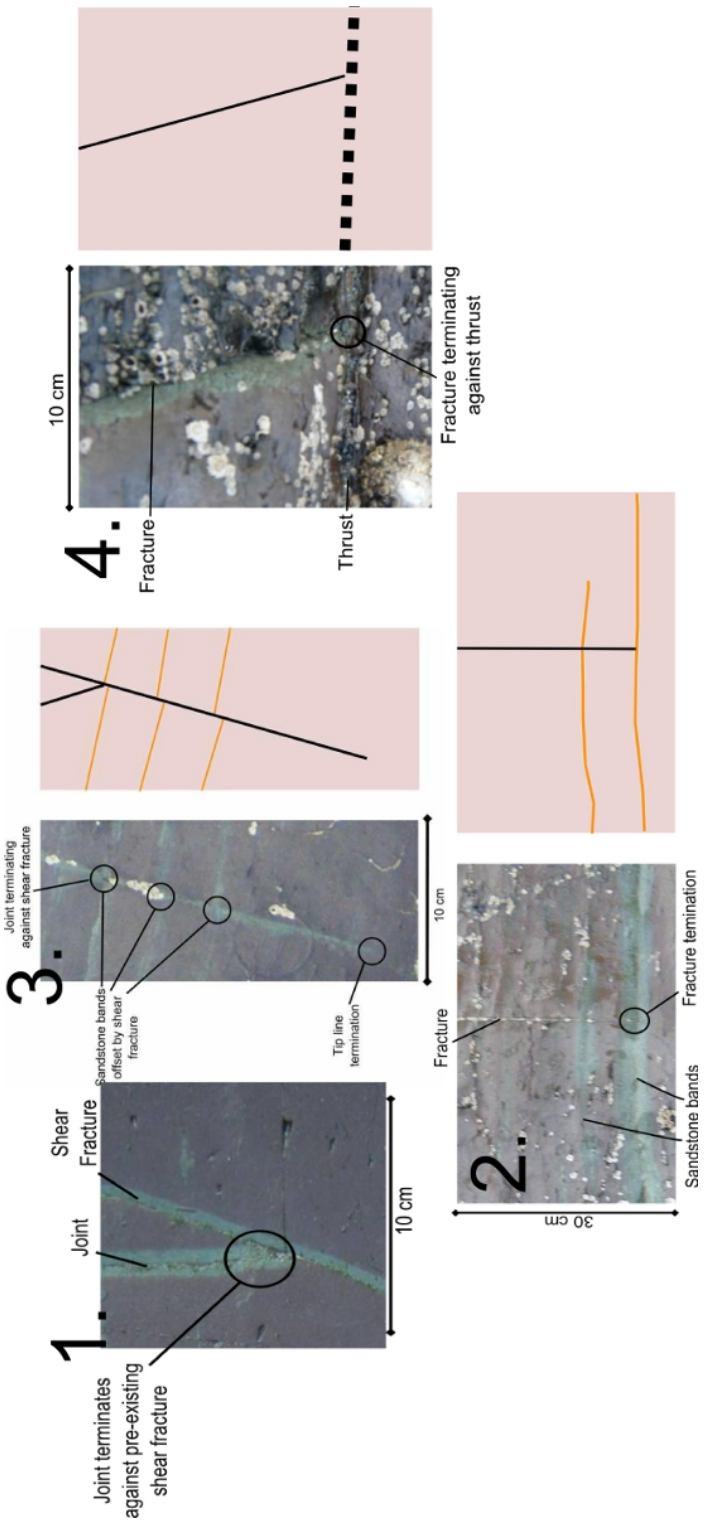

Figure 5.22: 1. Joint terminating against a shear fracture. Both features are surrounded by a green halo and show very thin carbonate fill. 2. Carbonate filled joint propagating through sandstone band before terminating against thicker lower sandstone band. 3. Shear fracture with a green halo runs through the mudstone offsetting three sandstone bands. In the top of the figure a joint terminates against the shear fracture. Towards the bottom of the picture the shear fracture terminates within the mudstone. 4. Fracture which shows a green halo and carbonate fill terminating against a bedding parallel thrust fault. Brecciated material can be seen in the thrust fault.

terminations were in areas of poorer exposure or it was not clear the mode of fracture termination, these fracture terminations were not recorded in the dataset. This may lead to bias in some of the results as cover follows certain features meaning terminations against these features would not be visible. For example the cover in the southern area follows the strike of one of the thrust faults, many fractures propagate into the cover and may have been terminated by the thrust fault. There also could have been another category of fault terminations, but the gully surrounding the strike-slip faults prevent any data on this to be collected.

In the southern area fracture termination accounts for the fewest terminations, with the other termination modes divided almost equally. The southern area also has the lowest fracture density which may have meant there was not as much opportunity for fractures to terminate against each other as in the other areas of the field site.

In the central area fracture termination is the most common termination mode, but is not dominant, with 34% of the terminations. The high fracture density found in the central area along with the wider orientation spread compared with the southern area probably means there is more chance of any two fractures intersecting and one terminating against the other. There is a much lower proportion of sandstone band termination in the central area compared with the southern area.

In the northern area sandstone band terminations show a similar proportion at the central area. Fracture and tip-line termination make up a lower proportion of terminations in the northern area than the central area due to thrust fault terminations dominating the termination mode in the northern area (59%).

Mechanics of fracture termination over the field site

The displacement discontinuities presented by the fractures and thrust faults have been observed to terminate the propagation of fractures in the field site. The driving stresses at the fracture tip cause propagation of the fractures (Schultz and Fossen 1992) . These stresses cannot transfer across the free surface presented by the gaps in the rock within other fractures or thrust faults in the rock. Therefore the fracture

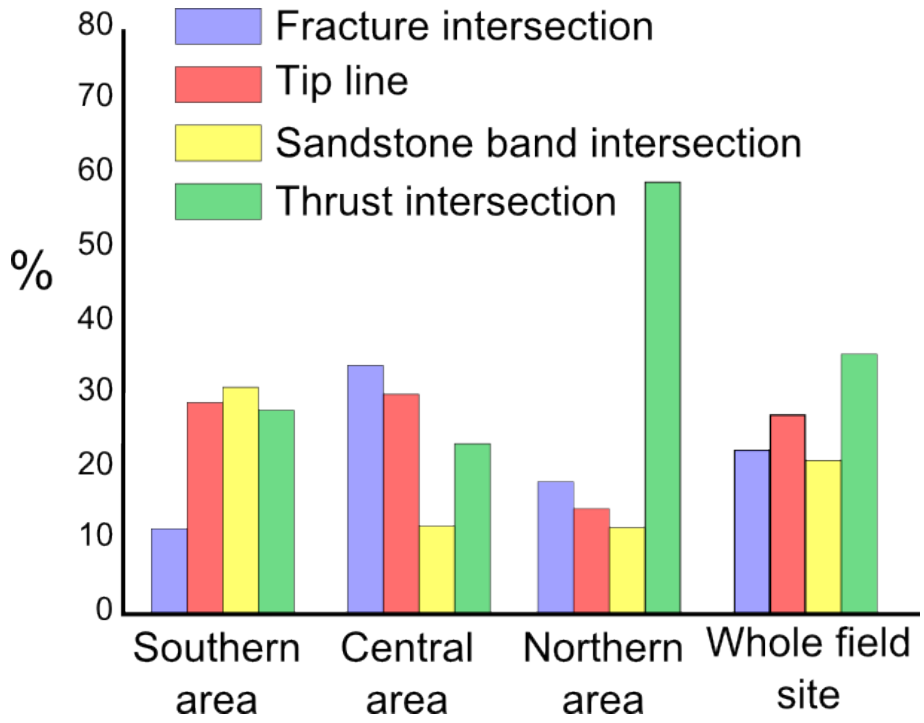

Figure 5.23: Chart showing proportion of termination mechanisms observed on different areas of the field site.

propagation cannot continue across an intersected fracture or thrust fault and a **fracture termination** or **thrust fault termination** is formed. This effect can be clearly seen in figure 5.24 where damage from blasting operations is controlled by a pre-existing natural fracture in the rock. Alternatively if the stress concentration at the tip reduces, due to relaxation of regional stress or fluid pressure, then the fracture propagation ceases (Gross et al. 1995) resulting in a **tip-line** termination.

Joints and shear fractures terminate against thrust faults within the northern area and central area, however in the northern area the long shear fractures were observed to propagate through the thrust faults. Cooke et al. (2006) found that fractures propagating normal to bedding but within thicker units (therefore the fractures are longer before intersecting with a mechanical boundary) are more likely to propagate through a mechanical boundary, this could be the relationship in the main part of the northern area. But there is a change in behaviour in the NE part of the northern

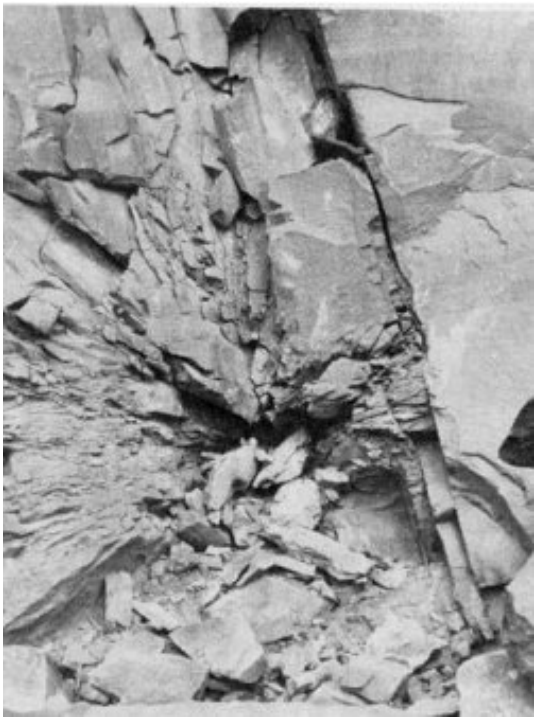

Figure 5.24: Photograph showing radial fractures emanating from blasting terminated by the presence of a natural fracture already existing in the rock. From Gretener 1983.

area, where close to the second strike-slip fault gully most fractures are terminated by a thrust fault. (labelled on figure 5.1)

Bedding interfaces can create displacement discontinuities, similar to those presented by fractures and thrust faults, in the rock if there is poor cohesion between the layers (Cooke et al. 2006 and 2000). This effect is often observed when there are thinner layers material (which can accommodate larger strains without fracturing) interbedded within a material which localises strain as fractures, such as a carbonate reservoir rock with thin shale layers. However the mudstone and sandstone bands at the field site both deform, currently in a, plastic manner (i.e. stress and strain accommodated through the creation of fractures). Additionally, during sampling (with a mallet and chisel) there was good cohesion between the beds, i.e. the rock did not preferentially break along bed boundaries. However these are the modern properties of the rock, so cohesion between the layers may have been poor during

the episodes of fracturing. If the fracture propagation is driven by fluid pressure it is possible that when the fracture intersects with a sandstone band the fluid pressure dissipates. There is evidence for the sandstone bands acting as conduits for fluid flow (discussed in chapter 6). If a fracture filled with pressurised fluid intersected one of these sandstone bands the fluid could have been released into the sandstone band relieving the fluid pressure and increasing the effective stress, creating a stable stress condition for the fracture.

5.4 Discussion: structural framework

5.4.1 Key findings from structural framework investigation

- Three groups of structural features have been identified: thrust faults, strike-slip faults, and fractures.
- Joints and shear fractures both showed a spread of distributions. Joints were spread around NW-SE, whereas shear fractures had a main cluster WNW-ESE and smaller clusters at NW-SE and NNW-SSE.
- Influences on fracture connectivity (density, orientation) vary between the southern, central, and northern areas.
  - Connectivity highest in central area, where strike-slip faults are closely spaced.
  - Connectivity of features a critical factor in the permeability of fractured rocks.
  - How connectivity influences fluid flow is further explored in chapters 6 and 7.

5.4.2 Palaeo-stress regime of the field site during fracturing events

Structural features will form in particular orientations relating to the stress field orientation and distribution within the rock volume. Fault orientation may indicate particular stress conditions (Anderson 1951) which can be corroborated by the orientations of shear fractures and joints. This means that a palaeo-stress evolution can be reconstructed, caution must be applied with these reconstructions as simulations have shown the deformation shape can have non-unique geomechanical causes (Lewis et al. 2007).

As discussed in chapter 3 the folding of the bedding at Girvan is related to NW-SE compression. The strike of the bedding indicates a limb of the monoclinal fold with plunge along SW-NE and dipping towards the NW. No information on plunge angle was obtained. The folding is the first stage of structural deformation that was observed on the field site. However in the study area this strain appears to have been accommodated relatively homogeneously and has not left any discontinuities that could form fluid flow pathways.

After the folding, further compression was accommodated by a thrusting event (figure 5.25). During the thrusting event σ_1 likely remained NW-SE while σ_2 was SW-NE and σ_3 was vertical. The thrust fault strikes SW-NE and has moved the Lower Whitehouse Group NW over the Upper Whitehouse Group. This indicates that $\sigma 1$ remained NW-SE during the thrusting. A thrust fault regime is indicative of a vertical $\sigma 3$ and therefore $\sigma 2$ is SW-NE or perpendicular to σ_1.

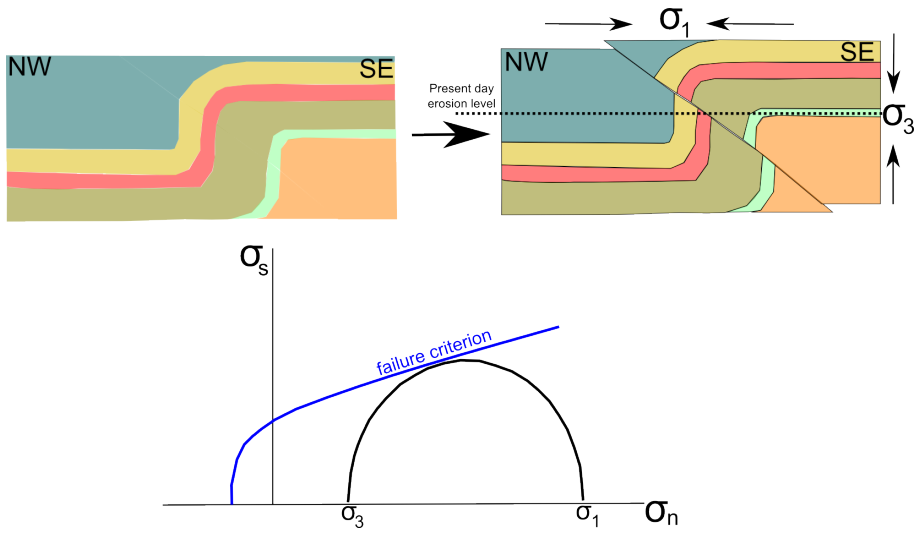

Figure 5.25: Cartoon showing vertical cross-section of the folding of the beds and formation of thrust fault after the folding with stress regime. The Mohr's circle shows a representation of the stress conditions reaching failure in the shear failure envelope leading to thrusting.

The conjugate strike-slip faulting (creating the faults which offset the bedding) shows there was a change to a strike-slip stress regime (figure 5.26 after the thrusting

events. The strike-slip faults were observed to offset the near vertical bedding. The orientation of the strike-slip faults indicate that $\sigma 1$ likely remained NW-SE, as the dextral and sinstral faults are orientated either side of the NW-SE direction. The strike-slip nature of the faults shows that that $\sigma 2$ was likely vertical and $\sigma 3$ is SW-NE or perpendicular to σ_1. The change in faulting style shows a re-orientation of the stress regime, however the differential stress (difference between σ_1 and σ_3) would still need to be large enough to become unstable in the shear failure region of the failure criterion.

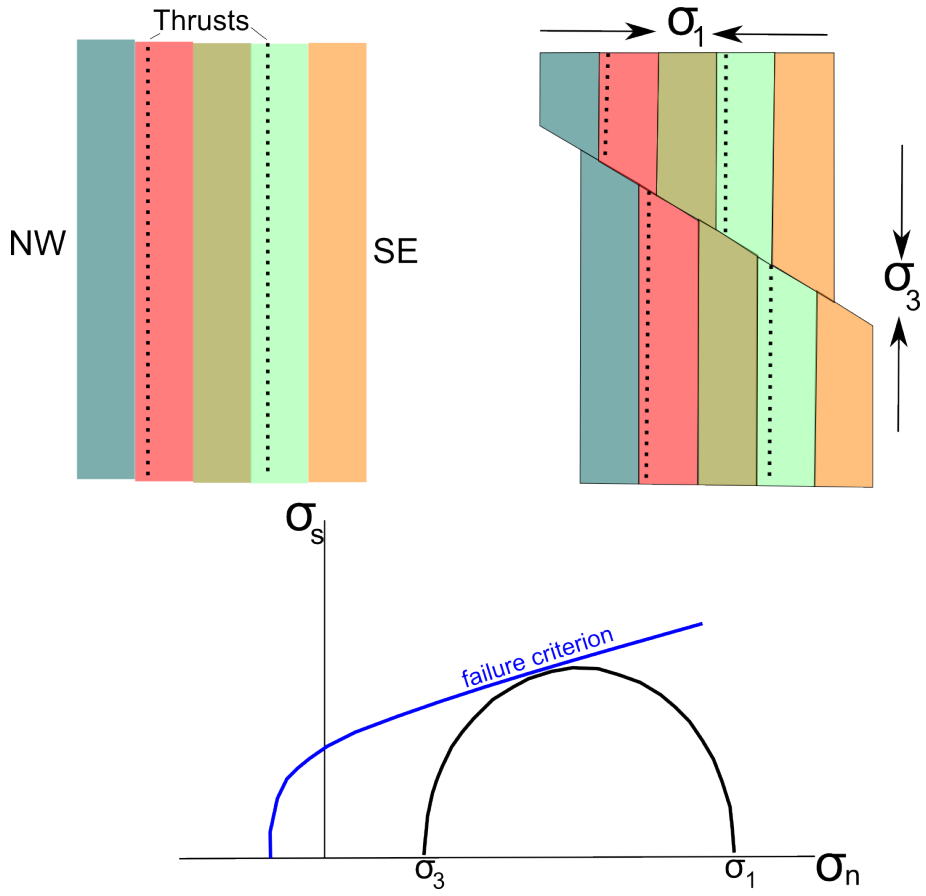

Figure 5.26: Cartoon showing a simplified plan-view of Girvan foreshore before and after the strike-slip faulting event. σ_3 is now horizontal rather than vertical in the thrusting event (figure 5.25), however failure still occurs on the same region of the failure envelope on the Mohr's circle.

Also having the joints preferentially striking perpendicular to SW-NE further indicates that this is a likely orientation for $\sigma 3$.

In this stress regime there are two possible mechanisms for the formation of joints. Stress changes during uplift or hydraulic fracturing. Joints will often form during uplift in layers that are more competent than surrounding rocks (Engelder (1985), i.e. sandstone surrounded by shale. This is due to the different Young's modulus and Poisson ratio of the rocks resulting in the rocks accommodating stress differently; by ductile deformation for the shale. This probably isn't representative of the causes of the jointing on the field site, as the joints are located in the shale (less competent material) rather than in surrounding sandstones (more competent material) which would be expected by this model. The other possible mechanism is hydraulic fracturing where pressurised fluid lowers the effective stress, moving the fracture into the tensile stress regime (as introduced in section 5.3.5). In the next chapter evidence is presented for fluid flow episodes flowing through the fractures, these episodes might have caused the pore fluid pressure that dropped the effective stress into the tensile region creating the joints (figure 5.27).

The deformational structures tell a story of a relatively consistent σ_1 orientation during the deformational events, being orientated NW-SE. Initially this stress field caused folding that rotated the beds to almost vertical which meant that σ_1 was then perpendicular to the beds. The structural features indicate that initially σ_2 was orientated SW-NE before changing to the vertical for the strike-slip regime whereas σ_3 initially was vertical but then rotated to SW-NE. That is σ_2 and σ_3 were essentially reversed between the thrusting and strike slip events.

Rotation and interchanging of principal stresses can be observed even within one borehole (e.g. Talbot and Sirat 2001). It is speculated that after thrusting there was additional burial that increased the overburden stress raising the vertical stress (formerly σ_3) above that of the minimum horizontal stress (formerly σ_2), so that vertical stress became σ_2.

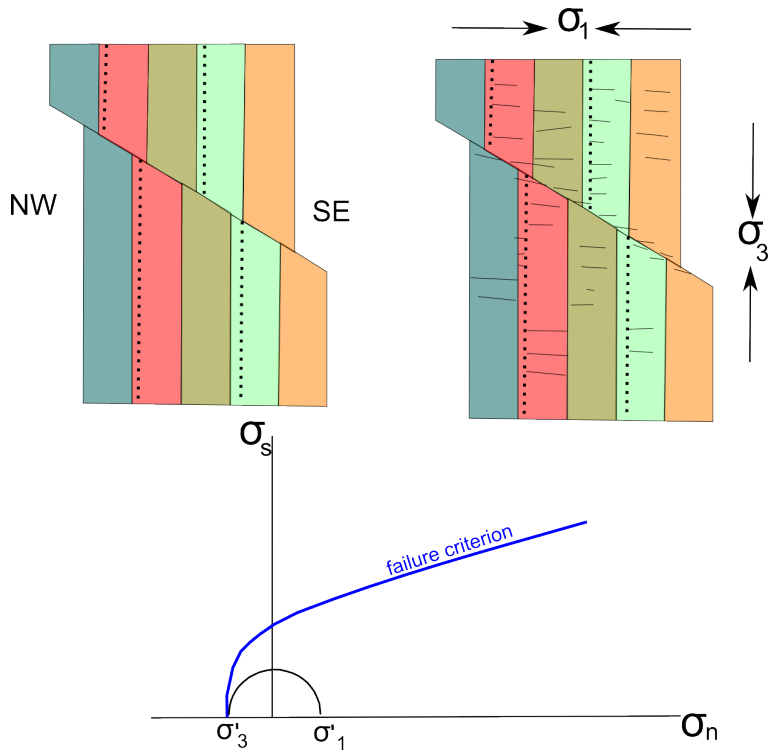

Figure 5.27: Cartoon showing the simplified plan-view of Girvan before and after the interpreted fracturing event. The orientations of the principal stresses are the same as for the strike-slip event (figure 5.26) but the stress differential ($\sigma_1 - \sigma_3$) is much less, so failure occurs at a different region of the failure criterion which favours the formation of joints

5.4.3 Influences on fracture connectivity

Four different fracture properties: density, orientation, connectivity, and termination vary between the different fault bounded areas of the field site. Density and orientation spread can influence how likely a fracture is to be connected with another fracture, which is a key component of the permeability of fracture networks. A higher fracture density would make fracture intersections more likely increasing the chance of a connected fluid flow network through the mudstone layer (Berkowitz 1995). A wider range of orientations also means fractures are more likely to intersect. For example, parallel fractures would never intersect no matter how long they

	Connectivity	Density	Orientation Range
southern area	Lowest	Lowest	Lowest
central area	Highest	Highest	Medium
northern area	Medium	Mediun	Highest

Table 5.1: Showing a summary of fracture properties in the three different structural areas

were. Whereas the closer fractures are to perpendicular to each other then generally the less distance the fractures need to propagate to intersect.

The data collected about the fracture density, orientations and connectivity across the field site is qualitatively summarised in table 5.1 with each field area being labelled if it is comparatively the lowest, highest, or the medium value of the three field areas. Connectivity and density both could be quantitatively assessed by comparing medians and quartile ranges while orientation range was interpreted from the rose diagrams in figure 5.16.

The connectivity most strongly reflects the fracture density of the southern, central, and northern areas. The southern area has the lowest values of connectivity and also has the lowest density values and lowest orientation range. The low density and orientation in the southern area mean that it is less likely that fractures will intersect with each other compared with the central and northern area. The central area has the highest density and highest connectivity, where the majority of fractures connect to at least one other fracture.

The enhanced fracture trace density in the central area of the field site reflects that of studies which find enhanced fluid flow activity in fault interaction areas (Curewitz and Karson 1997, Gartrell et al. 2004, Ligtenberg 2005). The central area has two strike-slip faults in close proximity, the main strike-slip fault and splay fault, which may have created a region of dilatent stress (e.g. Gartrell et al. 2004) and strain enhancing fracture density beyond background levels, such as shown in figure 5.28. Previous fault outcrop studies (Savage and Brodsky 2011, pg. 159 Fossen 2012) in

different rock types have found a higher density of smaller deformational structures (deformations bands and fractures) adjacent to a fault i.e. within the damage zone of a fault. The fault-fracture distribution at the Girvan field site resembles the Curewitz and Karson 1997, Gartrell et al. 2004, and Ligtenberg 2005 studies rather than the Savage and Brodsky 2011 study. Although the one high density value found in the fault gully of the southern area hints at a region of higher fracture density in close proximity to the fault it was impossible to get more data from the fault gully to further explore this possibility. However this could be due to the scale investigated, a possibility is that the damage zones of the faults extend out for many metres into the mudstone before dropping to "background" levels. With this scenario due to the relatively close proximity of the faults to each other then any area of mudstone is not sufficiently far from a fault to have fracturing at this unfaulted background level. This explanation doesn't account for the different fracture density properties in the three areas of the field site. Therefore for any particular point on the field site, the distance between the two fault that surround that point could be the crucial factor for predicting the fracture connectivity near that point. Instead of proximity of that point to the nearest fault.

Fracture density seems to control the fracture connectivity over the field site (Cox 2010) the higher the fracture connectivity the more likely a better connected fracture network will exist across the mudstone. Figure 5.29 shows traced out connected networks of fractures and thrust faults in the three field areas. These are 2D traced out networks when in reality the fracture system is in 3D. Being in 3D allows more possibilities of fracture connections, as two closely spaced fractures could dip towards each other thus connecting below the exposed outcrop. Therfore the 3D network could be more connected than the 2D example shown in figure 5.29. Connected networks spread over much of the northern and central area, but comparatively less on the southern area. However this chapter has shown that there is interactions between the sedimentary features and the fractures, with fractures terminating against the sandstone bands. So perhaps the fracture networks should not be considered in isolation of the sandstone bands. The impact, on connected networks and fluid flow properties of those networks, of considering the sandstone bands and fractures

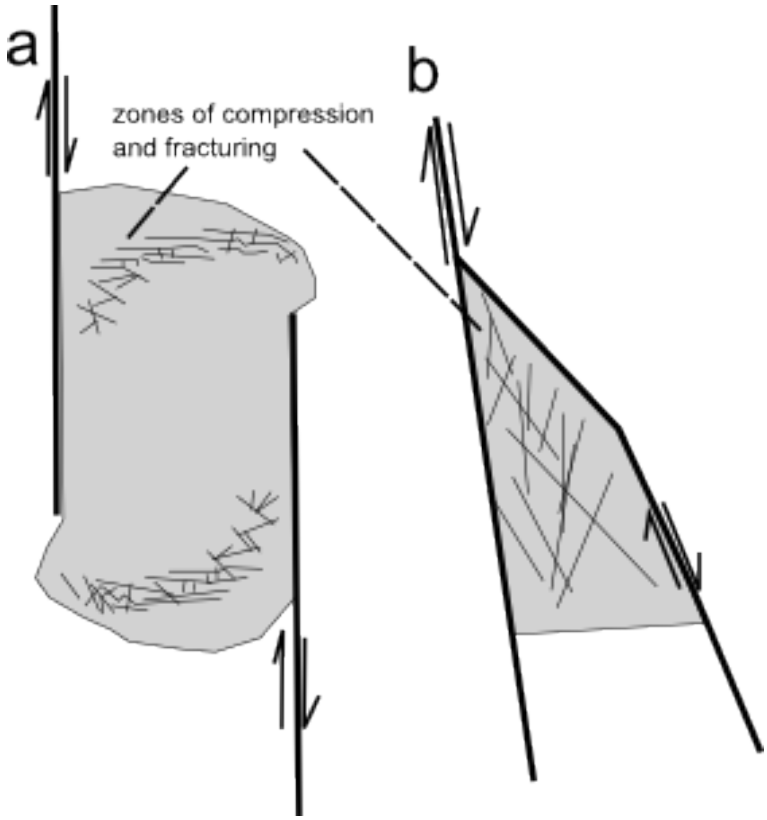

Figure 5.28: Cartoon showing enhanced fracturing in areas of fault interaction. From Curewitz and Karson 1997

networks together is explored in the following chapter.

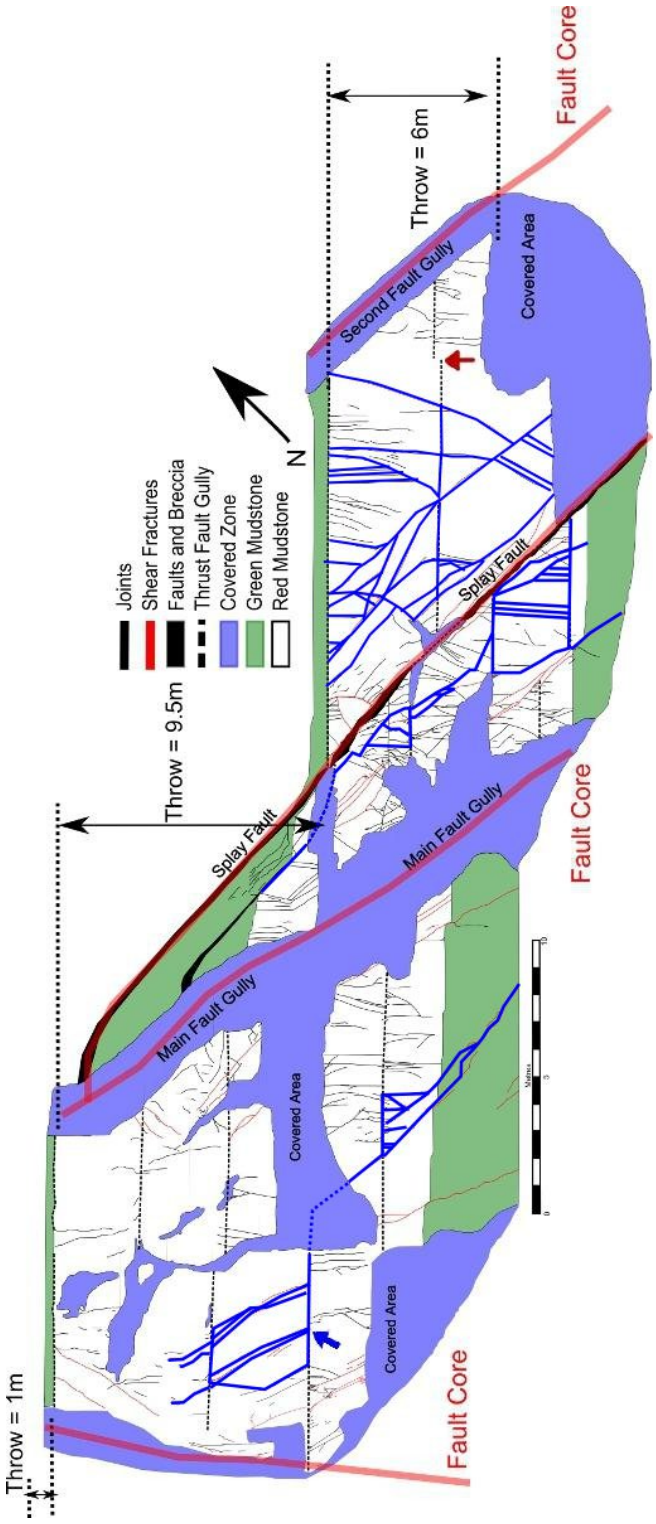

Figure 5.29: Interpreted flow paths through the mudstone (thick blue lines). Made using fractute connections across the map from figure 5.1

5.5 References

Anderson, E. M. 1951. The dynamics of faulting. Oliver and Boyd, Edinburgh.

Berkowitz, B. 1995. Analysis of Fracture Network Connectivity using Percolation Theory. *Mathematical Geology.* v.**27** no.**4**. pp. 467-483.

Berg, S. S. and Skar, T. 2005. Controls on damage zone asymmetry of a normal fault zone: outcrop analyses of a segment of the Moab fault, SE Utah. *Journal of Structural Geology.* v.**27** i.**10**. pp. 1803-1822.

Brogi, A. 2008. Fault zone architecture and permeability features in siliceous sedimentary rocks: Insights from the Rapolano geothermal area (northern Apennines, Italy). *Journal of Structural Geology.* v.**30** i.**2**. pp. 237-256.

Burhannudinnur, M. and Morley, C. K. 1987. Anatomy of growth fault zones in poorly lithified sandstones and shale; implications for reservoir studies and seismic interpretation; Part 1, Outcrop study. *Petroleum Geoscience.* v.**3**. pp. 211-224.

Caine, J. S., Bruhn, R. L. and Forster, C. B. 2010. Internal structure, fault rocks, and inferences regarding deformation, fluid flow, and mineralization in the seismogenic Stillwater normal fault, Dixie Valley, Nevada. *Journal of Structural Geology.* v.**32** i.**11**. pp. 1576-1589.

Caine, J.S., Evans, J.P. and Forster, C.B. 1996. Fault zone architecture and permeability structure. *Geology.* v. **24** No. **11**. pp. 1025-1028.

Cooke, M. L., Simo, J. A., Underwood, C. A. and Rijken, P. 2006. Mechanical stratigraphic controls on fracture patterns within carbonates and implications for groundwater flow. *Sedimentary Geology.* v.**184** i.**3-4**. pp. 225-239.

Cooke, M. L. and Underwood, C. A. 2000. Fracture termination and step-over at bedding interfaces due to fractional slip and interface opening. *Journal of Structural Geology.* v.**23**. pp. 223-238.

Cox, S.F. 2010. The application of failure mode diagrams for exploring the roles of fluid pressure and stress states in controlling styles of fracture-controlled permeability enhancement in faults and shear zones. *Geofluids*. v. **10**. pp. 217-233.

Curewitz, D. and Karson, J.A. (1997). Structural setting of hydrothermal outflow: Fracture permeability maintained by fault propagation and interaction. *Journal of Volcanology and Geothermal Research*. **79**. pp. 149-168.

Eichhubl, P and Boles, J. 2000. Rates of fluid flow in fault systems - evidence for episodic rapid fluid flow in Miocene Monrerey Formation, Coastal California. *American Journal of Science*. v.**300**. pp. 571-600.

Engelder, T. 1985. Loading paths to joint propagation during a tectonic cycle: an example from the Appalachian Plateau, U.S.A. *Journal of Structural Geology*. v.**7**. pp459-476.

Fossen, H. 2012. Structural Geology. Cambridge University Press, New York.

Gartrell, A., Zhang, Y., Lisk, M. and Dewhurst, D. 2004. Fault intersections as critical hydrocarbon leakage zones: integrated field study and numerical modelling of an example from the Timor Sea, Australia. *Marine and Petroleum Geology*. vol **21**. pp. 1165-1179.

Gretener, P.E. 1983. Remarks by a geologist on the propagation and containment of extension fractures. *Bull. Ver Schweiz Petroleum-Geol Ing*. v.**49**(116). pp. 29-35.

Gross, M. R., Fischer, M. P., Engelder, T. and Greenfield, R. J. 1995. Factors controlling joint spacing in interbedded sedimentary rocks: interpreting numerical models with field observations from the Monterey formation, USA. In: Ameen, M. S. (Ed.), Fractography: Fracture Topography as a Tool in Fracture Mechanics and Stress Analysis, Geological Society of America Special Publication. v.**93**, pp. 215-233.

Hinds, J. J., Bodvarsson, G. S. and Nieder-Westermann, G. H. 2003. Conceptual evaluation of the potential role of fractures in unsaturated processes at Yucca Moun-

tain. *Journal of Contaminant Hydrology*. v.**62-63**. pp. 111-132.

Ingham, J. K. 1978. Geology of a continental margin 2: Middle and Late Ordovician transgression. Geol. J. Spec. Issue No. 10, 115-138.

Lewis, H., Hall, S. A., Guest, J. and Couples, G. D. 2007. 2007. Kinematically-equivalent but geomechanically-different simulations of fault evolution: the role of loading configuration. *From*: Jolley, S. J., Barr, D., Walsh, J. J. and Knipe, R. J. (eds) *Structurally Complex Reservoirs*. Geological Society, London, Special Publications, **292**, 75-87.

Ligtenberg, J.H. 2005. Detection of fluid migration pathways in seismic data: implications for fault seal analysis. *Basin Research*. v.**17** i.**1**. pp. 141-153.

Mauldon, M., Dunne, W. M. and Rohrbaugh Jr., M. B., 2000, Circular scanlines and circular windows: new tools for characterizing the geometry of fracture traces, *Journal of Structural Geology*, **Vol. 23**, pp. 247-258.

Micklethwaite, S. and Cox, S. F. 2006. Progressive fault triggering and fluid flow in aftershock domains: Examples from mineralize Archaen fault systems. *Earth and Planetary Science Letters*. v.**250**. pp. 318-330.

Nelson, S. T., Mayo, A. L., Gilfillan, S., Dutson, S. J., Harris, R. A., Shipton, Z. K. and Tingey, D. G. 2008. Enhanced fractue permeability and accompanying fluid flow in the footwall of a normal fault: The Hurricane fault at Pah Tempe hot springs, Washington County, Utah. *GSA Bulletin*. v.**121** i.**1-2**. pp. 236-246.

Pollard, D. D. and Aydin, A. 1988. Progress in understanding jointing over the past century. *GSA Bulletin*. v.**100** no.**8**. pp. 1181-1204.

Rowland, J. and Sibson, R. 2004. Structural controls on hydrothermal flow in a segmented rift system, Taupo Volcanic Zone, New Zealand. *Geofluids*. v.**4**. pp. 259-283.

Savage, H. M. and Brodsky, E. E. 2011. Collateral damage: Evolution with displacement of fracture distribution and secondary fault strands in fault damage zones.

Journal of Geophysical Research. v.**116**. B03405, doi:10.1029/2010JB007665.

Schultz, R. A. and Fossen, H., 2002. Displacement-length scaling in three dimensions: the importance of aspect ratio and applications to deformation bands. *Journal of Structural Geology.* v.**24**. pp. 1389-1411.

Rohrbaugh, M. B., Dunne, W. M. and Maulton, M. 2002. Estimating fracture trace intensity, density, and mean length using circular scan lines and windows. *AAPG Bulletin.* v.**86**. no.**12**. pp. 2089-2104.

Talbot, C. J. and Sirat, M. 2001. Stress control of hydraulic conductivity in fracture-saturated Swedish bedrock. *Engineering Geology.* v.**61** i.**2-3**. pp. 145-153.

Twiss, R.J. and Moores, E.M. Structural Geology, WH Freeman and Company, Oxford (1992).

Wilkins, S. J., Gross, M. R., Wacker, M., Eyal, Y. and Engelder, T. 2001. Faulted joints: kinematics, displacement-length scaling relations and criteria for their idenitification. *Journal of Structural Geology.* v.**23** i.**2-3**. pp. 315-327. http://dx.doi.org/10.1016/S0191-8141(00)00098-5.

Younger, P. L. and Manning, D. A. C. 2010. Hyper-permeable grainte: lessons from test-pumping in the Eastgate Geothermal Borehole, Weardale, UK. *Quarterly Journal of Engineering Geology and Hyrdogeology.* v.**43** i.**1**. pp. 5-10.

Chapter 6

Evidence for palaeo fluid flow

> "Drainage! Drainage, Eli, you boy. Drained dry. I'm so sorry. Here, if you have a milkshake, and I have a milkshake, and I have a straw. There it is, that's a straw, you see? You watching?. And my straw reaches acroooooooss the room, and starts to drink your milkshake... I... drink... your... milkshake!" – Daniel Plainview

6.1 Introduction

This chapter explores how the distribution and properties of the sedimentary and structural features may have influenced fluid flow through the red mudstone. The sandstone bands were shown to have predictable thickness distributions, while data were collected about the connectivity and extent of the sandstone bands (chapter 4). Data were also collected about fracture properties: i.e. density, orientations, connectivity and controls over fracture termination (chapter 5). These data are used, in this chapter, to answer questions on which of the relationships and properties have larger influences over the formation of fluid flow networks and the level of channelisation of flow within these networks.

Identifying which features are likely to be fluid flow conduits, and under what conditions this may change, is vital for robust predictions of subsurface fluid flow. Data from well bores (Losh et al. 1999, Younger and Manning 2010) and subsurface drifts (Talbot and Sirat) in fractured granite has found the majority of flow can come from very few features. In the granite studies (Losh et al. 1999, Talbot and Sirat 2001, Younger and Manning 2010) flow was compartmentalized with Losh et al. (1999) finding that 5% of fractures were responsible for 95% of flow. Such compartmentalised behaviour is not limited to fractured granite but has also been reported in sedimentary rock (Rowland et al. 2008, Fairley and Hinds 2004). Determining if the fault and fracture networks, recorded on the Girvan field site, behave in a similar or different way to the previous studies in fractured granite (mentioned above) will provide insights into the fluid flow controls in distal turbidite formations which are cut by sub-seismic faults.

Evidence exists for two palaeo-fluid flow episodes within the mudstone. It is possible that there were many more fluid flow episodes that passed through the field site without leaving any traces. No inferences could possibly be made about these "invisible" events so they will not form any part of the discussion.

This chapter is split into four sections.

- **Section 6.2**, The evidence for two fluid flow episodes is presented. The first fluid flow episode is observable due to deposition of calcite within fractures and sandstone bands. The second fluid flow episode created a green halo around utilised fractures and sandstone bands.
- **Section 6.3**, The networks of features that the fluid flow episodes utilised is presented with the field maps. The differences between the networks utilised by the two fluid flow episodes is discussed, including details on the permeability behaviour of the fault architecture.
- **Section 6.4**, The sedimentary and structural relationships are investigated with respect to how they have controlled or influenced the fluid flow networks.

- **Section 6.5**, Past fluid flow episodes through the red mudstone are discussed, leading to discussion on how this information could be used in future subsurface surveys and fluid flow prediction.

6.2 Evidence for past fluid flow episodes

Evidence for two fluid flow episodes which occurred on the field site comes from two main observations; one episode deposited calcite within sandstone bands, thrusts and within a subset of the fractures (figures 6.1-a and b), the other episode created a green halo around the thrusts and around a subset of the sandstone bands and fractures (figures 6.2-a and b).

6.2.1 Calcite deposition

The calcite was identified with reactions with HCl in the field and observations under thin section. Calcite is a carbonate mineral ($CaCO_3$) often found in ocean-deposited sedimentary rocks, as with aragonite it is a common constituent of vertebrate shells. Calcite can be dissolved and precipitated by different fluids in the subsurface such as: meteoric, groundwater, and mobile deep seated brines (Nuriel et al. 2002). It is beyond the scope of this project to determine the source of the calcite however the Myoch formation is underlain by limestone flysch deposits which could have provided the source material for the calcite.

The calcite can be observed to fill a subset of shear fractures and joints (figure 6.1-c). The veins appear to have grown in an antitaxial manner, that is mineral growth begins within the fracture before growing out towards the fracture walls (Becker et al. 2011, Cox and Etheridge 1983). The absence of a mid-line in the centre of a fracture is evidence that the vein minerals did not propagate from the two edges of the fracture towards the middle. However the vein minerals may have also grown from one side of the fracture to the other. In some veins (such as the example shown in figure 6.1-c) multiple layers of calcite can be seen in the vein. This layers are indicative of multiple calcite deposition episodes. However, these layered veins are only observed in small subset of the veins and would require isotope analysis to pick apart the different flow episodes thus has not been considered as part of this thesis but considered in future work in section 9.2. The calcite can also be seen in all the

thrusts, once the debris has been excavated from the gullies.

Calcite is present within the sandstone bands, and can be observed under thin section (figure 6.1-a). The sandstone bands react with HCl, whereas the surrounding red mudstone does not, indicating the presence of calcite within the sandstone band but not within the surrounding red mudstone.

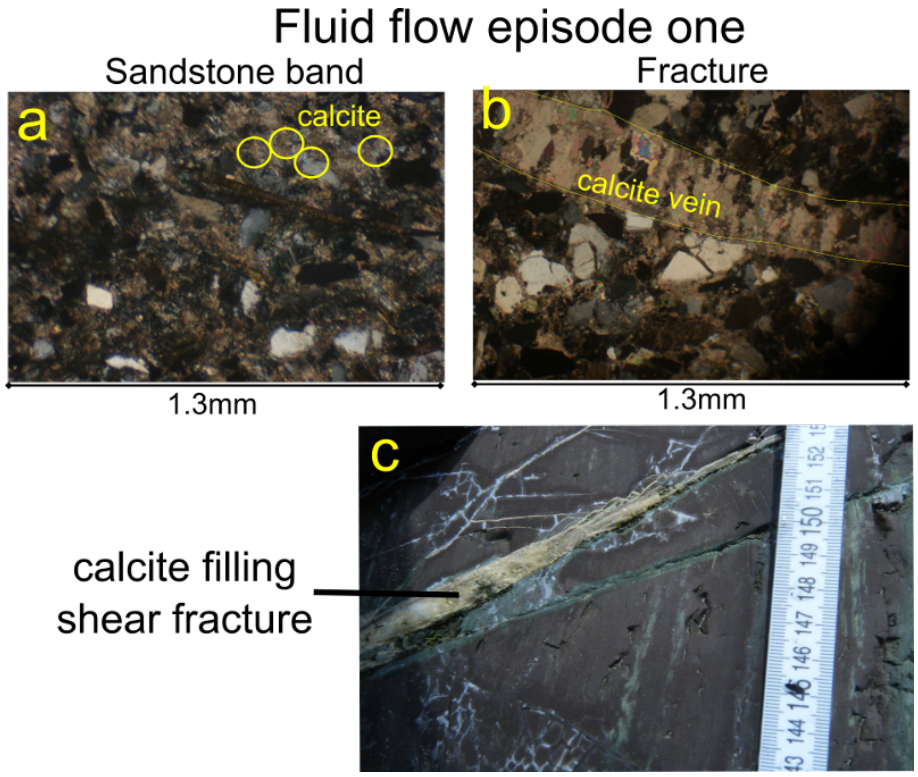

Figure 6.1: a. Crystals of carbonate can be seen under cross polarised light in thin section in the sandstone bands, no carbonate is observed in the surrounding mudstone. b. Thin section of a calcite vein viewed under an optical microscope. c. Field example of a shear fracture filled by calcite (fractures are also surrounded by green halos).

6.2.2 Green halos

Green halos surround a subset of the shear fractures and joints (figure 6.2-b), thrusts, and sandstone bands (figure 6.2)-a and b). They are usually less than one centimetre

thick. The halo has a sharp contrast with the rest of the mudstone, although the halos around the sandstone bands seem to be slightly less sharp than the halos around the fractures, i.e. the transition from green to red occurs over less distance. This is possibly due to the reducing fluid lingering in sandstone bands after it was flushed from the fractures by a subsequent fluid flow episode. Chemical alteration has previously been used to determine fractures that have acted as conduits for fluid flow. Fleischmann (1993) and Eichhubl et al. (2009) used the evidence of bleaching of fractures in sandstone to determine which fractures acted as conduits for palaeo-fluid flow. Similarly to these previous studies, the green halos have been used as a proxy to determine which features have behaved as fluid flow conduits during the episode which caused the halos.

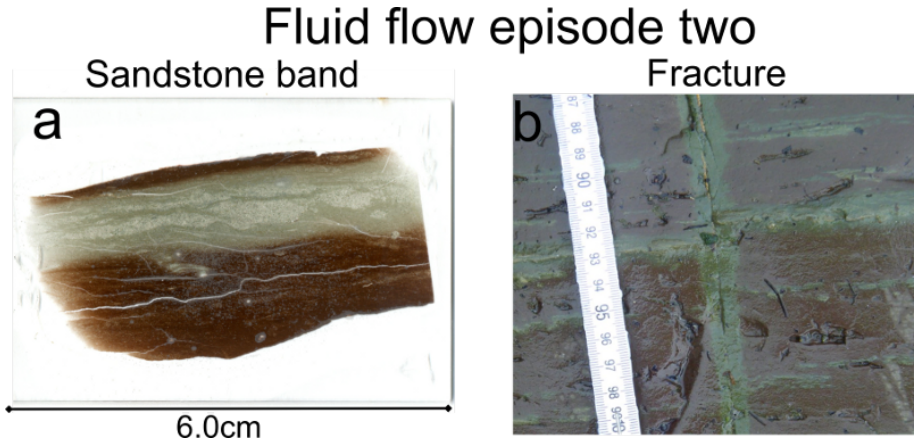

Figure 6.2: c. Thin section of a sandstone band surrounded by a green reduction halo. d. Fracture surrounded by green reduction halo within the fracture is also a thin carbonate vein, fracture offsets several sandstone bands.

It is beyond the scope of this project to find the source of the fluid and the reactions which have caused the colour change. However green alteration in mudstone has previously been found to be due to the reduction of Fe^{3+} to Fe^{2+} (Mykura and Hampton 1983, Beddoie-Stephens 1980). Mudstone and slates (metamorphosed mudstone) in the UK also show green reduction spots and bands. The chemical causes of the green reduction has been shown to be more complicated than simply iron reduction, with the transportation by diffusion of several minerals involved in

the process (Borradaile et al 1991).

SEM analysis was used to determine if there is a correlation between Fe oxidation states and the colour of the mudstone. Grains of iron oxide were identified using secondary electron imaging. Then x-ray diffraction was used to gain a diffraction spectra. By comparing the sizes of the peaks for Fe and O on these spectra it was determined whether the iron oxide was FeO (Fe^{2+}) or Fe_2O_3 (Fe^{3+}). Iron oxide grains were analysed in both green mudstone and red mudstone areas.

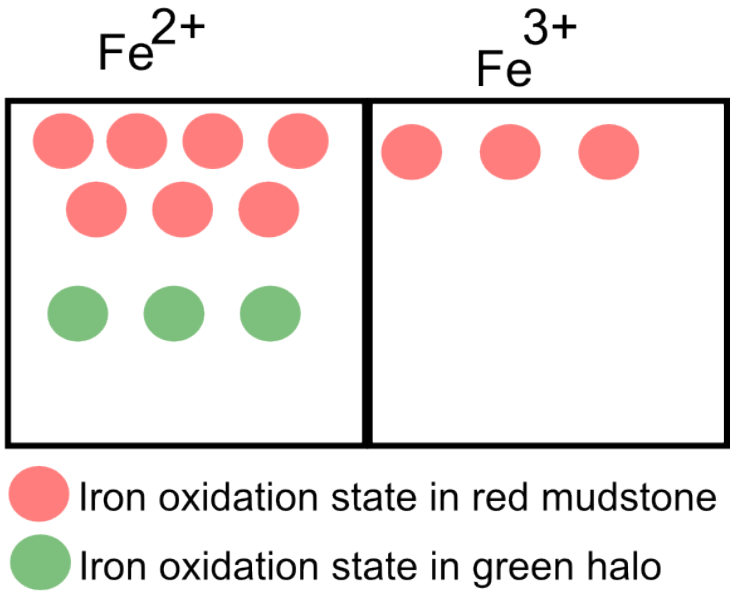

Figure 6.3: Grains of iron oxide tested with XRD for oxidation state. 10 grains of iron oxide identified in the samples were from red mudstone and three from a green halo. All three iron oxide grains in the green halo had an oxidation state of Fe^2+ whereas the samples in red mudstone were mixed between Fe^2+ and Fe^3+

.

No simple correlation was found between red mudstone and Fe^{2+} and green halos and Fe^{3+} (figure 6.3). This lack of correlation does fit with the other studies which find that it can be difficult to single out a single mineral as being solely responsible for colour change in mudstone (Borradaile et al. 1991) and other sedimentary rocks

(Eichhubl et al. 2004).

6.3 Fluid flow networks.

6.3.1 Mapped evidence for palaeo-fluid-flow through the red mudstone

The sedimentary and structural features on the field site which show evidence for having been part of palaeo-fluid flow networks are shown in figure 6.4. This fluid flow map is a combination of the sedimentary map from chapter 4 and the structural map from chapter 5.

All of the features from the maps in chapters 4 and 5 are present within these flow maps. No "dry" features were mapped from the field site, which would be fractures without calcite fill or a surrounding green halo. These dry features would not have been utilised during either fluid flow episode. However any dry features observed on the field site were too small to even be included in this detailed mapping.

Only two fluid flow episodes have left evidence for their existence on this field site. However it is likely there has been many more fluid flow episodes during the geological evolution of this rock. That these episodes left no evidence behind means it would be impossible to even speculate as to their pathways through the mudstone. Therefore no inferences or hypothesis have been made beyond the two fluid flow episodes already discussed.

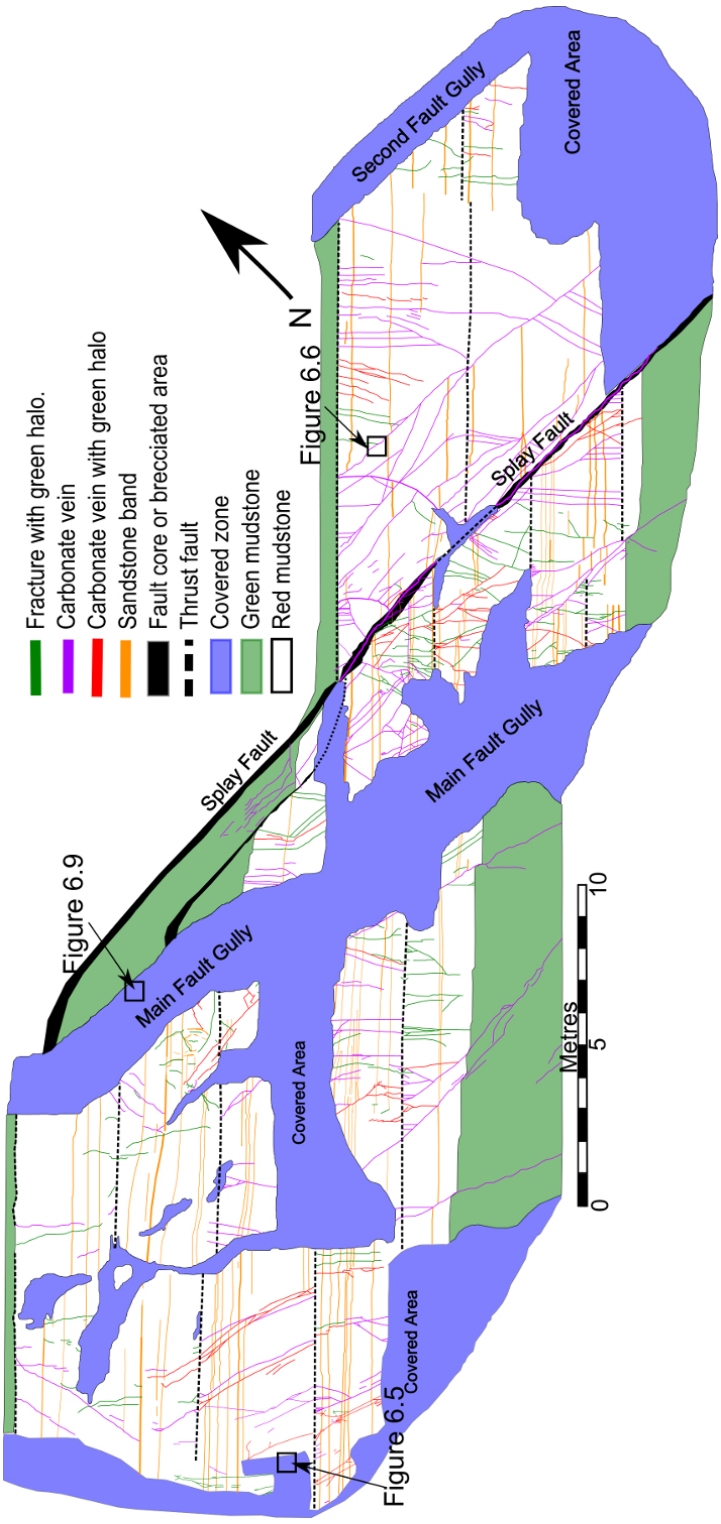

Figure 6.4: Mapped features which have evidence for being part of a fluid flow network during the history of the mudstone. Fractures are mapped as coloured lines and have been split into three groups: purple lines are fractures which show carbonate fill, red lines are fractures which show carbonate fill and a green halo, green lines are fractures which show only a green halo. Boxes show locations of photographs in figures 6.5, 6.6 6.9. Sandstone bands which have shown evidence of hosting fluid flow (for either episode) are shown in yellow, sandstone bands with a green halo were also assumed to have hosted flow in the calcite depositing episode.

6.3.2 Evidence for relative timing of fluid flow events

Field observations indicates that the fluid flow episode which deposited calcite preceded the fluid flow episode which caused the green halos. Two pieces of evidence indicate this order of fluid flow episodes.

The first evidence comes from interactions between calcite veins and green halos observed in several shear fractures. Most field observations were that when a shear fracture contains both a calcite vein and a green halo (red lines - figure 6.4), the green halo is on both sides of the fracture. However in some shear fractures the green halo is only on one side of the fracture, and occasionally switches sides (figure 6.5).

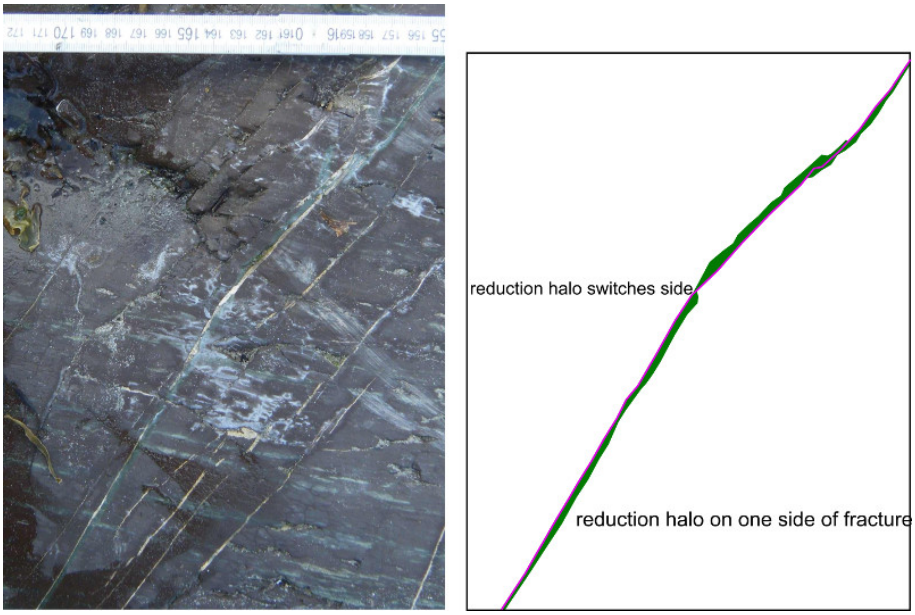

Figure 6.5: Green halo on one side of carbonate vein, note how the green halo switches to other side of carbonate vein at kinks where the vein has a slight change in strike. Other carbonate veins within photograph are not included in the sketch. Location of photograph marked on figure 6.4.

The example shown in figure 6.5 has been interpreted as follows; initially the shear fracture was filled by calcite. Then during fluid flow episode two (which caused the

green halos) the fluid entered the fracture on one side of the calcite vein, allowing only this side of the fracture wall to be altered to green, as the calcite formed a barrier to the reaction preserving the red mudstone on the other side of the shear fracture. Around the middle of the fracture the halo changes sides (annotated on figure 6.5) at a kink in the fracture, where the fracture has a sharp but slight change in orientation. At this kink then the calcite and fracture wall have become separated on the opposite side which acted to channel the fluid flow at this side, therefore the halo switches side.

However this raises the question of why most shear fractures have a halo on both sides but some show this side switching behaviour. There is no brecciation of the calcite implying that this failure was due to fracture opening rather than shearing. Where the green halo is visible the calcite cement bond with the fracture wall must have failed. In these "switching" fractures the bond between the calcite cement and the fracture wall could have been stronger on one side than the other. One explanation is that a rougher fracture surface would allow more surface area for a cement bond. Alternatively the fracture may have been "opened" by pressurised fluid entering at only one side of the calcite cement, preferentially opening that side of the fracture wall. Either hypothesis would be valid for calcite precipitation preceding the green halos, whereas no hypothesis could be devised that would allow the green halo to precede the calcite precipitation.

The second piece of evidence comes from termination relationship between the fractures. Joints that have only a green halo terminate against shear fractures which contain only calcite fill (figure 6.6). This pattern was observed multiple times across the outcrop, but never the reverse, i.e. a calcite filled fracture terminating against a fracture surrounding by a green halo was never observed.

The termination of a green joint against a shear fracture filled by calcite is interpreted as the shear fracture forming first. The shear fracture was then filled by calcite. Subsequently a new joint propagated, but terminated against the shear fracture. The lack of brecciation in the shear fracture indicates that there was no shearing after calcite precipitation. During the second fluid flow episode the joint

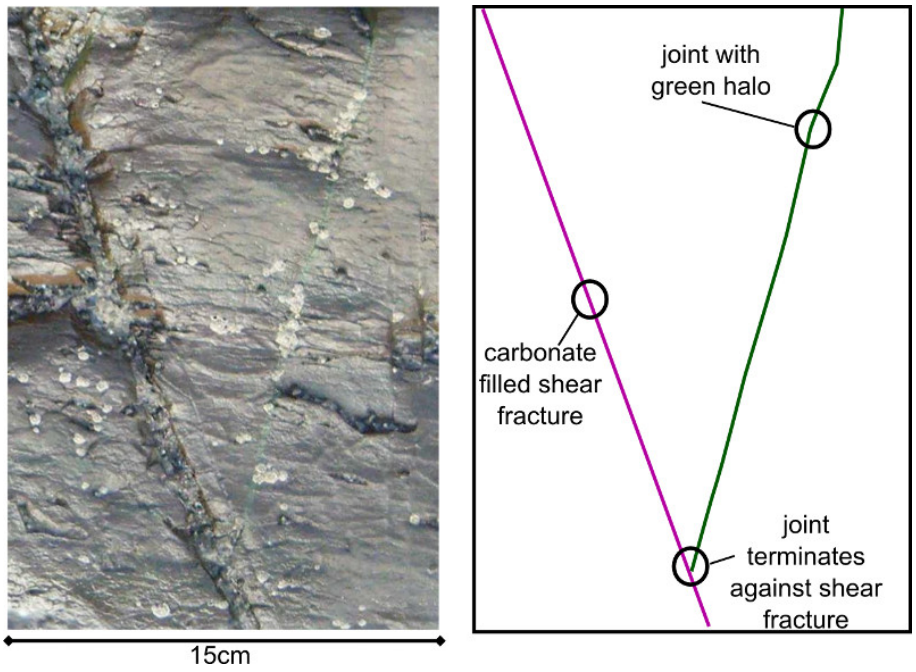

Figure 6.6: Green joint terminating against pre-existing carbonate shear fracture. Location of photograph marked on figure 6.4.

was open to the fluid but the shear fracture was not, resulting in the joint having a green halo but not the shear fracture. An alternative interpretation is that the shear fracture and joint formed prior to either fluid flow episode, and that changing differential stress meant that different fractures were critically stressed during each fluid flow episode. This alternative interpretation does not provide any information about the order of the fluid flow episodes.

The two repeated observations provide strong support for the following order of fluid flow episodes:

- Fluid flow episode one - calcite depositing.
- Fluid flow episode two - caused green halos.

These two observations are only consistent with the calcite depositing episode occurring prior to the episode which caused the green halos, and not the opposite.

Another possibilities is the same fluid flow episode caused both the calcite precipitation and the green halos concurrently. However the presence of calcite in fractures with no green halos shows this to not be the case. Therefore the above order of fluid flow episodes is considered most likely to be accurate and will be used for the rest of the data analysis and discussion of the fluid flow properties of the mudstone. The calcite depositing episode was fluid flow episode one (FFE1) and the green halo altering episode was fluid flow episode two (FFE2).

6.3.3 Evolving fluid flow networks

Different fractures were part of the connected network during the different fluid flow episodes, although some were part of both fluid flow events. Figure 6.7 highlights the groups of fractures that, along with the sandstone bands, represent the changing fluid flow network.

Many of the long (several metres) shear fractures were part of the network of FFE1. Some of the main groups of these long shear fractures are highlighted by magenta outlines (figure 6.7). Although these fractures were part of FFE1, they were absent from FFE2 leaving relatively large expanses of mudstone effectively with no fractures during FFE2 especially in the northern area.

There are several clusters of joints that were part of FFE2 but not FFE1, examples of these are highlighted by the green outlines in the FFE2 map (figure 6.7). These joints would have either been closed during FFE1 due to unfavourable stress regime, or had not yet formed and propagate far enough to be part of the fluid flow network and were isolated within the mudstone during FFE1. Another possibility is that the fracture was "open" but there was no pressure gradient across theses fractures, meaning no flow occurred but they were fluid filled. A third group of fractures show evidence of being connected to both fluid flow events. Examples of clusters of these fractures are highlighted by red in figure 6.7.

The two different fluid flow networks presented in figure 6.7 shows how fracture

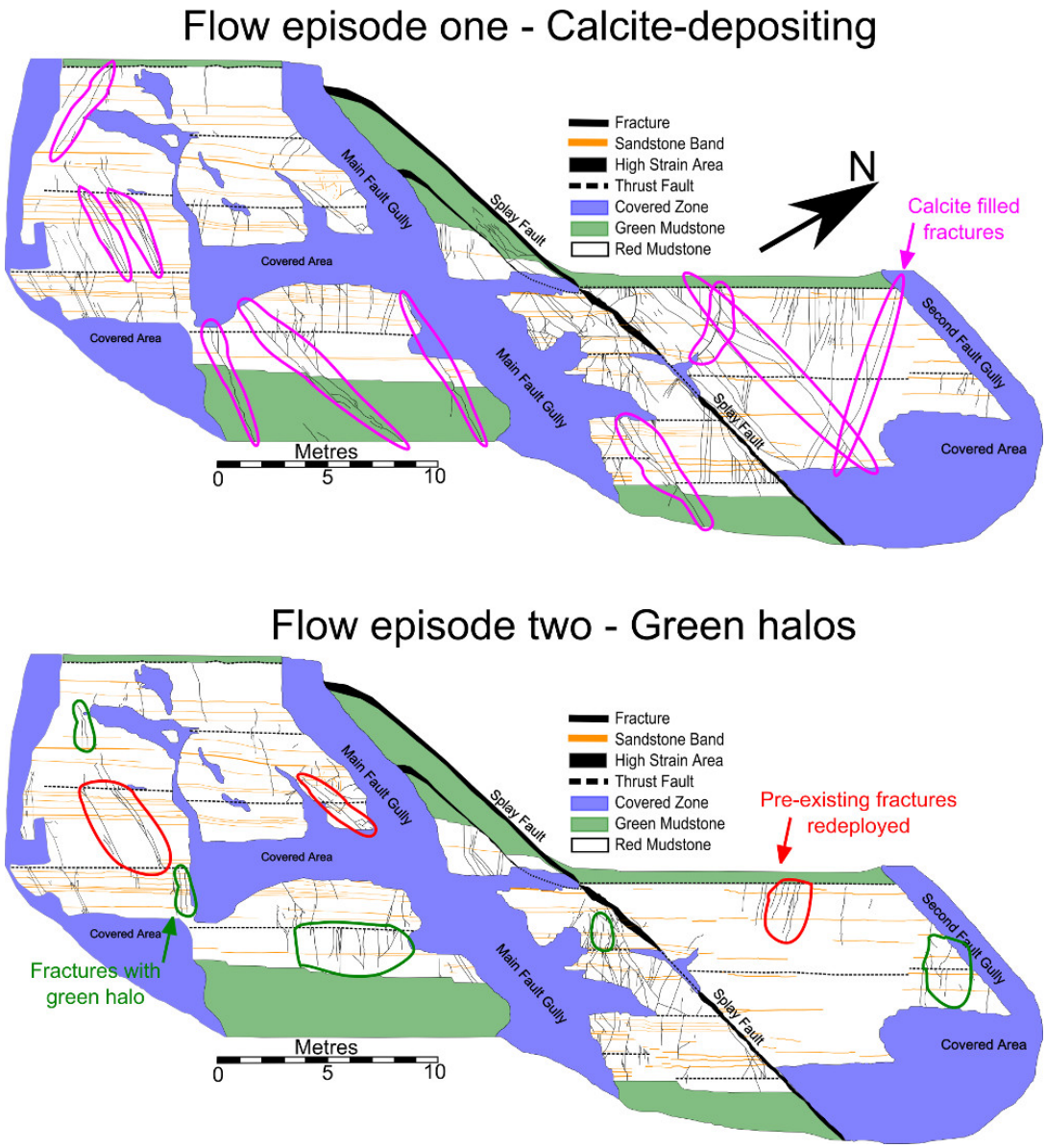

Figure 6.7: Top map shows all features (structural and sedimentary) which have evidence for having been utilised as fluid flow conduits during FFE1, bottom maps shows all features which were conduits during FFE2. Magenta highlights examples of the main features which contributed to flow event one but were closed off for flow event two. Green highlights examples of the fractures which only became open to fluid for flow event 2. Red highlights examples of clusters of fractures which were utilised by both fluid flow events.

networks are not static. Stress, chemical precipitation and dissolution, and fluid pressure changes can all act to open and close different fractures at different times. Which can lead to fractures connecting or disconnecting to the fluid flow network. The FFE1 network contains many long fractures that can cut almost or all the way through the red mudstone layer, which could allow fluid to bypass the low permeability mudstone. These long shear fractures have not been utilised during FFE2. Therefore a more complicated network of shorter joints would be needed to make a complete fracture network through the mudstone. This is due to longer fractures being more likely to intersect with other fractures as well as allowing a greater distance of low permeability bypassed by the flowing fluid. With a network of shorter fractures fluid flow would need to use a greater number of fractures to travel the same distance in a network of longer fractures. This leads to more tortuous and disperse fluid flow networks.

6.3.4 Fault architecture control over fluid flow

The strike-slip faults show evidence of being utilised during FFE1. A calcite vein runs along the splay fault (shown as the thick magenta line within the splay fault brecciated zone on figure 6.4). A calcite vein was also observed within the main fault in the small excavated area (figure 6.9). This calcite vein runs along the NE side of the brecciated fault core. Additionally just to the NE of the calcite vein the mudstone is relatively undeformed.

Another strike-slip fault was also partially exposed in the red mudstone, but not in the area of the detailed field study (shown in chapter 5 figure 5.8). This fault also showed a calcite vein running along one side of the brecciated zone, implying these observations are not specific to the area of the detailed field study. The brecciated regions of the fault cores consistently show no evidence for calcite between the clasts. The observations imply that during FFE1 the faults acted as conduits to fluid flow parallel to the faults, but barriers to across-fault fluid flow. Figure 6.8 shows a cartoon representation of the general fluid flow evidence relationships found around

the strike-slip faults.

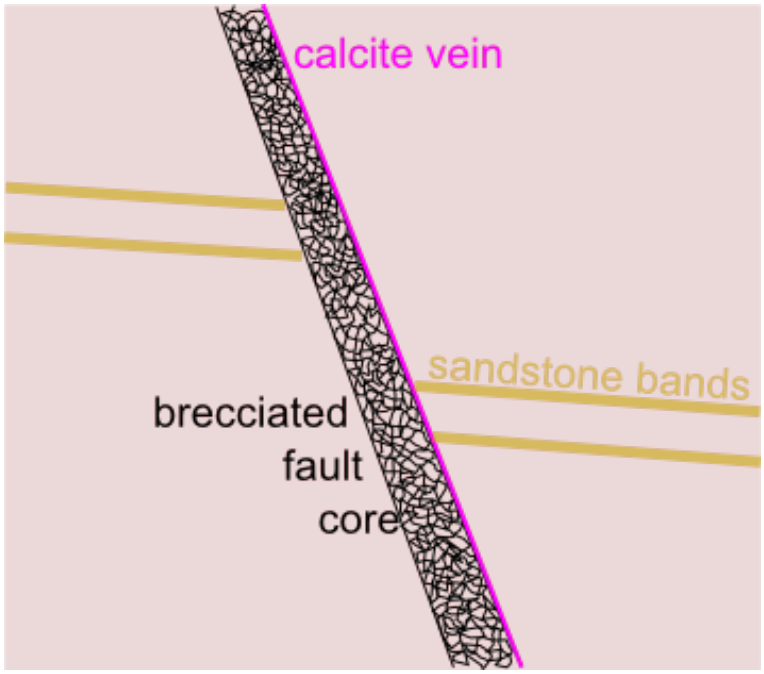

Figure 6.8: Cartoon showing general distribution of fluid flow features around the strike-slip faults. The faults have a "core" of brecciated mudstone which do not have any calcite precipitation or green alteration. A calcite vein is present running along one side of the brecciated core.

There are no green halos running alongside or within any faults exposed over the outcrop. This indicates that the faults were closed to fluid flow during FFE2.

The field evidence indicates that the faults were conduits to along-fault flow during FFE1 but barriers to across fault fluid flow, and closed to fluid flow all together during FFE2. As the largest structural features at the field site, the faults could be expected to have an important influence over fluid flow.

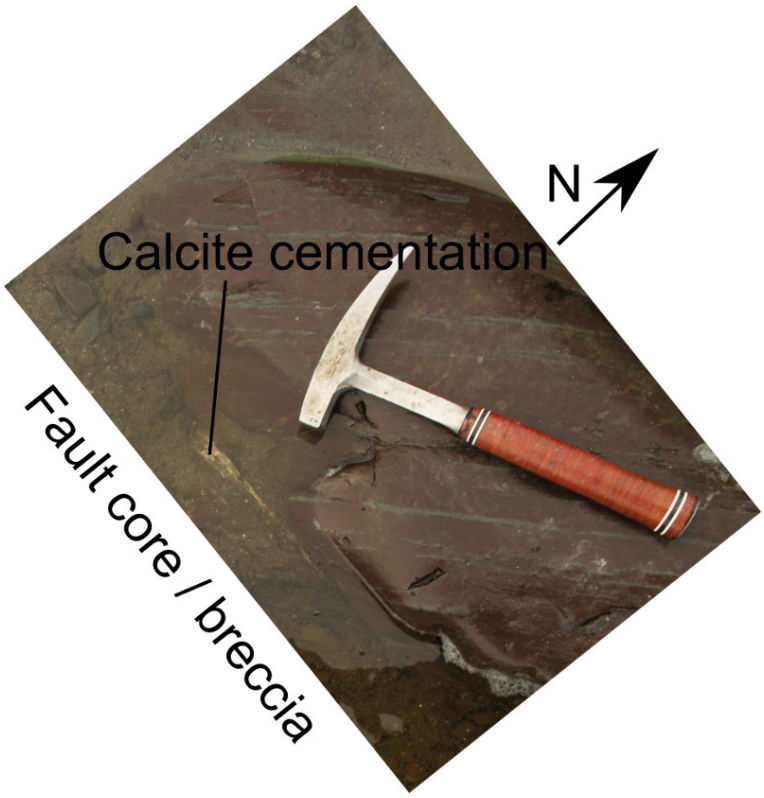

Figure 6.9: A section of the fault gully is exposed, the hammer lies on the hangingwall side of the breccia-filled fault core. The calcite cementation running down the hangingwall side of the fault core is exposed for a short distance under a small amount of sea water. The location of this photograph is shown on figure 6.4

6.4 Characterisation of fluid flow networks

6.4.1 Sandstone bands and fluid flow evidence

Figure 6.10 shows the results from the scanlines (chapter 4 figure 4.12), including data about which sandstone bands are surrounded by a green halo. Data were only collected for the sandstone bands which show a green halo and were therefore were part of the network during FFE2, while this data could could not be made in the field for the calcite precipitating FFE1. This is because these observations were made in the field where the green halos were visible, to see the calcite in the sandstone

bands requires thin section to be made.

Not all sandstone bands were part of the network during FFE2; only 33 of the 65 sandstone bands (51%) are surrounded by a green halo. Since approximately half of the sandstone bands were used during FFE2, this leads to the question of why some hosted fluid flow while others didn't. Are there any properties of the sandstone bands that make the bands more likely to have been connected to the pressure gradient the was driving fluid flow in FFE2.

6.4.2 Connectivity and extent of sandstone bands related to flow

In chapter 4 the sandstone bands were classified according to their connectivity and extent. These classifications are now compared to the evidence for the sandstone bands hosting flow in FFE2 or not.

Figure 6.11 shows the extent assessment of individual sandstone bands plotted against connectivity. There are six sandstone bands which show high connectivity and extensiveness (top right - figure 6.11), five of these sandstone bands (83%) were part of FFE2. In contrast only one out of the five (20%) sandstone bands with low connectivity and extent (bottom right - figure 6.11) was part of FFE2. This indicates that connectivity and extent may have influence over the likelihood of a sandstone band to be open to fluid flow.

Connectivity appears to exert more influence over the likelihood of a sandstone band having been part of FFE2 than extensiveness does. Looking just at extensiveness then only one out of five (20%) of low extensiveness sandstone bands have a green halo, compared with one out of two (50%) for medium extensiveness and 14 out of 33 (42%) for high extensiveness. However there is far greater variation from low to high connectivity. For low connectivity 9 out of 27 (33%) show a green halo, while it is two out of 7 (28%) for medium connectivity and five out of six (83%) for high connectivity.

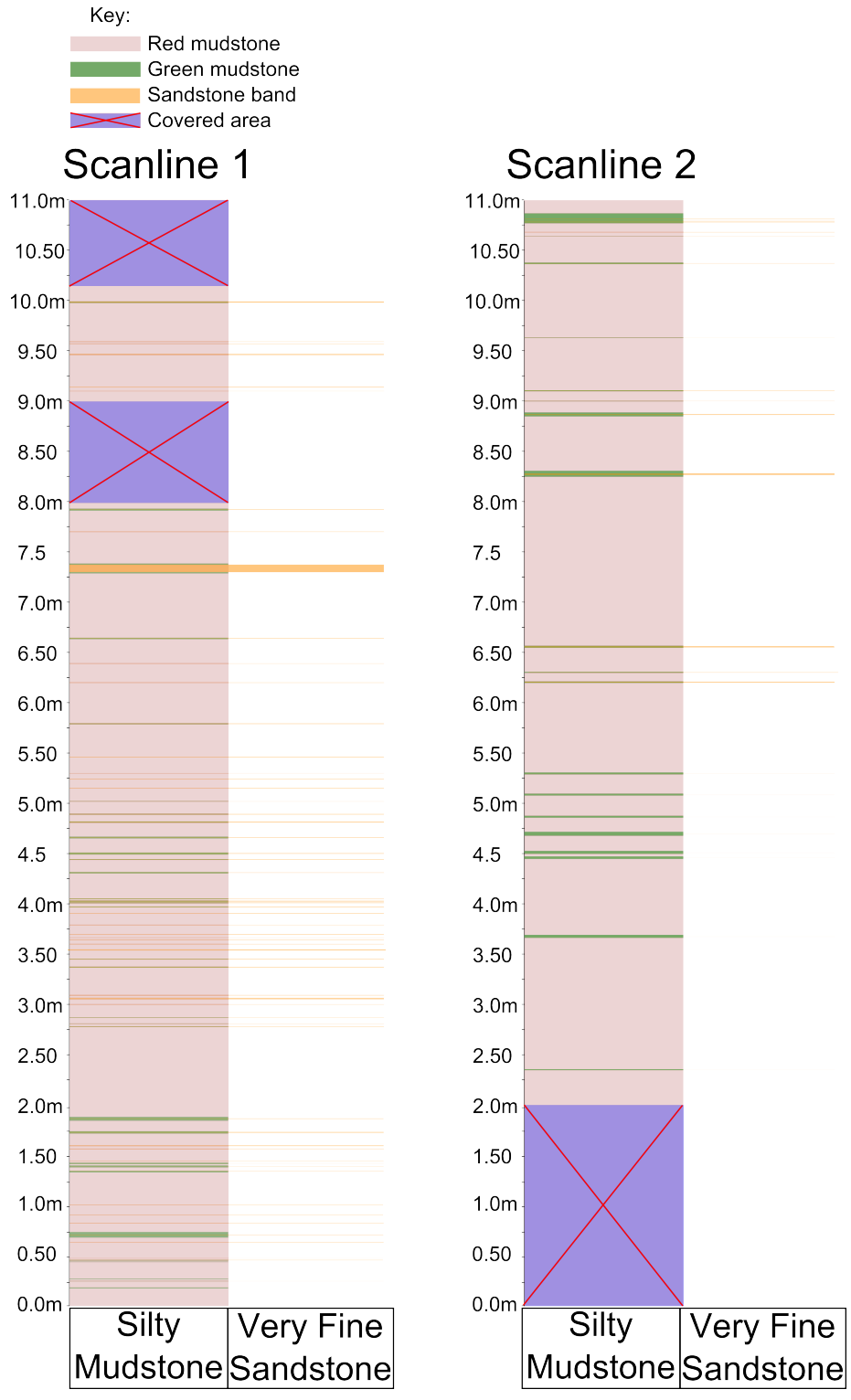

Figure 6.10: Transects of scanlines, showing sandstone bands with associated green halo. Thicknesses of the sandstone bands and green halos in the transects are proportional to their thicknesses as measured in the field.

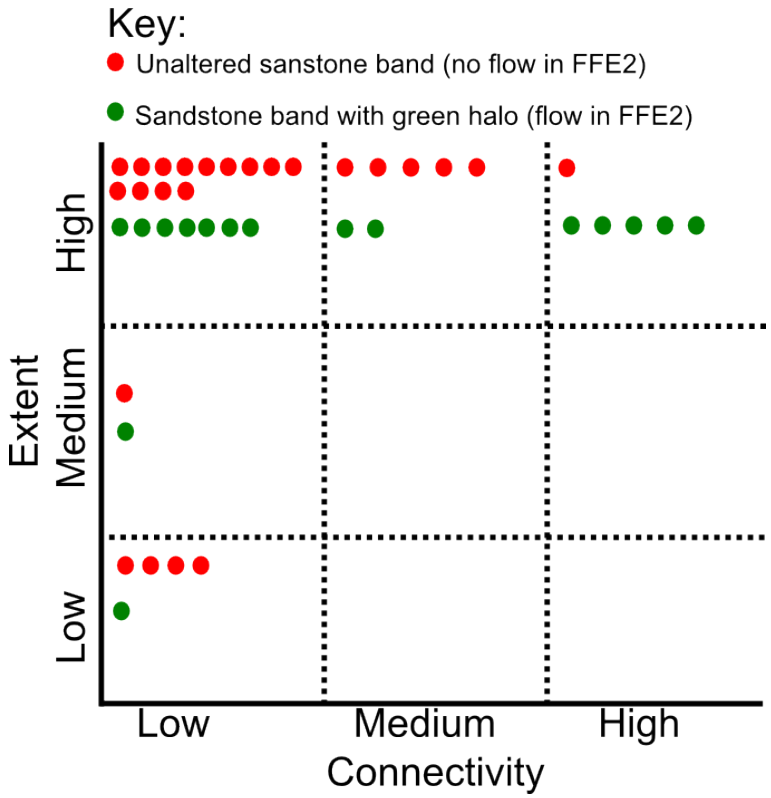

Figure 6.11: Comparing the influence of connectivity and extensiveness with presence and absence of a green halo. If the sandstone band has a green halo (altered) it is represented by a green dot, sandstone bands without green halos (not altered) are represented by a red dot. Sandstone bands with green halos are considered to have been part of the FFE2 network.

This relationship shows that the complicated small scale architecture of the pseudonodules identified in many of the sandstone bands are important features for determining the fluid flow properties of the sandstone bands. That is the segmented nature of the pseudonodule bands (low connectivity) means they have lower permeability than the better connected sandstone bands. However extent does not have as much importance for the fluid flow properties of the sandstone band.

6.4.3 Sandstone band thickness and probability of hosting FFE2

The sandstone bands were found to follow a log-normal thickness distribution (chapter 4), that reflected that of other studies of thicker turbidite sequences. Here it is investigated whether thickness has any influence on likelihood of sandstone bands being part of FFE2. Figure 6.12 shows a histogram of the sandstone band thickness, but each of the columns has been split between the sandstone bands with and without a green halo.

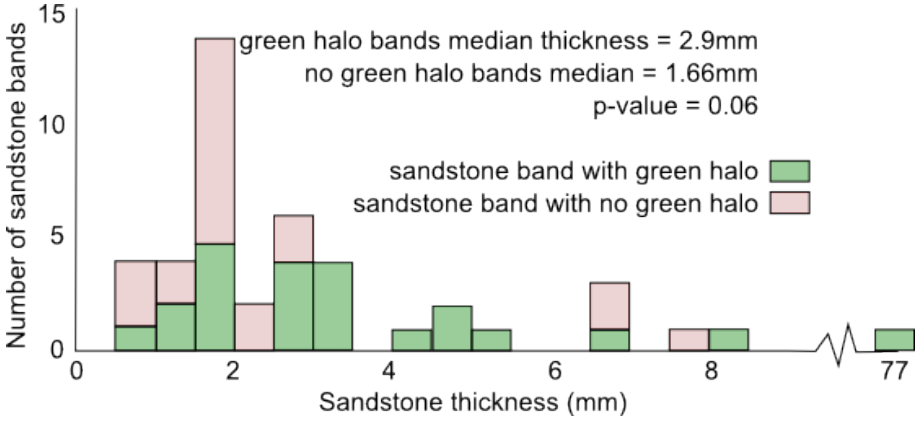

Figure 6.12: Histogram of thickness of sandstone bands, sandstone bands are split between those showing a green halo (green column section) and those which do not (pink column section).

Sandstone bands which were part of the fluid flow network during FFE2 are generally thicker than the sandstone bands which were not, as shown by the difference in median values (figure 6.12). This is shown by the median thickness for sandstone bands with a halo (2.9mm) being over one millimetre thicker than for sandstone bands without a halo (1.66mm). The p-value (showing significance of population differences) was found to be 0.06, usually significance is taken at a p-value of less than 0.05 (1 in 20 chance of difference occurring by chance). Because it can be misleading to use this test in dichotomous terms (Stang et al. 2010), it is worth noting that with a p-value of 0.06 the thicknesses differences are very nearly what would be considered statistically significant, so it could be said that thicker bands

may be more likely to have hosted fluid flow but thickness does not seem to have been a controlling property. However the relationship isn't so strong that it is clearly geologically significant, i.e. sandstone bands under a certain thickness can be ignored because they are so unlikely to be hosting fluid flow. Therefore sandstone bands of all thickness should be considered when characterising the fluid flow behaviour of the outcrop.

6.4.4 Fracture density differences between fluid flow events

The faults exert influence on the fracture density of the surrounding rock (chapter 5-section 5.3.3), but not all these fractures in high density areas may have been connected to the fluid flow network. Flowing fracture networks are often a small subset of the entire fracture network population (Talbot and Sirat 2001, Odling et al. 1999). The fracture density showed large changes between the three regions (southern area, central area, and northern area) bounded by the faults; there is a sudden and large change in fracture density recorded across the faults. The highest fracture density was found in the central area, and lowest in the southern area, while the northern area had a "medium" fracture density. This variation in fracture density would indicate that the central area may have been a region of enhanced fluid flow. It is now investigated whether this relationship is reflected in the densities of the fractures that show evidence of being part of either palaeo-fluid flow episode.

The fracture density of fractures involved in each of the two fluid flow episodes are shown in figure 6.13. Perpendicular distance from the main fault core is plotted on the x-axis and the grey areas show the regions of fault breccia and associated debris cover. Fracture trace density (the number of fracture trace mid-points per m^2) is plotted on the y-axis. Each symbol on the graph represents a data point collected from a circular scanline.

The density of fractures involved in FFE1 shows similar patterns as the whole fracture population; but not exactly the same. The highest values of density are found on the circles that crossed the splay faults during data collection, due to the small

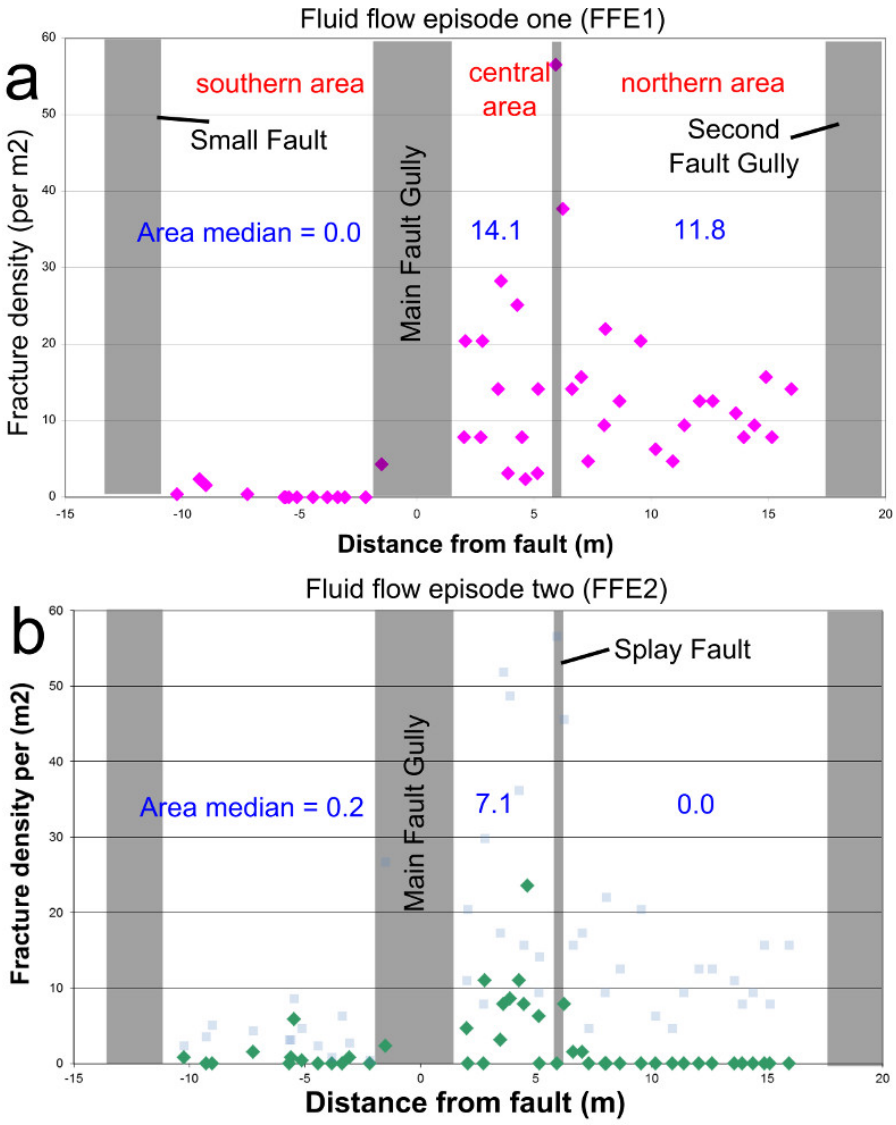

Figure 6.13: Data points from individual circular scanlines showing density of features associated with FFE1 (a) and FFE2 (b). Main structural faults are shown in grey. For general comparison the grey data points on b show the fracture density of all fractures, not just the ones which were part of the fluid flow networks.

carbonate-filled ladder like fractures between the splay fault and synthetic shear fractures. Beyond the splay fault the general pattern is similar between the central area and northern area, with density ranging from 3 to 29fracs/m^2 with a median of

14.1fracs/m^2 in the central area and 5 to 22fracs/m^2 with a median of 11.8fracs/m^2 in the northern area. The southern area has very low fracture density for FFE2, with a median value for the area of 0.0fracs/m^2.

The fracture density for FFE2 is quite different from the distribution of the whole fracture population found in the previous chapter. The southern area shows very low fracture density with a median of 0.2fracs/m^2 (figure 6.13). The northern area also has very low fracture density with a median of 0fracs/m^2. Additionally it is worth noting that in the northern area the two data points closest to the splay fault are the only ones which are greater than 0fracs/m^2 . The highest fracture densities for FFE2 are found in the central area, which shows greatly enhanced fracture density, with a median of 7.1fracs/m^2, compared with the southern or northern area. The two circles intersecting with the splay fault do not show the greatly enhanced fracture density for FFE2 as with FFE1; the small ladder fractures and splay do not contribute to FFE2.

In the central area the density of fractures used in FFE1 is generally greater than during FFE2, resulting in FFE1 having double the median density of FFE2 in the central area. The northern area also has significant differences between the densities of the fluid flow episodes, with FFE1 having a median of 11.8fracs/m^2 compared with zero for FFE2. This shows that FFE1 had a significantly denser network of fractures than in FFE2 which could be seen in the field map (figure 6.4). Both fluid flow episodes have similar very low densities of fractures in the southern area, with 0.0fracs/m^2 for FFE1 and 0.2fracs/m^2 for FFE2.

Both fluid flow episodes have a reduced density compared to the whole fracture population. This reflects results from previous studies that suggest only a few fractures are open to fluid flow at any one time (Rowland et al. 2008, Fairley and Hinds 2004, Losh et al. 1999, Talbot and Sirat 2001, Younger and Manning 2010). Taking data from the whole fracture population would therefore overestimate the fluid flow properties of the fracture network, this issue is further discussed in section 6.5.

The data also highlights the issues of changing fluid flow fracture networks, this effect is particularly striking in the southern area where a density of flowing fractures reduces from a median of 11.8 to 0fracs/m^2 between the two fluid flow episodes. Fractures open or close due to a mixture of hydro-mechanical, kinematic or chemical influences but the fracture must still be connected with a pressure gradient for fluid to flow through. Such influences can change over time as a pressurised reservoir is depleted or from temporal changes in the regional stress field. These changing fracture properties could mean that the different areas of the field site show very different bulk permeability properties between the two fluid flow episodes, this is explored by modelling in the following chapter.

When collecting data from the circular scanlines the diameters of the circles were made large enough to take a representative area of the fracture network. To be representative a circle must be larger than fracture blocks (Rohrbaugh et al. 2002). A fracture block is considered an area of intact rock bounded by fractures. However when using a subset of the fractures, involved in either fluid flow episode, this diameter may not be large enough to be representative of the areas of sparser fractures, due to the larger spacing between sparse fractures. In the denser areas (FFE1 central and northern area, FFE2 central area) the circles likely still accurately represent the fracture densities. In the sparser areas the density is often 0fracs/m^2, this could be due to once the natural fracture density falls below a certain threshold (e.g. 3fracs/m^2) the smaller circles could no longer pick up the data. This does not seem to have unduly influenced the key information gained from the data, as it is still clear where the high and low fracture density areas are. The quantitative data collected using the circular scanlines allows confidence in the data showing differing fracture density properties of the regions within the outcrop, beyond that which can be observed by the mapping.

This technique was chosen as it could be used to obtain samples of fracture density from individual locations across the field site. This is different to how the circular scanline technique was originally intended which was to get representative density values for a wider fracture population (Mauldon et al. 2000, Rohrbaugh et al. 2002).

However the advantage of having no scanline orientation bias associated with the data means the circular scanline is ideal for the needs of this study. However, there could be spatial bias with the data, as some areas of the field site could not be samples due to tidal cover, or unconcious placement of circular scanlines on areas of higher fracture density as that is of interest to the researcher. To attempt to avoid such bias, a selection of circles from disperse enough locations was made.

6.4.5 Fracture orientation

In chapter 5 it was shown that the joints and shear fractures preferentially strike in different directions, with joints preferentially striking NW-SE and shear fractures WNW-ESE or NNW-SSE. Here it is investigated if the fractures utilised in either fluid flow episode are a subset of the whole fracture population with a specific orientation.

The stereonets and rose diagrams in figure 6.14 show the orientation of the fractures used in FFE1 and FFE2. Orientation data were recorded in the field from 69 fractures used in FFE1 and 93 used in FFE2. Both joints and shear fractures are shown in the stereonets, with the shear fractures being dark purple great circles in both stereonets.

The fractures used in FFE1 have three general subsets of preferred orientation with two main collections of fractures striking WNW-ESE and NW-SE, while a smaller group strikes NNW-SSE. It is predominantly joints which strike NW-SE, while the WNW-ESE and NNW-SSE groups are a mixture of joints and shear fractures. This reflects the attributes of the whole fracture population presented in chapter 5 in section 5.3.2.

The fractures used in FFE2 predominantly strike NW-SE, with a small number of fractures spreading out between WNW-ESE and NNW-SSE. Most of the fractures striking NW-SE are joints but there are three shear fractures also striking in this orientation. FFE2 shear fractures are more predominant in the small group of

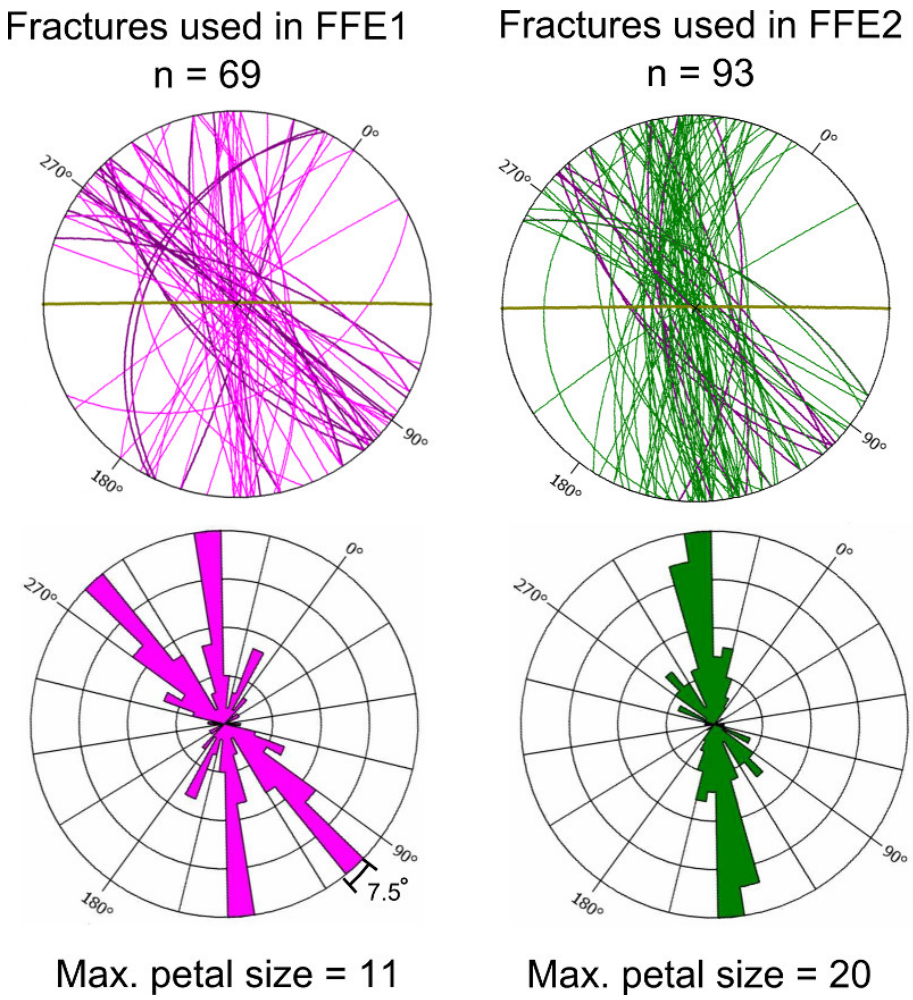

Figure 6.14: Stereonets and rose diagrams of fractures utilized during either flow event. Images have been rotated to show bedding horizontal, joints are more likely to strike NW to SE while shear fractures tend to strike West to East. Great circles of FFE1 joints are lighter purple colour, of FFE2 joints are green, and shear fracture in both FFE1 and FFE2 stereonets are dark purple. Great circles of bedding orientation are marked as dark yellow (horizontal line) on top stereonets.

fractures striking WNW-ESE, this is similar to both the fractures in FFE1 and the whole fracture population.

The fractures used during each fluid flow episode show generally similar orientations, but show differences in preferred strike. Fractures involved with FFE1 generally

strike NW-SE or WNW-ESE whereas during FFE2 fractures generally cluster nearer to NW-SE. However there are small subsets of fractures for each fluid flow episode striking outwith these preferred orientations. The generally wider range of strike orientations in FFE1 means that the fractures were more likely to intersect thus creating an enhanced fluid flow network through the mudstone.

6.4.6 Feature connectivity variations between fluid flow episodes.

The connectivity of the fractures were counted for each fluid flow episode, as in section 4.4.3 of chapter 5. Connections were counted as intersections with other fractures, sandstone bands, and thrusts. If a fracture of solely one fluid flow episode connects with a fracture of the other fluid flow episode this is not counted, as it would not have been a permeable connection during either fluid flow episode. The results of the connectivity count are presented in figure 6.15, and are split between the three fault-bounded field areas.

For both the fluid flow episodes, all field areas have a median connectivity of two, therefore at least 50% of fractures in the field site have at least two connections. This is a threshold for a fracture to be part of the fluid flow network. Only the Northern Area during FFE1 shows a first quartile of two, the other five graphs show a first quartile value of one. This highlights the highly connected nature of the fractures during FFE1 in the Northern Area with at least 75% of fractures having two connections.

Unlike the fracture density there are no stark differences in connectivity between the field areas and fluid flow episodes. Fracture density is usually an important component of fracture connectivity in networks of only fractures. However when sandstone band are included as permeable features which are part of the network then this appears to allow a highly connected network even within sparsely populated areas.

This connectivity data is all for the 2D system exposed on the modern day out-

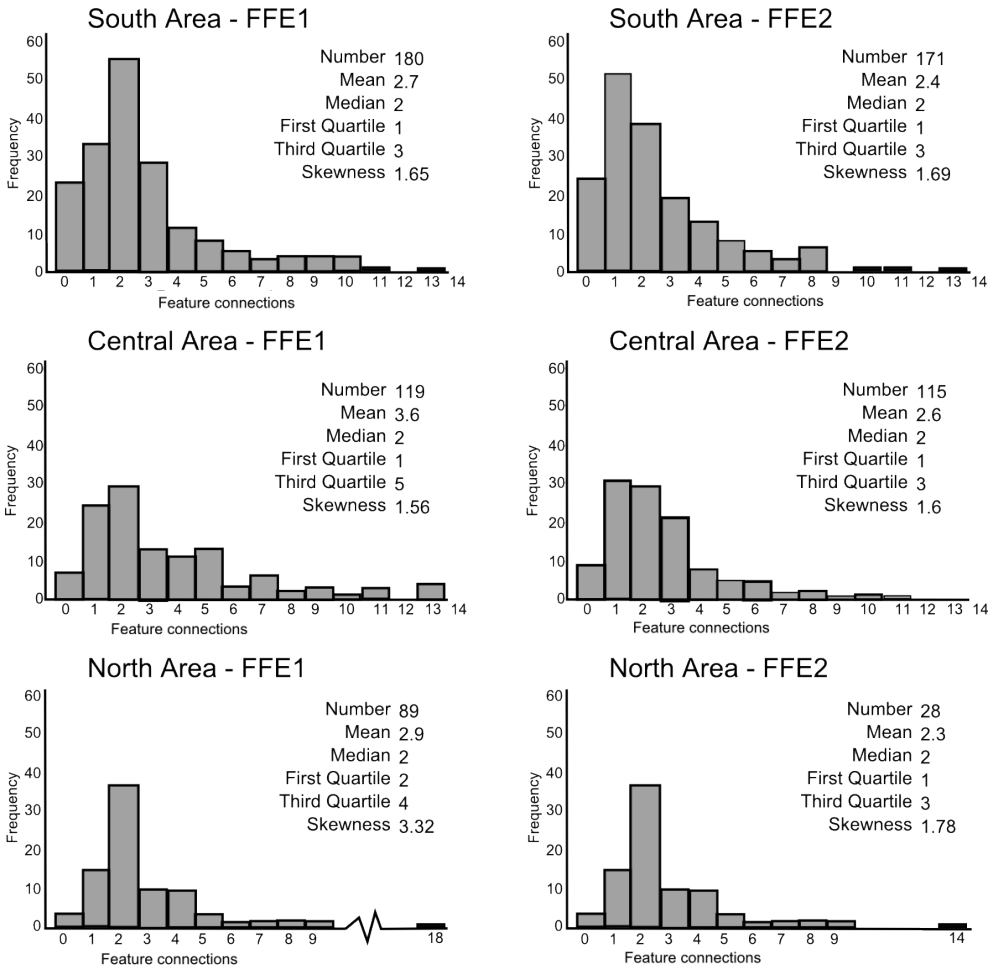

Figure 6.15: Histograms of feature connectivity for FFE1 and FFE2 in the three fault-bounded field areas.

crop. When pressure gradients were driving flow during FFE1 and then FFE2 through a 3D network of fractures, faults, and sandstone bands. Converting 2D fracture data into 3D is non-trivial (Berkowitz 2002) and there is likely to be too few traces mapped in this study to provide a basis for any meaningful conversion to 3D (Berkowitz and Adler 1998). However a 3D system is likely to be more connected than this 2D system, as there are more opportunities for connections to be made between the potential fluid flow features. This is further discussed in section 6.5.4.

6.4.7 Variations in reduction halo thickness surrounding fractures.

What information is gained from the thickness of reduction halos

A thicker green halo could be indicative of the fracture being open to fluid flow for a longer time. The green halo is likely caused by a chemical reaction front moving into the mudstone from the fracture face. In such low permeability rock the likely mechanism for penetration of reactants is diffusion. Diffusion is described in equation 6.1 which is Fick's second law of diffusion (Fick 1855).

$$\frac{\partial C}{\partial t} = \omega D_d \frac{\partial^2 C}{\partial x^2} \tag{6.1}$$

Where:

- C is concentration ($\frac{mol}{m^3}$)
- t is time (s)
- ω is a tortuosity coefficient
- D_d is diffusion coefficient ($\frac{m^2}{s}$)
- x is position (m) i.e. penetration into mudstone from fracture

"x" would determine how far into the mudstone the halo propagates (halo thickness). "x" would be primarily proportional to "t" (time) in these cases. This is mainly due to the other properties likely being constant between the fractures or not controlled by the fracture properties. Concentration would refer to the relative amount of reacting fluid within the fractures. This would not change with fracture properties but due to changes in the inflowing fluid. ω and D_d are both related to pore scale connectivity in the mudstone so would not alter depending on fracture properties. Under thin section using optical microscope and SEM no micro-fractures

were observed in the walls of the fractures, varying micro-fracturing would influence ω and D_d but no information could be gathered as to extent of micro-fracturing at the time of FFE2. Fluid flow rate is proportional to fracture aperture, therefore fractures with greater aperture would have the reactant fluid refreshed more quickly than fractures with smaller apertures. This could have the affect of larger aperture fractures maintaining a larger concentration gradient; more effectively driving the reactant halo deeper into the mudstone. However aperture data is not available, as the modern day aperture would be different to fracture aperture during FFE2. For this reason fracture aperture has not been considered in this investigation.

Other factors which control the rate of diffusion were likely constant throughout the mudstone, for example temperature. The only controlling factor which could change between different fractures during FFE2 remains the length of time that the fracture was part of the fluid flow network. Being part of the fluid flow network for longer means that the reactive fluid is present in the fracture for longer. This allows the concentration gradient to be maintained for longer (t in equation 6.1) and the reaction front to penetrate further into the mudstone from the fracture.

Individual fracture properties (length, dip, and strike) are compared with the thicknesses of the halo surrounding that fracture. This will provide information as to which properties may have been more important for connecting fractures with the fluid flow network during FFE2. A longer fracture is more likely to intersect with other fractures or sandstone bands, and therefore is more likely to be connected to the fluid flow network. Fractures of different orientations may be closer to or further from being critically stressed (see section 2.3 for explanation of critically stressed fractures); fractures closer to being critically stressed could stay open to fluid flow longer if fluid pressure dropped over time.

The halo width data was screened for any values that may have been influenced by fractures interacting with other features. That is, halos near to fracture-fracture intersection, or fracture-sandstone band intersection are not included in these analyses. This was to try and isolate the individual fracture properties which may have led to thicker halos on certain fractures.

The maximum halo width measured around individual fractures is plotted on figure 6.16 against fracture trace length. No correlation is found between fracture trace length and halo thickness around fractures.

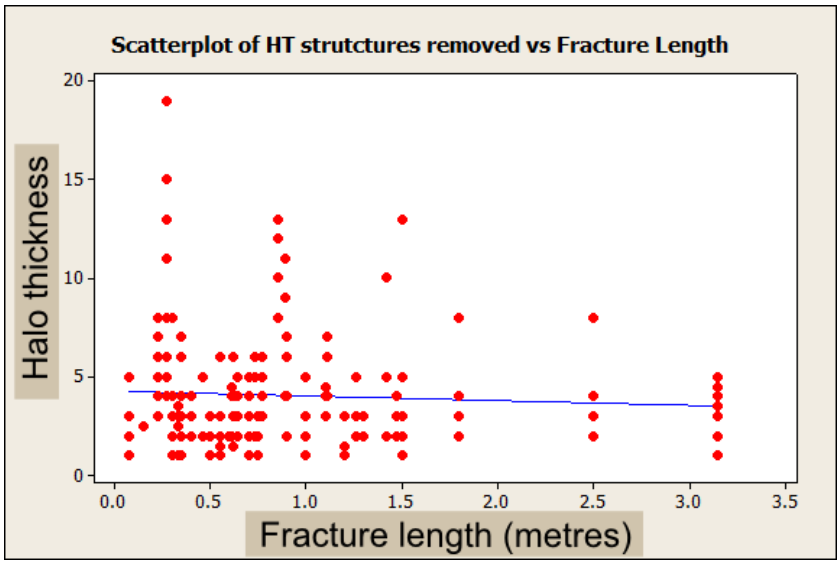

Figure 6.16: Fracture length is plotted against the maximum halo width measured on the fracture. No correlation exists between fracture trace length and halo thickness.

Figure 6.17 shows halo width data plotted against fracture dip. It was difficult to get reliable dip data from the outcrop due to very flat topography in some places of the field site, so there are relatively few data for fracture dip. Halos widths do not show any correlation with fracture dip.

Fracture orientation (relative to interpreted σ_1) against halo width is shown in figure 6.18. The fracture orientations are relative to σ_1 because in chapter 5 σ_1 was interpreted as being orientated NNW-SSE (approximately perependicular to the sandstone bands). By converting the fractures to be orientated with respect to σ_1 it makes it clearer the effect that the fracture orientation may have had, with the stress, on keeping the fracture open. Therefore on figure 6.18 fractures with 0° are parallel to σ_1 and 90° are perpendicular to σ_1.

The joints in figure 6.18 show increasing halo size as they get closer to 90° (perpendicular to sandstone bands). From 0-70° halo thickness around joints does not rise

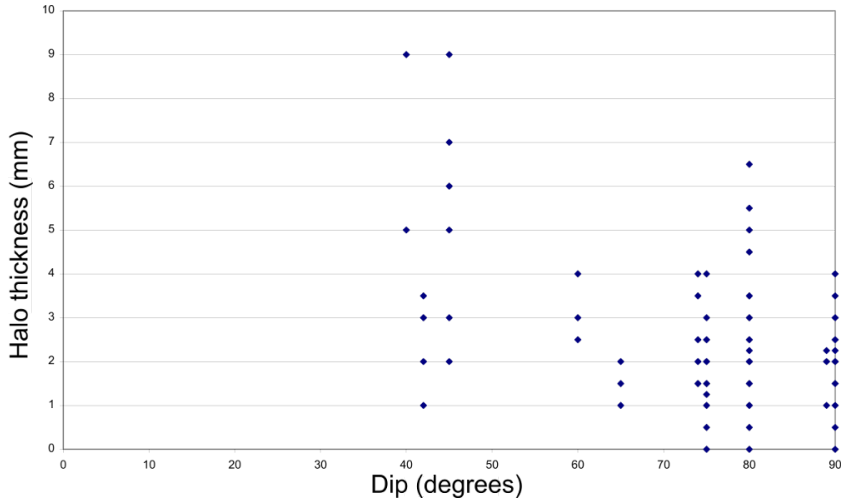

Figure 6.17: Graph showing relationship of fracture dips to halo widths

above 6mm, but from 70° to 90° there is a steady rise in halo thickness. Similarly, the shear fractures generally do not have halo thicknesses above 6mm. However between 40° and 45° the halo thickness of shear fracture do rise above this 6mm threshold.

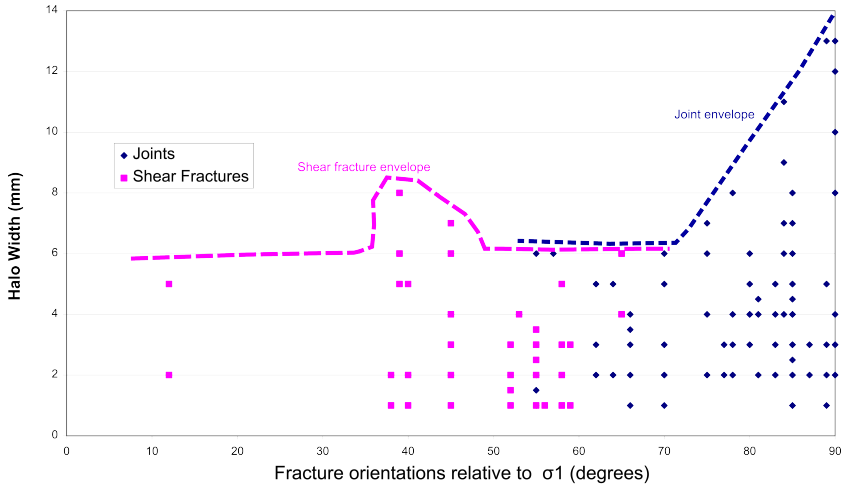

Figure 6.18: Graph showing relationship between halo width and fracture strike (relative to interpreted σ_1). Data has been divided between measurement taken from joints (dark blue) and from shear fractures (purple). Envelopes have been added to the shear fracture and joint data sets to highlight the areas where there are increased halo thickness.

The orientation of the joints with the thickest halos matches the most common orientation set of the joints (figure 6.19). This could be due to the stress conditions during FFE2 causing these orientations of joints to be critically stressed and therefore held open under reduced fluid pressures. The oreintation of the shear fractures with the thickest halo is not exactly on the largest group of shear fractures, as it is for the joints.

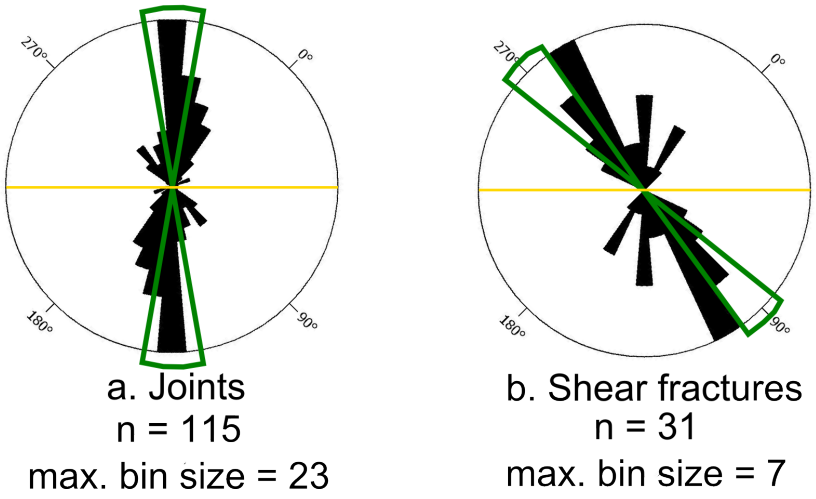

Figure 6.19: Strike orientation of a. joints and b. shear fractures. Green areas outline the orientation range where green reduction halo width exceeds 6mm on figure 6.18.

The joints and shear fracture with halos thicker than 6mm are measured to be located within 6m perpendicular from the main fault core (figure 6.20). There is also a significant cluster of joints with thick halos that are connected to the same thrust fault (blue arrow - figure 6.20). It is possible that being connected to the large structural features of the thrusts meant that the fractures were better connected to the fluid flow networks. However many fracture in both the South and central areas are connected to the thrust but do no show thicker halos. Additionally there are no clear networks of fractures with thicker halos, where all the thicker halo fractures are interconnected. This indicates that the thicker halos are more associated with individual fractures on the exposed outcrop, rather than a specific

network of fractures. This fits with the data showing that fractures of specific orientations show a thicker halo, rather than interconnected fractures of different orientations.

Orientation is the biggest influence on halo thickness that was found, and therefore could be the most important factor in how long a fracture was open to fluid flow. Other possible influences (length, location) were also tested but no relationships were found that affected fracture width.

One of the main reasons that fracture orientation appears to have been a major influence on fluid flow through fractures, could be that orientation is a key component of whether or not a fracture is critically stressed or not. A fracture is said to be critically stressed when it is near the point of failure and may propagate further throughout the rock. For the joints, this appears to be the joints which are inline with interpreted σ_1 so it is speculated that these were held open while a pressure gradient existed to drive fluid through these fractures. Thus replenishing the concentration gradient between the fluid in the fracture and the fluid in the mudstone fracture walls. However for shear fractures the relationship is less clear, so with this evidence it is difficult to even speculate if orientation of shear fractures and if they were critically stressed had any influence at all.

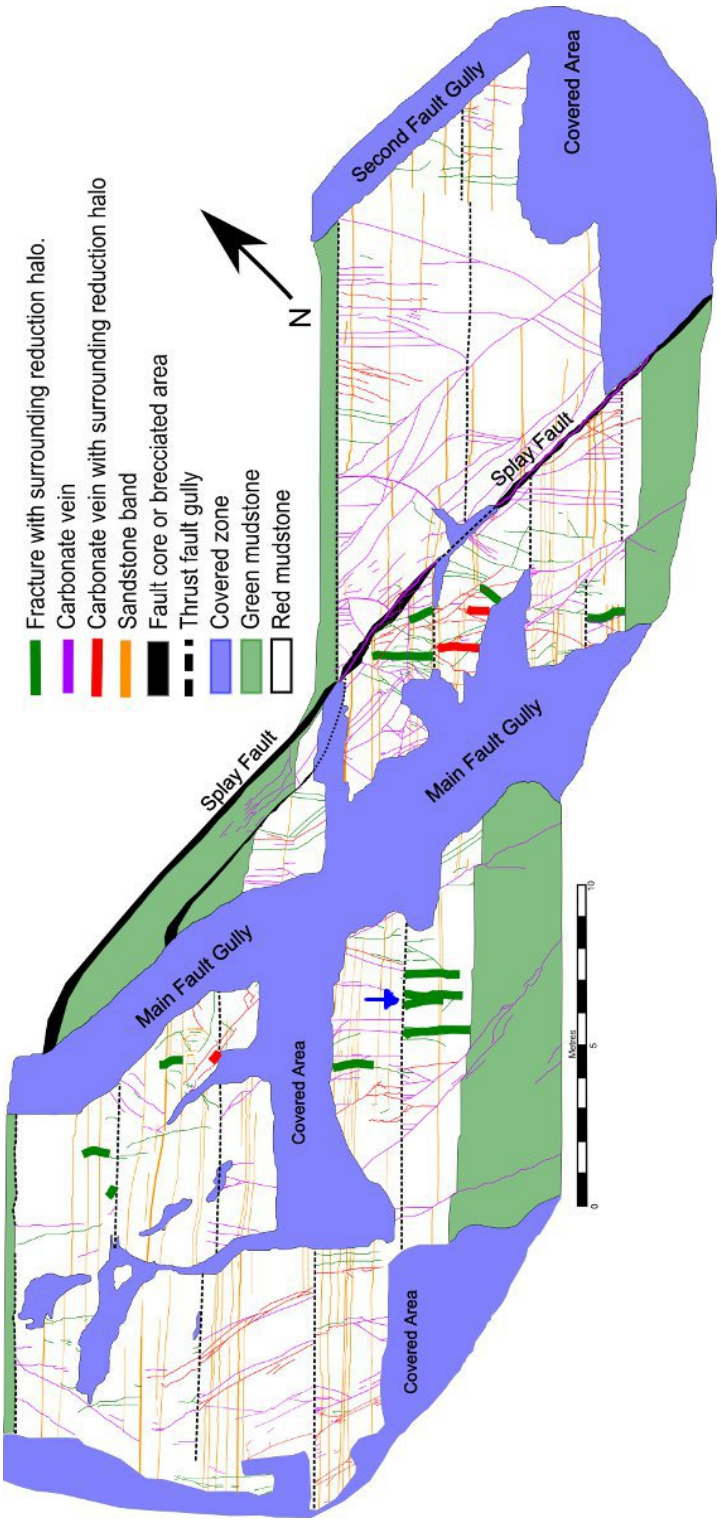

Figure 6.20: Map from figure 6.4, the fractures with halos thicker than 6mm have been highlighted on the map by considerably increasing their thickness. Blue arrow highlights fractures connected to a thrust as discussed in the text.

6.5 Discussion: palaeo-fluid flow

6.5.1 Key findings from palaeo-fluid flow investigation

- Field evidence available for two palaeo-fluid flow episodes
  - The first deposited fluid flow episode calcite (FFE1)
  - The second fluid flow episode created green halos around fluid flow conduits (FFE2)
- The connectivity of the pseudonodules in sandstone bands influences how likely they were to be part of the palaeo-fluid flow network.
  - Connectivity appears to be more important than thickness for likelihood of a sandstone bands being utilised by palaeo-fluid flow episode.
- For FFE1 the central and northern areas show high fracture density, but only the central area for FFE2.
- Feature connectivity was high for FFE1 in the central and northern areas, but the same as FFE2 in the southern area.
  - This shows that fracture density has a key influence on the connectivity of the features (including sandstone bands) in the flow networks.
  - FFE2 likely lower bulk permeability due to flow networks than FFE1, particularly in the northern area.

6.5.2 Key influences on fluid flow

The connectivity of the sandstone bands was the most important factor for determining whether a sandstone band was conductive to fluid flow during FFE2. Figure 6.21 shows a cartoon representation of fluid flow being able to travel between fractures along a high connectivity sandstone band but not a low connectivity pseudonodule

band. The connected nature of the sandstone band architecture was more influential than how far a sandstone band extended over the outcrop, or the thickness of the sandstone band. Chapter 4 showed evidence that thicker sandstone bands were more likely to be a single continuous band whereas thinner sandstone bands were more likely to be a poorly connected pseudonodule band. So, although it is connectivity that ultimately has control over fluid flow in a sandstone band, this connectivity is correlated the thickness of a sandstone band.

Without the presence of the open fractures or faults the sandstone injectites would be the only viable hydraulic connections between the sandstone bands. However the presence of the faults and fractures, and relative sparse nature of the sandstone injectites (introduced in section means the injectites have much less of an influence over the flow networks.

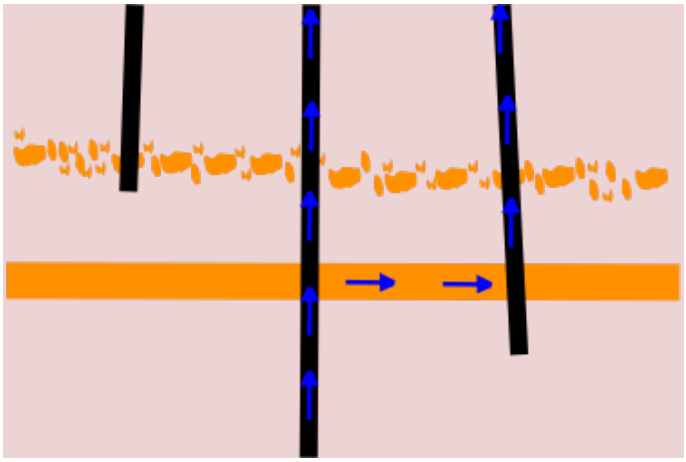

Figure 6.21: Cartoon of a series of joints connected by sandstone bands, but not all are connected as part of a flow network.. The middle joint host flow which travels through the lower "high connectivity" sandstone band to the fracture on the right. The "low connectivity" upper sandstone band does not connect fracture on the left to the flow network.

The differences in fracture orientation between the fluid flow episodes are not large. However FFE1 does preferentially utilise shear fractures compared with FFE2. In the study area shear fractures tend to be longer features than joints partly due to

many of the shear fractures having propagated through thrusts and sandstone bands which joints readily terminated against (figure 6.22). Thus, because FFE1 preferentially favours orientations that are more likely to be shear fractures compared with FFE2 then the features in FFE1 are more likely to be better connected than in FFE2 (figure 6.22).

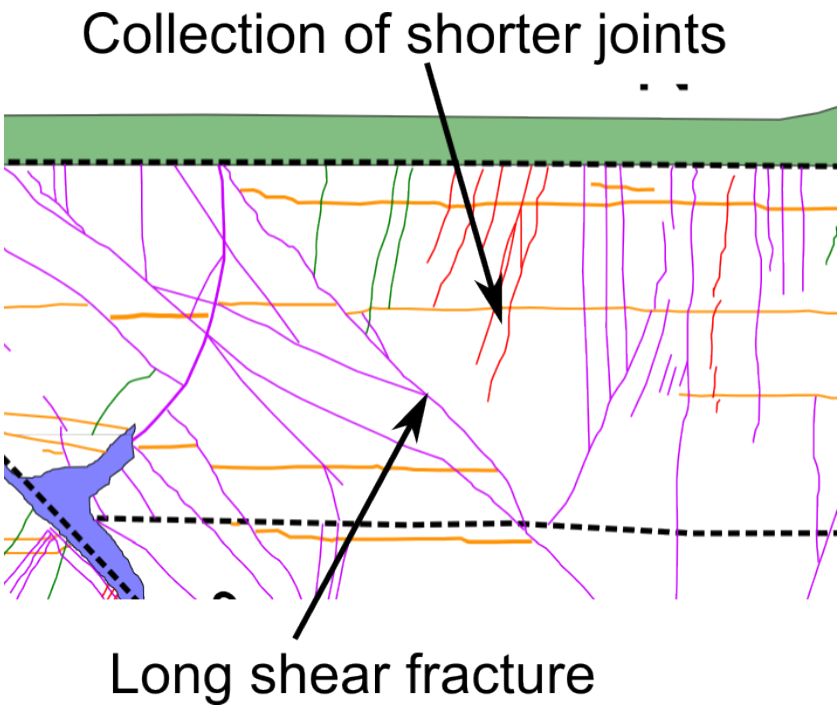

Figure 6.22: Upper section of northern area, showing a long well-connected shear fracture that was part of the network for FFE1. The collection of joints nearby which were part of the network for FFE2 (and some for both fluid flow episodes), in contrast show much less connectivity.

Density is usually considered one of the key influences on the connectivity (Odling et al. 1999) and therefore on bulk permeability of a fracture network, however due to the presence of the sandstone bands it is not the only influence connectivity in this field example. Feature connectivity (as described in section 6.4.6) was less influenced by fracture density then solely fracture connectivity was (chapter 5 section 5.3.4). Areas of low fracture density showed similar feature connectivity to areas of high fracture density. More importantly the majority of fractures showed two or more

permeable feature connections even in the areas of low fracture density. Having two or more connections is means that a feature will act as a conducting part of the fluid flow network, rather than features with only one connection which represent a dead end in a network. However in 3D these fractures may connect and not be dead ends.

As both structural and sedimentary features show evidence of being used by both fluid flow episodes it is clear the flow networks consisted of both the sedimentary and structural networks. This sedimentary-structural flow network behaviour means different properties have key influence over the flow networks compared to sedimentary or structural flow networks considered in isolation. E.g. in this field example fracture connectivity is not so vital as connectivity is boosted by presence of sandstone bands.

6.5.3 Temporal changes in fluid flow network: differences between fluid flow episodes.

The two fluid flow episodes utilised different subsections of the whole population of fluid flow-hosting features. The major differences in the flow networks across the field site and between the two fluid flow episodes are in the fractures utilised. The flow networks have differing fracture properties of density and orientation. The differences in the networks of the two fluid flow episodes also show how the fluid flow network evolved over time.

The faults are the largest structural features in the field site and have behaved as a conduit-barrier system during FFE1 but complete barrier during FFE2. As the largest features they may be the most influential over fluid flow. The calcite vein running alongside the brecciated core shows that during FFE1 the fault behaved as a conduit for fault-parallel fluid flow. However the lack of calcite cement between the brecciated clasts indicated that the fault also behaved as a barrier to fault-perpendicular fluid flow. The lack of any green halos around the fault structures indicated that faults behaved completely as a barrier during FFE1. This change

in behaviour would have had a profound affect on fluid flow within the mudstone. The faults are relatively long features that cut all the way through the mudstone from the bottom right to the top; potentially providing a single high permeability pathway bypassing the low permeability matrix of the mudstone. This could provide connections between higher permeability material (e.g. reservoirs) either side of the mud-dominated formations found on the Whitehouse Shore. However this high permeability pathway presented by the faults was not open for the entirety of its existence and was closed to fluid flow during or after FFE1. This would have meant that other more tortuous pathways would need to be used if fluid was to bypass the mudstone matrix by using a series of interconnected smaller features. Therefore the faults being open for FFE1 but closed for FFE2 is likely to result in large bulk permeability differences between the two fluid flow networks.

The differing flow network properties between the fluid flow episodes lead to FFE1 having fractures that are better connected to other permeable features, compared with FFE2. For FFE1 the Central and northern area show greatly enhanced fracture density compared with the southern area. Conversely for FFE2 only the central area shows enhanced fracture density, although the density values for FFE2 in the central area are much lower than for FFE1. This shows the importance of the fault in creating regions of certain fracture properties bounded by the faults. In addition to having relatively low density, the fractures for FFE2 are more orientated around one direction (NW-SE) than the fractured used during FFE1. This lower spread of orientations would mean the fractures used in FFE2 were less likely to intersect. These different networks were visualised by tracing out connected networks from the bottom to top of the red mudstone (figure 6.23) based on the flow map (figure 6.4). In FFE1 there are areas where extensive connected networks can be traced out, whereas for FFE2 the connected networks are much more meagre. Although the sandstone bands act to connect much more fractures to the network in FFE2 than would be the case if they weren't considered.

In the areas with low fracture density the flow networks are more likely to be reliant on the sandstone bands to create a connected network. This could still lead to

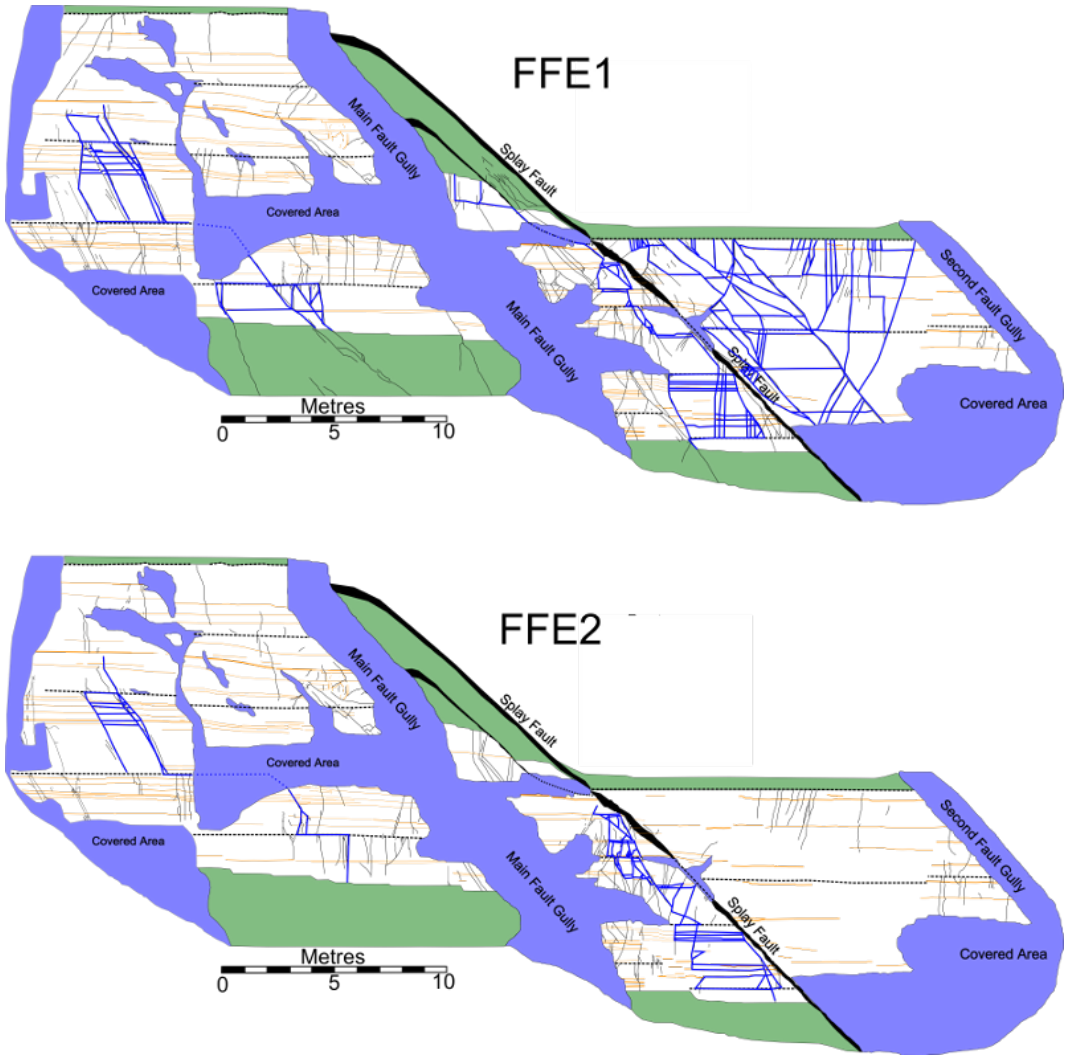

Figure 6.23: Blue lines show complete networks through the red mudstone. These networks were created by tracing out mapped connected features in the different field regions for FFE1 and FFE2.

significant differences in the resulting bulk permeabilities in the different areas of the field site and between the fluid flow episodes. These differences will be explored using numerical modelling in the following chapter.

6.5.4 Connectivity of fluid flow networks in three dimensions

The differences between fault and fracture populations in 1D, 2D, and 3D have been previously raised by a number of studies (Harris et al. 2003, Bonnet et al. 2001 Borgos et al. 2000, Odling et al. 1999, Marret and Allmendinger 1991). The main commercial driver for this research is from the petroleum industry as often data needs to be interpreted from 1D logs or 2D analogues into the 3D subsurface system of interest (Harris et al. 2003).

The field site in this study is a 2D window into a complicated 3D system of structural and sedimentary geological features. Previous studies have found that converting fault distributions into 3D from 2D is "non-trivial" (Harris et al. 2003), even from a single population of faults created by the same tectonic process. However in this field site there are thrusts that are created from a different stress field to the faults and fractures, in addition to the complication of the sandstone bands.

This study has emphasized the importance of connectivity to the fluid flow network. Harris et al. (2003) investigated the problem of the fluid flow properties of small faults surrounding seismically resolvable larger faults. They acknowledge the importance of connectivity to these fluid flow networks but, due to available subsurface data constraints, focus on influences on connectivity. These are: fault size distribution, fault density, and fault spatial distribution. Although it may not be within the scope of this project to provide a framework to convert the 2D connectivity results from section 6.4.6 to 3D, it is possible to use the understanding gained from the previous studies to make predictions about the nature of the 3D network of this field site.

The main difference of the 3D network to the 2D on this field site may be the connectivity between the thrusts and sandstone bands. In the 2D outcrop the sandstone bands and thrusts are sub-parallel to each other so there is no connection between them. However the thrusts dip towards the South East so would intersect (and offset) the sandstone bands, which dip almost vertically, providing connectivity not

observed on the outcrop.

The orientation data (section 6.4.5) shows the fractures are generally steeply dipping, but they are not dipping parallel to each other showing a range of dip directions. Closely spaced, but not connected fractures, could therefore be connected with the unexposed rocks. This would further increase the connectivity of the fracture-sandstone band connectivity network.

The two key points above suggest that the 2D connectivity of the field site is a underestimate of the true 3D connectivity of the system. However even in a 3D system there is likely to be relation to the observations made from the 2D outcrop. That is the faults bounding the central area would project into the rock maintaining that central area of raised fracture density, and therefore enhanced fracture-only connectivity.

6.6 References

Barton, C. A., Zoback, M. D. and Moos, D. 1995. Fluid flow along potentially active faults in crystalline rock. *Geology.* **v.**23 no.8. pp. 683-686.

Becker, S., Hilgers, C., Kukla, P. A. and Urai, J. L. 2011 Crack-seal microstructure evolution in bi-mineralic quartz-chlorite veins in shales and siltstones from the RWTH-1 well, Aachen, Germany. *Journal of Structural Geology.* v.**33**. pp. 696-689.

Beddoe-Stephens, B. 1980. *Uraniferous' Fish-eyes' in Upper Carboniferous Red Marls from Warwickshire.* Report no. 258, Applied Mineralogy Unit, Institute of Geological Sciences, London.

Berkowitz, B. 2002. Characterizing flow and transport in fracture geological media: A review. *Advances in Water Resources.* v.**25**. pp. 861-884.

Berkowitz, B., and Adler, P. M. 1998. Stereological analysis analysis of fracture network structure in geological formations. *Journal of Geophysical Research.*

1997;102(B8):18121-5.

Bonnet, E., Bour, O., Odling, N. E., Davy, P., Main, I., Cowie, P. and Berkowitz, B. 2001. Scaling of fracture systems in geological media. *Review of Geophysics*. v.**39**. pp. 347-383.

Borgos, H. G., Cowie, P. A. and Dawers, N. H. 2000. Practicalities of extrapolating one-dimensional fault and fracture size-frequency distributions to higher-dimensional samples. *Journal of Geophysical Research*. v.**105** no.**B12**. pp. 28,377-28,391.

Borradaile, G. J., Mackenzie, A. and Jensen, E. 1991. A study of colour changes in purple-green slate by petrological and rock-magnetic methods. *Tectonophysics*. v.**200** i.**1-3**. pp. 157-172.

Cox, S. F. and Etheridge, M. A. 1983. Crack-seal fibre growth mechanisms and their significance in the development of orientated layer silicate microstructures. *Tectonophysics*. v.**92**. pp. 147-170.

Eichhubl, P., Taylor, W. L., Pollard, D. D., Aydin, A. 2004. Paleo-fluid and deformation in the Aztec Sandstone at the Valley of Fire, Nevada — Evidence for the coupling of hydrogeologic, diagenetic, and tectonic processes. *GSA Bulletin*. v.**116**. p. 1120 - 1136.

Eichhubl, P., Davatzes, N. C. and Becker, S. P. 2009. Structural and diagenetic control of fluid migration and cementation along Moab fault, Utah. *AAPG Bulletin*. v.**95** i.**5**. pp. 653-681.

Fairley, J.P. and Hinds, J.J. 2004. Rapid transport pathways for geothermal fluids in an active Great Basin fault zone. *Geology*. v.**32**. pp. 825-828.

Fick, A. 1855. Ueber Diffusion. *Annalen der Physik*. v.**170** i.**1**. pp. 59-86.

Fleischmann, K. H. 1993. Shallow fluid pressure transients caused be seismogenic normal faults. *Geophysical Research Letters*. v.**20** i.**20**. pp. 2163-2166.

Harris, S. D., McAllister, E., Knipe, R. J. and Odling, N. E. 2003. Predicting the three-dimensional population characteristics of fault zones: a study using stochastic models. *Journal of Structural Geology*. **25**. pp. 1281-1291.

Jaeger, J. C. and Cook, N. G. W. 1979. Fundamentals of rock mechanics (fourth edition): New York, Chapman and Hall. pp. 28-30.

Losh, S., Eglington, L., Schoell, M. and Wood, J., 1999, Vertical and lateral fluid flow related to a large growth fault, South Eugene Island Block 330 field, offshore Louisiana. *AAPG Bulletin*. v.**83**. pp. 244-276.

Marret, R. and Allmendinger, R. 1991. Estimates of strain due to brittle faulting: Sampling of fault populations. *Journal of Structural Geology*. **13**. pp. 735-738.

Mauldon, M., Dunne, W. M. and Rohrbaugh Jr., M. B., 2000, Circular scanlines and circular windows: new tools for characterizing the geometry of fracture traces, *Journal of Structural Geology*, **Vol. 23**, pp. 247-258.

Mykura, H. and Hampton, B. P. 1984. On the mechanism of formation of reduction spots in the carboniferous/permian red beds of Warickshire. *Geological Magazine*. v.**121** i.*1*. pp 71-74.

Odling, N. E., Gillespie, P., Bourgine, B., Castaing, C. Chiles, J-P., Christensen, N. P., Fillion, E., Genter, A., Olsen, C., THrane, L. Trice, R. Aarseth, E. Walsh, J. J. and Watterson, J. 1999. Variations in fracture system geometry and their implications for fluid flow in fractured hydrocarbon reservoirs. *Petroleum Geoscience*. v.**5**. pp. 373-384.

Rohrbaugh, M. B., Dunne, W. M. and Maulton, M. 2002. Estimating fracture trace intensity, density, and mean length using circular scan lines and windows. *AAPG Bulletin*. v.**86**. no.**12**. pp. 2089-2104.

Rowland, J.C., Manga, M. and Rose, T.P. 2008. The influence of poorly interconnected fault zone flow paths on spring geochemistry. *Geofluids*. v.**8** i.**2**. pp. 93-101.

Stang, A., Poole, C. and Kuss, O. 2010. The ongoing tyranny of statistical significance testing in biomedical research. *European Journal of Epidemiology.* v.**25** i.**4**. pp. 225-230.

Talbot, C. J. and Sirat, M. Stress control of hydraulic conductivity in fracture-saturated Swedish bedrock. *Engineering Geology.* v.**61**. pp. 145-153.

Younger, P. L. and Manning, D. A. C. 2010. Hyper-permeable granite: lessons from test-pumping in the Eastgate Geothermal Borehole, Weardale, UK. *Quarterly Journal of Engineering Geology and Hydrogeology* v.**43** i.**1**. pp. 5-10.

Chapter 7

Modelling palaeo-fluid flow episodes

> "I never satisfy myself until I can make a . . . model of a thing" – William Thomson

7.1 Introduction

7.1.1 Aims of the modelling

The main aim of the modelling is to improve understanding of palaeo-fluid flow within the red mudstone and how it was influenced by different rock and fracture properties. This will help to answer some fundamental questions about the hydraulic properties of the mudstone, such as:

Which features controlled fluid flow within the red mudstone?

Did the controls on fluid flow change between the two fluid flow episodes?

Which other features contributed significantly to the fluid flow properties?

Did the differing fracture properties in the three fault bounded areas lead to significant variations in fluid flow behaviour?

Insights to the answers to these questions will be achieved by simulating the palaeo-fluid flow episodes through the mudstone.

This chapter begins with a brief discussion about how different modelling methods currently used for subsurface fluid flow investigations and which method will be used for the models presented in this chapter (sections 7.1.2 and 7.1.3). Then the method for creating the models is described, along with the various assumptions that were required (section 7.1.4). The results of the modelling are then presented (section 7.2). How the results answer the previous questions is then discussed (section 7.3) along with discussion about the variations in fluid flow behaviour across the field site.

7.1.2 Background information to the modelling approach

There are several packages and techniques available for representing faults in reservoir flow simulations. Some methods focus on the permeability properties that control across fault flow attempting to predict locations of hydrocarbon columns in the subsurface (Manzocchi et al. 1999, Yielding et al. 1997). Other models are of mechanical rock properties with strain indicated by seismically resolvable faults to constrain areas of varying fracture properties (Dee et al. 2007). This mechanical based approach may be useful for the Girvan field site, where areas of high fracture density are spatially correlated with the faults implying the possibility of mechanical control of the faults over fracture formation. However these types of models are designed to predict where the areas of fracturing are, this study has been able to locate these areas and is aiming to model their fluid flow behaviour.

One of the main issues with large reservoir models (mentioned above) is the gap be-

tween fine scale (centimetres) borehole data and coarse scale (>10s of metres) seismic data. Outcrop studies, such as this, provide these missing scales of information, albeit as analogues to the subsurface. Modelling rock at this scale has previously been attempted using several different approaches. Two common approaches are Discrete Fracture Network (DFN) and Dual Porosity Dual Permeability (DPDP). DFN does not consider the matrix in the model as it is assumed to be only the fractures which transmit fluid flow so would be difficult to use this approach to model complicated sedimentary and fracture interaction as found at the field site.

The previous chapters investigated the influence of permeable feature connectivity on the fluid flow system within the mudstone. This is important because a connected network (of high permeability features) is necessary to bypass the low permeability mudstone. Percolation theory (introduced in section 2.3) has previously been applied to investigate how fracture networks connect and hence their permeability (de Dreuzy et al. 2001, Renshaw 1999). Berkowitz (1995) used power law fracture size and random orientation distribution of fractures to model when a critical threshold was reached in a fracture network. This critical threshold is when all boundaries of the model are connected through a fracture network. Similar approaches were later used by de Dreuzy et al. (2001) and Renshaw (1999). Manzocchi (2002) further improved this percolation approach to fracture networks by creating fracture networks with constraints on their orientation and propagation; creating a much more "life-like" fracture network. In this study a percolation theory approach could investigate how the introduction of sandstone bands reduces the fracture density required to reach the critical threshold of connectivity. Such an approach is discussed in future work (section 9.2).

The field outcrop in this study is essentially a 2D cross-section of the 3D rock mass. The fluid flow models, in this chapter, will reflect these dimensions and will also be 2D. This could lead to connectivity between the features being underestimated as the fractures create 3D systems (Odling 2001). Underestimation is due to the features extending into the outcrop, where they cannot be observed, and they may well intersect when they appear as unconnected on the outcrop (further explained

in section 6.5.4).

It is necessary to have a model that accurately incorporates the properties of the mapped mudstone, sandstone bands, and structural features (thrusts, fractures, and faults). Lunn et al. 2008 have previously converted field maps of geological fluid flow features into 2D flow models, to aid prediction of the fluid flow properties of sub-seismic features. A similar method will be employed in this study to achieve fluid flow models from the mapped field area. The field maps can be used because they are accurate enough representations of the outcrop, due to the extensive field mapping and ground-truthing to create the maps. These maps will therefore provide an ideal base to create a flow model to be representative of the palaeo-fluid flow episodes. Such groundwater flow modelling will allow the identification of key features to fluid flow and determine how fluid travels through the connected sandstone band-fracture network.

7.1.3 Choice of software

MODFLOW, developed by the USGS, has been used to simulate the fluid flow in the models (Harbaugh 2005). It was developed by the USGS to solve groundwater flow problems and has been used for a variety of purposes throughout its development.

Mflab (developed by Theo Olstroom at Delft University of Technology) has been used to apply MODFLOW. Mflab uses a series of MATLAB scripts and excel files to execute modelling processes with MODFLOW. One of the main reasons for using mflab is the field maps can be simply converted into input files. This allows direct transfer of the model of the features of a field site to a model of fluid flow through those features. This modelling approach also allows different permeabilities to be assigned to each modelled features, creating flexibility of the hydraulic behaviour of the features.

MODFLOW has previously been used to model fractured mudstone. However previous approaches do not explicitly represent the fractures but incorporate the fractures

into upscaled permeability of the mudstone (e.g. Dennis et al. 2010, Myers 2012). Another approach has been to run DFN models alongside MODFLOW groundwater flow models to compare the results (Chapman et al. 2013). This approach in this study uses MODFLOW to explicitly represent the different features of the fluid flow networks (i.e. faults, fractures, and sandstone bands). Literature searches indicate MODFLOW may not have been used previously in this way.

7.1.4 Modelling method

The models are based on conventions of Darcian fluid flow through porous media. Darcy flow is applied to rock that allows flow through inter-granular pores, such as sandstone. This fluid flow law was developed by Henry Darcy in the 1850s using a series of column experiments in sand, from which were produced a series of equations governing fluid flow. One of which is used to calculate flow in the models (Darcy 1856).

$$Q = -KA\frac{(P_b - P_a)}{L}) \tag{7.1}$$

where Q is discharge (volume/time), K is hydraulic conductivity (distance/time), A is cross-sectional area, P_b-P_a/L is change of head with time. Equation 7.1 shows that flow through a system is based on how large that system is, how well it transmits fluid, and the pressure gradient across the system. The modelling presented in this chapter focuses on how well the system transmits the fluid from one side of the model to the other. The areas modelled are chosen as representative to attempt to simulate the general flow behaviour through the mudstone. One disadvantage is the lack of 3D information for the model, where connections and features that may have had a large influence over the real 3D flow network cannot be modelled in such a 2D representation.

The inputs to the fluid flow model are converted versions of the detailed field maps presented in previous chapters. This conversion process is described in the following section 7.1.5.

The outputs of the model are mapped streamlines (figure 7.1), hydraulic-head, and a calculated bulk permeability. The streamlines can be thought of as visually representing the pathways of fluid flow through the model. The gap between streamlines represents proportionally how much flow there is in that area. For example, if there were one hundred streamlines flowing from one side of the model to the other, then between each pair of streamlines would be 1% of the flow. The streamlines therefore can be used to determine the controls on fluid flow as any feature which has a large number of streamlines within it is acting to concentrate the flow. That is, larger fluxes are acting where the stream lines are closely spaced. The head gradient outputs show the areas of the models that are more hydraulically linked, and therefore where the main barriers to fluid flow are (figure 7.2).

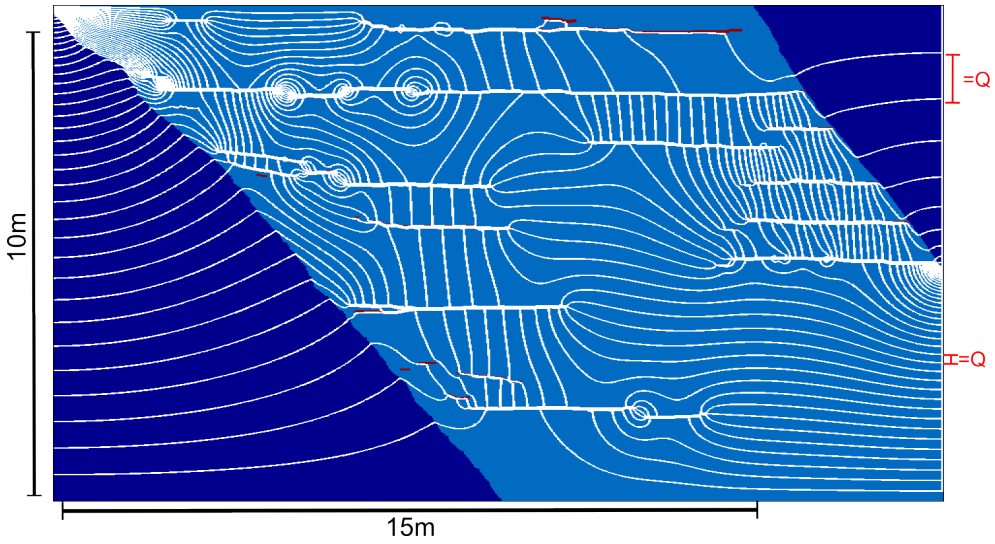

Figure 7.1: Streamlines flowing from left to right in model output. Streamlines are concentrated in the high permeability areas then spread out in the low permeability mudstone. The labels on the right of the model show how the space between each pair of streamlines represents a fixed area of fluid being drained. The higher density of streamlines in the light blue section represents higher flow rates than the dark blue section above.

Bulk permeability is calculated in these MODFLOW models using equation 7.2 (Harbough 2005).

$$k = \frac{K\mu}{\rho g} \tag{7.2}$$

Where K is hydraulic conductivity (m/s), μ is fluid viscosity, ρ is fluid density, and g is gravity. In the models μ, ρ and g are all constant. So bulk permeability completely reflects changes in the hydraulic conductivity of the different features in the model.

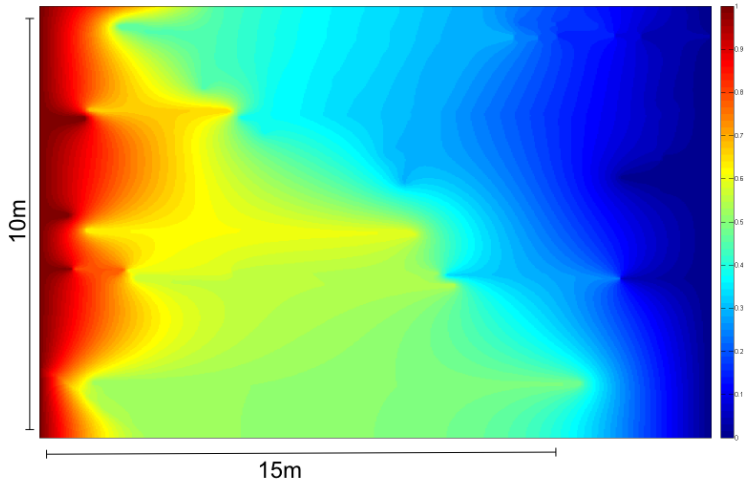

Figure 7.2: Hydraulic-head distribution in the model output. Head is set it at 1m on left boundary and at 0m on right boundary, top and bottom boundarys are set at no-flow. With no permeable features there would be a steady transition from read to blue, but the permeable features distort the head gradient.

The different rock types and features on the site were all assigned a representative permeability. These representative permeabilities were developed with a literature review of comparable rock types. Although permeability of rock samples can be tested in the laboratory using techniques such as steady state gas and liquid parameters, such tests were not done for this study as the timings of the fluid flow in relation to burial history have not been constrained. Therefore permeability changes, subsequent to the fluid flow episodes, caused by burial, uplift and in particular weathering processes (discussed in section 4.5.3) would be difficult to compensate for hampering the ability of these sophisticated tests to give an accurate result of properties during the palaeo-fluid flow episodes.

The input maps are made of a grid of individual pixels. Each of these pixels is a

1x1cm square and is assigned an isotropic permeability depending on what rock type or feature it contains. The assigned permeabilities attempt to accurately represent the fluid flow conduit features and their networks within the mudstone. So as the fluid flow evidence shows fractures and sandstone bands acted to concentrate the fluid flow then the pixels representing these features should have significantly higher permeabilities than the mudstone. Previous modelling work (J. Ma and G. Couples personal communication) has found that permeability of different modelled features need not differ by more than 3 orders of magnitude. As at this difference flow is essentially dominated by the higher permeability network.

Pixels containing only mudstone have been assigned a permeability of 10^{-3}milliDarcys (mD). The permeabilities of mudstone and shale can vary over several orders of magnitude, between 10^{-6} to 10^{-2}mD (Todd and Mayes 2005, Dewhurst and Siggins 2006, Yang and Aplin 2007). Whether a mudstone is at the higher end of this range is heavily influenced by the clay fraction of the rock (Yang and Aplin 2010). The representative permeabilities of the mudstone pixels have been based on studies of core samples of intact mudstone analysed in the laboratory. Well tests can also give information about the permeability of a mudstone formation, but fractures can influence the results of these tests giving results that are a mixture of intact and fractured rock; so would not be appropriate to form the basis for these mudstone pixel permeabilities. Mudstone and shale have been found to be anisotropic, with higher bedding-parallel permeability (Armitage et al. 2011) due to fabric properties introduced by depositional and deformational processes (Day-Sirrat et al. 2010, Josh et al. 2012). This permeability anisotropy can be estimated from observing laminations in the microfabrics (Josh et al. 2012), where a more laminated mudstone generally will have greater permeability anisotropy. No laminations were observed under thin sections of mudstone samples from the field site. Therefore any permeability anisotropy of this mudstone is likely to be low, so the mudstone has been assumed to be isotropic to avoid increasing the model complexity. Any anisotropy of the formation is more likely to be controlled by the sandstone bands.

Pixels containing sandstone bands have been assigned a permeability of 1mD. Per-

meability of sandstone has previously been measured over a range of 10^{-3} to over 10^2mD (Todd and Mayes 2005, Perera et al. 2011, Tuechmantel et al. 2012). Generally in reservoir analysis sandstones are considered lower permeability or tight if they are 1mD or below and higher permeability if above 1mD (Spencer 1989). The permeability of sandstone can be affected by several factors such as sorting (Masch and Denny 1966) or degree of cementation Waldschmidt 1941, Heald 1956, Hawkins 1978). The sandstone bands are poorly sorted so are likely to be at the lower end of the permeability range. However the evidence from the field site indicates that the sandstone bands did act as fluid flow conduits so must have had permeabilities higher than that of the surrounding mudstone. The pixels representing these smaller sandstone bands would really be a mixture of sandstone and mudstone. Therefore due to the range of sandstone band thicknesses, then different sandstone bands will have been modelled at different permeabilities. This is because a 1mm sandstone band would be 10% of the pixel but a 5mm sandstone band would be 50% of the pixel, so the sandstone/mudstone ratio would be different but the pixels modelled as the same permeability. As a result of this the individual sandstone bands are best described as being modelled as a range of between 1 through 5 mD; both of these values are within the ranges quoted in past studies (Todd and Mayes 2005, Perera et al. 2011, Tuechmantel et al. 2012).

Pixels containing fractures have been assigned a permeability of 10^2mD. Fractured rock can have permeability ranges between 1 and over 10^3mD (Todd and Mayes 2005, Ishii et al 2011, Manda et al. 2012). Additionally the presence of a joint in a rock sample can increase the permeability of that sample by five to ten orders of magnitude (Wong et al. 2013). The pixels that contain a fracture in the field mapping models are five orders of magnitude higher permeability than the unfractured mudstone; at the conservative end of any expected increase in permeability. Fractures in this model are treated as very high permeability matrix, rather than incorporating Navier-Stokes equations to solve fracture flow or creating a Dual Porosity Dual Permeability model. This approach is to keep the model simple while still keeping a reasonably accurate portrayal of the fluid flow system. All fractures were assigned the same permeability, so have been assumed to be identical and constant aperture.

Fracture permeability is strongly dependent on the aperture of the fracture (equations 7.3); with fracture permeability rising sharply with aperture increase due to a cubic relationship. However fracture aperture is very difficult to measure in the field and will probably not be representative of the fracture aperture at depth anyway. Therefore a series of calculations were used to arrive at a possible representative permeability value for pixels containing a fracture; based on assumed fracture apertures. Equation 7.3 is used to approximate the permeability in a single fracture (Lomize 1951, Polubarinova-Kochina 1962, Snow 1965). This assumes that the fracture consists of two parallel sides, the controlling factor in fracture permeability is the aperture of the fracture (ω).

$$fracturepermeability(k_{frac}) = \frac{\omega^2}{12} \tag{7.3}$$

The fracture permeability found for a particular aperture in equation 7.3 can be put into equation 7.4 to find the average permeability for a pixel containing a fracture. Where $k_{mudstone}$ is 0.001 mD, and a is aperture of fracture and b is width of pixel (figure 7.3).

$$k_{pixel} = \frac{k_{mudstone}(b-a) + k_{frac}(a)}{b} \tag{7.4}$$

A fracture aperture of 0.05mm gives a final pixel permeability of 104mD, whereas a fracture aperture of 0.1mm gives a pixel permeability of 830mD. In all of the following simulations, a pixel containing a fracture is assigned a permeability of 100 mD, which is 5 orders of magnitude greater than the surrounding mudstone, and corresponds to a fracture aperture of approximately 0.05mm. As mentioned previously, any greater difference in permeability of the fractures would be unlikely to create noticeably different model results.

Pixels containing thrusts have been assigned a permeability of 1mD. Thrusts are structural features creating discontinuities in the mudstone similar to fractures, so why the difference in assigned permeability? Where exposed, the thrusts are filled

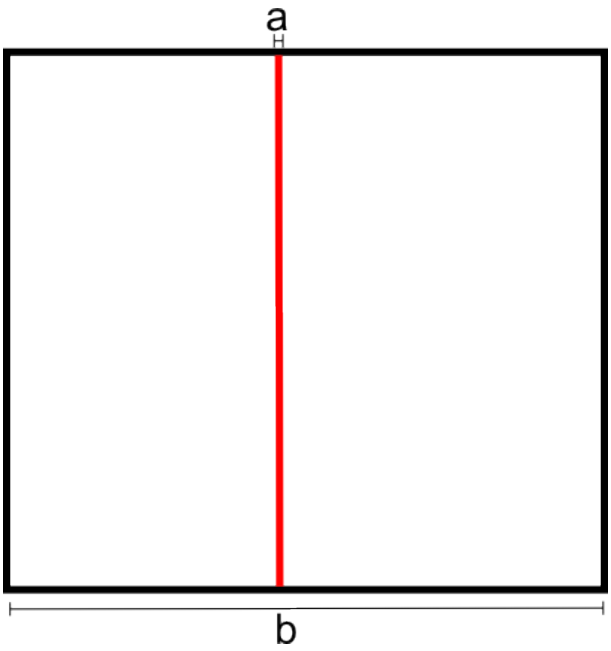

Figure 7.3: Cartoon of single pixel containing a fracture (red line) through mudstone. a is the fracture aperture and b is the width of the pixel.

with approximately one centimetre of breccia whereas the fractures are simple planar features with no fill between the sides (discounting the calcite). Due to the difficulties in obtaining samples of fault breccia there are no permeability values found that could be taken as representative of the thrusts on the field site.

Arguably any of these values (summarised in table 7.1) could be set higher or lower and still be within ranges reported in previous studies. However, the critical issue for understanding the fluid flow behaviour at this site (and hence the importance of collecting one data set versus another within a site investigation campaign) is having the correct relative permeabilities of groups of features compared to other groups of features from the field site. Hence, these values have been selected based on the palaeo-evidence for flow channelling and are suitable for addressing the questions raised in section 7.1.1 on the aims of the modelling. Table 7.1 shows a greater permeability difference (between the mudstone and fractures) than is suggested necessary by J. Ma and G. Couples (personal communication) for fluid flow network modelling. Such a large permeability spread was necessary to incorporate the mid-

Feature	Feature permeability (mD)	Pixel permeability
Mudstone	0.001	0.001
Sandstone band	1-5	1
Fractures and faults	83,000+	100
Thrust	??	1

Table 7.1: Permeability values of the features included in the flow modelling, and their input value to pixels containing that particular feature. How the values for the four features types were derived is explained further on in this section.

permeability features (sandstone bands and thrusts) into the model. Section 7.2.4 explores how changing these values affects the model behaviour and results.

7.1.5 Converting the maps into fluid flow model inputs

Sample areas of detailed field maps, presented in previous chapters, have been converted into input maps for MODFLOW (figure 7.4).

First the field maps were converted from the working vector graphics format into gifs. Fixed colours on the input map are essential as each colour is assigned a specific permeability value. The gif format was used for the fixed colour pallet, allowing security that complementary features (e.g. two calcite filled fractures) were exactly the same colour.

The next stage was to interpret the features into the covered areas. Without this additional interpretation the connectivity of the features would likely be underestimated in the model, leading to inaccurate results. Interpretation was derived from consistent observations of other similar features where they were fully exposed in the field. Thrusts and sandstone bands were assumed to be extensive so were continued until intersection with a fault or the map boundary. Joints and shear fractures that propagate into a covered area were assumed to continue until intersection with an interpreted thrust. Shear fractures were also interpreted in the covered area from

anomalous offsets in sandstone bands, and debris filled gullies that are orientated similar to the preferential orientations of shear fractures. In figure 7.4 the corners of the sample areas for the Northern, Central, and Southern areas can be seen to extend beyond the bounding faults of the area they are sampling. To focus the modeled fluid flow into the area of interest the pixels outside of the bounding faults were set as one magnitude lower permeability than the mudstone. However only the central area model has a sizeable fraction outside the area of interest.

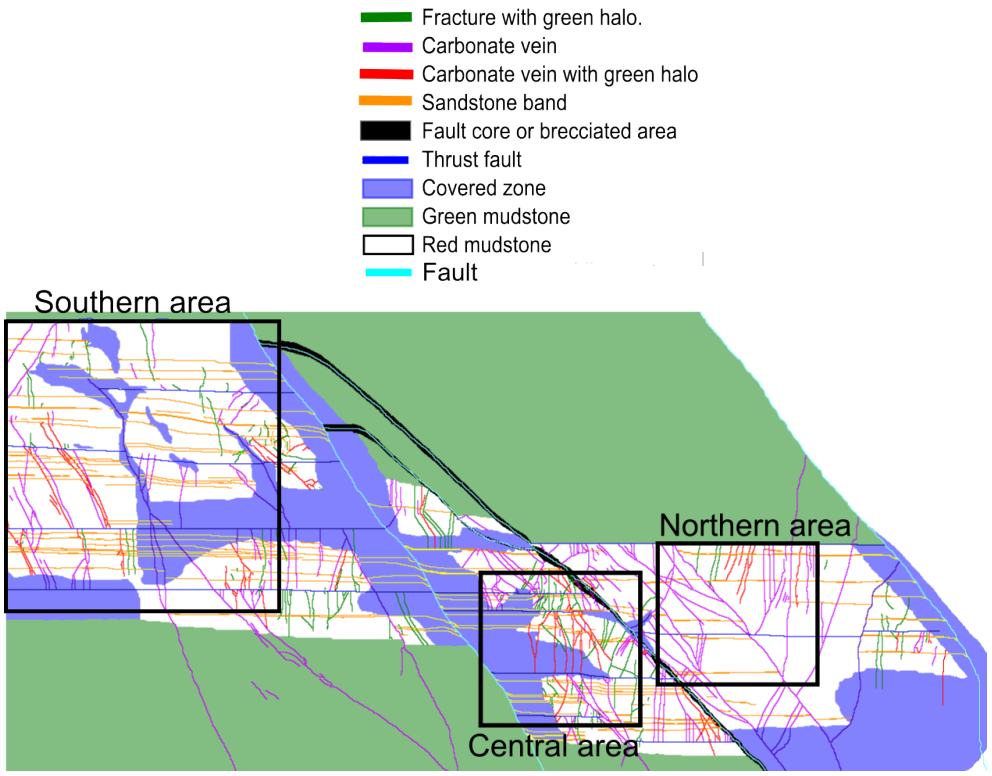

Figure 7.4: Input map for the model of the whole field area, showing interpretations of features into the covered area. Black boxes show the locations of modeled areas in section 7.2 .

7.2 Results

The three fault bounded areas (southern, central, and northern areas) have been modelled separately. This allows construction of detailed models and exploration of the effects of the different distributions of fluid flow conduits in the three field area has on bulk permeability. For each field area three different scenarios will be modelled for both fluid flow episodes and again for x direction and y direction head gradients. For x-direction head gradient then the top and bottom boundary are set as no flow. For y-direction head gradient then the left and right boundary are set as no flow. The three scenarios are as follows: one scenario only includes sedimentary features, one scenario only considers structural features, and the final scenario includes both sedimentary and structural features. The sedimentary and structural features are modelled separately to allow insights to be gained about how each sets of features influences fluid flow in isolation compared with their combined affects. This will provide further information about how the connectivity properties influence the fluid flow networks.

The outputs from the model are presented as tables showing the modeled bulk permeability for each scenario, and the permeability enhancement. The permeability enhancement is how many times the bulk permeability is beyond that if only mudstone was included in the model. This was done as it allowed more intuitive comparison between the different scenarios; with numbers being between 1 and 526 rather than 0.00088 and 0.51. The other outputs are the streamline maps, shown for each scenario model for the southern, central and northern area.

It should be noted that all streamline model outputs (figures 7.6, 7.7, 7.10, 7.11, 7.14, and 7.15) all have 100 streamlines. However the models with well developed flow networks looks like they have fewer streamlines, due to the amount of the streamlines concentrated within the fracture and sandstone band fluid flow conduits.

7.2.1 Southern area

The model domain of the southern area is shown in figure 7.5. The results are shown as a table summarising the modelled bulk permeabilities in y-direction and x-direction flow (tables 7.2 and 7.3) and modelled streamlines (figures 7.6 and 7.7).

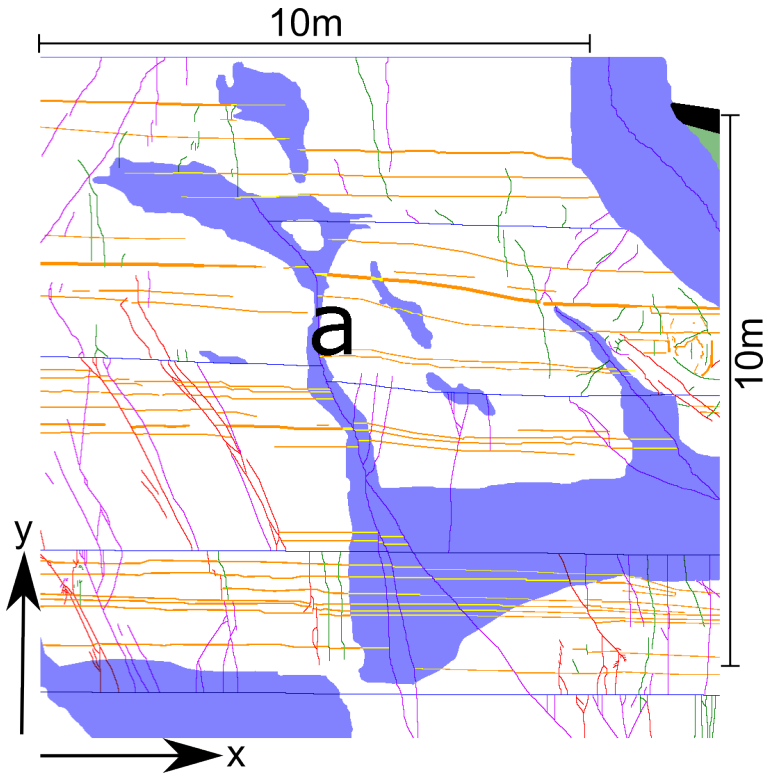

Figure 7.5: Southern area model domain, see figure 7.4 for the location of this domain within the whole field map.

The modelled bulk permeabilities for FFE1 are higher than those for FFE2, in the "structural only" and "all features" scenarios (tables 7.2 and 7.3). FFE1 bulk permeability is more than double that of FFE2 in the "all features" scenarios for both y-direction and x-direction flow. The concentration of streamlines in the long central fracture (labelled a in figure 7.5) can be seen in figure 7.6-1b and 1c, this features was open to fluid flow in FFE1 and not FFE2. This fracture is well orientated for y-direction flow as it almost connects the top and bottom of the model. However in the x-direction flow it acts as a vital connection between the sandstone bands and thrusts

y-direction flow	Bulk permeability (mD)	Permeability enhancement
Sedimentary features FFE1/FFE2	0.001	1.0
Structural features FFE1	0.006	6.0
Structural features FFE2	0.002	2.0
All features FFE1	0.014	14
All features FFE2	0.004	4.0

Table 7.2: Summary of bulk permeability and permeability enhancement of each of the modelling scenarios of the southern area in y-direction flow.

while the sandstone bands and thrusts provide the well orientated fluid flow conduits in these scenarios. The results show a good representation of what the fluid flow pathways may have been, as the streamlines (and therefore the majority of flux) is focussed into the high permeability features. The models show several gaps between the high permeability features which is likely a result of modelling a 3D system in 2D, where the connections between high permeability features may be hidden. However the results still provide useful comparisons of the bulk permeabilities of the different scenarios.

The structural features are more influential in y-direction flow and the sedimentary features in x-direction flow. This is determined by structural features having a larger enhancement of permeability for y-direction while the sedimentary features have larger permeability enhancement for x-direction flow. These effects area as expected as they are due to the different orientations of the sedimentary and structural features; that is the sandstone bands well orientated to the x-direction flow and the structural features to the y-direction flow. However in the combined model these two networks combine to form one network providing conduits in both directions.

x-direction flow	Bulk permeability (mD)	Permeability enhancement
Sedimentary features FFE1/FFE2	0.008	8.0
Structural features FFE1	0.007	7.0
Structural features FFE2	0.004	4.0
All features FFE1	0.040	40
All features FFE2	0.015	13

Table 7.3: Summary of bulk permeability and permeability enhancement of each of the modelling scenarios of the southern area in x-direction flow.

Distributions of head are shown in figure 7.8 for the all features scenarios for y-direction and x-direction models of FFE1 and FFE2. These are the head outputs for the models that produced the streamlines shown in figures 7.6-1c and 2c, and 7.6-1c and 2c.

In the y-direction scenarios FFE1 shows two distinct hydraulic zones, the boundary between these is where in figure 7.6-1c the streamlines can be seen to flow through the mudstone rather than the fracture-sandstone band network. In contrast FFE2 y-direction shows a more gradual head gradient across the model.

The head gradient distributions for the two x-direction scenarios are much more similar than for the y-direction. This reflects the larger influence of the sandstone bands and thrusts in the x-direction, meaning that there is less difference in the networks between FFE1 and FFE2.

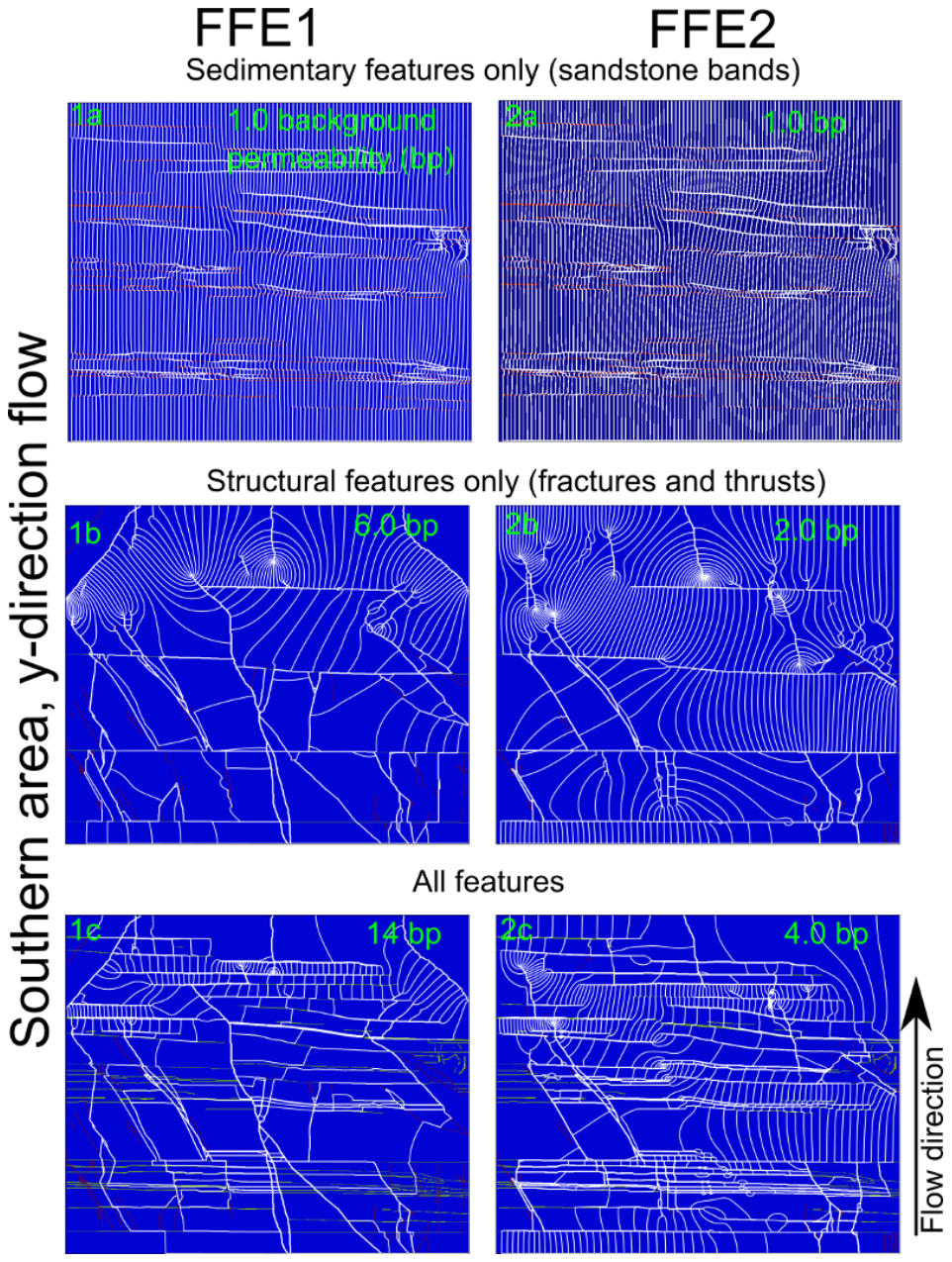

Figure 7.6: Streamlines for modelling scenarios of y-direction flow in a sample domain of the southern area. FFE1 models on the left FFE2 on the right. 1a and 2a are only sedimentary features, 1b and 2b only structural features, 1c and 2c are the entire flow network. bp in the streamline outputs refers to the permeability enhancement as show in tables 7.2 and 7.2.

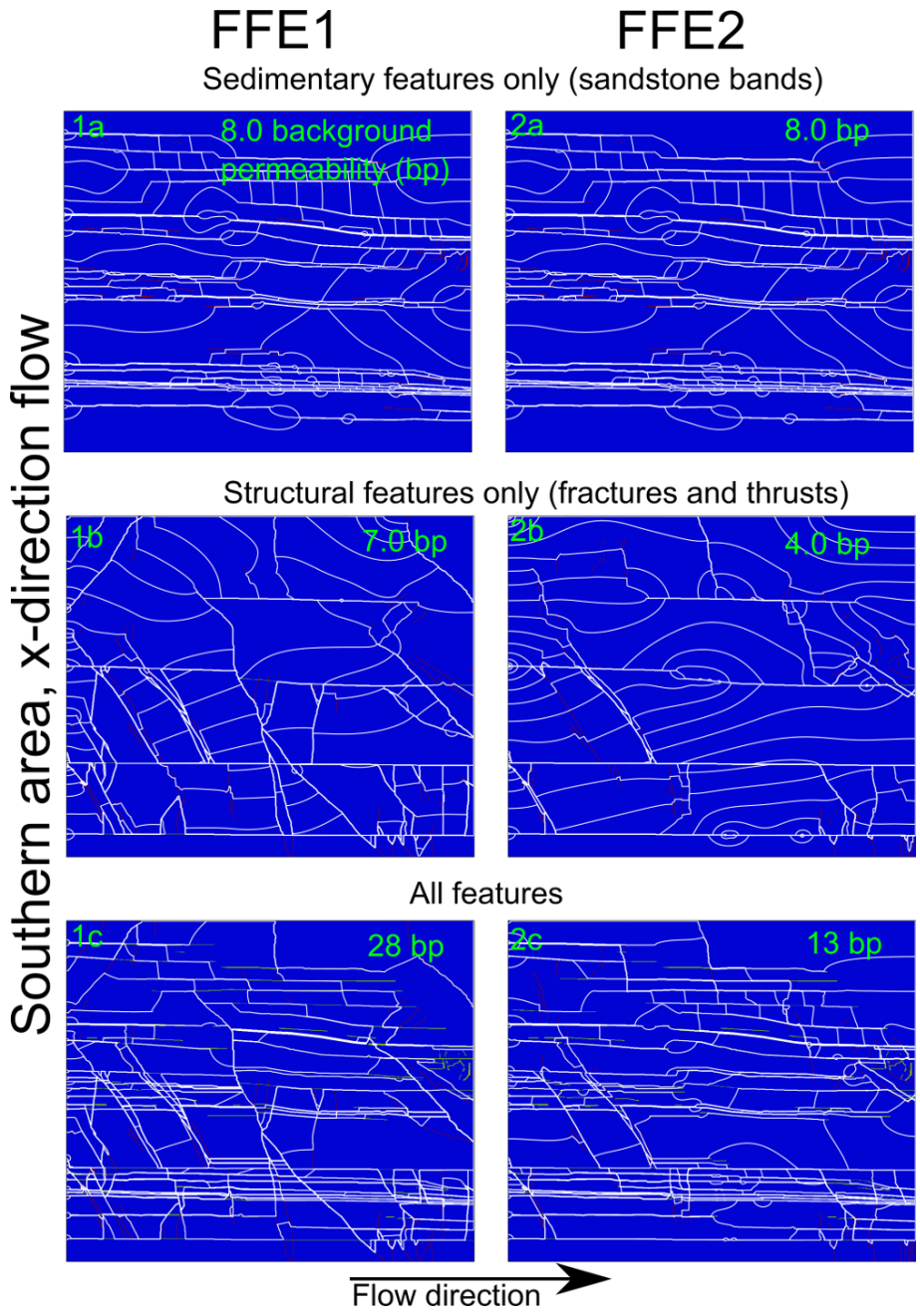

Figure 7.7: Streamlines for modelling scenarios of x-direction flow in a sample domain of the southern area. FFE1 models on the left FFE2 on the right. 1a and 2a are only sedimentary features, 1b and 2b only structural features, 1c and 2c are the entire flow network.

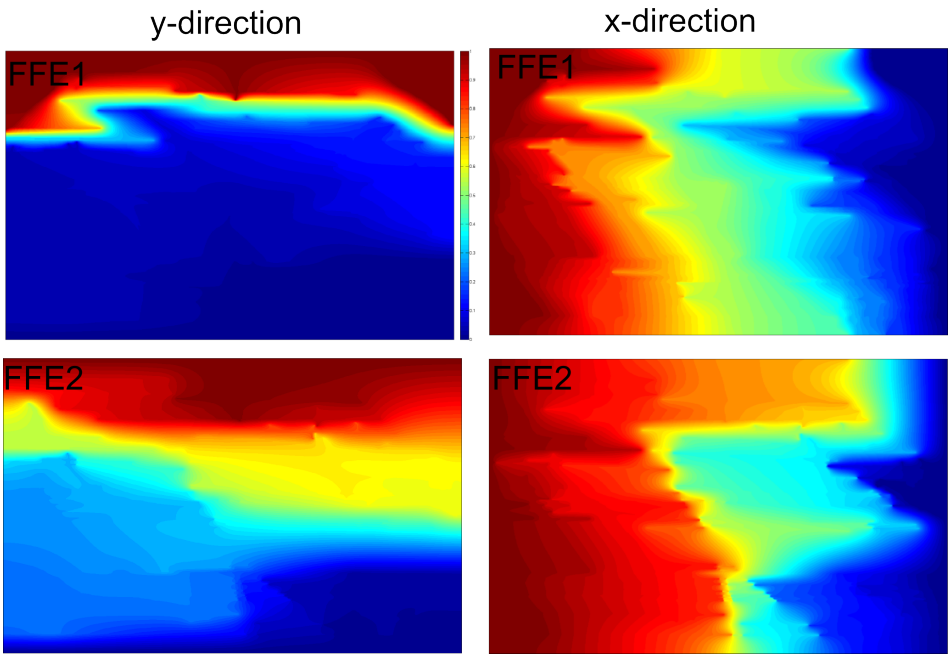

Figure 7.8: Head gradient for "all features" modelling scenarios of southern area.

7.2.2 Central area

The model domain of the central area is shown in figure 7.9. The grey area on either side of the model are outwith the central area. So were given permeabilities one order of magnitude below mudstone to ensure they had minimal influence over the modeled fluid flow.

For y-direction flow in the central area models, the bulk permeabilities are similar between the two fluid flow episodes (figures 7.4 and 7.10). With FFE1 being approximately 20% high than that of FFE2 for the "structural only" and "all features" scenarios. However for x-direction flow the relationships are more complicated (figures 7.5 and 7.11). With FFE1 being three times the bulk permeability of FFE2 when only the structural features are considered, but when the full flow network is considered (figure 7.11-1c and 2c) the values are very similar.

The influence of the fractures means that the models in the y-direction have more than double the bulk permeabilities of the models in the x-direction. This is due to

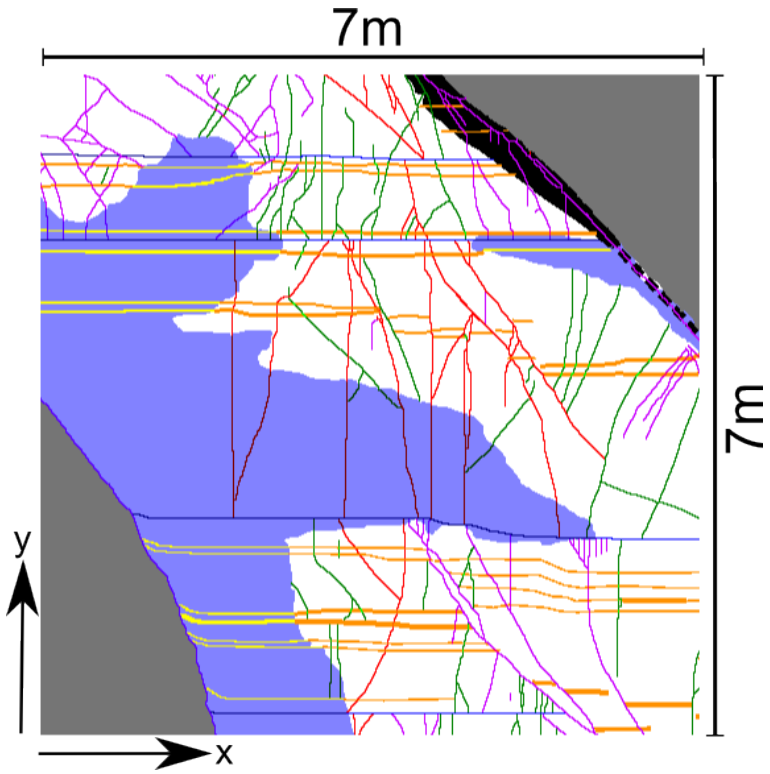

Figure 7.9: Model domain of the central area. See figure 7.4 for location of model domain in relation to whole field map.

the fractures creating a well connected high permeability flow paths from the bottom to the top of the model, with connectivity enhanced by the sandstone bands. The high density of fractures utilised by both fluid flow episodes in the central area means this well connected network exists for both FFE1 and FFE2.

y-direction flow	Bulk permeability (mD)	Permeability enhancement
Sedimentary features FFE1/FFE2	0.00088	1.1
Structural features FFE1	0.1	127
Structural features FFE2	0.08	101
All features FFE1	0.13	165
All features FFE2	0.11	139

Table 7.4: Summary of bulk permeability and permeability enhancement of each of the modelling scenarios of the central area in y-direction flow.

x-direction flow	Bulk permeability (mD)	Permeability enhancement
Sedimentary features FFE1/FFE2	0.003	4.1
Structural features FFE1	0.022	30
Structural features FFE2	0.008	11
All features FFE1	0.047	64
All features FFE2	0.049	67

Table 7.5: Summary of bulk permeability and permeability enhancement of each of the modelling scenarios of the central area in x-direction flow.

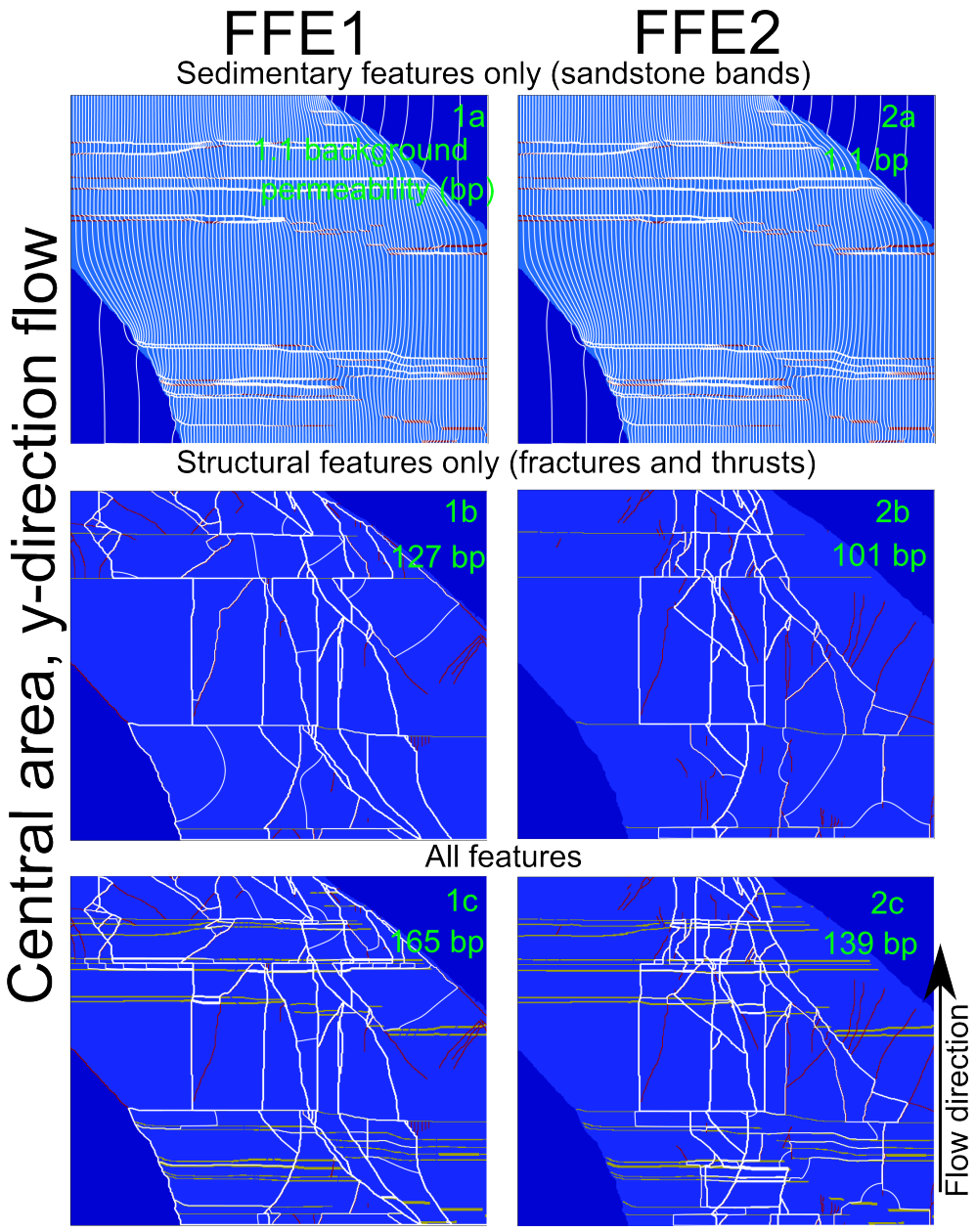

Figure 7.10: Streamlines for modelling scenarios of y-direction flow in a sample domain of the central area. FFE1 models on the left FFE2 on the right. 1a and 2a are only sedimentary features, 1b and 2b only structural features, 1c and 2c are the entire flow network.

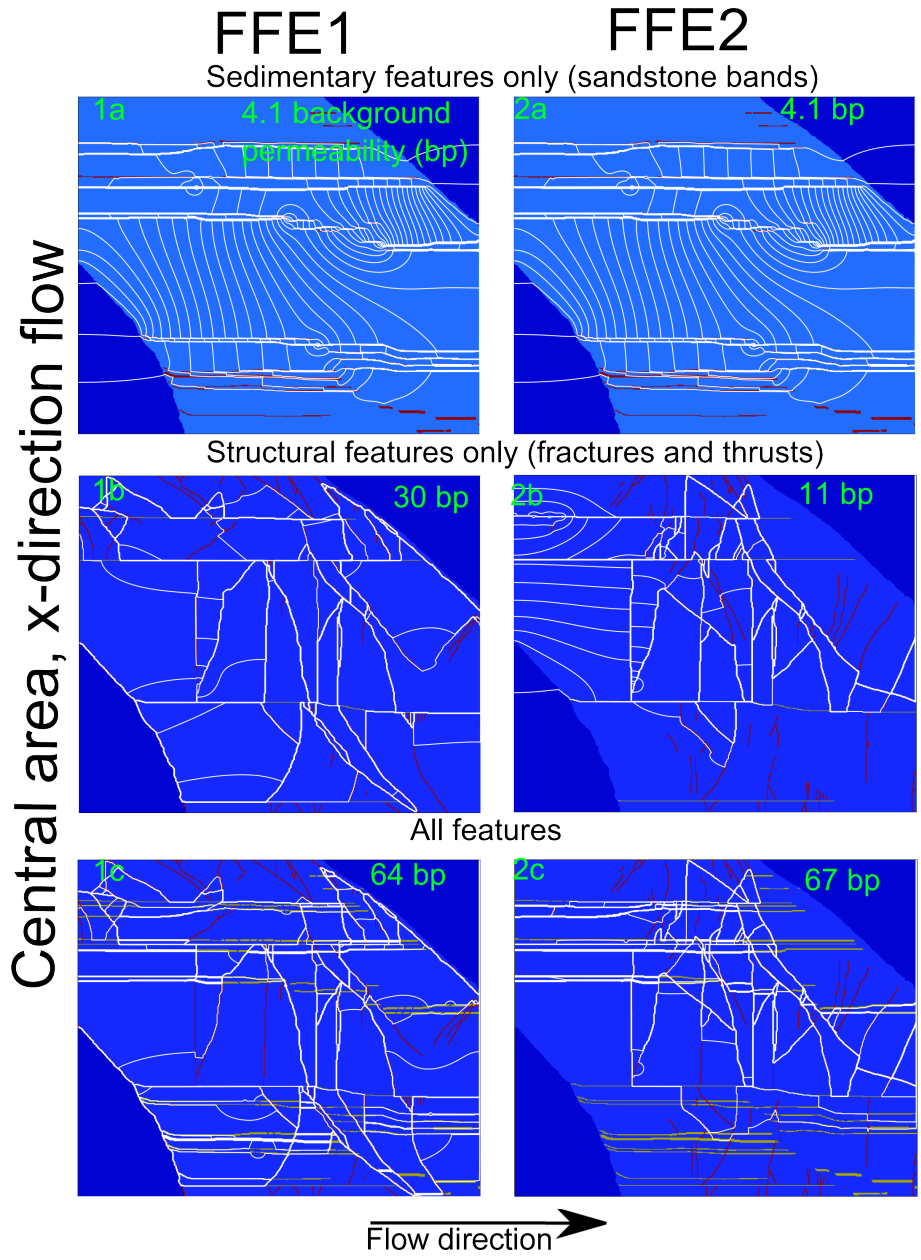

Figure 7.11: Streamlines for modelling scenarios of x-direction flow in a sample domain of the central area. FFE1 models on the left FFE2 on the right. 1a and 2a are only sedimentary features, 1b and 2b only structural features, 1c and 2c are the entire flow network.

The head gradient distributions (figure 7.12) for the northern area show differences between FFE1 and FFE2. In the y-direction a larger area of FFE1 is better connected to the lower boundary whereas for FFE2 the larger area is better connected to the upper boundary. In both cases the quick transition from red to blue represents the area where the fractures are likely most poorly connected.

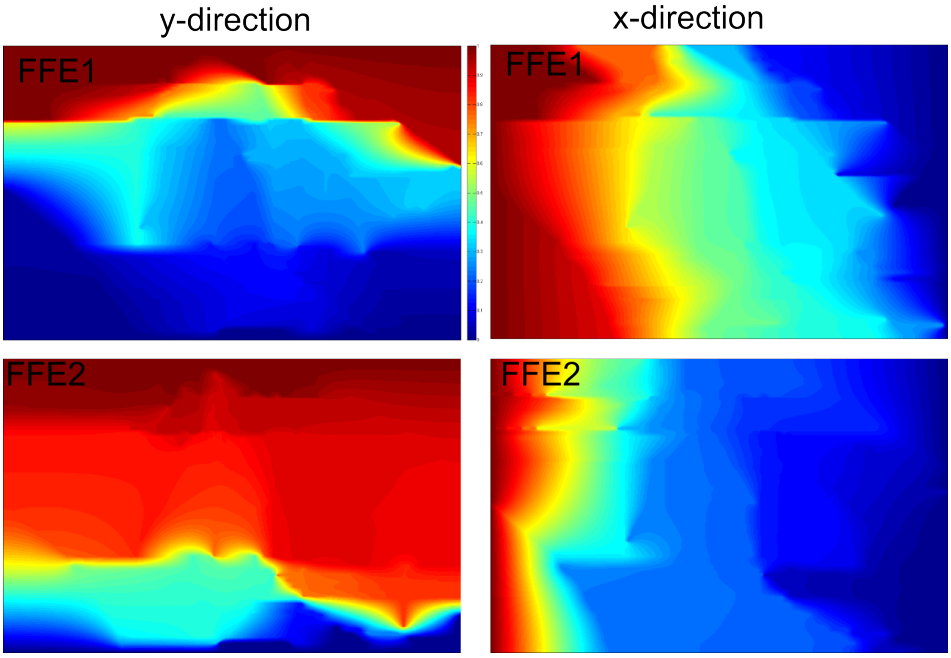

Figure 7.12: Head gradient for "all features" modelling scenarios of central area.

The head gradients in the x-direction appear to be strongly influenced by the strike-slips faults, which are modelled as open to fluid flow in FFE1 but closed in FFE2. The colour contours in FFE1 x-direction follow the strike-slip faults, particularly in the transition from light to dark blue. In the x-direction FFE2 model, the transition from light blue to yellow marks where on the streamlines (figure 7.15-2c) the flow goes from a fracture network into sandstone bands.

7.2.3 Northern area

The model domain for the northern area is shown in figure 7.13. As for the central area, the northern area has a small location in the bottom left corner which has been modelled one order of magnitude lower permeability than the mudstone. Because this location lies outside the bounding fault of the northern area.

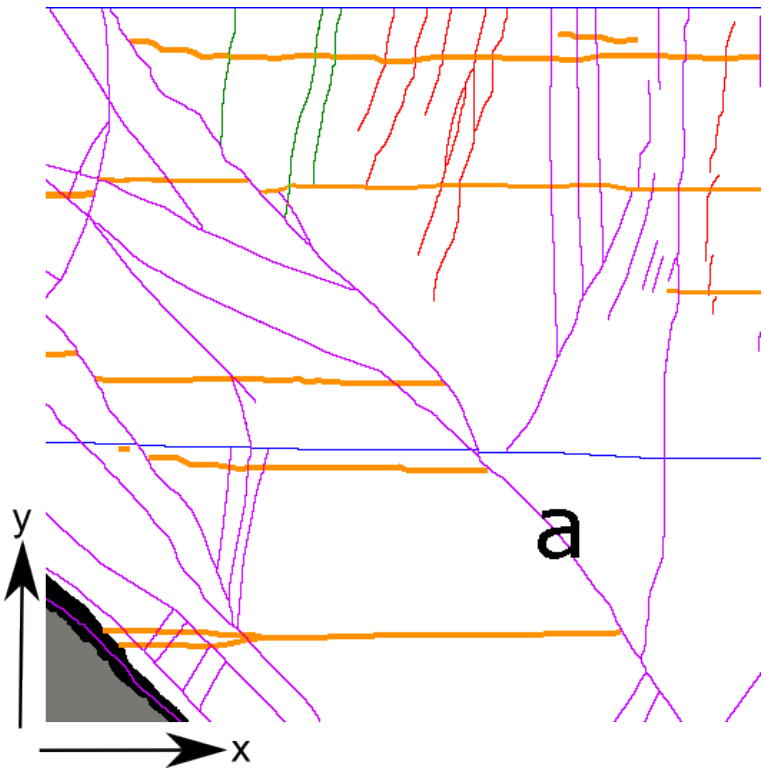

Figure 7.13: Model domain for the northern area. The location of the northern area model domain is shown on figure 7.4.

The northern area contains the modelling scenarios with the highest permeabilities of all the three field areas; that is the y-direction flow for "structural only" and "all features" scenarios for FFE1 (table 7.6 and figure 7.14). This is due to the long well connected fracture (labelled as a in figure 7.13) providing a high permeability conduit from the bottom to the top of the model. It should be noted that a slightly smaller model domain in the right position would mean that this feature would be a conduit for x-direction flow, so is not intrinsically a feature that will only enhance

y-direction flow	Bulk permeability (mD)	Permeability enhancement
Sedimentary features FFE1/FFE2	0.001	1.0
Structural features FFE1	0.48	494
Structural features FFE2	0.0013	1.3
All features FFE1	0.51	526
All features FFE2	0.0035	3.2

Table 7.6: Summary of bulk permeability and permeability enhancement of each of the modelling scenarios of the northern area in y-direction flow.

x-direction flow	Bulk permeability (mD)	Permeability enhancement
Sedimentary features FFE1/FFE2	0.0034	3.5
Structural features FFE1	0.034	35
Structural features FFE2	0.0035	3.6
All features FFE1	0.1	102
All features FFE2	0.008	8.2

Table 7.7: Summary of bulk permeability and permeability enhancement of each of the modelling scenarios of the northern area in x-direction flow.

fluid flow isotropically. This is shown in the results in x-direction flow, where the are large differences in the bulk permeability between FFE1 and FFE2 (table 7.7 and figure 7.15). On the streamline map it can be seen that in FFE1 (figure 7.15-1c) the streamlines are concentrated within this long fracture, whereas for FFE2 (figure 7.15-2c) there is no long fracture to connected the sandstone bands to create a complete flow network across the model.

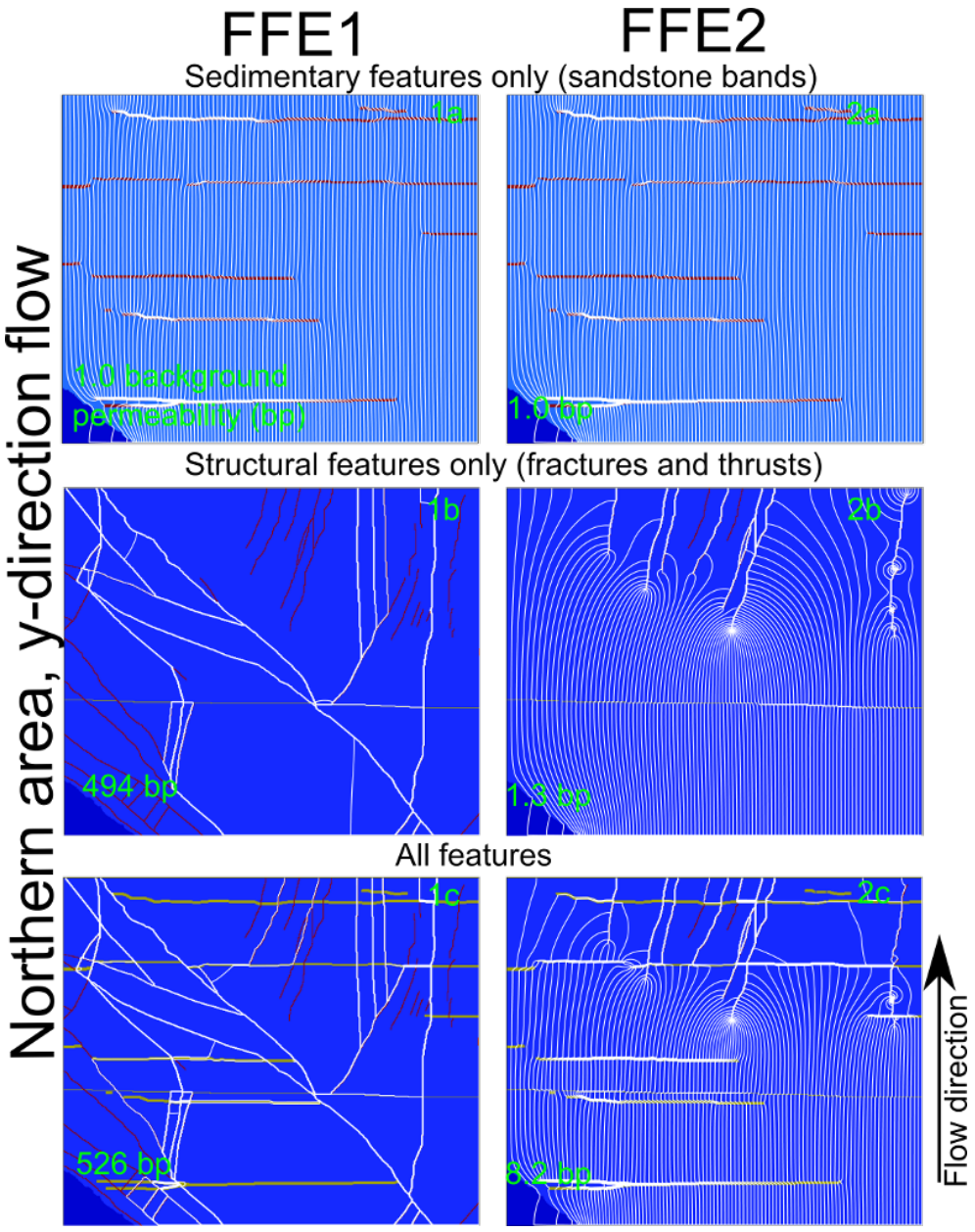

Figure 7.14: Streamlines for modelling scenarios of y-direction flow in a sample domain of the northern area. FFE1 models on the left FFE2 on the right. 1a and 2a are only sedimentary features, 1b and 2b only structural features, 1c and 2c are the entire flow network.

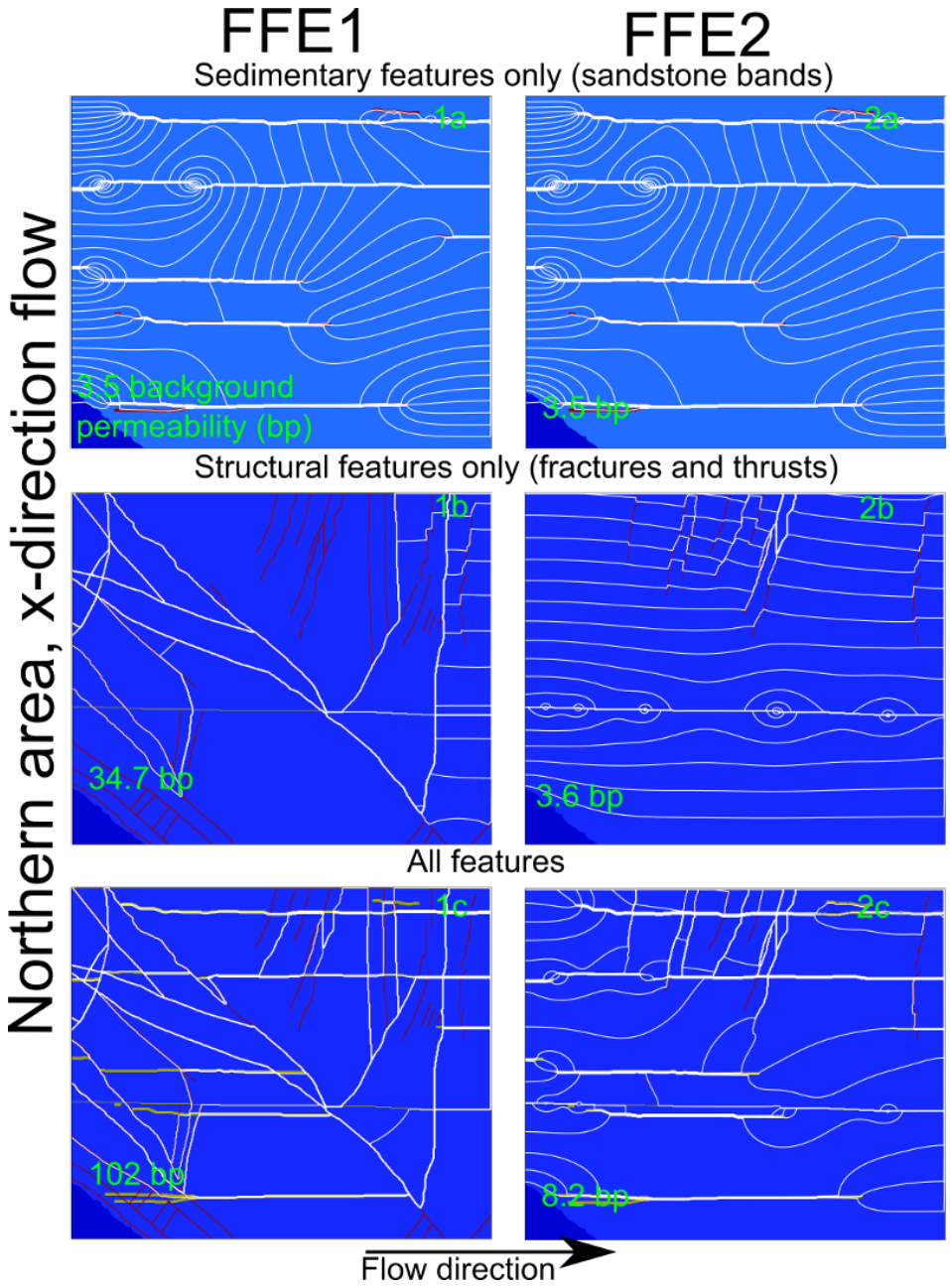

Figure 7.15: Streamlines for modelling scenarios of x-direction flow in a sample domain of the northern area. FFE1 models on the left FFE2 on the right. 1a and 2a are only sedimentary features, 1b and 2b only structural features, 1c and 2c are the entire flow network.

The head gradient diagrams highlight the major differences between FFE1 and FFE2 in the northern area (figure 7.16). The largely undisturbed contours for y-direction FFE2 is a result of the absence of flowing fractures in the lower part of this model. For y-direction FFE1 the head contours are largely perturbed by the fracture running top-left to bottom right of the model; in addition to adjoining the fractures also showing concentrated streamlines (figure 7.14-1c).

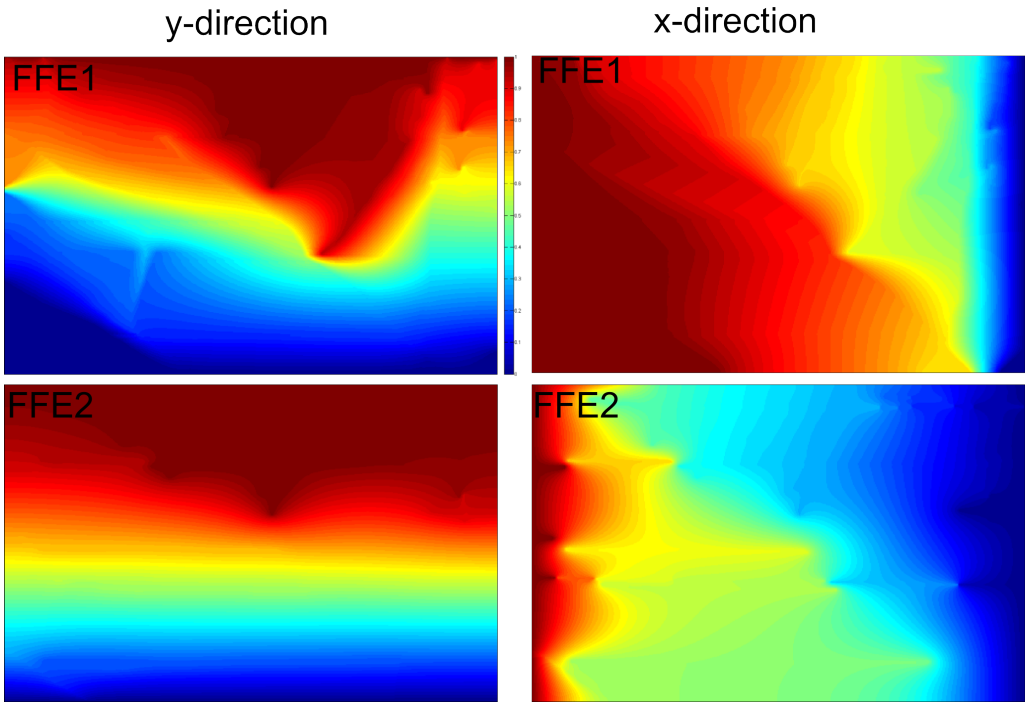

Figure 7.16: Head gradient for "all features" modelling scenarios of northern area.

For FFE1 x-direction the head contours are also strongly influenced by the large fracture running top-left to bottom-right. The early transition from blue to yellow on the right of the x-direction FFE1 model is due to only sandstone bands connecting the right boundary to the fluid flow network. The FFE2 x-direction model is mainly influenced by the sandstone bands which cause the horizontal perturbations in the head gradient. The sandstone bands were poorly connected so there aren't any connected hydraulic zones developed that would be visible on the head contours.

7.2.4 Sensitivity analysis of feature permeability

A sensitivity analysis was conducted to assess the dependency of the modelling results upon the permeability values chosen for the different features. The sensitivity analysis varied the permeability values of one of the features (mudstone, sandstone, thrusts, or fractures) while keeping the other features the same. Varying these values provided information about which features the modelled bulk permeability is most responsive to. These analyses were conducted using the southern area model as this model had the best mix between fractures, sandstone bands, and thrusts. The bulk permeability of the central and northern area may have been too controlled by a few individual features to test the overall sensitivity of the model to permeability changes. The results of the sensitivity analysis are presented in tables 7.8, 7.9, 7.10, and 7.11 as well as streamline outputs in figures 7.17 and 7.18.

Mudstone permeability was raised by two orders of magnitude to 0.1mD. Since mudstone was the already three orders of magnitude lower than the next permeability value then it was not tested what would happen if the permeability of the mudstone pixels was further lowered below 0.0001mD. Table 7.8 shows the bulk permeability of the raised mudstone (0.1mD) models compared with the models of original mudstone permeability (0.001mD). As expected, all four scenarios show higher bulk permeability as the models largely consist of pixels of mudstone. The modelled streamlines (figure 7.17-b) show that in the raised mudstone permeability scenario, then the contrast in permeability between the mudstone and the other features is not enough to allow the fluid flow to be concentrated in the other features. Which means that the field observations are not replicated in the modelling, as the observations showed that palaeo-fluid flow episodes were likely concentrated in the sandstone bands, thrusts, and fractures as shown in chapter 6.

Sandstone bands and the thrust faults were both assigned a mid-range value of 1mD in the previous modelling. To investigate the influences of both these features on modelled fluid flow they were both separately modelled as one order of magnitude lower (0.1mD) and one order of magnitude higher (10mD) in the sensitivity analyses.

Flow episode and direction	Bulk permeability with original **mudstone** permeability value (0.001mD)	Bulk permeability with raised **mudstone** permeability value (0.1mD)
FFE1 y-direction	0.014	0.28
FFE1 x-direction	0.04	0.18
FFE2 y-direction	0.004	0.16
FFE2 x-direction	0.015	0.15

Table 7.8: Table showing affect of raised mudstone permeability on bulk permeability of the different fluid flow episodes in the southern area model.

The affect these changes had on bulk permeability in the southern area for the different fluid flow scenarios are shown in tables 7.9 and 7.10.

Both the sandstone bands and thrust faults are "horizontal" features in the models, so would be expected to be more influential over the x-direction model scenarios. The results show this is true for the FFE2 y-direction scenarios with changes both in the sandstone bands and thrust faults having little effect over bulk permeability. However there is a noticeable increase and decrease in bulk permeability related to changes in the sandstone bands for FFE1 y-direction (table 7.9). This could be because one or two sandstone bands form a vital connection between the fractures which influence fluid flow in the y-direction models whereas the thrust faults do not.

The lower and higher permeabilities of the sandstone bands more strongly influence bulk permeability for the FFE1 x-direction model than the thrust faults. The affect of this can be seen in the streamlines (figure 7.17-c) as they are concentrated within the higher permeability sandstone bands more than in the higher permeability thrusts (figure 7.17-e). Conversely, for FFE2 x-direction the thrust faults enhance the bulk permeability more than the sandstone bands.

Fractures were previously modelled with the highest permeability (100mD); two orders of magnitude higher than the sandstone bands and thrusts. The fracture permeability was lowered to 10mD to test the affect this would have over the bulk

Flow episode and direction	Bulk k with original **sandstone band** k value (1mD)	Bulk k with lowered **sandstone band** k value (0.1mD)	Bulk k with raised **sandstone band** k value (10mD)
FFE1 y-direction	0.014	0.008	0.022
FFE1 x-direction	0.04	0.012	0.23
FFE2 y-direction	0.004	0.003	0.005
FFE2 x-direction	0.015	0.007	0.022

Table 7.9: Table showing affect of raised and lowered sandstone band permeability (k) on bulk permeability (k) of the different fluid flow episodes in the southern area model.

Flow episode and direction	Bulk k with original **thrust fault** k value (1mD)	Bulk k with lowered **thrust fault** k value (0.1mD)	Bulk k with raised **thrust fault** k value (10mD)
FFE1 y-direction	0.014	0.013	0.014
FFE1 x-direction	0.04	0.033	0.080
FFE2 y-direction	0.004	0.003	0.0055
FFE2 x-direction	0.015	0.013	0.032

Table 7.10: Table showing affect of raised and lowered thrust fault permeability (k) on bulk permeability (k) of the different fluid flow episodes in the southern area model.

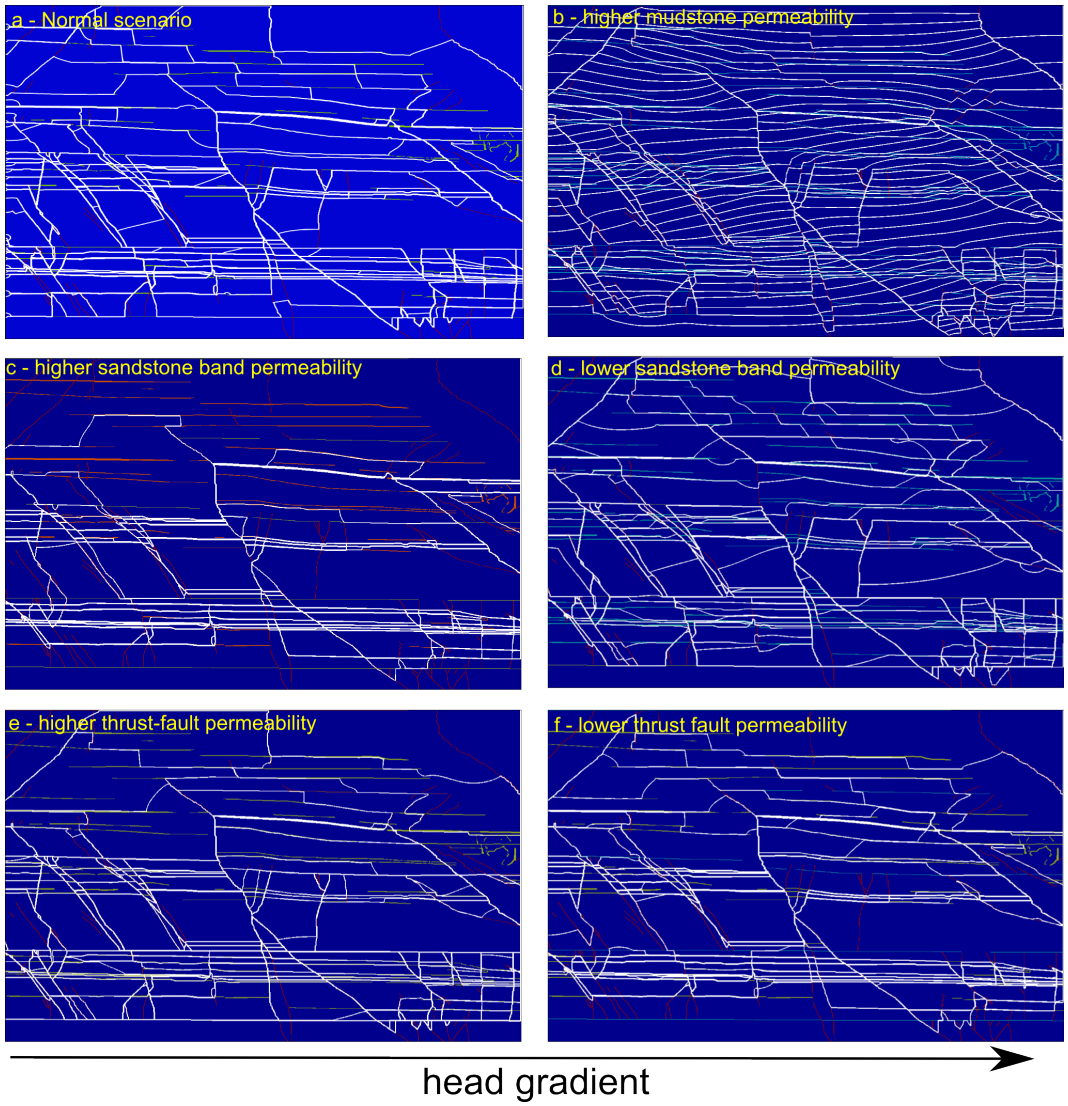

Figure 7.17: Streamlines for sensitivity analysis of southern area during FFE1 with x-direction flow. The "normal scenario" in a is the same as figure 7.7-1c, where the permeability values are the same as for the analysis above.

permeability of the models. For the four scenarios in the southern area (table 7.11) there were modest decreases in bulk permeability. Even though fractures would be expected to be most influential in the y-direction, there was no significant differences in the bulk permeability reduction between the x-direction and y-direction scenarios. This is likely a reflection of the combined network in the southern area, where

Flow episode and direction southern area	Bulk permeability with original **fracture** permeability value (100mD)	Bulk permeability with lowered **fracture** permeability value (10mD)
FFE1 y-direction	0.014	0.01
FFE1 x-direction	0.04	0.033
FFE2 y-direction	0.004	0.0038
FFE2 x-direction	0.015	0.011
Flow episode and direction northern area	Bulk permeability with original **fracture** permeability value (100mD)	Bulk permeability with lowered **fracture** permeability value (10mD)
FFE1 y-direction	0.51	0.068

Table 7.11: Table showing affect of lowered fracture permeability on bulk permeability of the different fluid flow episodes in the southern and northern model.

fractures connect with the sandstone bands and thrusts to form fluid flow networks through the mudstone. This can be seen in the differences between figures 7.18-a and c, where in the reduced fracture permeability scenario for y-direction flow the sandstone bands and thrusts contain more concentrated streamlines. However the reduced fracture permeability still seems enough to concentrate the fluid flow within the permeable features, an aim of the modelling.

The reduced fracture permeability was also modelled for the FFE1 y-direction scenario in the northern area because fractures were likely particularly influential in these models. The results in table 7.11 show almost one order of magnitude decrease in bulk permeability related to the reduction in the fracture permeability; highlighting how much influence the fractures have in the northern area models compared with the southern area models. Figures 7.18-b and d show the differences in the streamlines produced by the reduced fracture permeability compared with the "normal" scenario. Despite this large reduction in bulk permeability the streamlines (and therefore fluid flow) are still concentrated within the fractures; replicating the field observations.

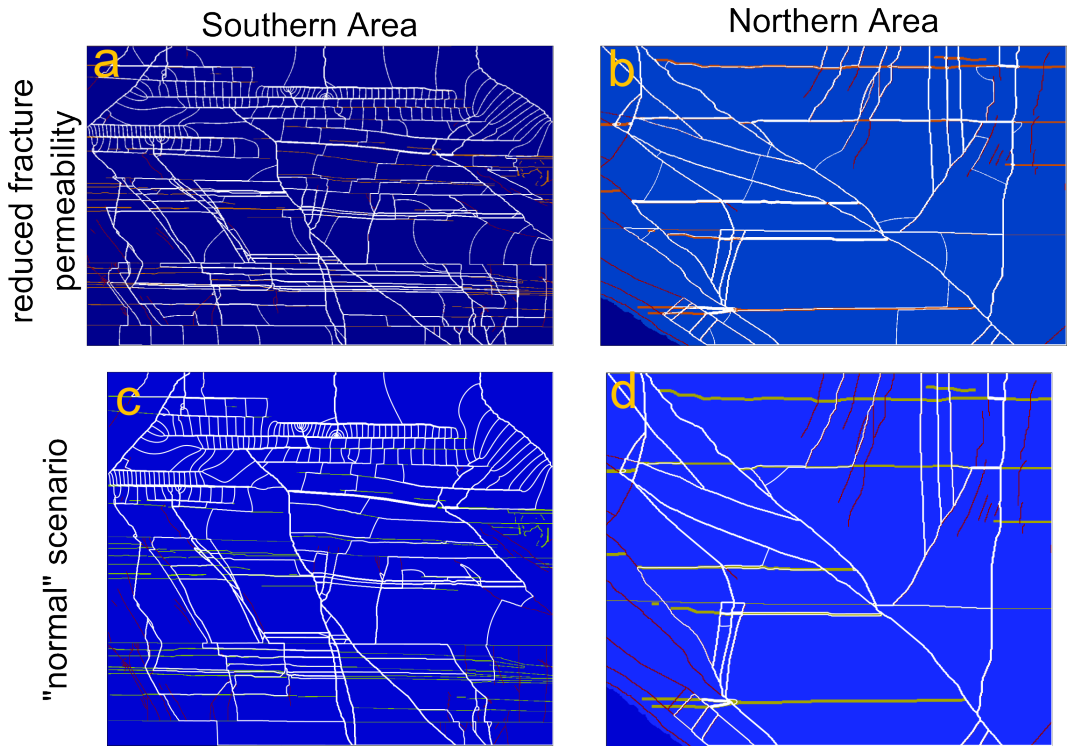

Figure 7.18: Streamlines for y-direction head gradient in sensitivity analysis of fracture permeability in southern area (a and c) and northern area (b and d). c is the same streamline image as 7.6-1c and d the same as 7.14-1c.

These sensitivity analysis confirm that the influence a group of features has over the bulk fluid flow of these models is not just dependant upon the assigned value of permeability. The influence is also dependent upon the orientation of the group of features relative to head gradient and how the groups of features interact to produce fluid flow networks through the mudstone.

7.3 Discussion: flow modelling

7.3.1 Aims of the modelling - answered

Which features controlled fluid flow within the red mudstone?

The longer shear fractures act as vital connections between the faults, further enhancing the affects of the faults. The streamlines show that during FFE1 flow is concentrated in the long shear fractures, where they are present. This leads to high enhancement of bulk permeability in FFE1 compared with FFE2.

The models of FFE2 show much less connectivity and therefore lower bulk permeability than for FFE1. New joints opened for FFE2 that were not open for FFE1. However these do no compensate for the permeability loss caused by the closing of the longer shear fractures after FFE1.

Did the controls on fluid flow change between the two fluid flow episodes?

The fluid flow evidence shows the long shear fractures were open during FFE1 but not FFE2. These long shear fractures "closing" to fluid were the likely cause of the drop in bulk permeability between FFE1 and FFE2 in the northern area. This is also reflected in the northern area sensitivity analysis, where bulk permeability dropped significantly in response to a reduction in assigned fracture permeability. The opening and closing of these shear fractures and faults is the main control on permeability change between the fluid flow events.

Chapter 2 introduced concepts that fluid pressure could initiate and propagate fracturing in rock. This means that the fluid is not passive in the permeability evolution of the rock, but that if fluid flow episodes had different pressures then this could account for part of the difference in fracture properties between the two studied fluid flow episodes.

Which other features contributed significantly to the fluid flow properties?

The central area does not contain the long shear FFE1 fractures that are present in the southern and the northern area. The central area still shows enhanced bulk permeability for both FFE1 and FFE2 without these long features. In the central area shorter fractures and sandstone bands combine to make flow networks that act to enhance the bulk properties.

Did the differing fracture properties in the three fault bounded areas lead to significant variations in fluid flow behaviour?

The model results show large permeability differences between the three fault-bounded areas. These differences appear primarily related to the fracture networks, as they are present in the structure only models. These permeability variations generally follow fracture density patterns found in the previous two chapters. The relationships between the model results and field data will be further explored in the following chapter.

7.3.2 Comparisons of the three field areas

There are large differences between the modelled bulk permeabilities of the three field areas (collated in figure 7.19). This gives insights into not only how the variations in fluid flow behaviour is governed by the different properties in the fault areas but also how these properties have changed with time.

In FFE1 the models for y-direction flow of the central and northern area both show two orders of magnitude enhancement of bulk permeability as does FFE2 central area models. This is caused by well developed connected networks running through the mudstone. Whereas the southern area had important gaps in the network leading to a lower enhancement of background permeability by only one order of magnitude. The southern area also shows different permeability anisotropy to the central and northern areas. In the central and northern areas y-direction flow has higher bulk permeability enhancement than the x-direction whereas it is the opposite for the southern area.

These modelled bulk permeability results reflect the data and observations collected from the field site. For fractures contributing to the FFE1 network in the central and northern area and for FFE2 in the central area, there were high fracture densities recorded. This appears to be the main factor which led to the better connectivity between the fractures in the central and northern area.

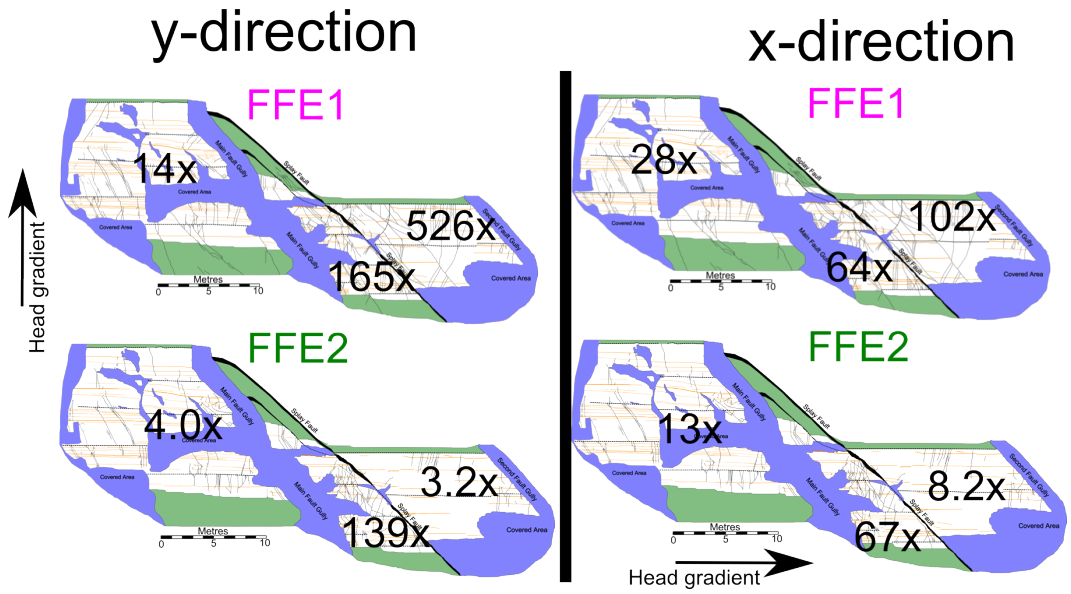

Figure 7.19: Summary of bulk permeabilities for footwall, central area and hangingwall when modelling the complete flow network. Showing the differences between flow event one and flow event two. Also when left to right head gradient or bottom to top head gradient applied to model.

For FFE2 the bulk permeability story of the three field areas is different than for FFE1. It is only the central area, for FFE2, that shows significant permeability enhancement beyond that found in both the northern and southern area. The higher permeability in the y-direction in the central area is indicative of the dominant influence of the fractures providing conduits for fluid flow, with connectivity between fractures enhanced by sandstone bands. This is in comparison to FFE2, in the central and northern area, where fractures are the dominant influence on flow with sandstone bands and thrusts providing connections between the fractures.

In most cases bulk permeability was much greater for FFE1 than for FFE2, the

only exception is x-direction flow in the central area. Since sandstone bands were modelled identically for both fluid flow episodes these changes in bulk permeability are due to the difference in fracture networks. Which is, again, reflected in the different fracture data recorded from the field site. With the northern and central areas especially showing much denser fracture data for FFE2 than FFE1.

7.3.3 Upscaling the models

Each field area could be one cell within a larger reservoir model (Zhang et al. 2008). Reservoir models often attempt to simulate fluid flow over large volumes of rock, which means that grid-cells can have dimensions of 20 metres. Such large grid cells are neceassary as the models simulate such expansive volumes that to run the model with smaller grid cells would take an undesirable amount of time. This means the permeability properties would need to be upscaled to be input into a single permeability grid cell. The bulk permeabilities of each field area could be used for this purposes. But what if the grid was coarser, and the cells were the site of the whole field area, what sort of bulk permeability would the whole field site have? Here, average permeability of the field site is found to answer this question, however including the faults in this understanding makes matter more complicated and is discussed at the end.

Figure 7.20 shows a simplified model of the field site that has been used to calculate average permeabilities.

To calculate the average bulk permeability for y-direction flow (Q_1) the following equations is used (Bear and Verruijt 1987).

$$k_{av} = \frac{1}{B} \sum_{i=1}^{3} k_i B_i \tag{7.5}$$

Which becomes the following when considering the simplified scenario shown in figure 7.20.

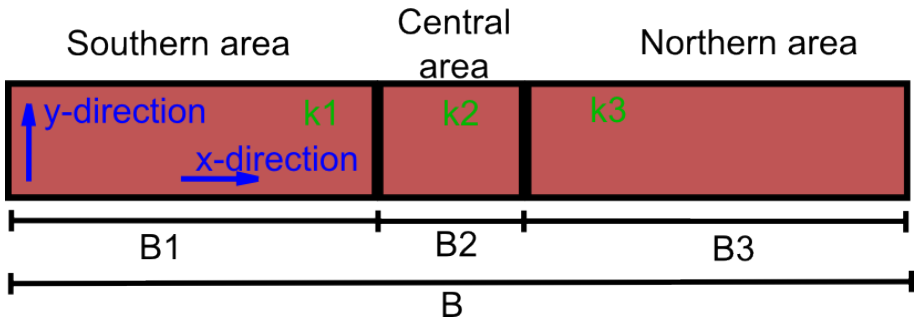

Figure 7.20: Simplified model of the field site used to calculate average bulk permeability. k_1, k_2 and k_3 are the calculated bulk permeability from the models in section 7.2. B_1, B_2 and B_3 are the widths of each section, B1=20m, B2=8m, B3=16m, and B=44m.

$$k_{av} = \frac{(k_1 B_1) + (k_2 B_2) + (k_3 B_3)}{B} \tag{7.6}$$

For FFE1 y-direction fluid flow the permeabilities input to equation 7.6 would be: k_1=0.014,k_2=0.13, k_3=0.51. For FFE2 y-direction fluid flow the permeabilities input to equation 7.6 would be: k_1=0.004,k_2=0.11, k_3=0.0035.

To calculate the average bulk permeability for left to right fluid flow direction (Q_2) the following equations is used (Bear and Verruijt 1987). This is because the fluid flow goes across several zones of different permeability, meaning that the harmonic mean was used to calculate average permeability.

$$\frac{B}{k_{av}} = \sum_{i=1}^{3} \frac{B_i}{k_i} \tag{7.7}$$

Which becomes the following when considering the simplified scenario shown in figure 7.20.

$$k_{av} = \frac{B(k_1 k_2 k_3)}{(B_1 k_2 k_3) + (B_2 k_1 k_3) + (B_3 k_1 k_2)} \tag{7.8}$$

For FFE1 x-direction fluid flow the permeabilities input to equation 7.8 would be:

y-direction flow	Bulk permeability (mD)	Permeability enhancement
FFE1	0.27	270
FFE2	0.02	20

Table 7.12: Averaged permeability of the field site for y-direction flow for FFE1 and FFE2.

x-direction flow	Bulk permeability (mD)	Permeability enhancement
FFE1	0.04	40
FFE2	0.01	10

Table 7.13: Averaged permeability of the field site for x-direction flow for FFE1 and FFE2.

k_1=0.028,k_2=0.047, k_3=0.1. For FFE2 x-direction fluid flow the permeabilities input to equation 7.8 would be: k_1=0.013,k_2=0.049, k_3=0.008.

Tables 7.12 and 7.13 show the averaged permeabilities for the field site. Y-direction flow has a greater permeability than x-direction flow for both FFE1 and FFE2. And FFE1 is greater than FFE2 for both flow directions.

The average bulk permeability values obtained could be used as the basis for a permeability tensor for the field site. However these do not incorporate the effect that the faults would have. During FFE1 the faults provided high permeability conduits to fluid flow through the field site, approximately in the y-direction flow. However the field evidence indicates the faults were closed to fluid flow during FFE2.

Since the length of the faults are probably much greater than the field site, it would be difficult to accurately portray the fluid flow properties of the faults by incorporating them into average properties of the field site. As the faults would provide a conduit for fluid flow over a distance much larger than the field area. The issues related to incorporating such large dominant flow features into models and the different methods developed that would be useful for accurately modelling similar rock types to the field site are discussed in the following chapter.

7.4 References

Armitage, P. J., Falkner, D. R., Worden, R. H., Aplin, A. C., Butcher, A. R. and Iliffe, J. 2011. Experimental measurement of, and controls on, permeability and permeability anisotropy of caprocks from the CO_2 storage project at the Krechba Field, Algeria. *Journal of Geophysical Research - Solid Earth.* v.**116**. 10.1029/2011JB008385

Bear, J. and Verriujt, A. 1987. *modelling Groundwater Flow and Pollution: Theory and Applications of Transport in Porous Media.* Dordrecht, Holland. D. Reidel Publishing Company.

Berkowitz, B. 1995. Analysis of Fracture Network Connectivity Using Percolation Theory. *Mathematical Geology.* v.**27** i.*4*. pp. 467-483.

Couples, G. Professor, Institute of Petroleum Engineering. Heriot-Watt University. 19 March 2013.

Darcy, H. Les Fontaines Publiquesa de la Ville de Dijon, Dalmont, Paris (1856).

Dee, S. J., Yielding, G., Freeman, D., Healy, D., Kusznir, N. J., Grant, N., and Ellis, P. 2007. Elastic dislocation modelling for prediction of small-scale fault and fracture network characteristics. *from*: Lonergan, L., Rawnsley, and Sanderson, J. (eds). *Fractured Reservoirs.* Geological Society, London, Special Publication. **270**. pp. 139-155.

Dennis, I., Pretorius, J. and Steyl, G. Effect of fracture zone on DNAPL transport and dispersion: a numerical approach. *Environmental Earth Science.* v.**61**. pp. 1531-1540.

Dewhurst, D. N. and Siggins, A. F. 2006. Impact of fabric, microcracks, and stress field on shale anisotropy. *Geophys. J. Int.* v.**165**. pp. 135-148.

de Dreuzy, J-R., Davy, P and Bour, O. 2001. Hydraulic properties of two-dimensional random fracture networks following a power law length distribution: 1. Effective

connectivity. *Water Resources Research*. v.**37** i.**8**. pp. 2065/2078.

Harbaugh, A.W., 2005, MODFLOW-2005, the U.S. Geological Survey modular ground-water model – the Ground-Water Flow Process: U.S. Geological Survey Techniques and Methods 6-A16, variously p.

Hawkins, P. J. 1978. Relationships between diagenesis, porosity reduction, and oil emplacement in late Carboniferous sandstone reservoirs, Bothamsall Oilfield, E Midlands. *Journal of the Geological Society*. v.**135**. pp. 7-24.

Ishii, E., Sanada, H., Fanaki, H., Sugita, Y. and Kurikami, H. 2011. The relationship among brittleness, deformation behaviour, and transport properties in mudstones: An example from the Horonobe Underground Research Laboratory, Japan. *Journal of Geophysical Research*. v.**116** i.**B9**. 10.1028/2011JB008279.

Lomize, G. M. Flow in Fracture Rocks (in Russian), 127 PP., Gosenergoizdat, Moscow, 1951.

Lunn, R. J., Shipton, Z. K. and Bright, A. M. 2008. How can we improve estimates of bulk fault zone hydraulic properties? *Geological Society, London, Special Publication*. v.**299**. pp. 231-237.

Ma. J. Lecturer in Multi-Physics Modelling in Porous Media. 19 March 2014.

Manda, A. K., Mabee, S. B., Boutt, D. F. and Cooke, M. L. 2012. A method of estimating bulk potential permeability in fractured-rock aquifers using field-derived fracture data and type curves. *Hyrdogeology Journal*. v.**21**. pp. 357-369.

Manzocchi, T., Walsh, J. J., Nell, P. and Yielding, G. 1999. Fault Transmissibility Multipliers for Flow Simulation Models. *Petroleum Geoscience*. **5**. pp. 53-63.

Manzocchi, T., 2002. The connectivity of two dimensional networks of spatially correlated fractures. *Water Resources Research*. v.**38**. DOI:10.1029/2000WR000180

Masch, F. D. and Denny, K. J. 1966. Grain Size Distribution and Its Effect on The Permeability of Unconsolidated Sands. *Water Resources Research*. v.**2** i.**4**. pp.

665-677.

Myers, T. 2012. Potential Contaminant Pathways from Hydraulically Fractured Shale to Aquifers. *Grouwn Water*. v.**50** no.**6**. pp. 873-882.

Odling, N. E., Gillespie, P., Bourgine, B., Castaing, C. Chiles, J-P., Christensen, N. P., Fillion, E., Genter, A., Olsen, C., THrane, L. Trice, R. Aarseth, E. Walsh, J. J. and Watterson, J. 1999. Variations in fracture system geometry and their implications for fluid flow in fractured hydrocarbon reservoirs. *Petroleum Geoscience*. v.**5**. pp. 373-384.

Perera, M. S. A., Ranjith, P. G., Choi, S. K. and Airey, D. 2011. Numerical simulation of gas flow through porous sandstone and it's eperimental validaton. *Fuel*. v.**90**. pp. 547-554.

Polubarinova-Kochina, P. Ya. *Theory of Groundwater Movement* translated from Russian by J. M. R. DeWiest. 613 pp., Princeton University Press, Princeton. N. J. 1962.

Renshaw, C. E. 1999. Connectivity of joint networks with power law length distributions. *Water Resources Research*. v.**35**. i.**9**. pp. 2661-2670.

Snow, D. T. 1965. A parallel plate model of fractured permeable media. Ph.D. thesis. 331 pp., Univ. of Calif. Berkeley.

Spencer, C. W. 1989. Review of Characteristics of Low-Permeability Gas Reservoirs in Western United States. v.**73**. pp. 613-629.

Tiedeman C. R., Lacombe, P. J. and Goode, D. J. 2010. Multiple Well-Shutdown Tests and Site-Scale Flow Simulation in Fractured Rocks. *Groundwater*. v.**48** i.**3**. pp. 401-415.

Todd, D. K. and Mays, L. W. 2005. *Groundwater Hydrology*. Hoboken. John Wiley and Sons Incorporated.

Tuechmantel, C., Fisher, Q. J., Grattoni, C. A. and Aplin, A. C. 2012. Single and

two phase fluid flow properties of cataclasitc fault rocks in porous sandstone. *Marine and Petroleum Geology*. v.**29**. pp. 129-142.

Waldschmidt, W. A. 1941. Cementing materials in sandstones and their probable influence on migration and accumulation of oil and gas [Rocky Mountain Region]. *AAPG Bulletin*. v.**25**. pp. 1839-1879.

Wong, L. N. Y., Li, D. and Liu, G. 2012. Experimental Studies on Permeability of Intact and Singly Jointed Meta-Sedimentary Rocks Under Confining Pressure. *Rock Mechanics and Rock Engineering*. v.**46** i.**1**. pp. 107-121.

Yang, Y. and Aplin, A. C. 2010. A permeability-porosity relationship for mudstones. *Marine and Petroleum Geology*. v.**27**. pp. 1692-1697.

Yang, Y. and Aplin, A. C. 2007. Permeability and petrophysical properties of 30 natural mudstones. *Journal of Geophysical Research: Solid Earth*. v.**112** i.**B3**. DOI:10.1029/2005JB004243.

Yielding, G., Freeman, B. and Needham, D.T. 1997. Quantitative fault seal prediction. *AAPG Bulletin*. v.**81** i.**6**. pp. 897-917.

Zhang, P., Pickup, G. E., Manfared, H. and Christie, M. A. 2008. Flow upscaling in highly heterogeneous reservoirs. *From*: Robinson, A., Griffiths, P., Price, S., Hegre, J. and Muggeridge, A. (eds) *The Future of Geological Modelling in Hydrocarbon Development*. The Geological Society, London, Special Publications, **309**. pp. 135-144.

Chapter 8

Discussion

"The most exciting phrase to hear in science, the one that heralds new discoveries, is not 'Eureka!' but 'That's funny...' " – Isaac Asimov

8.1 Review of research applications

Research into fluid flow in mudstone has important applications such as geological disposal of radioactive waste, carbon capture and storage, and hydrocarbon exploration and production. Mudstones are typically considered as low permeability barriers to fluid flow (i.e. caprocks and seals), and are thus generally considered as impermeable (Aplin and Macquaker 2011); on human timescales at least. However, as the results from this study have shown, sub-seismic features within mudstone compromise sealing ability, due to the presence of connected low displacement faults, fractures, and thin sandstone bands within the mudstone. Characterising the distribution and connectivity of such sub-seismic flow networks in mudstone is therefore key to constraining mudstone permeability characteristics. This thesis has combined fieldwork with fluid flow models to study palaeo-flow episodes through the mudstone. The field work describes in detail sub-seismic mudstone features, from a site in Girvan, which create permeable flow networks through an otherwise low

permeability formation. These networks are defined by interactions between thin sandstone bands, fractures and faults. The interaction between these structural and sedimentary features enhances the network connectivity (and therefore permeability) beyond that of either the sandstone bands or fractures considered in isolation. These key observations provide new data for this low permeability environment.

Previous work have investigated faults in mudstone (Dewhurst et al. 1999, Ingram and Urai 1999, Eichhubl and Behl 1998) and found episodic fluid flow behaviour; reflecting the differences between the two fluid flow episodes in this study. Fractures have also been investigated for the permeability enhancement they create in mudstone (Engelder et al. 2009, Lash et al. 2004). Sandstone bands within mudstone have been found to allow fluid to drain from mudstone relieving overpressure (Guo et al. 2013), additionally previous studies describing sandstone bands in distal turbidite formations were conducted to understand the depositional setting and processes (Sinclair and Cowie 2003, Carlson and Grotzinger 2001, Turcotte 1997). This study adds to previous work by making detailed observations of the interaction between faults, fractures, and sandstone within a mudstone to constrain the fluid flow networks; at a finer scale than previous studies in structurally complex turbidite formations (e.g. Childs et al. 2007). Further more, high resolution logging while drilling tools in 2012 shed new light on a complex reservoir consisting of thin permeable laminations and fractures (Railton et al. 2012); highlighting how networks of small features can be necessary useful to characterise in subsurface investigations. The following discussion emphasises the importance and difficulties of sub-seismic scale geological investigations into caprock and source-rock permeability, and the implications of these results for industrial applications.

This study has described in detail the fluid flow features of one exposed mudstone formation. However many other mudstone formations in the UK are of comparable properties. The Bowland shale is currently the most promising shale gas reservoir in the UK and is described as "impermeable, very stiff and brittle rock, with many faults and fractures" (Pater and Baisch, 2011); a comparable description with the mudstone in this study. Indeed it was in the Bowland shale that unexpected

fault-fluid interaction caused tremors (in April 2011), resulting in a moratorium in shale gas activities in the UK. Such unexpected fluid flow related seismic activity highlights the need for thorough understanding of fluid flow through shale and its interaction with structural features. The St. Bees Formation in Cumbria was part of a proposed host area for radioactive waste in the UK (McKeown 1997). The formation contains mudstones which may have been considered a barrier between the geological disposal facility and the Earth's surface; in the event that radioactive legacy waste were located in this region. The St Bees formation consists of red siltstones, mudstone and sandstone (Strong et al. 1994, Jackson et al. 1987) similar to the formations on the Girvan foreshore described in this study. The St Bees formation is also fractured, with a subset of fractures being filled as veins (Strong et al. 1994), showing that it too behaves in brittle rather than ductile manner. Shale gas reservoirs in the U.S.A also contain natural fractures which are observed when reservoir rock outcrops (Lash et al. 2004). Areas of high fracture density are targeted as sweet spots in unconventional reservoirs; from which economic rates of natural gas can be produced (Hart 2006). The findings from this study could be applied to more accurately predict fluid flow through mudstones, in areas beyond the examples above.

8.2 Overview of the permeability evolution of the mudstone and the influences of geological processes

Based on observations from the Girvan from this and previous studies (Woodcock 2012, Ince 1984, Ingham 1978), this section overviews the geological processes and events that have formed the mudstone and the fluid conduit features. These processes and events have influenced the permeability properties of the mudstone. The main stages of spatial distribution of fluid flow conduits are shown in figure 8.1. How the permeability of the mudstone likely changed in response to burial, faulting

and fracturing is also outlined in this section. Figure 8.2 outlines the permeability enhancements to bed-perpendicular flow, that has occurred due to the geological events. The values in figure 8.2 are based on the modelling conducted in the previous chapter.

When deposited, muds can have 80-90% porosity, however this decreases to 5% after burial of 6km and 200°C (Aplin and Macquaker 2011). The small amount of chlorite observed in the thin sections (section 4.3) would suggest the mudstone reached these burials and temperatures. After deposition and compaction (figure 8.1-a), the mudstone would likely be a very low permeability of between 10^{-6} to 10^{-2}mD (Todd and Mayes 2005, Dewhurst and Siggins 2006, Yang and Aplin 2007), which would mean the mudstone likely behaved as a seal to any fluid flow across it (figure 8.2). However the sandstone bands within the mudstone are likely to have been fluid flow conduits (due to evidence of the palaeo fluid flow episodes being focussed in the sandstone bands). So when considering the unit as a whole (mudstone and sandstone bands) there may have been significant permeability anisotropy. Before fracturing occured there was likely little vertical communication between the sandstone bands and therefore the sandstone bands would not have provided a seal bypass through the mudstone.

The initial structural deformation of the mudstone was folding due to NW-SE compressional stresses. This deformation is most likely related to the closing of the Iapetus and collision of Avalonia with Laurentia (Woodcock 2012). The folding resulting in the bedding being tilted 90° in the field site area. Thrusting then occurred related to the same stress direction as the folding. The thrusting resulted in the older formations being transported NW over the younger formations, and is exposed currently as the Whitehouse Shore Thrust Fault. This main thrust fault has smaller related thrusts that are present in the studied field area. These smaller thrust-faults are exposed as sub-parallel to the sandstone bands so probably had a similar effect on bulk permeability as the bands.

Faulting and fracturing occurred throughout the mudstone as a result of continued NW-SE compressional stress. Due to an inferred swap of σ_2 and σ_3 direction the

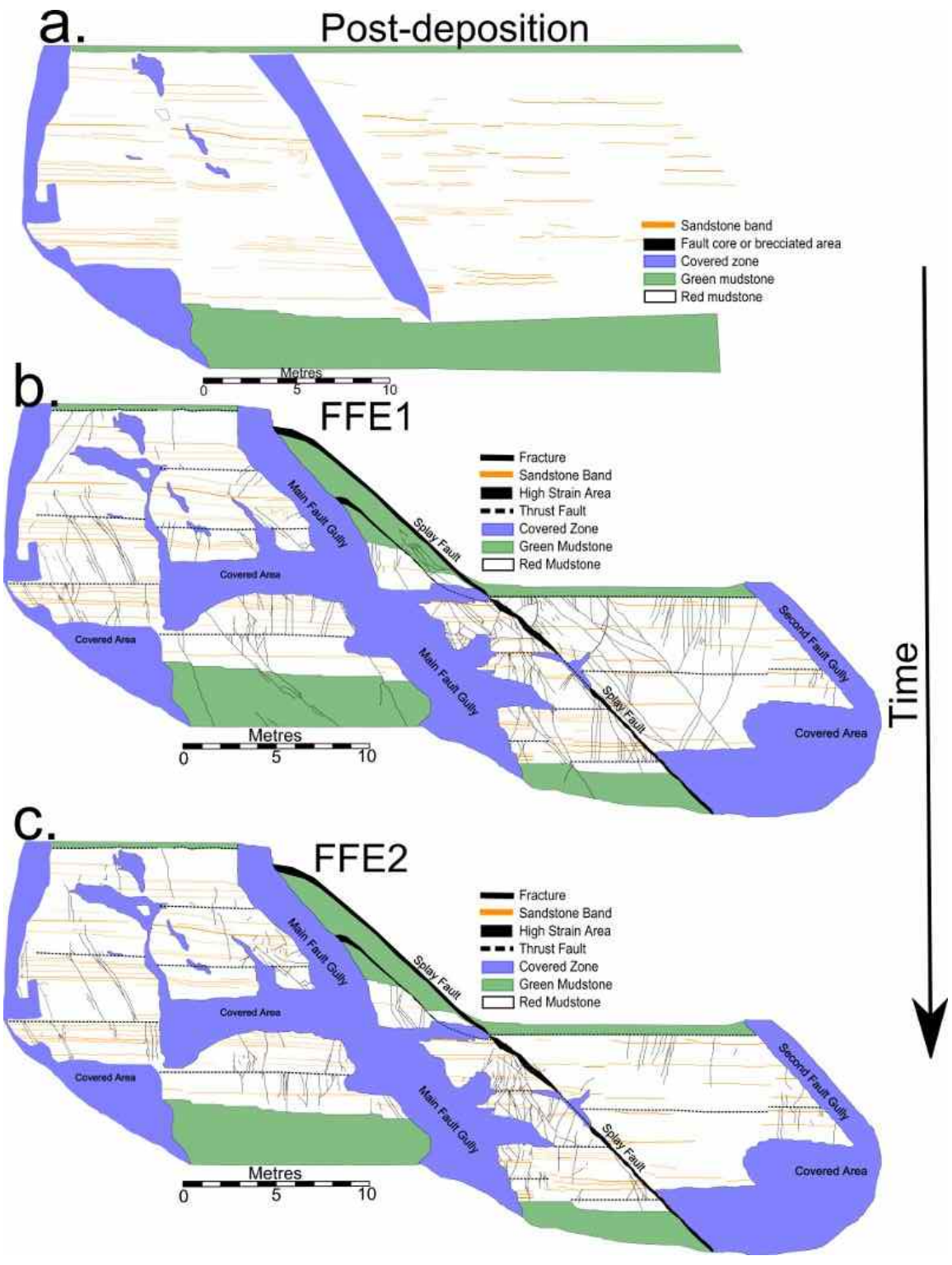

Figure 8.1: Field maps showing evolution of flow-conduit networks. Note the faults have been approximately restored on the post-deposition map (a).

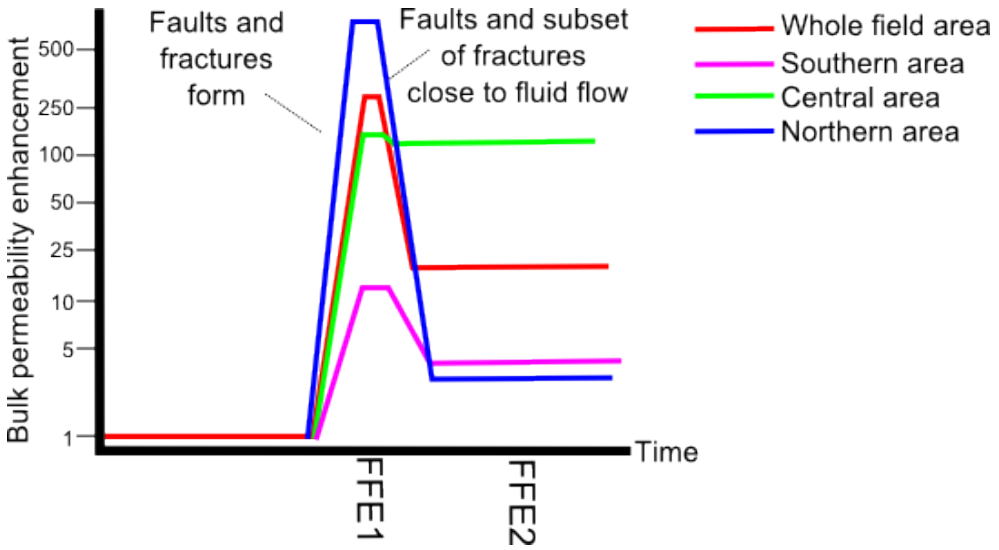

Figure 8.2: Bulk permeability enhancement over time for the southern, central, northern area, and averaged field site. Graphs based on y-direction bulk permeability modelled values from previous chapter, note that the y-axis is log-scale. Relative and schematic timing locations of FFE1 and FFE2 labelled on x-axis.

faulting regime changed from thrusting to strike-slip. The faulting and fracturing created a series of well-connected relatively high-permeability flow conduits (figure 8.1-b). These conduits had the effect of enhancing the bulk permeability of the formation, shown in the rising limbs of the graphs in figure 8.2 prior to FFE1. The features open to flow at this time are evidenced by calcite precipitation in faults, fractures and sandstone bands. Conditions during this time may have been similar to that described above in the Bowland Shale, with many faults and fractures critically stressed.

The flow networks shown by the calcite precipitation (FFE1) may represent the time of the largest permeability differences between the individual field areas: Long well-connected fractures in the northern area, and short but dense fractures in the central area created well-connected networks with the sandstone bands, the southern area had less well-connected networks, so the modelled permeability enhancement was not as large.

In a further stage of deformation (FFE2), additional fractures are created and open to fluid flow, but many of the fracture from the previous phase (FFE1) remain sealed by calcite. This resulted in a permeability decrease that is most marked in the northern area which changes from being the area with the highest modelled bulk permeability to the lowest (blue line-figure 8.2). However in the central area, between two closely spaced faults, there is a denser fracture network creating a zone of enhanced permeability within the mudstone (green line-figure 8.2). These faults localised the deformation and stress (e.g. Gartrell 2003) maintaining open fractures in this area.

8.3 Detection of permeable features during subsurface investigation

Evidence presented in this thesis has shown how complicated networks of faults, fractures and sandstone bands can create networks of fluid flow conduits through otherwise impermeable rock. To accurately characterise such networks in future subsurface investigations then certain properties of the features will need to be known or predicted.

For sandstone bands, the spatial distribution would need to be determined to allow prediction of how the bands interact with faults and fractures to create fluid flow networks. This spatial distribution needs to incorporate sandstone bands with thickness of less that one centimetre, since they are shown to be a key component of the flow network.

For fractures, the spatial distribution properties will need to be characterised such as, orientation and length. These properties govern the probability of features interconnecting to form networks. Additionally, the orientation within the local stress field needs to be established, as fractures were found to be more likely to be open to palaeo-fluid flow when critically stressed.

The process of collecting subsurface data is not straightforward, and the key fluid flow network properties mentioned above may be missing from a data set or the data may only exist for larger features. Due to these issues, the following subsections explore how the obstacles for accurate characterisation of such sub-seismic scale fluid flow networks can be overcome.

8.3.1 Detection and prediction of sandstone bands

The small size of the sandstone bands in these very distal turbidites mean they would be difficult to detect during subsurface investigations; 3D seismic surveys do not have the required resolution to detect such small features. A typical rule of thumb used is that beds less than 10 metres thick are unlikely to be distinguishable using seismic surveys. Borehole data is currently the only conceivable way these features could be detected. There are two methods that may be able to detect sandstone bands as thin as those observed in this study (<1cm), core logging or wireline logging. Although a drill hole is only a one dimensional transect through a complicated four dimensional system it provides valuable information.

Core logging is where a cylinder of rock (or drill core) has been removed from the subsurface during drilling (figure 8.3). This allows close inspection of the lithology. Observations made of the drill core could be made at similar, if not better, resolution than was achieved in the field, which would allow for accurate data collection on band thickness but provide no information about lateral extent. However collecting drill core requires removing the drill string so is an expensive and slow process which carries an element of risk to the borehole. Hence, core logging is typically avoided in favour of other options where available. Mud logging of drill hole cuttings may show the presence of sandstone bands or even the % of sandstone, but will give no information on the thickness or spatial distribution of the bands.

Wireline logging involves suspending a device down the well which can measure the resistivity and natural potential of the rock (Robinson and Coruh 1988). There are many different types of wireline logging equipment but micrologs can detect sedi-

Figure 8.3: Example of rock core. Photograph taken from British Geological Survey core store.

mentary features down to five millimetres thick. For example: the Schlumberger FM1 Fullbore Formation Micrologger which has resolution down to 5.08mm. However this still won't be able to detect the majority of the sandstone bands observed within the red mudstone in this study. Figure 8.4 shows the histogram of sandstone band thicknesses presented in chapter 4, but with the observation threshold of the micrologging techniques.

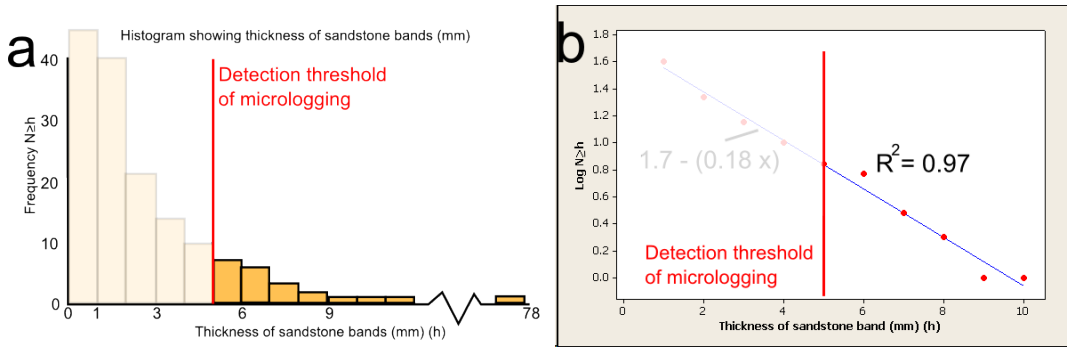

Figure 8.4: a. Histogram showing the number of sandstone bands above a certain thickness (N>h). b. The same data converted to log scale on y-axis to allow clearer view of the thickness distribution. The red line on each graph indicates the approximate detection threshold for micrologging. The "undetectable" data are included but faded out in both graphs.

For accurate prediction of "undetectable" data (left of detection threshold on figure

Data include	Regression equation	estimation of $N \geq 1$
All data	$1.73 - (0.18x)$	35
4mm and above	$1.77 - (0.18x)$	39
5mm and above	$1.83 - (0.19x)$	44
6mm and above	$2.25 - (0.25x)$	100

Table 8.1: Summary of regression line equations developed when applying different sandstone band detection thresholds to the population from this study. And how many sandstone bands at 1mm or thicker the regression estimates.

8.4) with the field data, then the regression line of just the detectable data (right of detection threshold on figure 8.4) should be similar to that of the entire data set. At Girvan, the regression line for the entire data set is $1.7 - (0.18x)$, the censored data regression line could vary significantly from that of the entire data set.

The different regression lines calculated for several detection thresholds are shown in table 8.1 along with the number of sandstone bands of 1mm thickness or above that are predicted by the regression line. The true value of sandstone bands of 1mm ($N \geq 1$)or over is 40, therefore even the regression line including all the data underestimates this by giving a value of 35. The regression line from the detection threshold at 5mm overestimates the number of thinner sandstone bands, giving a value of 44 bands that are 1mm or thicker.

To investigate what effect slight changes in the detection threshold would have, regression lines were calculated from data of only sandstone bands 4mm or thicker and 6mm or thicker. A detection threshold of 4mm creates a regression line that, in this data set, is a more accurate predictor of the very thin sandstone bands than the regression line calculated from all the data. But this is almost definitely a chance quirk of the data, and 4mm should not be considered as some desirable threshold for detection of sandstone bands based on this. However when the threshold is increased to 6mm large inaccuracies in predicting the thinner sandstone bands are introduced. This gives more than double the number of thinner sandstone bands predicted from the regression line calculated from the data of 6mm or thicker.

These data show that it is possible to predict the number of thinner sandstone bands based on distributions of thicker units, depending on the required accuracy. However studies of different field sites shows varying distributions (Sinclair and Cowie 2003, Talling 2001). But, how do the distribution of these thinner sandstone bands relate to previously observed distributions in thicker units?

Previous studies on turbidite thickness distributions have focussed on thicker beds than were measured in this study of very distal turbidites, e.g. Sinclair and Cowie (2003) and did not record any turbidites below 10cm thickness. Even in these studies of thicker turbidites there is no simple relationship accepted for predicting thickness distributions of turbidite deposited sandstone bands (Sinclair and Cowie 2003, Bokman 1953, Atkinson 1962). Different studies found exponential (Sinclair and Cowie 2003), log-normal (Talling 2001) or power law (Hiscott et al. 1992) distributions of turbidite thicknesses (figure 8.5). The variations in thickness distribution are attributed to differences in the depositional topography, e.g. channelised vs non-channelised material flows (Carlson and Grotzinger 2001). Log-normal distributions have been attributed to under-sampling of thin beds although it is disputed whether this distribution is due to under-sampling or a true reflection of material deposition (Talling 2001).

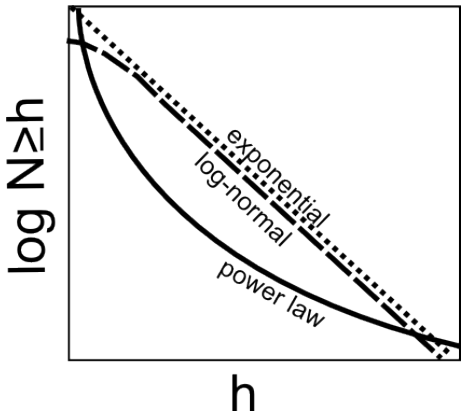

Figure 8.5: Different thickness distributions proposed for turbidite beds on log(y) vs. x axis, from Sinclair and Cowie 2003. "h" is thickness of sandstone bands, therefore "N≥h" is number of bands greater than or equal to the respective thickness.

The data collected from the Girvan field site show that these distal turbidite deposits follow an negative exponential distribution (figure 8.4). Note that the slope of the regression was 0.18 when the beds were plotted in millimetres (i.e. figure 8.4) but is now 180 when plotted in metres (figure 8.6). In figure 8.6 the thickness data distribution from this study is compared with a previous study by Sinclair and Cowie 2003, which did not record any bands of less than 10cm thickness. Sinclair and Cowie (2003) found that the distribution generally followed a negative exponential trend with a slope of 0.33. However in the thinner beds the slope increased to 1.3 (figure 8.6). The slope of the distribution in this study is 180 which is two orders of magnitude steeper than from Sinclair and Cowie (2003).

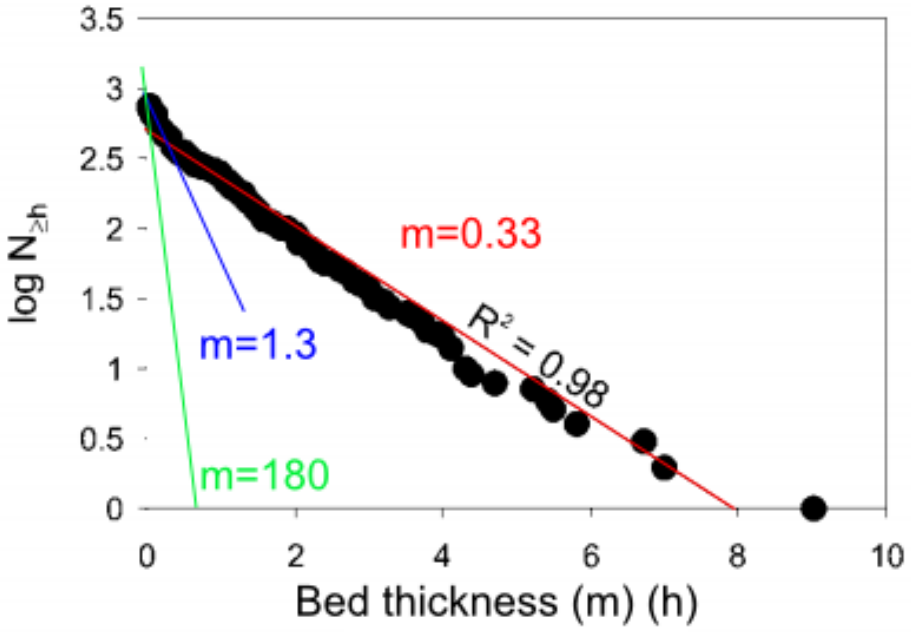

Figure 8.6: Cumulative frequency - thickness plot of turbidite thicknesses of the Annot Sandstone. A regression line with slope of 0.33 fits the data, for the smallest turbidites the slope of the regression line steepens to 1.3, from Sinclair and Cowie 2003. The 180 slope of the green line is an approximation of the trend of the data presented in this thesis from figure 8.4.

Due to such thin turbidites (<1cm) previously being poorly reported, they are cautiously compared directly with past studies at different field locations. A compli-

cated range of factors affect thickness distributions, such as depositional setting, location within depositional setting and magnitude of triggering event (Carlson and Grotziner 2001, Turcotte 1997). Additionally a turbidite flow undergoes buoyancy changes as it travels and deposits material therefore becoming a "thinner" mass flow (Pritchard and Gladstone 2009); which may also create difficulties comparing thicker and thinner deposits. These factors show the importance of basin modelling and correct characterisation of depositional environments in making accurate predictions of such fluid flow networks. Sedimentary logging from drilling would give quite different results in different areas of a submarine fan, for example. It would be necessary to position the drill was in the submarine fan environment (i.e. distal or proximal) to be able to extrapolate the results to areas between the exploratory boreholes. A further consideration is that mudstone formations (such as the formation studied in this thesis and the Bowland Shale in NW England) may be deformed, such as by folding. Such deformation would require restoration to better constrain the distribution of sedimentary features within the formation. These restorations would allow clearer analysis of the depositional setting, allowing predictions to be combined with fault distributions the predict the locations of key networks which might act to focus fluid flow.

Despite these difficulties this study does show that with careful logging, it may be possible to predict the distribution of very thin undetectable sandstone bands. Further field studies are needed to characterise the controls on the thickness distribution of very thin (<1cm) bands in the most distal part of turbidite sequences.

8.3.2 Detection and prediction of faults and fractures

Almost all the structural features described over the field site are at a sub-seismic scale so would not be detected by seismic surveys; if seismic detectability is assumed to be a fault offsetting the bedding by 10m. The 9.5m combined offset of the main and splay faults could possibly be detected if strong reflectors were intersected. Faults and fractures could be detected by exploratory drilling (Gutmanis et al.

1998, Seeberger and Zoback 1992, Paillet et al. 1987, Pezand et al 1988) although larger features are easier to detect. However the faults described in this study are thin features in complicated three dimensional space, meaning that any one borehole will only intersect a sample of the regional fault population, if any at all. Horizontal drilling would be much more likely to intersect (and therefore detect) steeply dipping faults; as long as the drilling is closer to perpendicular than parallel to the fault strike. Even with horizontally deviated drilling the problem of predictability of sub-seismic faults remains, as only a subset would be detected. As a consequence it is necessary to be able to predict the frequency, orientations and connectivity of small fractures and faults from available data. There are relationships between fault throw and abundance that show smaller throw faults to be more common than larger throw faults (figure 8.7) with a power-law distribution (Bonnet et al. 2001, Manzocchi et al. 2009). Populations of sub-seismic faults could therefore potentially be estimated from the number of larger faults resolved from seismic data. Furthermore even though the subseismic faults are "invisible" prior to drilling they could still be targeted via their mechanical relationship to large faults (figures 8.7 and 8.8). Subseismic fault orientations could be predicted from analysing the orientations of seismic faults. This would allow orientations of investigative drilling to be established i.e. horizontal drilling perpendicular to prevailing fault strike. Such targeted drilling would allow optimum data collection to be able to characterise the spatial and orientation distributions of subseismic faults.

Stress regimes can also be assessed during drilling by geophysical techniques (Lei et al. 2012) and stress-induced borehole breakouts (Shamir and Zoback 1992). Results in this study indicate that fractures preferentially orientated within the proposed palaeo-stress field were open to fluid flow for a longer time. Therefore stress regimes can be used to identify likely orientations of sub-seismic faults that are more likely to behave as fluid flow conduits (i.e. critically stressed), in addition to information gathered from seismically resolvable fault orientations.

Gartrell et al. (2004) found seismic scale fault intersections created areas of hydrocarbon leakage. This is also found in mineral deposits (Micklethwaite and Cox

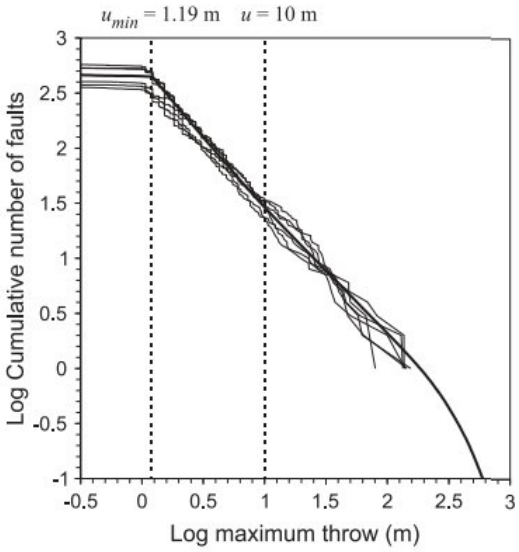

Figure 8.7: Field data gathered on cumulative distributions of throw, showing a power law distribution. From Manzocchi et al. 2009.

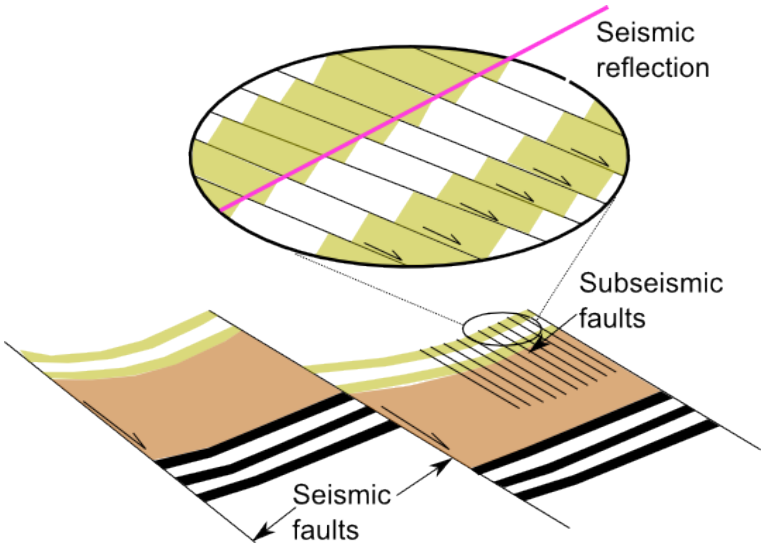

Figure 8.8: Cartoon showing relationship between seismically resolvable and subseismic faults. Pink line shows approximate layer boundary that would be picked up by seismic surveys, which would give no indication of the presence of the subseismic faults. From Fossen 2008.

2004). The central area between the two closely spaced faults has hosted continued enhanced fluid flow due to the higher fracture density. The enhanced fracture density and connectivity between the main fault and splay fault shows that sub-seismic faults could have similar influences on fluid flow. Although creating statistical populations of sub-seismic fault populations from seismic and drill data may be possible, the research from Girvan corroborates past studies that often find that the fault interaction areas are the most important for fluid flow.

8.3.3 Designing subsurface investigation to be able to detect both sandstone bands and fractures

Above, methods are discussed and proposed for detecting the sandstone bands or the fractures with the faults. Exploratory drilling with appropriate logging tools or core logging are currently the only viable methods for detection of small-scale sedimentary and structural features during subsurface investigation. Borehole orientation is a key parameter to gain good data for characterising both the distribution of sandstone bands and the distribution of faults and fractures by intersecting as many features as possible. However where flow networks are formed by two sets of intersecting features with different orientations multiple borehole orientations will be needed. In this field example orientation of faults and fractures are $+/-$ 30° of NNW-SSE, quite different to the observed ESE-WNW orientation of sandstone bands.

To test how orientations and locations of exploratory boreholes influences data collection, a number of "boreholes" were drawn across the field map in five different orientations (figure 8.9). The five example borehole directions are Bed perpendicular (y-direction), bed parallel (x-direction), into the page (z-direction), fault parallel (FPa), and fault perpendicular (FPe).Three boreholes were drawn for three of the five different orientations (y1-y3, FPa1-FPa3, FPe1-FPe3) to provide more information on how borehole locations in different areas of the field site would affect which features are intersected. This was not done for x-orientation as high or lower borehole lines on the map would mean the borehole intersected large areas outside the detailed study area. Table 8.2 shows how many of the different features were intersected by each borehole normalised by length. Features were best detected by boreholes that are nearer to perpendicular to the general orientation distribution of a set of features.

The sandstone bands were best detected by the y-orientation boreholes (figures 8.9 and 8.10), also several of the fault-perpendicular and also fault-parallel orientation boreholes provided good detection of the sandstone bands (FPa1, FPa2, FPe1,

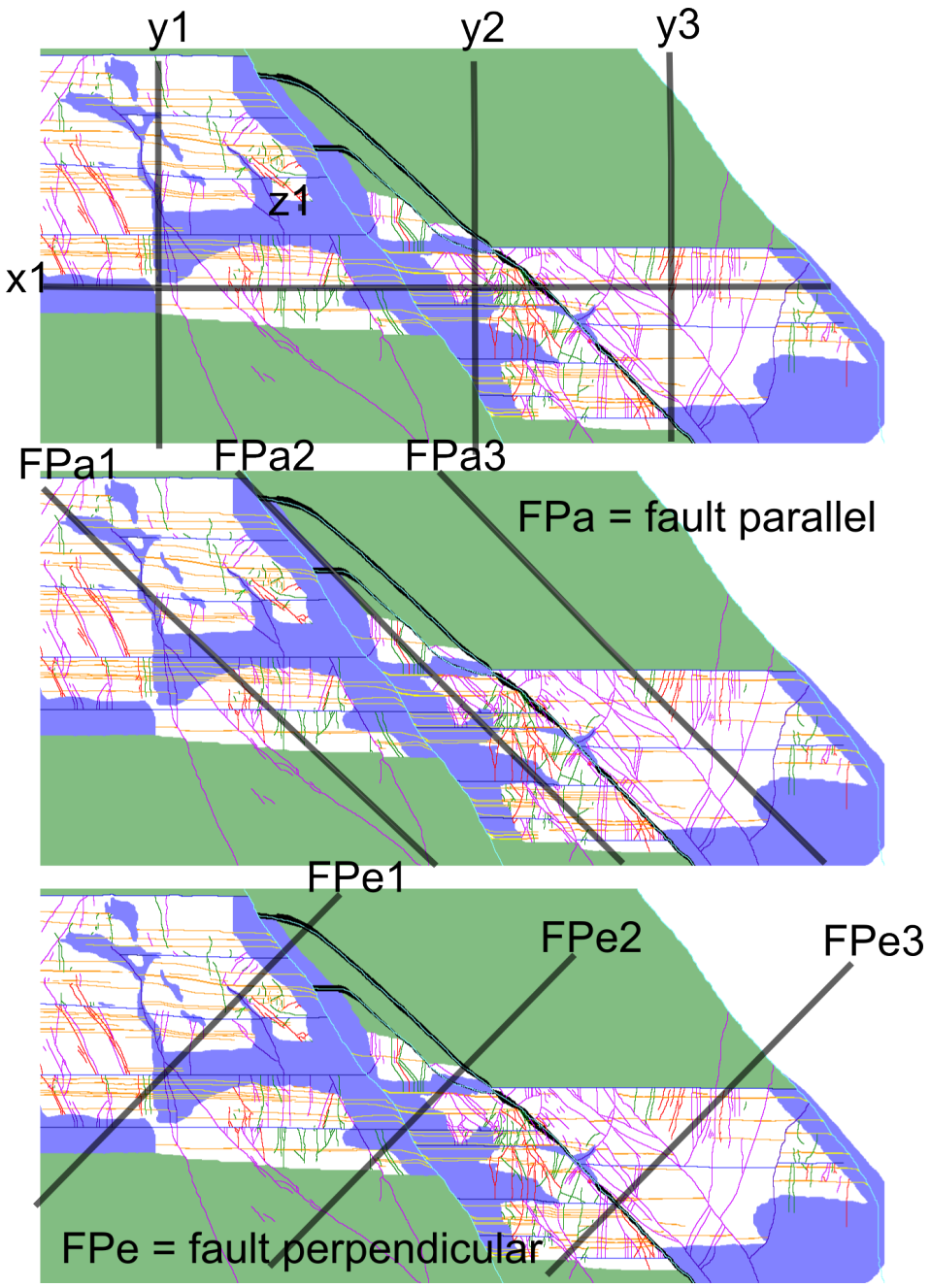

Figure 8.9: Different borehole directions and locations over field site. z1 only shows as a dot as the orientation is directly into the page.

FPe3). The thrusts are the same orientation as the sandstone bands on the map so were well detected by the same boreholes. In three dimensions the thrusts would

Drill example	faults detected	fractures	sandstone bands	Thrusts
y1	0	12.4	71.3	15.5
y2	15.3	25.5	76.5	10.2
y3	3.9	31.2	27.3	7.8
x1	3	73	2	0
z1	0	0	0	0
FPa1	0	36	45.6	7.2
FPa2	5.1	37.4	30.6	6.8
FPa3	0	42.9	7.8	7.8
FPe1	5.6	33.6	47.6	11.2
FPe2	14.1	32.9	32.9	4.7
FPe3	6.8	88.4	44.2	10.2

Table 8.2: Numbers of each features intersected by the borehole examples shown in figure 8.9. These numbers have all been normalised with respect to borehole length within the mudstone (white area of figure 8.9). This table is presented graphically in figure 8.10.

dip into the page so z1 would be the preferred orientation of the example boreholes to detect the thrusts. The faults were detected well by the x-direction borehole and also by FPa2, FPe1, FPe2, FPe3 and y2. However for FPa2 and y2 this was due to fortunate location rather than preferential orientation and the other boreholes of these orientations failed to detect the faults. x1 is also an orientation that gives good detection of the fractures (figure 8.10). FPa1-3 and FPe1-3 also provide good orientation to the fractures, particularly FPe3.

Variations occur in features intersected between example boreholes of the same orientation. I.e. y1 intersecting the equivalent of 71.3 sandstone bands but y3 only 27.3 (table 8.2). This is due to the variations in the density of sandstone bands and fractures across the field site.

An optimum borehole would be one which is able to collect enough information to characterise both the sedimentary and structural features. The fault-perpendicular orientations (FPe1-FPe3) intersect with a subset of both sandstone bands and struc-

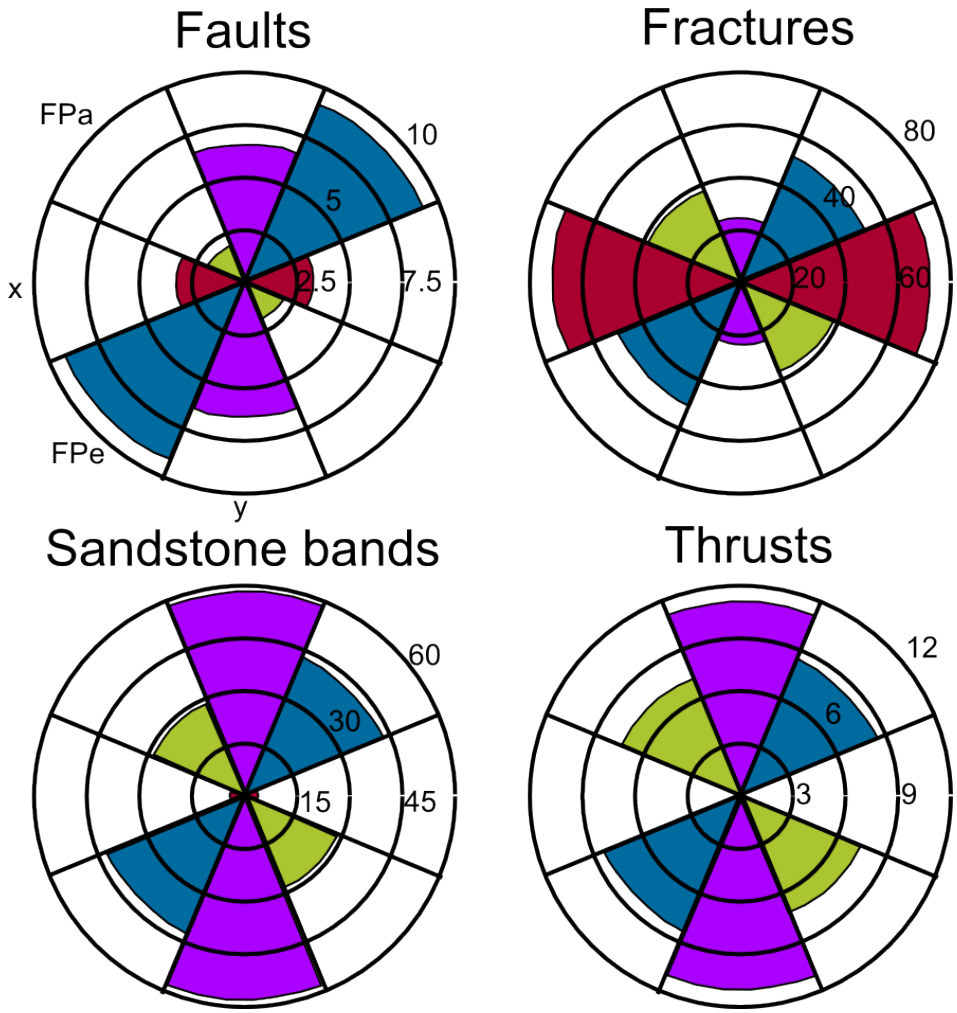

Figure 8.10: Rose diagram graphical representation for values from table 8.2. Green petals show frequency of features intersection in FPa-direction, red in x-direction, blue in FPe-direction, and purple in y-direction. Rose diagrams and petals are orientated to match directions of example boreholes in figure 8.9. The numbers on the concentric circles show the relative magnitude for each rose diagram. Mean values are used for orientations with more than one example borehole (i.e. FPa, FPe, and y).

tural features. This is shown by the fault-perpendicular orientations having consistently larger petal magnitudes in the rose diagrams of figure 8.10. Whereas y or x direction petal magnitude varies considerably between different rose diagrams.

Using multiple boreholes to fully characterise different parts of similar fluid flow sys-

tems may seem like the best solution from these hypothetical examples. With each borehole orientation designed to detect specific features. These borehole examples show that both sub-seismic sedimentary and structural features can be detected by boreholes with orientations that are optimal, fault-perpendicular orientations would be most optimal in this field example. However exploratory boreholes are expensive to drill, and would be much wider spaced than the field site in this study. For example, in a previous Nirex study to characterise the fluid flow systems in the Sellafield area boreholes were spaced hundreds of metres to kilometres apart (Gutmanis et al. 1998). Additionaly each borehole is creates an added risk of providing a new fast flow path from depth to the surface, if there are occurrences of casing failure.

Planning such optimal borehole orientations would require prior information on likely orientations of features identified as key potential fluid flow pathways. For sub-seismic faults this could be achieved by orientations of seismically resolvable faults. For sedimentary systems by applying knowledge of the influence of palaeo-topography of the depositional setting on the course of the turbidite flows. Outcrops of targeted formations would also provide information on the size, properties and spatial distribution of small scale fracture and sedimentary features. Which was necessary, for instance, to begin to understand the flow regimes of the Clair oil field (Wilson et al. 2010).

Such borehole data can be corrected to compensate for preferential orientaion of different features (Terzaghi 1965). The orientation bias corrections are based on the concept that the number of observations of a set of features is a function of the angle between that set of features and the borehole (Terzaghi 1965). An equation Terzaghi 1965 used to correct the orientation bias is

$$N_{90} = \frac{N_a}{sin(a)} \tag{8.1}$$

where N_a is number of features intersected by a borehole at an angle of a to these features. N_{90} is number of features that would have been intersected if the borehole was 90° to the features.

Figure 8.11 show the data from table 8.2 and figure 8.10 corrected for orientation

bias using equation 8.1. To simplify the correction process the fractures have been assumed to be all of the same orientation perpendicular to the sandstone bands, a more thorough correction would split the fractures into groups depending on their orientation and apply the correction factor to each of these groups.

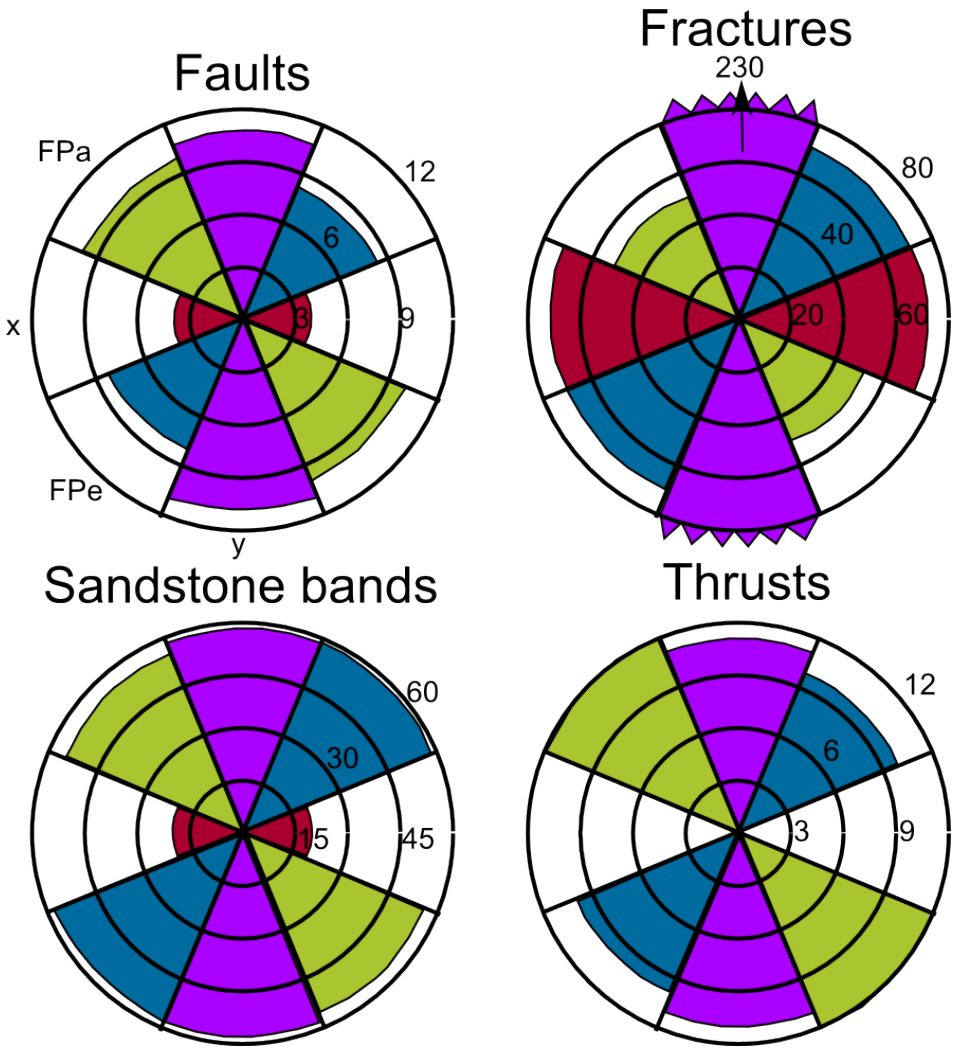

Figure 8.11: Rose diagram graphical representation for values from table 8.2 which have been corrected for orientation (Terzaghi 1965). The y-direction (purple petal) borehole detected fractures were several times higher than the other orienations due to the correction bias, for this reason the scale on this rose diagram has been condensed to allow clearer comparison betwen the other orienations.

The petal sizes for the fault parallel (FPa) and fault perpendicular (FPe) examples borehole orientations (figure 8.11) are much more similar than the uncorrected data (figure 8.10). Although the correction does not lead to perfectly matching results, as the fault-parallel example boreholes (FPa-green petals figure 8.11) have a higher estimate for the number of faults and thrusts than the the fault-perpendicular example boreholes (FPe-blue petals figure 8.11). Conversely, the fault-perpendicular has a higher estimate for the fractures than the fault-parallel example boreholes. The corrections for both fault-parallel and fault-perpendicular are particularly effective for estimation of sandstone bands, with both being close to the y-direction example borehole which is the optimal orientation for collecting data about the sandstone bands. This technique has not worked as well for features sub-parallel with the example boreholes. Some features are over-estimated such as the fractures intersected by the y-direction borehole (purple petal figure 8.11), while others are under-estimated such as both the sandstone bands and thrusts intersected by the x-direction borehole (maroon petal 8.11). However this may be due to the scale of the outcrop. In a larger outcrop area an example borehole sub-parallel to a set of features would be more likely to intersect a small but representative sample of these features.

A range of borehole orientations would therefore still be useful to constrain the distribution of features, even with the application of orientation bias corrections. Although useful to estimate how much a certain set of features is under-estimated in the data, these orientation corrections are strongly influenced by small changes in small samples of data collected of features sub-parallel to the borehole. Using multiple orientation of boreholes allows checks to be made for significant under or over estimation of intersected features for boreholes of a particular orientation.

8.4 Incorporating these results in a large scale geological flow model

Faulted rocks have previously been modelled as a series of fault bounded blocks (Hoffman and Neave 2007) with permeability applied to each fault block. However in a closely spaced subseismic fault block system only a very few fault blocks will be intersected by exploratory drilling. This requires the remaining population to be predicted based on distributions of seismically resolvable faults and borehole data.

During this study, the field site was split into three fault-bounded blocks, the southern, central and northern area. Fluid flow modelling showed the features in the three fault blocks resulted in significant differences in bulk permeability. Bulk permeability of the fault blocks is represented in figure 8.12, as ellipses where length and width is proportional to the log of modelled bulk permeability. These bulk permeability variations were caused by contrasting poorly and well developed flow networks in the different fault blocks. A well developed flow network was maintained in the central area in between fluid flow episodes, whereas in the southern and northern areas calcite mineralisation of fractures removed them from the flow network, leading to the smaller ellipses for FFE2 shown in figure 8.12.

When closed to fluid flow (as was the case for FFE2) the faults may create compartmentalisation between the flow networks in the fault blocks. Several algorithms exist that attempt to predict the sealing behaviour of faults and incorporate fault seal into reservoir models (Manzocchi et al. 1999, Fisher and Jolley 2007). Allan Diagrams analyse the juxtaposition of different rock units across a fault to estimate sealing behaviour of faults in sand/shale sequences. Shale Gouge Ration (SGR) uses the amount of shale in a faulted sequence and combines that with faults throw (Yielding et al. 1997) to determine if there is enough shale material to create a seal to fault-perpendicular fluid flow. Figure 8.13 shows how with higher SGR values a higher pressure difference can be supported across a fault. Both of these approaches would predict the faults studied to be good seals throughout the field site at Girvan. The SGR of the Girvan field site is shown with the red line in figure 8.13 and is

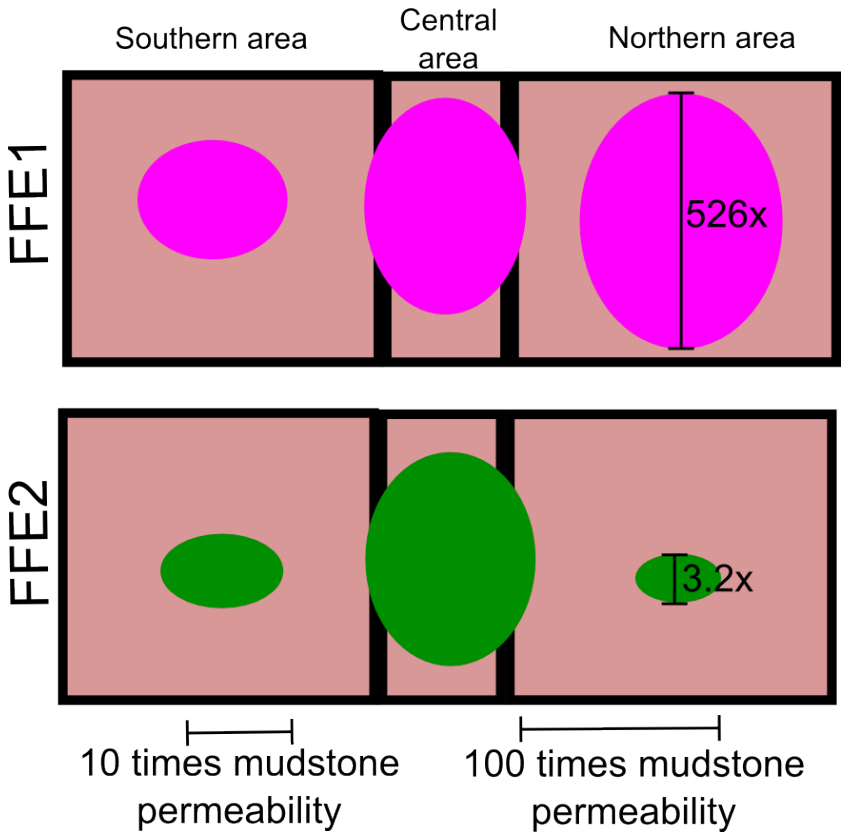

Figure 8.12: Ellipses show permeability enhancement of different fault blocks relative to each other, based on modelling in chapter 7. The vertical axis of ellipse shows the y-direction permeability (bottom to top of page) the horizontal axis the x-direction permeability (left to right of page). Permeability is shown in a log scale on the ellipses, annotations show values for y-direction permeability enhancement in northern area for FFE1 and FFE2 and scale bars show magnitude for 10 and 100 times mudstone permeability enhancement.

sealing for a large range of across fault pressure differences. This was calculated with the following equation:

$$SGR = \frac{\sum shale\ bed\ thickness}{fault\ throw} \tag{8.2}$$

However a more accurate version of SGR takes into account the clay content. This was calculated in chapter 4 to be 50%. This is shown in the blue line on figure

8.13, and shows the fault to be still sealing but to less of a pressure difference than with the simpler equation. The blue line value was calculated with the following equation:

$$SGR = \frac{\sum[zone\ thickness\ x\ zone\ clay\ fraction]}{fault\ throw} \tag{8.3}$$

This sealing behaviour is not supported by the evidence of past mineralisation that demonstrates the occurrence of palaeo-fluid flow events. The faults during FFE2 showed similar sealing behaviour as that predicted by SGR, however the sealing behaviour was due to calcite mineralisation not the properties of the mudstone.

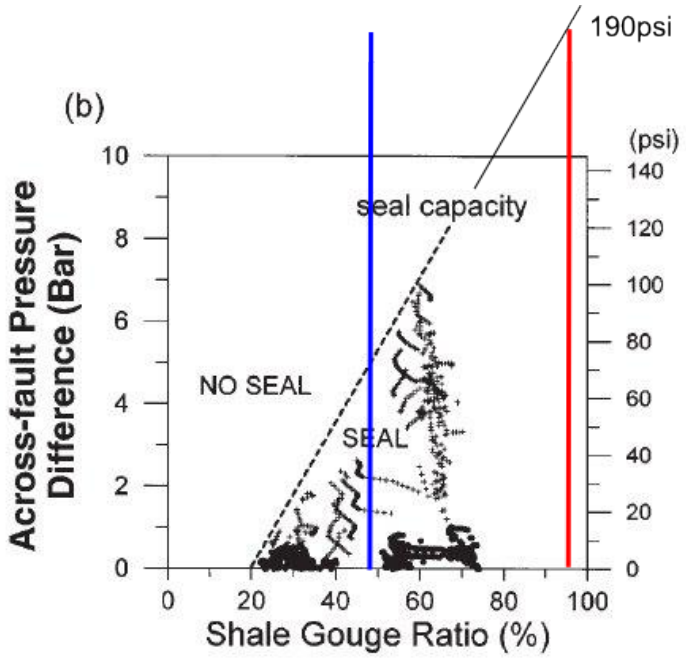

Figure 8.13: Graph of SGR from Yielding et al. 1997. Red line shows where the faults at Girvan would be according to the SGR algorithm; very far into the sealing side of the graph. The continued seal/no seal boundary shows that a fault like the main fault at the field site could hold a hydrocarbon column generating a pressure of 190psi.

SGR and Allan diagrams do not take into account fault parallel fluid flow which occurred during FFE1 when the faults presented conduits to flow along fault-strike.

These thin conduits would result in significant permeability anisotropy and lead to preferential flow directions for fluid migration. Due to the scale of reservoir models they are too numerically intensive to discretely represent all such sub-seismic faults (Harris et al. 2007). Flow anisotropy presented by the faults is therefore upscaled as anisotropic grid cell permeability or as inter-cell transmissibility multipliers (Knai and Knipe 1998). Although these approaches attempt to broadly represent the bulk flow rates of a system, the fast flow paths which can be created by faults (e.g. Fairley and Hinds 2004) are not well represented and can lead to inaccurate predictions and problems such as unexpected water breakthrough in hydrocarbon reservoirs (e.g. Al-Dhafeeri and Nasr-El-Din 2007).

Approaches such as percolation theory may help to estimate bulk permeability properties in these situations. Using a percolation theory approach (e.g. Renshaw 1999) permeability would be increased when the fracture system was above the critical percolation threshold, i.e. where a connected fracture system existed across the mudstone. However past percolation theory investigations have not considered a system such as this; where the presence of sandstone bands provides additional permeable pathways between the fractures. With the sandstone bands the bulk permeability may respond twice to two different percolation thresholds (figure 8.14). An increase in fracture density increases the likelihood of the existence of a a combined sandstone band - fracture network; the system has reached the sandstone band percolation threshold (SMBT). Further increases in fracture density may mean that the fracture network reaches percolation threshold (FOPT-figure 8.14) without the support of sandstone bands. Such an adapted percolation theory approach may be useful for predicting areas of enhanced permeability in a similar mudstone to this study. It would require further investigation to test how accurately such a sandstone band-fracture system could be simulated with a percolation theory approach.

Based on the research presented in this thesis, sedimentary-structural fluid flow networks can exert important controls on subsurface fluid flow. The requirement to explicitly represent such networks, however, depends on the industrial application and the scale of the analysis. For example, a model which has large grid cell

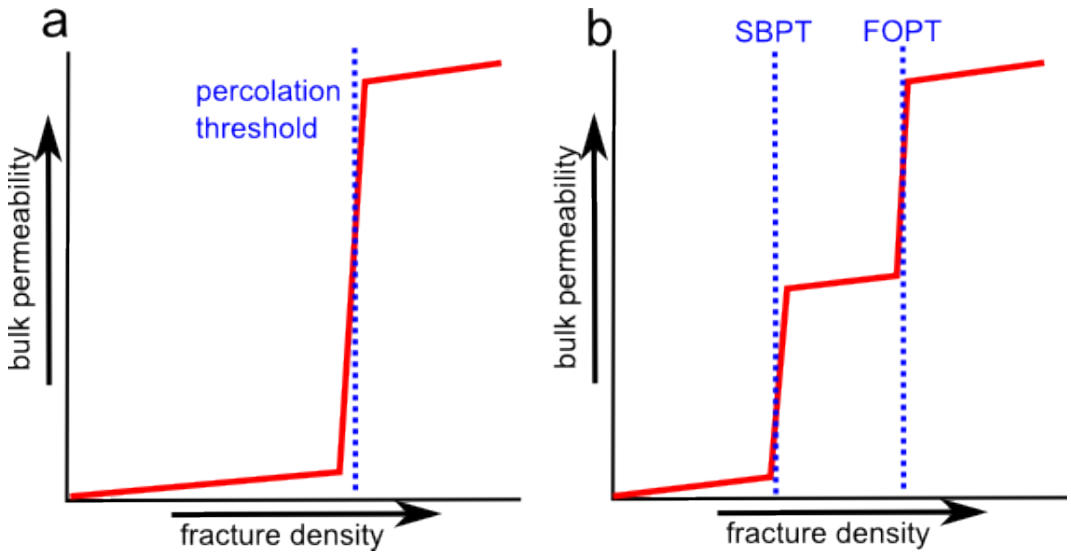

Figure 8.14: a. As fracture density increases the percolation threshold is reach resulting in enhanced bulk permeability. b. As fracture density increases the sandstone band percolation threshold (SBPT) is reached with a small enhancement in bulk permeability then further increases in fracture density allows the fracture only percolation threshold (FOPT) to be reached further enhancing bulk permeability.

sizes (e.g. a hydrocarbon reservoir model) may be able to adequately incorporate sedimentary-structural networks using an average anisotropic grid cell permeability if the cells are sufficiently large, in comparison to the density of high permeability features, so that they form a "representative elementary volume (REV)". Even in this case, however, whilst flow may be well predicted, the connectivity of the network may still have a strong influence on contaminant migration and which could lead to significant over-estimates of contaminant dispersion. Hence in applications such as geological disposal of radioactive waste, it may be necessary to develop other modelling approaches that better represent the structural and sedimentary heterogeneity and hence can better constrain key uncertainties such as the transport time for radionuclide migration from depth to the ground surface.

8.5 References

Al-Dhafeeri, A. M. and Nasr-El-Din, H. A. 2007. Characteristics of high-permeability zones using core analysis, and production logging data. *Journal of Petroleum Science and Engineering*. v.**55** i.**1-2**. pp. 18-36.

Aplin, A. C., Macquaker, J. H. S. 2011. Mudstone diversity: Origin and implications for source, seal, and reservoir properties in petroleum systems. *AAPG Bulletin*. v.**95** i.**12**. pp. 2031-2059.

Atkinson, D. J. 1962. Tectonic control of sedimentation and the interpretation of sediment alternation in the Tertiary of Prince Charles Foreland. *Geological Society of America Bulletin*. **73**. pp. 343-364.

Bokman, J. 1953. Lithology and petrology of the Stably and Jackfork formations. *Journal of Geology*. v.**61**. pp.

Carlson, J. and Grotzinger, J. P. 2001. Submarine fan environment inferred from turbidite thickness distributions. *Sedimentology*. v/textbf48. pp. 1331-1351.

Childs, C., Walsh, J. J., Manzocchi, T., Strand, J., Nical, A., Tamosso, M., Schopfer, M. P. J. and Aplin, A.C. 2007. Definition in a fault permeability predictor from outcrop studies of a faulted turbidite sequence, Taranaki, New Zealand. *From*: Jolley, S. J., Barr, D. Walsh, J. J. and Knipe, R. J. (eds) *Structurally Complicated Reservoirs*. Geological Society, London, Special Publications, **252**. pp. 235-258.

Curewitz, D. and Karson, J.A. 1997. Structural setting of hydrothermal outflow: Fracture permeability maintained by fault propagation and interaction. *Journal of Volcanology and Geothermal Research*. **79**. pp. 149-168.

Dewhurst, D. N., Yang, Y. and Aplin, A. C. 1999. Permeability and fluid flow in natural mudstones. *From*: Aplin, A. C., Fleet, A. J. and Macquaker, J. H. S. (eds). *Muds and Mudstones: Physical and Fluid-Flow Properties*. Geological Society, London, Special Publication. **158**. pp. 23-43.

Dewhurst, D. N. and Siggins, A. F. 2006. Impact of fabric, microcracks, and stress field on shale anisotropy. *Geophys. J. Int.* v.**165**. pp. 135-148.

Eichhubl P. and Behl R.J. 1998. Diagenesis, deformatiojn, and fluid flow in the Miocene Monterey Formation, Arroyo Burro Beach, Santa Barbara, California. *In*: Eichhubl, P. (Ed.), Diagenesis, Deformation, and Fluid Flow in the Miocene Monterey Formation of coastal California. SEPM Pacific Section Special Publication. **83**. pp. 15-36.

Engelder, T., Lash, G. G. and Uzcategui, R. S. 2009. Joint sets that enhance production from Middle and Upper Devonian gas shales of the Appalachian Basin. *AAPG Bulletin*. v.**93** no.**7**. pp. 857-889.

Fairley, J.P. and Hinds, J.J. 2004. Rapid transport pathways for geothermal fluids in an active Great Basin fault zone. *Geology*. v.**32**. pp. 825-828.

Fisher, Q. J. Jolley, S. J. 2007. Treatment of faults in production simulation models. *From*: Jolley, S. J., Barr, D., Walsh, J. J. and Knipe, R. J. (eds) *Structurally Complex Reservoirs*. Geological Society, London, Special Publications, **292**, 219-233.

Gartrell, A., Zhang, Y., Lisk, M. and Dewhurst, D. 2003. Enhanced hydrocarbon leakage at fault intersections: an example from the Timor Sea, Northwest Australia. *Journal of Geochemical Exploration*. v.**78-79**. pp. 361-365.

Guo, J., Underwood, M. B., Likos, W. J. and Saffer, D. M. 2013. Apparent overconsolidation of mudstones in the Kumano Basin of southwest Japan: Implications for fluid pressures and fluid flow within a forearc setting. *Geochemistry, Geophysics, Geosystems*. v.**14** i.**4**. pp. 1023-1038.

Hart, B. S. 2006. Seismic exression of fracture-swarm sweet sports, Upper Cretaceous tight-gas reservoirs, San Juan Basin. *AAPG Bulletin*. v.**90** no.**10**. pp. 1519-1534.

Harris, S. D., Vaszi, A. Z. and Knipe, R. J. 2007. Three-dimensional upscaling of

fault damage zones for reservoir simulation. *From*: Jolley, S. J., Barr, D., Walsh, J. J., and Knipe, R. J. (eds) *Structurally Complex Reservoirs*. Geological Society, London, Special Publications, **292**, pp. 353-374.

Hiscott, R. N. Colella, A., Pezard, P., Lovell, M. A. and Malinverno, A. 1992. Sedimentology of deep-water volcaniclastics, Oligocene Izu-Bonin forearc basin, based on formation microscanner images. *In* Taylor, B. and Fujioka K., eds. Proceedings of Ocean Drilling Project, Scientific Results 126: pp. 75-96.

Hoffman, K. S. and Neave, J. W. 2007. The fused fault block approach to fault network modelling. *From*: Jolley, S. J., Barr, D., Walsh, J. J. and Knipe, R. J. (eds) *Structurally Complex Reservoirs*. Geological Society, London, Special Publications, **292**, 75-87.

Ince, D. (1984). Sedimentation and tectonism in the middle Ordovician of the Girvan district, SW Scotland. *Transactions of the Royal Society of Edinburgh: Earth Sciences*. v.**75**. pp. 225-237.

Ingham, J. K. 1978. Geology of a continental margin 2: Middle and Late Ordovician transgression. Geol. J. Spec. Issue No. 10, 115-138.

Ingram, G. M and Urai, J. L. 1999. Top-seal leakage through faults and fractures: the role of mudrock properties. *From*: Aplin, A. C., Fleet, A. J. and Macquaker, J. H. S. (eds). *Muds and Mudstones: Physical and Fluid-Flow Properties*. Geological Society, London, Special Publication. **158**. pp. 125-135.

Jackson, D. I., Mullholland, P., Jones, S. M. and Warrington, G. 1987. The geological framework of the East Irish Sea Basin. 191-203 in Brookes, J. and Glennie, K. (editors), *Petroleum Geology of North West Europe*.

Knai, T. A., and Knipe, R. J. 1998. The impact of faults on fluid flow in the Heidrun field. *In*: Jones, G., Fisher, Q. J., and Knipe, R. J. (eds) *Faulting, Fault Sealing and Fluid Flow in Hydrocarbon Reservoirs*. Geological Society, London, Special Publications, **147**, pp. 269-282.

Lash, G., Loewy, S. and Engelder, T. 2004. Preferential jointing of Upper Devonian black shale, Applalachian Plateau, USA: evidence supporting hydrocarbon generation as a joint-driving mechanism. *From:* Cosgrove, J. W. and Engelder, T. (eds). *The Initiation, Propagation, and Arrest of Joints and Other Fractures.* Geological Society London, Special Publications, **231**, 129-151.

Lei, T., Sinha, B. and Sanders, M. 2012. Estimation of horizontal stress magnitudes and stress coefficients of velocities using borehole sonic data. *Geophysics.* v.**77** i.**3**. pp. 1-26.

Manzocchi, T, Walsh, J. J. Nell, P. 1999 Fault transmissibility multipliers for flow simulation models. *Petroleum Geoscience.* v.**5** i.**1** pp. 53-63.

Mazureck, M., Alt-Epping, P., Bath, A., Gimmi, T. and Waber, H. N. 2009. Natural Tracer Profiles Across Argillacious Formations: The CLAYTRAC Project. *Nuclear Energy Agency - Organisation for Economic Co-Operation and Development.*

McKeown, C. 1997. *A model approach to radioactive waste disposal at Sellafield.* Ph.D. Thesis. University of Glasgow: UK.

Micklethwaite, S. and Cox, S. F. 2004. Fault-segment rupture, aftershock-zone fluid flow, and mineralization. *Geology.* v.**32** no.**9**. pp. 813-816.

Paillet, F. L. Hess, A. E. Cheng, C. H. and Hardin, E. 1987. Characterization of fracture permeability with high-resolution vertical flow measurements during borehole pumping. *Ground Water.* v.**25**. pp. 28-40.

Pater, C. J. and Baisch, S. 2011. Geomechanical Study of Bowland Shale Seismicity. *Caudrilla Synthesis Report.*

Pritchard, D. and Gladstone, C. 2009. Reversing buoyancy in turbidity currents: developing a hypothesis for flow transformation and for deposit facies and architecture. *Marine and Petroleum Geology.* v.**26**. pp, 1997-2010.

Railton, A. and Clark, C. 2012. High-resolution LWD imaging provides fresh insights into offshore Angola's Pinda reservoir. *World Oil Magazine.* v.**223** no.**1**.

Renshaw, C. E. 1999. Connectivity of joint networks with power law length distributions. *Water Resources Research*. v.**35**. i.**9**. pp. 2661-2670.

Robinson, E. S., and Coruh, C. Basic Exploration Geophysics. John Wiley and Sons, New York.

Shamir, G. and Zoback, M. D. 1992. Stress orientation profile to 3.5km depth near the San Andreas Fault at Cajon Pass, California. *Journal of Geophysical Research: Solid Earth*. v.**97** i.**B4**. pp. 5059-5080.

Sinclair, H. D. and Cowie, P. A. 2003. Basin-Floor Topography and the Scaling of Turbidites. *The Journal of Geology*. v.**111**. pp. 277-299.

Strong, G. E., Milodowski, A. E., Pearce, J. M., Kemp, S. J., Prior, S. V. and Morton, A. C. 1994. The petrology and diagenesis of Permo-Triassic rocks of the Sellafied area, Cumbria. *Proceedings of the Yorkshire Geological Society*. v.**50** p.**1**. pp. 77-89.

Talling, P. J. 2001. On the frequency distribution of turbidite thickness. *Sedimentology*. v.**48**. pp. 1297-1329.

Terzaghi, R. D. 1965. Sources of Error in Joint Surveys. *Geotechnique*. v.**15** i.**3**. pp. 287-304.

Todd, D. K. and Mays, L. W. 2005. *Groundwater Hydrology*. Hoboken. John Wiley and Sons Incorporated.

Turcotte, D. L. 1997. Fractals and chaos in geology and geophysics. Cambridge, Cambridge University Press, pp. 397.

Wilson, R. W., Holdsworth, R. E., Wild, L. E., Mccaffrey, K. J. W., England, R. W., Imber, J. and Strachan R. A. 2010. Basement-influenced rifting and basin development: a reappraisal of post-Caledonian faulting patterns from the North Coast Transfer Zone, Scotland. *From*: Law, R. D., Butler, R. W. H., Holdsworth, R. E., Krabbendam, M. and Strachan, R. A. (eds) *Continental Tectonics and Mountains*

Building: The Legacy of Peach and Horne. Geological Society London, Special Publications, **335**, 795-826.

Woodcock, N. H. 2012. Early Devonian Sedimentary and Magmatic Interlude and Iapetus Closure. In: Woodcock, N. H. and Strachan R. A. ed. 2012 *Geological History of Britain and Ireland*. Blackwell Publishing Ltd. pp. 110-111.

Yang, Y. and Aplin, A. C. 2007. Permeability and petrophysical properties of 30 natural mudstones. *Journal of Geophysical Research: Solid Earth*. v.**112** i.**B3**. DOI:10.1029/2005JB004243.

Yielding, G. Freeman, B. and Needham, D. T. 1997. Quantative fault seal prediction. *AAPG Bulletin*. v.**81** i.**6**. pp. 897-917.

Chapter 9

Conclusions and future work

> "I don't pretend we have all the answers. But the questions are certainly worth thinking about." – Arthur C. Clarke

9.1 Conclusions

This thesis provides a detailed study of a mudstone outcrop which extends conceptual understanding of fluid flow through such low permeability siliclastic settings. The results of the field study corroborate previous models (Cartwright et al. 2007, Ingram and Urai 1999) that suggest that under brittle mechanical conditions faults and fractures form the key conduits for fluid flow through mudstone seals. However a major uncertainty is the accurate prediction of the effect these features have on the permeability of mudstone (Ingram and Urai 1999).

The detailed field study of the mudstone outcrop showed how faults, fractures and sandstone bands can interact to form complicated fluid flow networks. Stress changes and chemical precipitation acted to close some faults and fractures to fluid flow diminishing the enhancement these networks had on the bulk permeability of the mudstone. However in an area, bounded by closely spaced faults, fractures remained

open to fluid flow maintaining the permeability enhancement in this area of fault interaction.

In the introduction, four key research questions were proposed based on gaps in outcrop studies of mudstone. The key findings in this study related to each question are detailed below:

1. **What were the controls over palaeo-fluid flow episodes in the studied mudstone outcrop?**

    - Subseismic faults and long well-connected shear fractures would have acted as key conduits, providing these features were open to fluid flow. Sandstone bands acted both to enhance the connectivity of these key conduits and to provide bed-parallel flow conduits.
    - When these key conduits (faults and shear fractures) were closed to fluid flow, then complicated networks of smaller fractures and sandstone bands acted to provide fluid flow conduits. These networks provided connected conduits over distances much larger than individual features.

2. **How are the fluid flow conduits spatially distributed?**

    - The sandstone bands show a steep exponential decrease in the frequency as thickness increases, with over 40 bands being $\geq$1mm but only three bands $\geq$10mm. This frequency decrease is two orders of magnitude higher than that observed in less distal turbidite units.
    - Fracture density varies over the field site. Areas of high and low fracture density are separated by the sub-seismic scale faults.

3. **How have these fluid flow conduit distributions changed over time?**

    - Many fractures that acted as key fluid flow conduits for the first recorded fluid flow episode (FFE1) were closed for the second fluid flow episode (FFE2). This closure is likely due to a combination of mineral precipitation and changes in stress fields. The change in stress field may have been

a reduction in differential stress (i.e. $\sigma_1 - \sigma_3$) which favoured a different fracture orientation to be critically stressed. However the enhanced density of fractures open to fluid flow was maintained in the central area, which was the smallest of the fault blocks due to closely spaced subseismic faults. This reflects other studies finding that faults interaction areas can be zones of enhanced fluid flow (Gartrell et al. 2003, Curewitz and Karson 1997).

- In all fault blocks there was also a change over time in the orientation distributions of flowing features. During FFE1 there were a mixture of shear fractures and joints in the fluid flow networks. During FFE2 the fluid flow networks were much more dominated by joints, and as a result had a much narrower orientation distribution.

4. **What has been the effect of these spatial and temporal variations of fluid flow conduits over the permeability properties of the mudstone?**

    - During FFE1, the networks of sub-seismic faults, well connected shear fractures, and sandstone bands increased the bulk permeability of the mudstone by over three orders of magnitude.
    - During FFE2, the permeability enhancement was maintained in the central area fault block, due to a high density of fractures hosting fluid flow.
    - Key fractures closing to fluid flow in the northern and southern areas fault block reduced the bulk permeability compared wtih FFE1. However the network of sparse fractures and sandstone bands acted to keep some permeability enhancement beyond if only the sandstone bands or only the fractures were present; highlighting the importance of connectivity and interaction between permeable features.

These key findings show how sub-seismic fault, fractures and sandstone bands interact to form fluid flow networks through a formation that would otherwise be considered a seal to fluid flow. The permeability enhancement caused by these

networks is much higher than what would have been achieved alone by sandstone bands or fractures. The potentially predictable distributions of fluid flow conduits show how a robust characterisation of likely subsurface permeability properties can be achieved even with the incomplete data that typically accompanies geological investigation. This outcrop study provides an important bridge in understanding between the small scale data collected from drill core and the large scale surface geophysical data (e.g. seismic surveys). Although subseismic there are quantifiable relationships showing how the distribution of smaller flow conduit features relates to larger freatures. These findings add to the global research effort to better understand subsurface fluid flow, by providing field evidence of which data are required to predict possible areas of enhanced fluid flow.

9.2 Future Work

9.2.1 Future work at the field site

The data collected in this study allowed conclusions to be made about fluid flow through mudstone. However further work at the field site will allow the fluid flow behaviour of the field site to be further revealed and characterised and answer the following questions:

- **What were the burial depths and likely mechanical properties of the mudstone during the fluid flow episodes?** Geochemical analyses (raman spectroscopy and thermometry) of fluid inclusions could be used to determine burial depths and temperatures of fluid flow episodes. Providing further insight into when in the geological history of the mudstone these fluid flow episodes occurred. This will provide better understanding over the subsurface environment and conditions the results should be applied.
- **Can different mineralisation episodes be determined from the calcite veins?** The calcite veins may have been caused by multiple fluid flow episodes.

Isotope studies can be used to elucidate which fractures hosted fluid flow for each calcite fluid flow episodes (Cox 2007) providing further insight into fracture development and the evolving fluid flow networks.

- **What are the origins of the fluids?** It is hypothesised in this thesis that the calcite may have originated from more calcium rich beds in the Lower Whitehouse Formation which underlay the studied red mudstone outcrop. Constraining the origins of the fluids will provide better understanding of the regional fluid flow properties of the formation.

9.2.2 Future work to create a more generic understanding of this type of fluid flow system

- **What are the differences in other outcrops of mudstone of similar depositional settings?** To find if the same distribution of sandstone band thickness occurs in other outcrops of similar depositional setting. To see how these distributions vary with sequences less distal to the submarine fan. Additionally what effects different deformational histories have on the combined fault-fracture-sandstone bands flow network distributions. This will show how site specific these results are.

- **Further quantify which general sandstone band and fracture distribution properties lead to a connected network forming?** Percolation theory modelling (Berkowitz 1995, Manzocchi 2002) could be conducted but adding sandstone bands alongside the fractures. This will improve understanding of how the different relationships between distribution properties (e.g density, orientation, length) of fractures and sandstone bands interact to form connected fluid flow networks.

9.3 References

Berkowitz, B. 1995. Analysis of Fracture Network Connectivity Using Percolation Theory. *Mathematical Geology*. v.**27** i.*4*. pp. 467-483.

Cartwright, J., Huuse, M. and Aplin, A. 2007. Seal bypass systems. *AAPG Bulletin*. v.**91** no.**8**. pp. 1141-1166.

Cox, S. F. 2007. Structural and isotopic constraints on fluid flow regimes and fluid pathways during upper crustal deformation: An example from the Taemas area of the Lachlan Orogen, SE Australia. *Journal of Geophysical Research*. v.**112**. B08208, doi:10.1029/1006JB004734.

Curewitz, D. and Karson, J.A. 1997. Structural setting of hydrothermal outflow: Fracture permeability maintained by fault propagation and interaction. *Journal of Volcanology and Geothermal Research*. **79**. pp. 149-168.

Gartrell, A., Zhang, Y., Lisk, M. and Dewhurst, D. 2003. Enhanced hydrocarbon leakage at fault intersections: an example from the Timor Sea, Northwest Australia. *Journal of Geochemical Exploration*. v.**78-79**. pp. 361-365.

Ingram, G. M and Urai, J. L. 1999. Top-seal leakage through faults and fractures: the role of mudrock properties. *From*: Aplin, A. C., Fleet, A. J. and Macquaker, J. H. S. (eds). *Muds and Mudstones: Physical and Fluid-Flow Properties*. Geological Society, London, Special Publication. **158**. pp. 125-135.

Manzocchi, T., 2002. The connectivity of two dimensional networks of spatially correlated fractures. *Water Resources Research*. v.**38**. DOI:10.1029/2000WR000180

Appendix A

Travelling to the study area on the Whitehouse Foreshore

The field site is located on Whitehouse Shore, a rocky beach a few miles South of the town of Girvan, South Ayrshire. Figure A.1 shows the location of the field site in relation to the rest of Scotland. There are currently no access issues for getting onto the site.

Grid Reference NX, 165 948

Getting to the site...

To the Layby...

By car: Get yourself onto the A77, travelling North or South as required. The site (figure A.2) is a few miles South of Girvan, Ayrshire. There is a lay-by that is the best place to park approximately 100 m South of the entrance to *Ardmillan Castle Holiday Park*. There are no charges for parking and no vandalism or theft has been encountered during many visits.

By Public Transport: A train service operates from Girvan train station but not too frequently so make sure to check the timetable. From the station a local taxi can

Figure A.1: Location of Girvan field site.

be booked (or book ahead) to take you to the site. A walk, if the weather permits, can be quite pleasant along the shore taking around an hour to get to the layby near the site. Walking South through Girvan you have the choice to take in the town centre or you can head around the coast to walk besides the links and beach. There are pedestrian walkways for all but a few hundred yards to the site and even where these are lacking there is a grassy verge to keep you safe from the traffic. Alternatively a walk along the beach is slower, especially as you will be distracted by the conglomerates, but nicer. Keep walking past *Woodlands Farm Shop* and then a few hundred metres after *Ardmillan Castle Holiday Park* you will find the lay-by.

On to the site...

The mapped field site that is the focus of this field study can be found by walking South along the road from the lay-by. After a few hundred metres you will find a concrete *three mile marker* (figure A.3). Turn directly towards the sea at the marker (figure A.4), walk towards the sea being careful of the grassy slope. The large gully running West towards the sea is the main fault gully of the field site.

Figure A.2: Parking and finding the site.

Figure A.3: Mile post which is located directly towards the road from the location of the field site.

Figure A.4: View from mile post over the site.